Thesis

High-Voltage CMOS Pixel Detectors for the ATLAS ITk Upgrade

ZAFFARONI, Ettore

Abstract

In this work the characterization of two sensors produced using the H35 and aH18 technologies by ams AG, the H35DEMO and the ATLASPIX1, is presented. The characterization focused on the charge-collection performance, the particle detection efficiency and the spatial and time resolution, measured before and after irradiation using protons and neutrons. The charge-collection performance has been studied using the transient current technique. The results have shown that the depletion depth increases significantly due to the acceptor removal effect of irradiation, which can compensate for the charge carriers loss caused by trapping. The particle detection efficiency and the space and time resolution have been studied in several testbeam campaigns. Results have shown an excellent efficiency, larger than 99%, which does not degrade after neutron irradiation. Proton irradiation, instead, produces a decrease in efficiency to 95% at a fluence of 1e15 neq/cm^2. These measurements have also allowed identifying a few shortcomings in the read-out circuitry, addressed in subsequent designs.

Reference

ZAFFARONI, Ettore. *High-Voltage CMOS Pixel Detectors for the ATLAS ITk Upgrade*. Thèse de doctorat : Univ. Genève, 2020, no. Sc. 5455

URN : urn:nbn:ch:unige-1385772
DOI : 10.13097/archive-ouverte/unige:138577

UNIVERSITÉ DE GENÈVE
Section de Physique
Département de physique nucléaire et corpusculaire

FACULTÉ DES SCIENCES
Professeur Giuseppe Iacobucci
Docteur Sergio Gonzalez-Sevilla

High-Voltage CMOS Pixel Detectors for the ATLAS ITk Upgrade

THÈSE

présentée à la Faculté des Sciences de l'Université de Genève
pour obtenir le grade de Docteur ès sciences, mention physique

par

Ettore Zaffaroni

de Milan (Italie)

Thèse n. 5455

GENÈVE
Atelier d'impression ReproMail
2020

UNIVERSITÉ DE GENÈVE

FACULTÉ DES SCIENCES

DOCTORAT ÈS SCIENCES, MENTION PHYSIQUE

Thèse de Monsieur Ettore ZAFFARONI

intitulée :

«High-Voltage CMOS Pixel Detectors for the ATLAS ITk Upgrade»

La Faculté des sciences, sur le préavis de Monsieur G. IACOBUCCI, professeur ordinaire et directeur de thèse (Département de physique nucléaire et corpusculaire), Monsieur S. GONZALEZ-SEVILLA, docteur et codirecteur de thèse (Département de physique nucléaire et corpusculaire), Monsieur T. GOLLING, professeur associé (Département de physique nucléaire et corpusculaire) et Monsieur N. CARTIGLIA, professeur (Istituto Nazionale di Fisica Nucleare, Torino, Italia), autorise l'impression de la présente thèse, sans exprimer d'opinion sur les propositions qui y sont énoncées.

Genève, le 28 avril 2020

Thèse - 5455 -

Le Doyen

N.B. - La thèse doit porter la déclaration précédente et remplir les conditions énumérées dans les "Informations relatives aux thèses de doctorat à l'Université de Genève".

ABSTRACT

The Large Hadron Collider (LHC) will undergo a significant upgrade between 2024 and 2027, called High Luminosity LHC (HL-LHC), which will allow the increase of the instantaneous luminosity up to $\sim 5 \cdot 10^{34}\,\mathrm{cm}^{-2}\mathrm{s}^{-1}$. In order to cope with the augmented pile-up and radiation damage brought by the HL-LHC, the ATLAS experiment will also undergo a series of improvements of its sub-systems.

In particular, the Inner Detector will be replaced with a new Inner Tracker, completely based on silicon sensors. It will consist of five layers of pixel detectors in the inner part and strips in the outer. The pixel layers will be composed of hybrid modules, with planar or 3D sensors coupled to dedicated read-out ASICs.

The use of depleted monolithic pixel sensors, built using a commercial high-voltage CMOS technology, instead of the hybrid modules has been proposed for the outermost pixel layer. They present several advantages compared to the traditional hybrid detectors, like the lower cost and material budget, a faster processing time and the non-necessity of bump-bonding. These sensors must withstand the harsh radiation conditions expected at the HL-LHC, namely a particle fluence up to $\sim 1 \cdot 10^{15}$ 1 MeV $\mathrm{n_{eq}}/\mathrm{cm}^2$ and an ionizing dose of $\sim$1 MGy, so they must be carefully characterized to ensure they respect these specifications.

In this work the characterization of two sensors produced using the H35 and aH18 technologies by ams AG, the H35DEMO and the ATLASPIX1, is presented. The characterization focused on the charge-collection performance, the particle detection efficiency and the spatial and time resolution, measured before and after irradiation using protons and neutrons.

The charge-collection performance has been studied using the transient current technique. The results have shown that the depletion depth increases significantly due to the acceptor removal effect of irradiation, which can compensate for the charge carriers loss caused by trapping.

The particle detection efficiency and the space and time resolution have been studied in several testbeam campaigns. Results have shown an excellent efficiency, larger than 99%, which does not degrade after neutron irradiation. Proton irradiation, instead, produces a decrease in efficiency to 95% at a fluence of $1 \cdot 10^{15}$ 1 MeV $\mathrm{n_{eq}}/\mathrm{cm}^2$. These measurements have also allowed identifying a few shortcomings in the read-out circuitry, addressed in subsequent designs.

RÉSUMÉ

Le grand collisionneur de hadrons (Large Hadron Collider, LHC) subira une maintenance importante de 2024 à 2027, appelée phase à haute luminosité (HL-LHC), qui permettra une augmentation de la luminosité instantanée jusqu'à $\sim 5 \cdot 10^{34}\,\mathrm{cm}^{-2}\mathrm{s}^{-1}$. Afin de supporter l'augmentation du taux d'empilement et des dommages liés aux radiations engendrées par cette phase, l'expérience ATLAS subira également une série d'améliorations de ses sous-systèmes.

En particulier, le détecteur interne sera remplacé par un nouveau trajectographe (Inner Tracker, ITK) entièrement basé sur des capteurs à silicium. Il sera composé de cinq couches de détecteurs pixels dans sa partie la plus interne et de capteurs à pistes sur l'extérieur. Des modules hybrides occuperont les couches de pixel, avec des capteurs planaires ou 3D couplés à des ASICs de lecture dédiés.

Pour la couche la plus externe, des capteurs monolithiques utilisant une technologie commerciale CMOS à haute tension sont proposés pour remplacer les capteurs hybrides. Ils présentent plusieurs avantages par rapport à ces derniers, tel un coût de fabrication et épaisseur d'interaction réduite, un temps de production plus court et l'absence de bump-bonding. Ces capteurs doivent supporter les radiations extrêmes attendues lors de la phase HL-LHC, avec un flux de particules atteignant $\sim 1 \cdot 10^{15}$ 1 MeV $\mathrm{n_{eq}}/\mathrm{cm}^2$ et une dose ionisante de ~ 1 MGy. Ils doivent donc être soigneusement caractérisés pour répondre à ces exigences.

Ce document présente la caractérisation des deux capteurs réalisé en utilisant les technologies H35 et aH18 par ams AG : le H35DEMO et l'ATLASPIX1. L'accent est porté sur les performances de collection de charge, d'efficacité de détection et de résolution temporelle et spatialle, mesurées avant et après irradiation par des protons et des neutrons.

La collection de charge a été etudiée en utilisant une technique de courant transitoire. Les résultats démontrent que la profondeur d'épuisement du capteur est augmentée significativement grace à l'effet de suppression des accepteurs, qui compense la perte de porteurs de charge par le piégeage.

L'efficacité de détection et les résolutions temporelle et spatialle, ont été étudiées lors de plusieurs campagnes de tests sous faisceau. Les résultats montrent une excellente efficacité, supérieure à 99%, qui n'est pas dégradée après irradiation par des neutrons. Une irradiation par un faisceau de protons produit néanmoins une perte d'efficacité jusqu'à 95% avec un flux de $1 \cdot 10^{15}$ 1 MeV $\mathrm{n_{eq}}/\mathrm{cm}^2$. Ces mesures ont permis également d'identifier plusieurs défauts dans le circuit de lecture, et de les corriger dans les versions ultérieures des productions.

CONTENTS

INTRODUCTION

ATLAS is one of the four large experiments at the Large Hadron Collider (LHC). It has been operating since 2009 and has a fundamental role in the study of particle physics, performing precision measurements of key parameters of the Standard Model and searching for new physics.

The LHC and the ATLAS detector will undergo a major upgrade during the Long Shutdown 3, from 2024 to 2027, aimed to increase the instantaneous luminosity of the collider. This upgrade will be performed to increase the precision of existing Standard Model measurements, to probe rare signatures and extend the search for physics beyond the Standard Model. The High-Luminosity LHC (HL-LHC) is expected to begin to take data in mid-2027.

The ATLAS Inner Detector will be replaced with a new Inner Tracker (ITk), completely based on silicon detectors, to be able to cope with the very high pile-up and radiation damage expected at the HL-LHC.

The ITk will be constituted of five layers of pixel detectors in the inner part and of strip detectors in the outer. Two sensors technologies will be used for the pixel detectors: 3D and planar sensors, coupled with bump bonds to the read-out ASIC. They are well established technologies, already in use in the ATLAS Inner Detector and in other experiments at the LHC.

Depleted monolithic pixel sensors, built using commercial High-Voltage CMOS (HV-CMOS) technologies, have been proposed as an alternative to replace the modules of the outermost pixel layer. They have several advantages over the traditional hybrid modules: they are built by CMOS foundries using industry-standard technologies, with a faster processing time compared to planar and 3D sensor. Furthermore, they do not need to be connected to a read-out ASIC with bump-bonds, removing the time, cost and possible yield loss of this process.

Monolithic CMOS sensors have never been used in a demanding environment as the HL-LHC, so a careful characterization to determine the feasibility of their use in the ATLAS ITk must be performed. Several aspects need to be studied, like the charge collection characteristics, the particle detection efficiency, the time and spatial resolution, the maximum data rate, the noise characteristics and the tolerance to radiation, in terms of ionizing and non-ionizing energy loss, but also in terms of single event upsets and latch-ups.

In this thesis, the characterization of HV-CMOS pixel detectors prototypes produced by ams AG is presented. It focuses on several fundamental aspects related to the performance of a pixel detector:

the charge collection, the particle detection efficiency, the time and spatial resolution have been studied before and after irradiation with protons and neutrons.

The charge collection has been studied using the Transient Current Technique (TCT), which allows studying the properties of the bulk and of the charge collection by shining a laser in the sensor. From these measurements, the evolution with irradiation of the depletion-region depth and of the effective doping concentration of the sensors have been characterized. Furthermore, the shape of the current pulses generated by the charge carriers in the depletion region has been studied.

The particle detection efficiency, the time and spatial resolution have been measured during several testbeam campaigns. They allow studying the performance of the sensors in an environment comparable to a real experiment, with the aid of a beam telescope. The latter is necessary to reconstruct the trajectories of the beam particles, which are used to estimate the performance of the sensor under study.

The LHC, ATLAS and the upgrades foreseen for the HL-LHC are introduced in Chapter 1, explaining the current status of the accelerator and of the experiment, its physics programme and the challenges expected in the future, with a particular focus on the pixel detector.

Chapter 2 introduces silicon detectors, starting from the physical and chemical properties of this element, explaining how they can be modified and how they can be exploited to detect subatomic particles. The detector technologies of interest for this work, along with the challenges related to radiation damage are described as well.

In Chapter 3 the project aimed to develop High Voltage CMOS detectors for the ATLAS upgrade is introduced. The detectors characterized in this work are described in detail.

The original work of this thesis is described in Chapter 4 and 5, where the characterization instruments and techniques are described in detail, along with the measurements performed and the results obtained.

1 THE ATLAS EXPERIMENT AT THE LHC

With the discovery of the W and Z bosons at the CERN proton-antiproton collider in 1983, the confidence in the Standard Model of particle physics increased greatly, but two elements were still missing to complete it: the top quark and the Higgs boson. Since the Higgs boson mass is not predicted by the Standard Model and a lower bound to its value was available at the time, the necessity for a hadron collider that could reach a centre of mass energy of several TeV became compelling.

Years of discussion in the particle physics community, with a series of conferences, workshops, feasibility studies of the accelerator and research on the necessary instrumentation led, in 1991, the CERN Council's to decide that the Large Hadron Collider (LHC) was the right project to be developed after the Large Electron Positron (LEP) collider.

In the coming years, after detailed studies, the construction of the LHC and the ATLAS experiment, one of the four experiments on this new collider, was approved: it began in 1997 for ATLAS and in 1998 for the LHC. Everything was complete in 2008, but an incident in the accelerator delayed the beginning of the operations to 2009, when the first collisions were recorded [1].

In this first chapter the LHC, ATLAS and the upgrades foreseen for the High Luminosity LHC will be introduced, explaining the current status of the accelerator and of the experiment, the physics measurements and the challenges expected in the future, with a particular focus on the pixel detector.

1.1 THE LARGE HADRON COLLIDER

The Large Hadron Collider (LHC) is the largest particle accelerator in the world. It has been built between 1998 and 2008 at CERN (*Conseil Européen pour la Recherche Nucléaire*, European Organization for Nuclear Research), near Geneva, in the 27 km long tunnel, 80–100 m underground, that previously hosted the LEP collider. It is located at the border between France and Switzerland (Figure 1.1).

The LHC accelerates two beams of protons[1] in opposite directions, up to an energy of 6.5 TeV per beam, for a final centre of mass energy at the collision points of $\sqrt{s} = 13$ TeV. There are four collision points

1 The LHC also accelerates heavy ions (mainly lead), up to an energy of 2.56 TeV per nucleon. Protons are the particles of interest for this work.

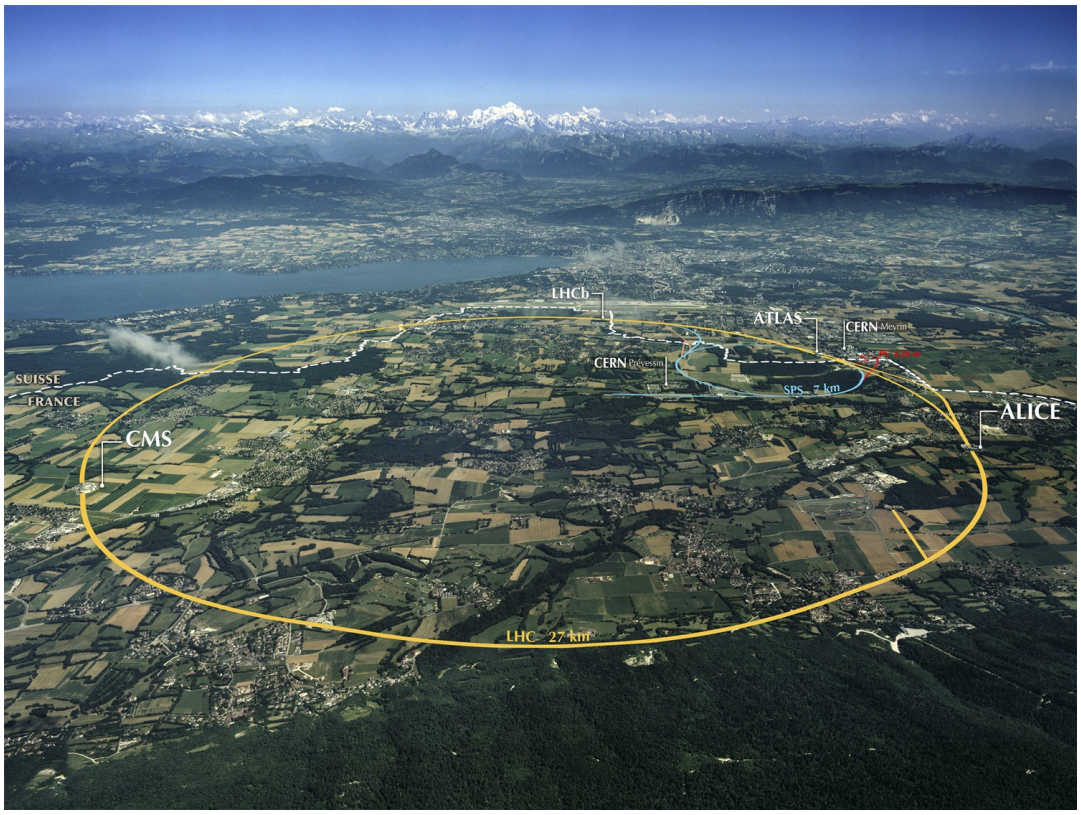

Figure 1.1: Aerial view of the CERN area, taken from over the Jura mountains. The PS, SPS and LHC accelerators are highlighted, along with the four major LHC experiments. In the background it is possible to see the Lac Léman, the Salève and the Alps, with the Mont Blanc [2].

corresponding to the four experiments: ALICE [3], ATLAS [4], CMS [5] and LHCb [6].

The LHC is the last element in a chain of increasingly more powerful accelerators, required to bring the protons from rest up to an energy of 6.5 TeV. The accelerators chain, shown in Figure 1.2 begins with LINAC 2, where hydrogen atoms are stripped of their electrons and accelerated up to 50 MeV, before being fed to the Proton Synchrotron Booster, which increases the energy up to 1.4 GeV and injects the beam into the Proton Synchrotron (PS), where the energy is raised to 25 GeV. The chain continues with the Super Proton Sychrotron (SPS) which accelerates the protons up to 450 GeV and finally injects the beam, with two separate lines, into the two pipes of the LHC.

The beams inside the LHC are composed of bunches of protons, each containing $\sim 1.5 \cdot 10^{11}$ particles, accelerated by 16 superconducting radiofrequency (RF) cavities (8 per beam). Each beam is composed of 2808 bunches, spaced 25 ns, leading to a Bunch Crossing (BC) frequency of 40 MHz [8].

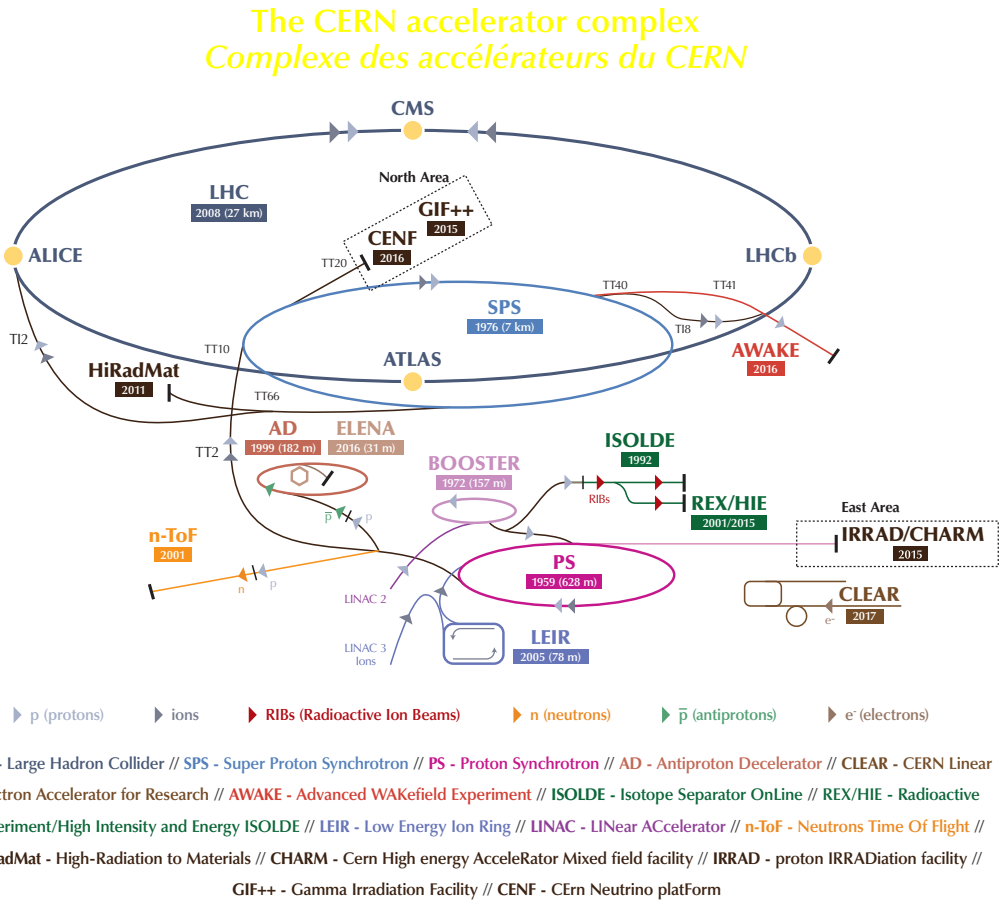

Figure 1.2: The CERN accelerator complex [7].

One important parameter of a collider is the instantaneous luminosity $\mathcal{L}$, which relates the number of events N per unit time of a physics process to its cross section σ:

$$\frac{\mathrm{d}N}{\mathrm{d}t} = \mathcal{L} \cdot \sigma. \tag{1.1}$$

The instantaneous luminosity depends on characteristic parameters of the collider:

$$\mathcal{L} = \frac{R n_b N_b^2 f_r \gamma}{4\pi\beta^* \varepsilon_n} \tag{1.2}$$

where n_b and N_b are the number of bunches and protons per bunch respectively, f_r is the revolution frequency of the bunches, γ is the Lorentz factor, ε_n is the normalized transverse emittance, β^* is the beta function at the point of collisions[2] and R is a constant taking into account the geometrical reduction factor due to the crossing angle

2 It can be thought as the focal length of the beam.

at the interaction point. The LHC features a nominal instantaneous luminosity of $1.5 \cdot 10^{34}\,\mathrm{cm}^{-2}\mathrm{s}^{-1}$.

This value of luminosity implies that at each bunch crossing, several proton-proton interactions take place: this is known as pile-up. The number of these interactions is indicated with μ and its distribution is shown in Figure 1.3: it can be observed that the mean number of interaction increased year by year, with an average of $\langle\mu\rangle \approx 34$ in the last four years, reaching a peak value of 60 to 70 in 2017.

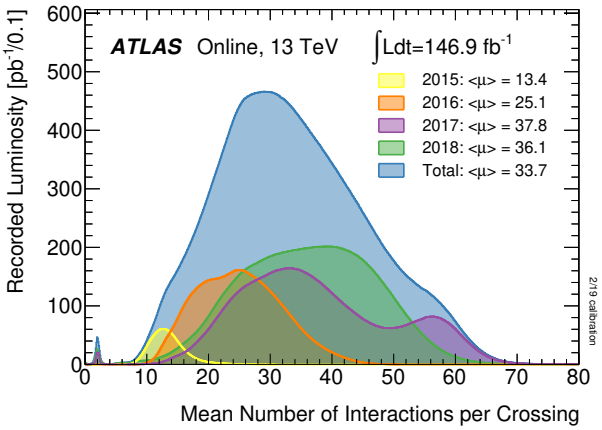

Figure 1.3: Distribution of the number of interaction per bunch crossing for the collisions at $\sqrt{s} = 13\,\mathrm{TeV}$, recorded by the ATLAS experiment [9].

If $\mathcal{L}$ is integrated over a period of time, the integrated luminosity is obtained:

$$L = \int_{t_1}^{t_2} \mathcal{L}\,\mathrm{d}t. \tag{1.3}$$

$1\,\mathrm{b} = 10^{-24}\,\mathrm{cm}^2$

This value is normally used to describe the amount of data collected in a period of time (usually a year or from the beginning of the experiment) and is measured in fb^{-1}. If multiplied by the cross section of a particular event, the expected number of events in the period of interest is obtained.

Since when the first collision occurred, in 2009, until the end of 2018, the LHC has delivered a total integrated luminosity of $\sim$150 fb^{-1}.

1.2 THE HIGH LUMINOSITY LHC UPGRADE

The LHC alternates operating periods (Run 1, Run 2, Run 3...) with long shutdown periods, to allow upgrading the accelerator and of the detectors, along with consolidation works and repairing (see Figure 1.4). At the end of 2018 the LHC entered the Long Shutdown 2 (LS2) and it will start Run 3 at the beginning of 2021, during which it will reach $\sim$300 fb^{-1} of collected data. At the end of Run 3, in late

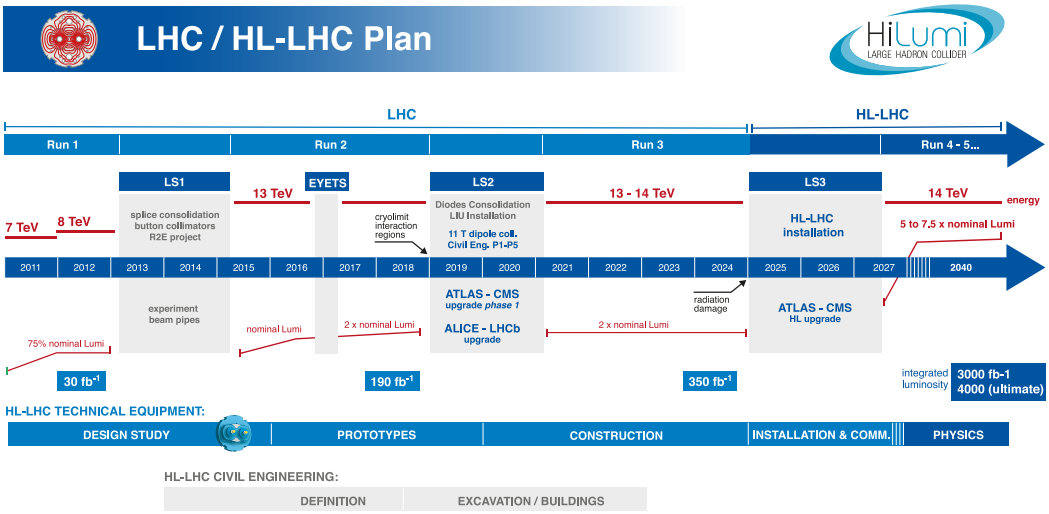

Figure 1.4: The timeline of the LHC and of the High-Luminosity LHC [10].

2024, it will enter the Long Shutdown 3, which will last 2 years and a half. During this period the LHC will undergo a major upgrade that is aimed to increase its luminosity to $5 \cdot 10^{34}\,\mathrm{cm}^{-2}\mathrm{s}^{-1}$, leading to a pile-up of $\langle \mu \rangle \approx 200$.

To achieve this goal several parameters of the beam must be enhanced: the number of protons per bunch will be increased from $1.5 \cdot 10^{11}$ to $2.2 \cdot 10^{11}$, the normalized transverse emittance will be decreased from 3.75 µm to 2.50 µm, β^* will be reduced from 0.55 m to 0.15 m, leading to the necessity of increasing the crossing angle from 285 µrad to 590 µrad. A wider crossing angle can cause a degradation of the luminosity and, to compensate for this effect, crab cavities can be used to align the bunches of the two beams in the interaction region (without them the geometrical reduction factor R would be 0.305, improved to 0.829 if they are used) [11].

These modifications require upgrades of several components of the accelerator: some parts of the magnet system, of the electronics and of the protection systems will need to be improved, to withstand the expected radiation dose, while the collimation must be able to cope with the increased beam intensity. A new cryogenic plant will be installed to separate the cooling of the superconducting RF cavities and of the magnets. Remote manipulation will also be improved to minimize the radiation dose during interventions.

The High-Luminosity LHC (HL-LHC) is expected to deliver, in 10 years of operation, an integrated luminosity of $3000\,\mathrm{fb}^{-1}$, 10 times the integrated luminosity that will be collected at the end of Run 3. This will enhance the precision of previous measurements and increase the sensitivity to rare processes and new physics [12], es explained in more details in Section 1.4.6.

The experiments will need to be upgraded as well, to be able to cope with the increased luminosity, that implies a greater occupancy in the detectors and a much more important radiation damage, especially in the sub-detectors (or sub-systems) closest to the interaction point.

1.3 THE ATLAS EXPERIMENT

The ATLAS (A Toroidal LHC ApparatuS) detector, shown in Figure 1.5, is a general purpose detector, aimed to measure and identify the particles produced in proton-proton collisions at the LHC. To achieve this purpose, it consists of several sub-detectors, each specialized in measuring specific properties of the crossing particles.

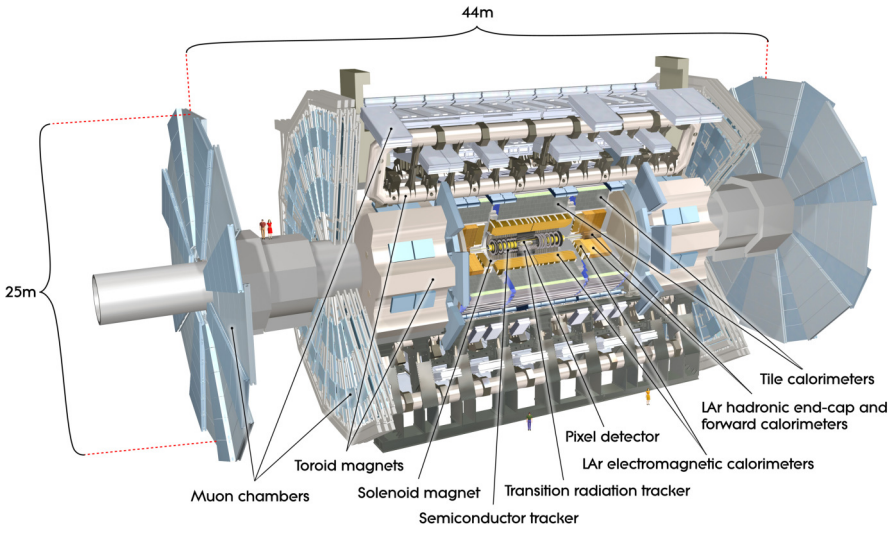

Figure 1.5: The ATLAS detector [4].

The Inner Detector, closest to the interaction point, is dedicated to reconstruct the trajectories of the charged particles created in the collisions and it is immersed in a magnetic field generated by a solenoidal coil, to be able to determine the charge and momentum of the particles. Then a calorimetric system is present, to measure the energy of electrons, photons and hadrons, which get stopped in it. Finally, in the outermost part of the detector, the muon spectrometer measures the trajectories of the muons, which are bent by a magnetic field generated by three toroidal coils, to measure their momentum. The different sub-detectors feature an approximately cylindrical shape, with the side indicated as the *barrel* and the bases as the *end-caps*. These sub-detectors and the trigger system will be described in more details in the following sections.

Before proceeding, the coordinate system used in the ATLAS experiment needs to be introduced. It has the origin placed at the nominal interaction point, with the z axis along the beam line and x and y per-

pendicular to it, pointing to the centre of the LHC ring and upwards respectively. Given the detector geometry, a cylindrical coordinate system is utilised: ϕ is the azimuthal angle (in the x-y plane), R is the radius and, instead of the polar angle θ (with respect to the z axis), the pseudorapidity η is used. It is defined as:

$$\eta = -\ln\left(\tan\left(\frac{\theta}{2}\right)\right). \tag{1.4}$$

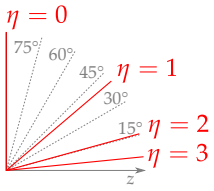

Another important quantity is the transverse momentum, defined as $p_T = \sqrt{p_x^2 + p_y^2}$: it is used because, at hadronic colliders with the beams crossing at almost 0°, the sum of the transverse momenta of all the particles resulting from a collision is zero, while this is not true for the longitudinal momentum. This happens because the interaction occurs between partons (quarks and gluons), which carry a fraction of the proton momentum, resulting in a collision that is not at rest in the frame of reference of the detector. If particles escape detection (*e.g.* neutrinos), the total transverse momentum measured by the detector will differ from zero and the missing transverse energy E_T^{miss} and momentum p_T^{miss} can be exploited for physics analyses.

1.3.1 *The Inner Detector*

The Inner Detector (ID), shown in Figure 1.6, is used to measure the trajectories of the charged particles originating from the collisions and to determine their momentum. It consists of three different sub-systems: the pixel detector, the silicon microstrip tracker (SCT, Semiconductor Tracker), which together cover the pseudorapidity region $|\eta| < 2.5$, and the Transition Radiation Tracker (TRT), which covers the region $|\eta| < 2.0$. The ID is immersed in a 2 T magnetic field generated by the central solenoid, which surrounds it.

The TRT, the outermost subsystem of the ID, is based on drift straw tubes of 4 mm diameter: they contain an anode wire in the middle and are filled with a special mixture of gas (70% Xe, 27% CO_2 and 3% O_2) which absorbs the low energy transition radiation photons emitted when a charged particle crosses the tube boundary. These photons provide much larger signal compared to the charged particles themselves. This sub-detector is composed of 73 planes of straw tubes in the barrel region, parallel to the beam axis, and 160 planes in the end-caps, with the tubes arranged radially.

The SCT, located between the TRT and the pixel detector, is composed of small-angle (40 mrad) silicon stereo strips[3] with a pitch of 80 µm. There are four layers of these modules in the barrel region, each of which has a set of strips parallel to the beam direction, and

3 Two strips sensors coupled together with a small angle between them.

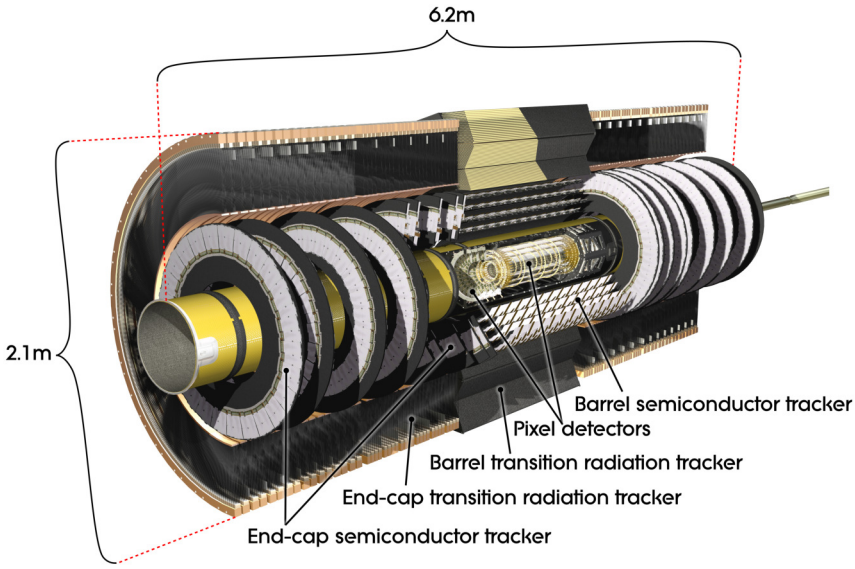

Figure 1.6: The ATLAS Inner Detector [4].

nine end-cap disks at each side, with one set of strips per module oriented radially.

The pixel detector is constituted of four layers in the barrel and three end-cap disks per side. The innermost of the four barrel layers is called IBL (Insertable B Layer) [13] and was added in 2014, so it features more advanced sensors and read-out electronics, while the others were present since the beginning of the experiment.

The original sensor modules feature a pixel size of $50 \times 400\,\mu m^2$, with the longest side being parallel to the beam direction. They are read-out by a dedicated front-end chip, the FE-I3 [14]. These modules are composed of one pixel sensor chip, built with a planar technology (more details about this technology will be given in Section 2.2.3), and of size $63.4 \times 24.4\,mm^2$, connected with bump bonds to 16 front-end chips, of size $10.8 \times 7.6\,mm^2$, each with 2880 electronics channels, arranged in 18 columns and 160 rows.

This assembly, called a *hybrid pixel detector* and described in more detail in Section 2.2.4, is glued to a flexible PCB (printed-circuit board) containing the control electronics, decoupling capacitors and a temperature sensor. . These modules (shown in Figure 1.7) are then arranged in staves in the barrel region: each one contains 13 modules, and there are a total of 112 staves. In the end-caps the modules are mounted on disks, each divided in eight radial sectors (see Figure 1.8).

The IBL sensors modules, instead, are partly built in planar technology and partly in 3D technology (more details about it will be given in Section 2.2.3). Their pixels have dimensions $50 \times 250\,\mu m^2$ and are read-out with a more modern front-end chip, the FE-I4B [16], larger than the FE-I3, being $20.2 \times 18.8\,mm^2$ and containing 26 880 pixels, arranged in 336 rows and 80 columns.

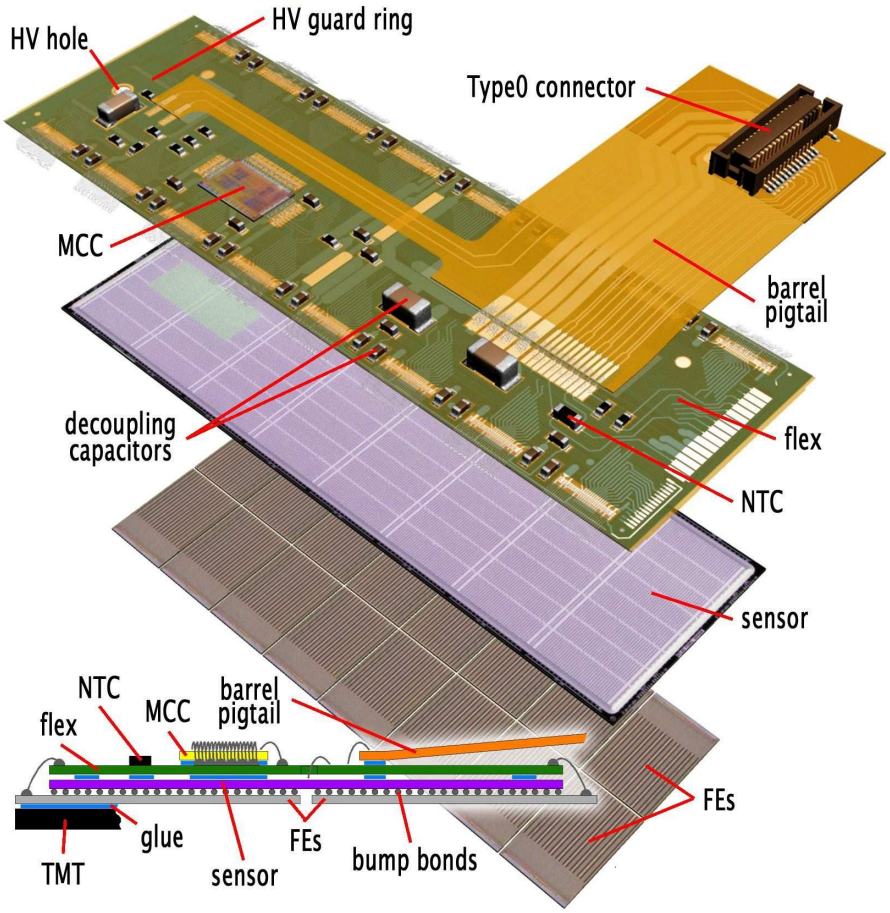

Figure 1.7: Schematic view of a barrel pixel module. FE indicates the front-end chips, MCC is the module-control chip [4].

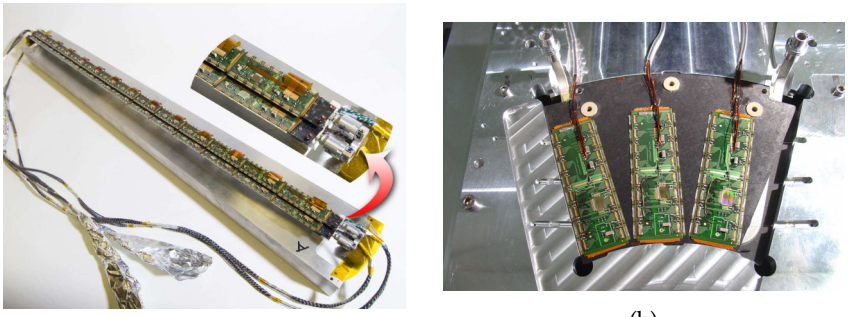

(a) (b)

Figure 1.8: Close up of a stave (left) and a pixel sector (right) loaded with modules [4].

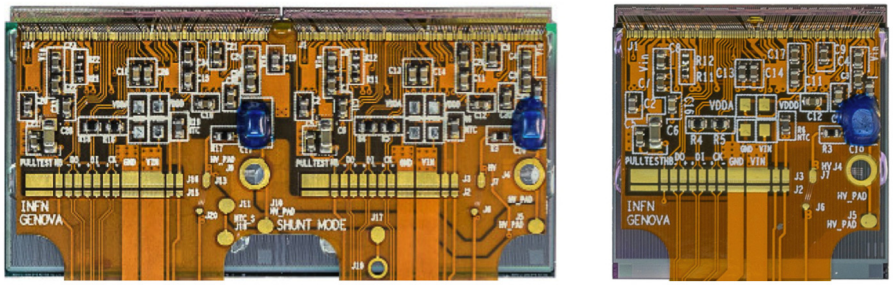

Figure 1.9: The IBL pixels modules with planar sensor on the left, 3D sensor on the right [15].

The IBL hybrid modules, shown in Figure 1.9, are composed of one sensor chip connected, via bump bonds, to one (3D) or two (planar sensors) FE-I4B chips. These modules are used in the barrel section only, arranged in 14 staves, each containing 12 planar modules in the central part and eight 3D modules at the edges (four per side).

1.3.2 *The calorimetric system*

The calorimetric system, shown in Figure 1.10, is necessary to measure the energy of photons, electrons and jets, but also to estimate the missing transverse energy of an event.

The characteristics of the various parts that compose the ATLAS calorimeter allow obtaining a good energy resolution, but also the reconstruction of the direction of an incoming object and the discrimination between isolated photons or photons produced by the decay of neutral particles, as the pion or the Higgs boson. The thickness of the calorimeter is important to prevent the punch-trough of jets in the muon spectrometer.

It is composed of two main sub-systems: the electromagnetic calorimeter and the hadronic calorimeter. The electromagnetic sub-system is composed of a barrel ($|\eta| < 1.475$) and two end-caps ($1.375 < |\eta| < 3.2$) sections. It is a sampling calorimeter with lead absorbers and liquid argon (LAr) as active material. The electrodes are accordion-shaped, providing a full ϕ coverage. Its thickness corresponds to $> 22X_0$ in the barrel and to $> 24X_0$ in the end-caps.

X_0, the radiation length, is the mean distance travelled by a high energy electron before losing all but $1/e$ of its energy by bremsstrahlung.

The electromagnetic calorimeter is segmented both in depth (two or three sections, depending on the pseudorapidity range) and η-ϕ (the granularity depends on the layer and on $|\eta|$). It features a presampler for $|\eta| < 1.8$ to estimate and correct for the energy loss of photons and electrons in the innermost part of the detector (beam pipe, Inner Detector and solenoid magnet).

The hadronic calorimeter exploits two different technologies: steel absorbers and scintillating tiles in the barrel and in the extended barrel, while it uses liquid argon in the end-caps, as the electromagnetic calorimeter but with different absorbers. The tile calorimeter extends

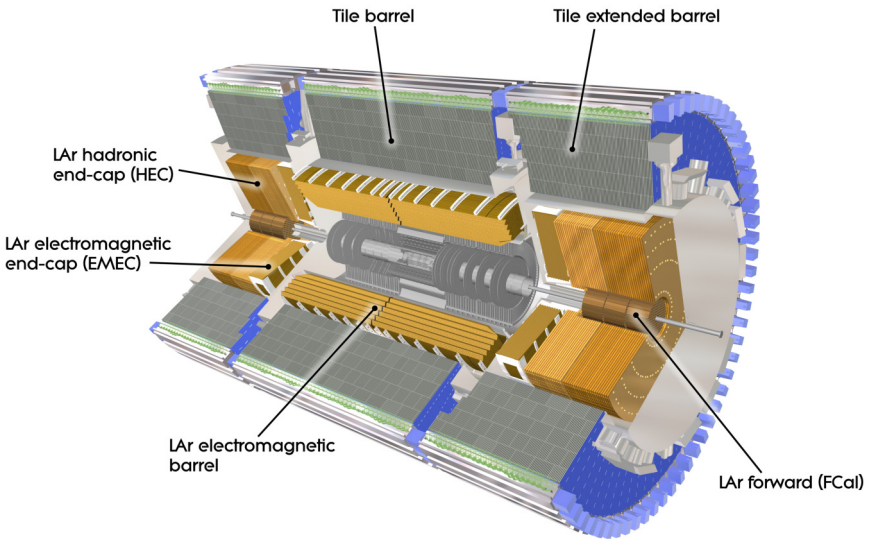

Figure 1.10: The different parts of the ATLAS calorimetric system [4].

up to $|\eta| < 1.7$ and it is read out by wavelength shifting fibres that transport the light to photomultiplier tubes. The tile calorimeter is segmented in depth and η-ϕ. Its thickness, combined with the electromagnetic calorimeter, adds up to 9.7λ at $|\eta| = 0$.

λ, the interaction length, is the mean distance travelled by a hadron before undergoing an inelastic collision.

The hadronic end-cap calorimeters consist of two wheels per side, covering the pseudorapidity region $1.5 < |\eta| < 3.2$. They are built with interleaved copper plates (used as absorber) and liquid argon (the active material). The forward calorimeter instead uses tungsten as an absorber and the read-out is performed by copper pipes and rods with liquid argon between them. This calorimeter covers the region $3.1 < |\eta| < 4.9$.

1.3.3 *The muon spectrometer*

The muon spectrometer, shown in Figure 1.11, is based on the deflection of these particles by a toroidal-shaped magnetic field. The muons are detected with several position-sensitive gas detectors, to estimate their momentum.

The magnetic field is provided by three magnets, the barrel toroid and the two end-cap toroids, each composed of eight coils. They provide a field of approximately 0.5 T in the central region and 1 T in the end-cap regions. The field is designed to be perpendicular to the trajectories of the muons arising from the collisions.

In the barrel region, the detectors are arranged in three concentric layers around the beam axis, between and onto the coils of the barrel toroid magnet. In the end-cap regions three layers on each side are present, in front and behind the end-cap toroid magnets.

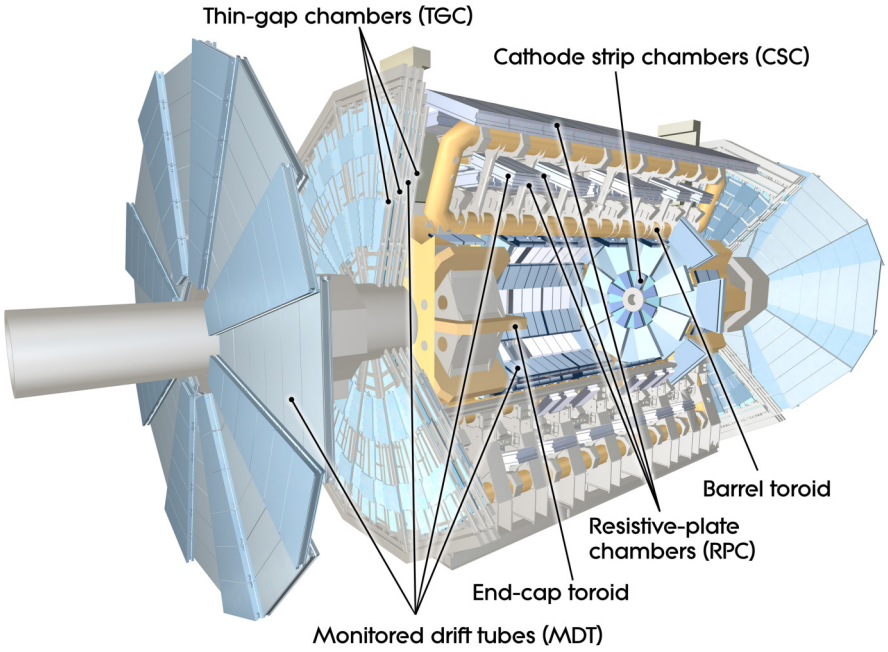

Figure 1.11: The ATLAS muon spectrometer and the toroid magnets [4].

The trajectories of the muons are measured with four types of detectors: Monitored Drift Tubes (MDT), Cathode Strip Chambers (CSC), Resistive Plate Chambers (RPC) and Thin Gap Chambers (TGC).

MDTs consist of cylindrical drift tubes of 3 cm diameter, with a central wire acting as an electrode and filled with a special mixture of gas (97% argon, 3% CO_2). They are used both in the barrel and end-cap regions and cover a pseudorapidity range up to $|\eta| < 2.7$ (except in the innermost layer, where they cover up to $|\eta| < 2$). MDTs feature an average resolution of 80 µm per tube and measure the trajectory of the muon in the bending direction only.

CSCs are used in the $2 < |\eta| < 2.7$ region of the innermost layer to overcome the limitation on the MDTs counting rates. CSCs are multi-wire proportional chambers, with the wires oriented in the radial direction and with segmented cathodes (one perpendicularly to the wires, the other parallel to them). They feature a spatial resolution of about 60 µm in the bending direction.

RPCs consist of two resistive plates, kept at a distance of 2 mm and filled with a mixture of $C_2H_2F_4$, Iso-C_4H_{10} and SF_6. They can provide a very fast signal (about 5 ns) with a very low jitter (smaller than 10 ns).

TGCs are multi-wire proportional chambers, with the wire-to-cathode distance smaller than the wire-to-wire distance, in order to have a high electric field around the wires, leading to a very good time resolution (99% of the signals arrive within a 25 ns time window).

While MDTs and CSCs only measure the position of the muons, RPCs and TGCs serve more purposes: being fast detectors, they also

provide bunch crossing identification and well-defined muons p_T thresholds for the trigger.

1.3.4 *The forward detectors*

Four smaller detectors are present in the ATLAS forward region: two of them, LUCID (LUminosity measurement using Čerenkov Integrating Detector) and ALFA (Absolute Luminosity For ATLAS) are used to measure the luminosity delivered to ATLAS.

LUCID is located at 17 m from the interaction point, at $|\eta| \approx 5.9$, and measures the online luminosity, while ALFA, located at 240 m from the interaction point, requires special beam conditions and it is used to measure the absolute luminosity.

The third system is ZDC (Zero-Degree Calorimeter), located at 140 m from the interaction point and measures neutrons with $|\eta| > 8.3$ in heavy-ions collisions, to determine the centrality of such collisions and to provide special trigger functionalities.

Finally, the ATLAS Forward Protons detector (AFP) is installed at 210 m from the interaction point to study soft and hard diffractive events at low luminosities [17].

1.3.5 *The trigger system*

The collision frequency of 40 MHz is too high to read out and store each event: the trigger system is responsible for selecting the interesting events to be saved, which typically contain high energy photons, leptons or jets, but also events with a significant missing transverse energy. The trigger system [18], schematically shown in Figure 1.12, consists of a first hardware-based trigger, called Level 1 (L1), and a second software based one, called High Level Trigger (HLT).

Level 1 is based on field programmable gate arrays (FPGAs) that collect data, at a reduced granularity, from the calorimeter and muon systems and make the decision to accept an event in 2.5 µs. It searches for electrons, photons, taus, jets, missing transverse energy (in the calorimeter) and high energy muons (in the muon spectrometer). Furthermore, it can perform more advanced selections based on the topology of the event, combining information like angular separation or invariant mass. This first level of trigger reduces the event rate approximately from 40 MHz to 100 kHz.

After an event has been accepted by L1, it is sent to the High Level Trigger [19], which uses the full granularity of the sub-detectors and runs more advanced algorithms, performing a full reconstruction of the event and making the decision to accept an event in 200 ms, on average. The events accepted by HLT are written to permanent storage for subsequent offline analysis. The HLT reduces the event rate to approximately 1 kHz.

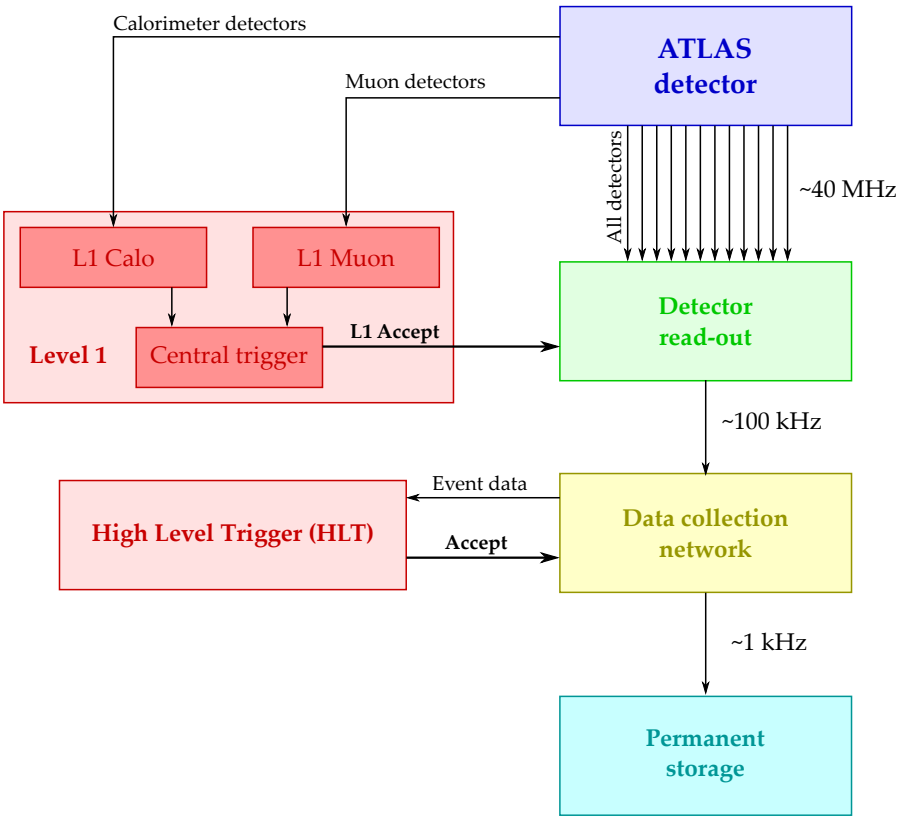

Figure 1.12: Simplified trigger scheme, with the event rates at each step.

1.4 THE ATLAS PHYSICS RESULTS AND PROGRAMME

The ATLAS experiment has a very rich physics programme, ranging from searches of new phenomena to precision measurements. At the beginning, one of the key strengths of the LHC and of the ATLAS physics programme was the confidence that the Higgs boson or new physics had to be found below the 1 TeV energy scale to assure that the cross section for the scattering of longitudinal W bosons would not grow indefinitely with energy.

In summer 2012, just three years after the collisions started to take place in the LHC, the discovery of the Higgs boson was announced by the ATLAS and CMS experiments [20, 21]: it has been one of the most important discoveries in the field of particle physics. It validates the Standard Model, adding the mechanism that generates the masses of fermions and bosons, and has an important impact in cosmology, being related to the stability of vacuum. The Higgs boson discovery has been followed by more precise measurements of its characteristics.

The ATLAS experiment has also performed important measurements of Standard Model processes to be compared to the increasingly more precise theoretical predictions, showing an impressive agreement and allowing the study of extremely rare processes.

In addition, ATLAS has an important role in the search of phenomena beyond the Standard Model: it is known that there are some questions that this theory does not address, like the mass of neutrinos, dark matter, the matter-antimatter asymmetry, etc. One of the goals of the experiment is to detect any new phenomena that could be present at the TeV scale.

These searches, along with the heavy ions physics and their evolution with the HL-LHC physics programme will be briefly summarized in the following sections.

1.4.1 *The Higgs sector*

At the beginning of the LHC operation there were some limits, put by earlier experiments, on the mass of the Standard Model Higgs boson: LEP had excluded it up to 114 GeV, while LEP, SLC and Tevatron provided an indirect upper limit of ∼150 GeV [22, 23].

At the LHC the Higgs boson can be produced in different processes, as shown in Figure 1.13. The main process is the gluon fusion ($gg \to H$), which has the highest cross section, despite having a loop in the Feynman diagram. It is followed by the vector boson fusion ($qq \to qqH$), W and Z *Higgs-strahlung* ($q\bar{q} \to WH$ and $q\bar{q} \to ZH$) and top fusion ($gg \to t\bar{t}H$).

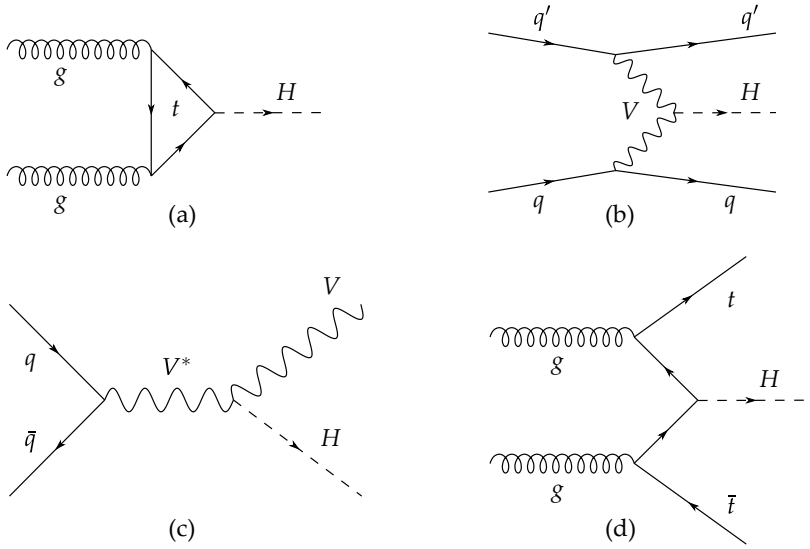

Figure 1.13: Higgs boson production channels at the LHC: gluon fusion (a), vector boson fusion (b), Higgs-strahlung (c) and top fusion (d). V indicates the W and Z bosons.

The Higgs boson has several decay channels: it can decay to a couple of Z or W bosons (one of which will be off shell), to two photons or gluons, through different heavy quarks or vector boson loops, and to two fermions (b quarks and τ leptons have the highest branching ratio, since the coupling is proportional to their mass).

The four leptons channels ($H \to ZZ^{(*)} \to 4\ell$ and $H \to WW^{(*)} \to \ell\nu\ell\nu$) and the diphoton channel ($H \to \gamma\gamma$) have been an important benchmark for the design of the ATLAS detector because they have the best signal/background separation (especially $H \to ZZ^{(*)} \to 4\ell$ and $H \to \gamma\gamma$, indeed the Higgs boson was discovered using these two channels).

The key element for the diphoton channel is the electromagnetic LAr calorimeter: in the range relevant for the $H \to \gamma\gamma$ process, it features a resolution on the invariant mass ranging from 1.2 GeV, for a high-p_T Higgs decaying to two photons in the central region of the detector, to 1.9 GeV if p_T is low or one of the photons is in the forward region. Furthermore, the transversal and longitudinal segmentation of the calorimeter is fundamental to estimate the shape of the shower, to distinguish between showers initiated by a photons and by a neutral pion.

The four lepton channel $H \to ZZ^{(*)} \to 4\ell$, with ℓ being an electron or a muon, is extremely important, despite its low branching ratio ($\sim$0.02%), because it is characterized by the highest signal to background ratio for the inclusive production of the Higgs boson.

In this channel it is extremely important to reconstruct leptons down to small transverse momenta to have a good rejection of non-prompt leptons (*i.e.* not coming from a W or Z boson), a good momentum resolution and an hermetic detector, to maximize the signal acceptance. The high granularity of the LAr calorimeter is fundamental, along with the Inner Detector and Muon Spectrometer. The ID drives the momentum resolution at low p_T (below 80 GeV in the central part and below 40 GeV in the forward part), while the MS has a fundamental role in the trigger muon identification and momentum resolution at high p_T. Combining their characteristics, a mass resolution of $\sim$1.6 GeV can be achieved.

The third channel, $H \to WW^{(*)} \to \ell\nu\ell\nu$, with ℓ being an electron or a muon, has a worse mass resolution, due to the presence of neutrinos, but features a higher branching ratio. Apart from the detector characteristics mentioned above, this channel requires an extremely precise estimation of the background created by non resonant $pp \to WW^{(*)}$, $t\bar{t}$ and W + jets, in addition to a very good missing transverse energy reconstruction.

The discovery of the Higgs boson was announced in the summer of 2012 [20, 21]: an excess of events was observed in the $H \to ZZ^{(*)} \to 4\ell$ and $H \to \gamma\gamma$ channels at an invariant mass of $\sim$126 GeV [20]. The plots of the invariant mass distributions for these two channels are shown in Figure 1.14.

In the following years more precise measurements of the mass, spin, couplings, production and decay rates were performed. The most recent value of its mass is (125.18 ± 0.16) GeV [24], the spin-parity has been measured to be 0^+ [25] and the couplings, production and decay

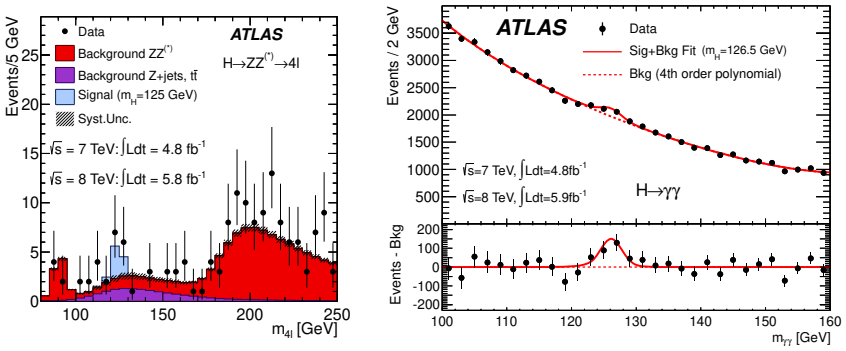

(a) (b)

Figure 1.14: The distributions of the invariant mass of four-lepton (a) and diphoton (b) candidates for the combined 7 TeV and 8 TeV data sample of the ATLAS experiment [20].

rates are compatible with the Standard Model [26]. New decay modes were observed: $H \to \tau\bar{\tau}$ in 2015 [27] and $H \to b\bar{b}$ in 2018 [28], while $H \to \mu\bar{\mu}$, $H \to c\bar{c}$ and $H \to gg$ still escape detection to this day.

1.4.2 *Standard Model processes*

The ATLAS experiment has an important role in the validation of the Standard Model (SM) predictions for pp collisions: the measurements of SM processes are compared to the theoretical predictions, allowing the search of possible shortcomings of the theory and thus establishing evidence for the presence of new physics.

These kind of measurements require an excellent understanding and control of the performance of the ATLAS detector, like high particle detection efficiencies, coupled with momentum calibration, but also reliable and precise predictions for the cross sections of SM processes in the complex hadron collider environment.

Figure 1.15 gives an overview of the cross sections for several processes involving the production of jets, vector bosons, top quarks, Higgs bosons, along with rare processes: this plot highlights the excellent agreement of the theory predictions with the data, but also shows that it is possible to study extremely rare processes (the rarest have a cross section which is around 14 orders of magnitude smaller than the total σ_{pp}).

The most abundant process at the LHC is the inelastic proton-proton interaction, $pp \to X$, where X is an unspecified set of final state particles: its total cross section has been measured for the first time at a centre of mass energy of several TeV at the LHC: ATLAS has used both the ALFA detector (described in Section 1.3.4) and the Minimum Bias Trigger scintillators, installed in the end-cap calorimeter cryostat. The results are shown in Figure 1.16. They have confirmed that the

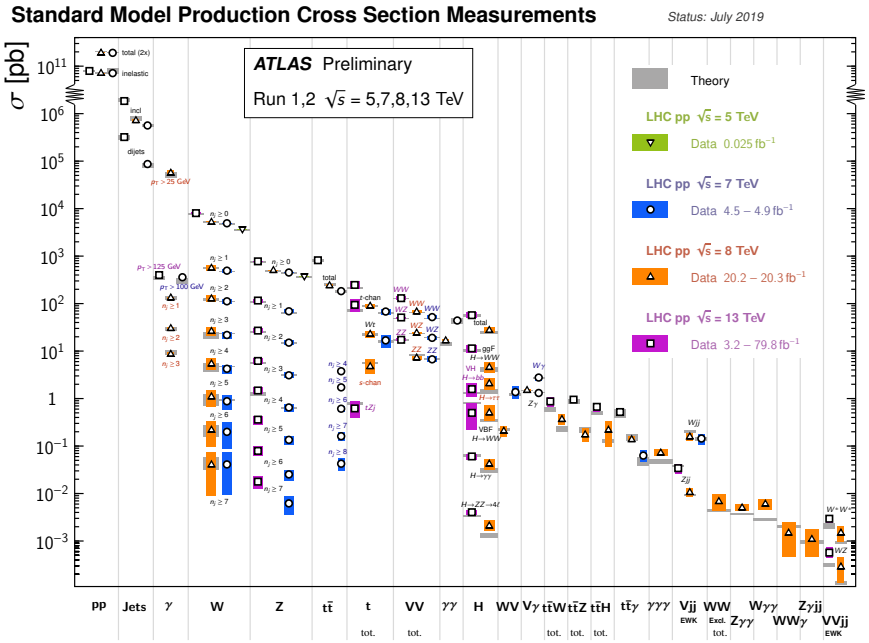

Figure 1.15: Summary of several Standard Model production cross section measurements, corrected for branching fractions, compared to the corresponding theoretical expectations. V indicates the W and Z bosons collectively [29].

theoretical predictions describe with reasonable accuracy the increase of the cross section with centre of mass energy [30].

Another abundant process is the production of energetic hadronic jets, produced by the interaction of quarks and gluons. ATLAS has measured the cross section for the production of jets on a wide range of p_T and compared them with the most recent quantum chromodinamics (QCD) calculation, showing again a good agreement. These measurements rely on an excellent modelling of the detector response, to have the best possible measure of the jet energy [31].

The precision measurements of production of Z and W bosons, through the electroweak interaction of the quarks composing the protons, combined with the cross sections predicted by the standard model, has allowed testing different sets of parton distribution functions (PDFs), which describe the composition of the protons in terms of quarks and gluons. Furthermore, the mass of the W boson has been measured to an unprecedented level of precision. These studies requires an excellent understanding of the behaviour of the leptons in the detector, calibrated using the more precisely known Z mass [29].

The measurement of interactions of the electroweak bosons, probed in events with two, three or four of them, is of major interest to test the coupling of γ, W and Z to one another: a deviation from the expected values could be indication of new physics. The theoretical calculations of these coupling have been done to a high degree of precision in

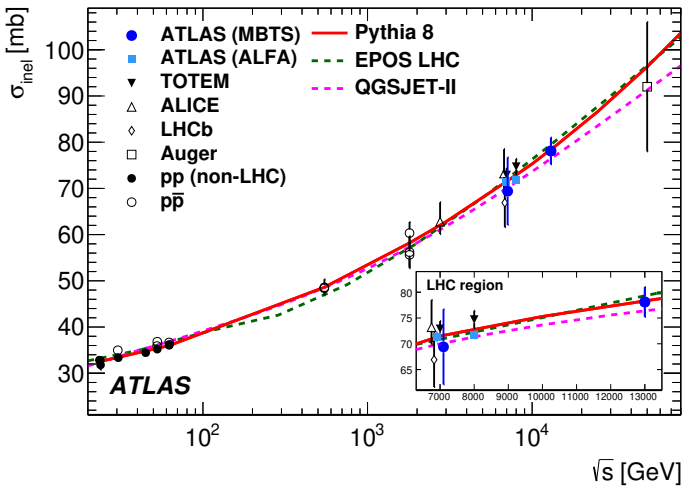

Figure 1.16: The inelastic proton-proton cross section versus $\sqrt{s}$. Some of the LHC data points have been slightly shifted in the horizontal position for display purposes. The data are compared to the PYTHIA8, Epos LHC and QGSJet-II Monte Carlo generator predictions [30].

recent years and by their comparison with data, anomalous coupling have been excluded [29].

ATLAS has also precisely measured the inclusive and differential cross section for the production of the top quark, and improved the precision on the estimation of its mass, which is an important parameter in the SM. Moreover, the studies of polarization, charge, spin correlations and search for strongly suppressed decays have allowed putting constraints on the nature of possible new physics beyond the Standard Model [29].

1.4.3 *Search of physics beyond the Standard Model*

The Standard Model has been validated in multiple experiments, at both high and low energies: no new phenomena, or deviation from its predictions have been observed yet. However, there are reasons to believe that that the Standard Model is not complete because several questions remain unaddressed. Some examples are given below.

NEUTRINO MASSES The SM is constructed assuming massless neutrinos, while flavour oscillations show that their mass is finite, albeit small. It is not known how they do acquire a mass and why it is so small compared to the other Standard Model particles.

DARK MATTER Astrophysical and cosmological measurements show that there are gravitational effects that cannot be explained by the visible matter alone. Dark Matter should account for ∼85% of the matter in the universe. If it is constituted of unknown

heavy subatomic particles which interact weakly with ordinary matter, it could be discovered at the LHC.

MATTER/ANTIMATTER ASYMMETRY There is an imbalance of matter and antimatter in the observable universe: the SM predictions for this asymmetry are in contrast with the observations by several order of magnitudes.

HIERARCHY PROBLEM Assuming that the Standard Model is valid up to the Planck scale, the value of the Higgs boson mass needs to derive from the cancellation of terms of order $\left(10^{19}\,\text{GeV}\right)^2$, requiring an extremely precise fine tuning of the parameters[4] of the theory to obtain the physics we observe. This is considered non-natural, in the sense that the free parameters or physical constants of a theory should be of the same order of magnitude.

The search for solutions to these and other inconsistencies is conducted in different ways, depending on what is the expected signature of new physics.

One example is the search for particles pair production: the mass distribution of lepton, photons and jet pairs is examined in order to find excesses above the Standard Model predictions, which could be an indication of presence of new particles. If no tension is found, limits can be placed on models or on the mass of these hypothetical particles.

Some examples are the search for excited quark states q^* (using jets), for W' and Z' bosons (using leptons) and new particles decaying into $t\bar{t}$ pairs [32]. These searches require an excellent identification and separation of jets, for which the calorimeters are fundamental, along with robust b-tagging algorithms and reconstruction of high momentum electrons and muons, which rely on the performance of the Inner Detector and muon spectrometer.

A different approach, used for example in the search for dark matter and extra dimensions, is the search of signals of new physics using the missing transverse energy [33]: examples are the study of a SM particle X recoiling against missing energy, in the search for dark matter and other weakly-interacting particles or just a very high E_T^{miss}, that could be associated with momentum escaping in different dimensions.

In these searches the backgrounds must be well understood (an example is $Z + X$ with the Z decaying to two neutrinos) and the momentum and energy of the detectable particles must be reconstructed precisely, along with their origin vertex, to reliably estimate p_T^{miss}

4 The relevant parameters here are the bare Higgs boson mass m_{H0} and the cut-off value Λ, the energy threshold up to which the Standard Model holds. The Higgs mass is be given by $m_H^2 \approx m_{H0}^2 - \frac{|\lambda_f|^2}{8\pi^2}\Lambda^2 + \ldots$, where λ_f is the fermion Yukawa coupling. If Λ is at the Planck scale, the Higgs boson mass results from the precise cancellation of two terms of order $\left(10^{19}\,\text{GeV}\right)^2$.

and E_T^{miss}. Thus far, no deviation from the Standard Model has been observed.

The searches mentioned above use "standard" objects, like jets, electrons, muons, etc. Some physics models predict hidden particles, which have a weak coupling to the SM particles, so they could produce vertices far from the interaction point, inside the Inner Detector, the calorimeters or the muon spectrometer [34]. Other models predict magnetic monopoles or massive particles with multiple or fractional electric charges: they would have the signature of a highly electrically charged massive particle, with the TRT and the electromagnetic calorimeter being particularly sensitive to it [35].

These hypotheses require unique trigger and reconstruction algorithms to be explored, and, even they were not foreseen during the design of ATLAS, they have been successfully implemented, thanks to the flexibility of the detector. Despite these diversified researches, no evidence of these exotic models has been found.

1.4.4 *Supersymmetry*

Supersymmetry (SUSY) is one of the candidate theories to address some of the shortcomings of the Standard Model mentioned in the previous section. SUSY introduces new partners (called superpartners) of the known particles, that share with them the same internal quantum numbers but have the spin different by $\frac{1}{2}$. Quarks have *squarks* $\tilde{q}$ as superpartners, while *sleptons* $\tilde{\ell}$ are the superpartners of leptons. Squarks and sleptons have the same charge as their SM counterparts, but have spin 0. *Gluinos* $\tilde{g}$ are superpartners of the gluons, while *neutralinos* $\tilde{\chi}^0$ and *charginos* $\tilde{\chi}^{\pm}$ are a mixture of the vector and Higgs bosons superpartners (higgsinos, winos and binos). They all have spin $\frac{1}{2}$.

This theory can address the hierarchy problem by providing corrections to the Higgs boson mass because the scalar particles would contribute with a correction $\Delta m_H^2 \approx 2 \cdot \frac{\lambda_S}{16\pi^2}\Lambda^2$, which cancels exactly the term $-\frac{|\lambda_f|^2}{8\pi^2}\Lambda^2$, since in supersymmetry $\lambda_S = |\lambda_f|^2$ [36]. Furthermore, it can provide a candidate for dark matter: some models predict the existence of so-called WIMPs (Weakly Interacting Massive Particles), which are neutral, stable, massive and interact weakly with ordinary matter: in some SUSY models the lightest supersymmetric particle (LSP) has all these characteristics.

The initial searches for supersymmetry were looking for superpartners with the same mass as the corresponding SM particle, but this scenario was quickly excluded, leading to the conclusion that SUSY, if existing, is a broken symmetry. This implies that $\lambda_S \neq |\lambda_f|^2$, so the correction to the Higgs boson mass is different from 0. Naturalness arguments, however, suggest that the mass of the supersymmetric

particles are not too different from the Standard Model ones [36], and for this reason they could be observed at the LHC.

Supersymmetry breaking implies that the experimental signatures depend on the symmetry breaking mechanism, the R-parity[5] conservation and the nature of the lightest and next-to-lightest supersymmetric particles: this very open theoretical framework provides a high number of SUSY models that can be explored.

The initial searches for SUSY in ATLAS were focused on the first and second generation squarks and on the gluino, which have strong couplings to the initial state partons, and so a higher production cross section. The expected process would involve a squark or a gluino decaying into the (undetectable) LSP and, because of colour conservation, the decay products would contain quarks that hadronize into jets: the searched signature would therefore be jets associated to missing transverse energy, but it could also be more complex, including one or more leptons. A summary plot of these searches and the ones mentioned in the following paragraphs, is reported in Figure 1.17, along with the references for each study.

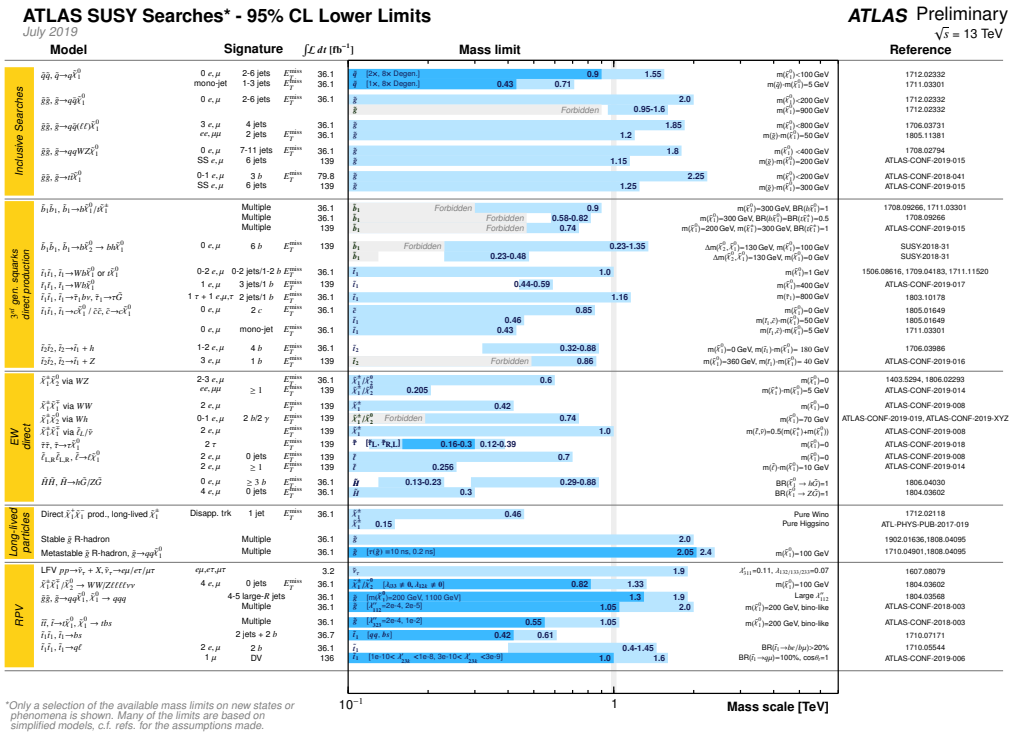

Figure 1.17: Mass exclusions of the ATLAS searches for Supersymmetry. Results are quoted for the nominal cross section in both a region of near-maximal mass reach and a demonstrative alternative scenario. In some cases these additional dependencies are indicated by darker bands showing different model parameters [37].

5 R-parity relates the leptonic and barionic numbers of a particle, L and B, to its spin s. It is defined as $R = (-1)^{3(B-L)+2s}$ and it is equal to 1 for SM particles and to -1 for SUSY particles.

After the discovery of the Higgs boson, the *stop* (the supersymmetric partner of the top quark) gained more attention: being the heaviest squark, it would be the one that contributes the most to the Higgs mass correction and it is not expected to exceed the TeV scale. An extensive search of the stop has been performed by ATLAS, exploiting new and more efficient b-tagging techniques, in addition to the excellent reconstruction of jets, leptons and missing transverse energy.

The superpartners of the electroweak sector, sleptons, charginos and neutralinos, are investigated as well: these searches are based on the assumptions that the LSP is the lightest neutralino, that R-parity is conserved and, by naturalness arguments, that the masses of at least some of these particles are of a few hundreds GeV. These searches are focused on the production of the second-lightest neutralino or the lightest chargino, which can decay to the LSP through a slepton, emitting two leptons, or through a gauge boson.

Here the mass differences of the involved particles are fundamental to determine the expected signature: mass hierarchies with the highest mass charginos and neutralinos very close to the LSP are expected in SUSY. If this difference is of the order of a few GeV, the final state leptons are very soft and require dedicated techniques, while if the difference is of the order of a few hundreds of MeV, they may become long lived and decay inside the detector, similarly to the exotic weakly interacting particles mentioned in the previous section.

Finally, R-parity violating scenarios are studied too: this violation can imply that the leptonic and barionic numbers are violated and that the LSP can decay into Standard Model particles in several ways. The interesting events are characterized by high lepton or jet multiplicities, with little or no missing transverse energy, making these searches particularly challenging, since without E_T^{miss} it is more difficult to distinguish these events from the SM background. If the mass hierarchy is very compressed, long-lived particles can arise in these scenarios as well.

1.4.5 *Heavy ions physics*

A part of the ATLAS physics programme is focused on heavy ions collisions (normally lead nuclei, with 208 nucleons each) to study the quark-gluon plasma, a state of matter in which quarks and gluons are freed of their strong attraction under extremely high energy densities. These collisions pose different experimental challenges compared to pp collisions: a single Pb-Pb collision can produce several hundreds of times more particles than a pp one.

However ATLAS, thanks to the large acceptance of the calorimeter and Inner Detectors and to the precision of the muon spectrometer, can cope with these harsh conditions (for example, the Inner Detector is capable of reconstructing thousands of tracks in each event and

associate them with a vertex). Furthermore, it features a dedicated detector, the Zero-Degree Calorimeter, to provide a robust experimental trigger and to distinguish strong processes from electromagnetic ones.

One of the most interesting results of these collisions is the first direct evidence of light-by-light scattering ($\gamma\gamma \to \gamma\gamma$), predicted by quantum-electrodynamics (QED). This process has been observed in the so-called "ultra-peripheral collisions", where the two nuclei interact at an impact parameter of at least twice the nuclear radius, so no strong interactions are possible. In these cases, the primary interactions are electromagnetic, which are enhanced compared to pp collisions, as the electric field strength scales with the square of the nuclear charge (82 for lead).

The cross section of light-by-light scattering is extremely small, being proportional to $\alpha_{\mathrm{EM}}^4 \approx 10^{-9}$, making the observation very challenging, but thanks to the large available data sample and carefully designed trigger, out of around 4 billion collected events, 13 di-photon candidates, with no additional activity, were observed in 2017 [38]. This observation has been confirmed in the following years, reaching a significance of more than 8 standard deviations [39]. An event example is shown in Figure 1.18.

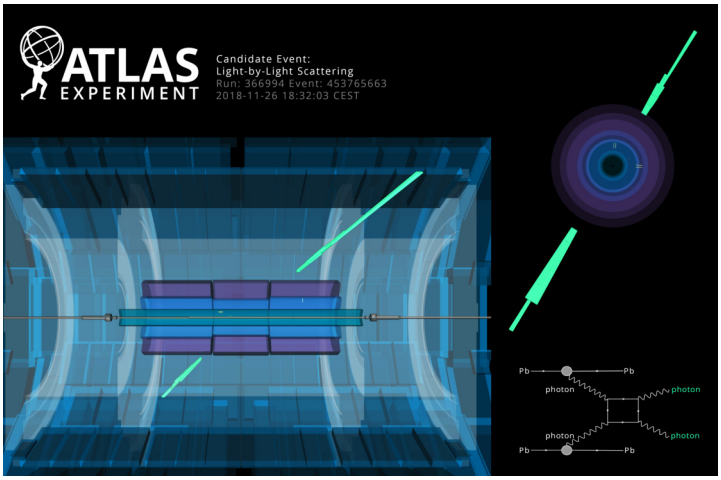

Figure 1.18: Event display for an exclusive $\gamma\gamma \to \gamma\gamma$ candidate. Two back-to-back photons with an invariant mass of 29 GeV and no additional activity in the detector are visible [39].

Another significant result is the observation of jet quenching in single events, obtained using the very first ATLAS heavy ion data [40]. This phenomenon is studied by using the asymmetry between the transverse energies of pairs of jets: pp collisions typically produce jets that are back-to-back with balanced transverse energies, while heavy ions produce one collimated jet with an opposite recoiling jet spread over large angles, due to energy loss in the nuclear medium.

1.4.6 *The ATLAS physics programme at the HL-LHC*

The ATLAS experiment will be significantly upgraded during the Long Shutdown 3: more details about the detector modifications will be given in Section 1.5. This upgrade will have an important impact on the physics programme, allowing for the increase of the precision of known processes and the sensitivity to rare ones.

In the Higgs sector, an increase in the precision of the coupling measurements is expected: it should reach ∼4% for vector bosons and ∼8% for fermions,[6] which is important because some BSM models expect the couplings to differ by ∼10% from the SM ones. High luminosity is crucial to be able to measure rare events as $H \to \mu\bar{\mu}$, for which an accuracy of 10% looks feasible, and $H \to J/\Psi\gamma$ to probe the Higgs coupling of the charm quark. Moreover, they will also allow investigating the Higgs boson self coupling by studying the production of pairs of H, for which it is expected to reach a significance of three standard deviations: more precise measurements will require new particle accelerators after the HL-LHC.

Standard Model measurements are expected to increase in accuracy and to be able to study unexplored rare signatures. One example is the vector boson scattering (VBS), which allows probing the electroweak symmetry breaking mechanism and is sensitive to new physics: its production cross section has been recently measured by ATLAS with a precision of 20% [41]. The HL-LHC will allow improving it to around 4%.

The direct searches for physics beyond the Standard Model, like dark matter, SUSY, etc. will greatly benefit from the increased luminosity, which brings a greater discovery potential for states with low production rates, increasing the particle mass range that can be explored (one of the most striking example is the increase of 50% of the mass reach for SUSY chargino-neutralino pairs [42]).

1.5 THE ATLAS UPGRADE FOR THE HL-LHC

In view of the HL-LHC, the ATLAS detector will need significant upgrades to its sub-systems. The Inner Detector will be replaced with a new Inner Tracker (ITk), containing ∼180 m^2 of silicon detectors (∼15 m^2 of pixel detectors and ∼165 m^2 of strips, a huge amount compared with the current ∼2 m^2 of pixels and ∼61 m^2 of strips) [43, 44]. The Inner Detector needs to be replaced for several reasons: the radiation damage at the HL-LHC will be an order of magnitude higher than what its sensor and electronics are able to withstand. Furthermore, the increased pile-up (Figure 1.19) will saturate the bandwidth of pixel and strip detectors, degrading their efficiency,

6 To be compared with the current precision of ∼8% for vector bosons and ∼20% for fermions [26].

and will cause a ∼100% occupancy in the TRT [45]. The ITk will be described in more details in the next section.

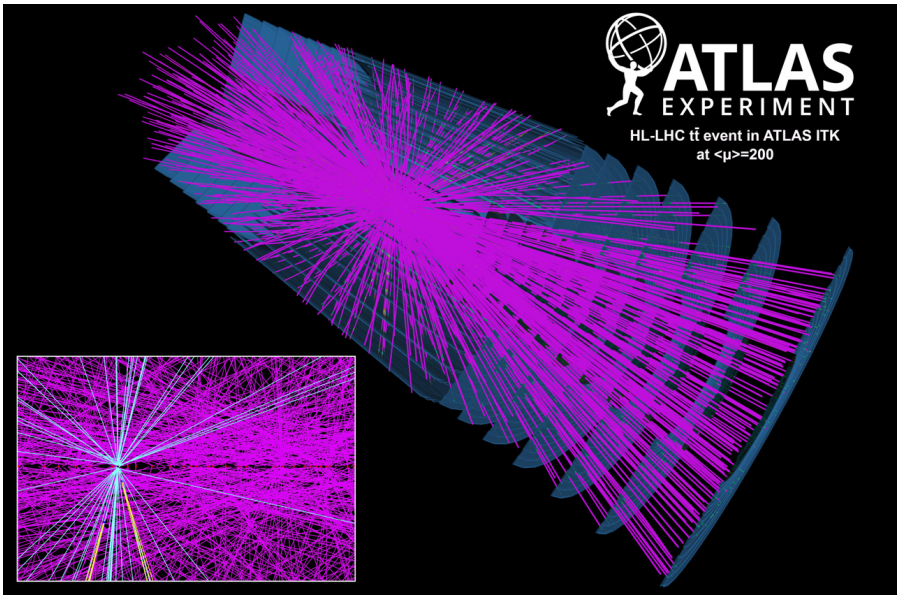

Figure 1.19: A simulated $t\bar{t}$ event at $\mu = 200$ in the ITk. The bottom-left inset is a 2D R-z view of the interaction region. The vertical scale is 2.5 mm and the horizontal one is 12 cm. All reconstructed tracks have $p_T > 1$ GeV. The tracks coming from the $t\bar{t}$ vertex are coloured in cyan. Two secondary vertices can be reconstructed and the tracks coming from them are highlighted in yellow. [46]

The granularity of the electromagnetic calorimeter for triggering purposes will be increased during LS2, while in LS3 all major front-end and back-end electronics of the electromagnetic and hadronic calorimeters will be replaced, to accommodate the increased trigger rates and to avoid complication caused by the ageing and radiation damage [47, 48].

The muon spectrometer will also see significant upgrades. During LS2 the CSCs and the MDTs of the innermost end-cap wheels will be replaced by Micromegas and small-strip TGCs. During LS3 most of the electronics and the power system for the RPCs, TGCs and MDTs will be replaced to make them compatible with the higher trigger rates and because of ageing and radiation damage. Furthermore, additional RPCs and TGCs will be added in the barrel to increase the robustness and acceptance of the trigger [49].

Finally, the trigger system will need important upgrades as well: as it has been mentioned earlier, the calorimeter and muon system will improve the resolution of the parts devoted to triggering, to suppress the pile-up. Furthermore, new algorithms will be implemented in the Level 1 trigger and the integration of tracking in the hardware based trigger is foreseen. Updates in the technology and the use of GPUs

and FPGAs in the software trigger are foreseen for HLT, since the time required for the reconstruction grows exponentially with pile-up [50].

1.5.1 *The new Inner Tracker*

The ITk will be composed of silicon detectors only, and will comprise two sub-systems: a pixel detector [43], closer to the beam pipe, and a strip detector [44], both with a cylindrical geometry, composed of barrel and end-cap modules.

The strip detector will have four barrel layers and six end-cap disks per side, covering up to a pseudorapidity of $|\eta| < 2.7$. Each layer and disk will contain double modules, at a small stereo angle, to add z resolution in the barrel and R resolution in the end-caps.

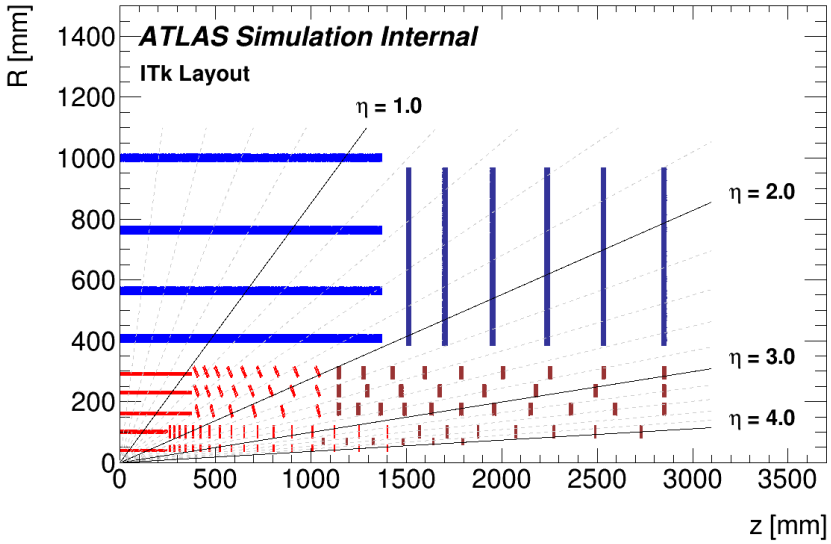

Figure 1.20: A schematic representation of one quadrant of the ITk layout, with the strip layers coloured in blue (end-caps in darker blue) and the pixel layers in red (end-caps in darker red) [51].

The pixel detector will feature five barrel layers (labelled 0 to 4) and several end-cap disks: the detailed layout is shown in Figure 1.20. The pixel modules in the centre of each barrel layer are parallel to the beam pipe, while at higher pseudorapidities they are inclined (in the three outermost layers) or perpendicular to the beam (in the two innermost ones): this configuration allows reducing the material-induced performance degradation at the transition between the barrel and the end-cap and reduces the amount of silicon surface area, compared to a completely flat barrel, thus reducing the necessary power and services. The pixel detector will cover up to a pseudorapidity of $|\eta| < 4$.

The outer pixel layers (2 to 4) will be operated to collect a total integrated luminosity of up to 4000 fb^{-1}, while the inner ones (layers 0 and 1) are designed to be replaced after collecting 2000 fb^{-1}, due to

the harsher radiation environment. All the components of the pixel detector will have to withstand extremely high levels of radiation: from $\sim 1 \cdot 10^{16}$ 1 MeV n_{eq}/cm^2 of fluence and ~ 5 MGy of ionizing dose in the innermost layer[7] to $\sim 1 \cdot 10^{15}$ 1 MeV n_{eq}/cm^2 and ~ 1 MGy in the outermost.

Different types of sensors will be used for the pixel layers: 3D sensors will be used in the innermost layer (layer 0), while planar silicon sensors will be used in layers 1 to 4. These sensors will be read out by a dedicated front-end chip [52], of size $\sim 19.2 \times 20\,mm^2$, developed at CERN by the RD53 collaboration [53].

Two types of modules will be produced: single and quad modules, composed by a sensor chip bump bonded to one or four front-end chips respectively. Single modules will be used in the innermost layer, which requires smaller sensors because of its small radius, while quad modules in the remaining ones.

A stave will be composed by 12 to 24 flat barrel modules and 12 to 34 inclined ones, depending on the layer, and there will be 16 to 56 staves in each layer. In the end-cap, each ring will contain from 20 to 52 modules, and the number of rings per layer will span from 6 to 24 per side. The details of the arrangement can be found in [51].

High-Voltage CMOS (HV-CMOS) sensors, integrating detector and readout functionalities in a single die, have been considered as a possible replacement for the modules of the outermost pixel layer, where their low cost and ease of production are expected to be very beneficial, given the large area to cover ($\sim$24% of the total pixel area). The work described in this thesis consists in the characterization of HV-CMOS pixel sensor prototypes, to assess the performance of this technology and the possibility to use them in the ITk.

7 These values take into account the substitution of the two innermost layers after $2000\,fb^{-1}$.

2 SILICON DETECTORS AND RADIATION DAMAGE

Semiconductor detectors have been used for particle physics experiments since the early 1950s [54–56]. Their major development, however, started in the late 1970s, when the groups involved in charm quark studies at CERN SPS were looking for new devices that could measure and identify, through the presence of secondary decay vertices, particles with a lifetime of around 10^{-13} s. This necessity led to the development of position sensitive silicon strip detectors, allowing tracking and decay vertex reconstruction of these particles.

In the mid 1980s VLSI (very large scale integration) devices started to be used for the read-out instead of discrete components, enabling great miniaturization of the detector assembly.

The first silicon pixel detectors were successfully installed in the WA97 [57], DELPHI[58] and NA60 [59] experiments at CERN in the second half of the 1990s. In the following decades, various detector technologies have been developed, targeting different requirements for various applications, *e.g.* 3D pixel sensors for high radiation environments, LGADs for excellent time resolution or monolithic pixel detectors for low material budget [60].

In this chapter, silicon detectors are introduced, from the properties of the silicon crystal that allow them to be used as particle detectors (mostly based on [61, 62]), to the different sensor options available for high energy physics experiments, with a focus on the current ATLAS pixel detector. CMOS devices will be explained as well, being of major interest for this work. Furthermore, radiation damage mechanisms are presented.

2.1 SILICON PROPERTIES

2.1.1 *Introduction*

Silicon is one of the most abundant elements on Earth, by mass around 28% of the Earth's crust. It has atomic number 14 and it is located in the group 14 of the periodic table, along with carbon, germanium, tin and lead. Its fourteen electrons are arranged in the configuration $[\mathrm{Ne}]\,3\,s^2\,3\,p^2$.

As other members of its periodic group, like carbon, the orbitals of the four valence electrons (3 s and 3 p) are hybridised and form four sp^3 orbitals arranged in a tetrahedral structure, shown in Figure 2.1a, which determines its crystalline structure.

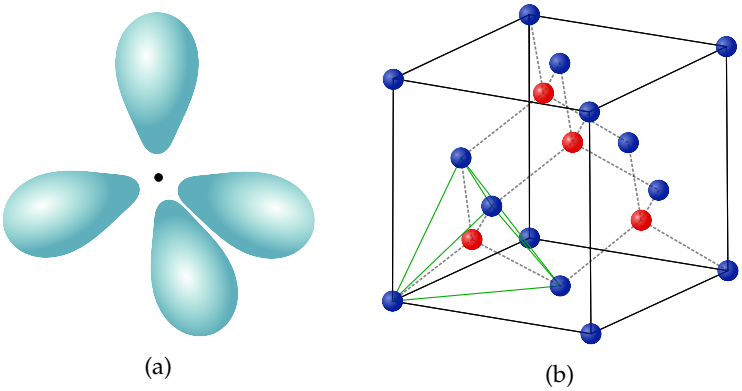

(a) (b)

Figure 2.1: (a) Simplified representation of the sp^3 orbitals with respect to the nucleus of the atom (shown as a black dot). Each orbital forms an angle of 109.5° with the others [63]. (b) Representation of the silicon crystalline structure. Each silicon atom (blue and red) has four covalent bonds with its nearest neighbours (indicated with the grey dashed lines), located at the vertices of a tetrahedron (highlighted in green). The blue and red colour of the atoms highlights the two interpenetrating face-centred cubic lattices.

In standard conditions it forms a covalent crystal with a tetrahedral structure: each atom is surrounded by four equidistant nearest neighbours, located at the corners of a tetrahedron. This lattice structure can be described as two interpenetrating face-centred cubic lattices (see Figure 2.1b). A schematic representation of this structure, which will be useful later to understand doping, is shown in Figure 2.2: each atom has four nearest neighbours, but the relative position is not conserved.

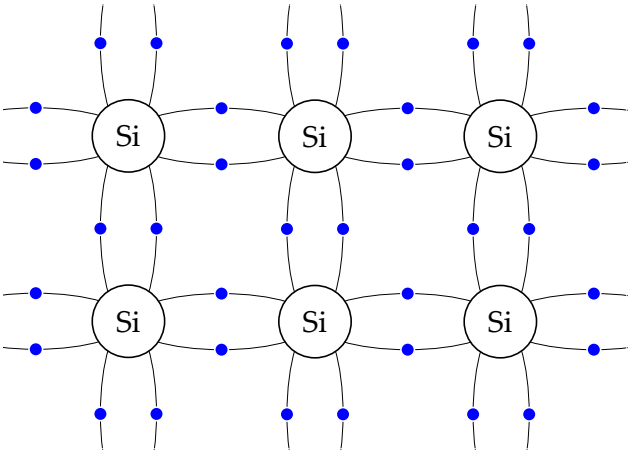

Figure 2.2: Schematic representation of a silicon crystal: each atom has four nearest neighbours and shares two electrons (the blue dots) with each one, forming covalent bonds.

A direct consequence of the crystalline structure is the formation of electron energy bands, rather than discrete energy levels: if there are N atoms in the crystal, each energy level should be N-fold degenerate,

but, since electrons are fermions, they split into N levels very close in energy to one another. For $N \to \infty$, which is a good approximation for a typical crystal, the various energy levels are so close that they can be considered as continuous energy bands.

The bands of interest for this work are the valence and conduction bands: they are defined, respectively, as the last filled and the first non-filled band. The conduction properties of a material depend on the separation (or lack thereof) and on the filling of these two bands (see Figure 2.3). A material is typically classified as:

- a conductor, if the two bands overlap or if the conduction band is partially filled.
- An insulator, if the conduction band is empty and it is separated from the valence band by a band gap of energy E_G big enough to prevent the thermal excitation of electrons (usually above 5 eV). An example is silicon oxide (SiO_2), which features a band gap of 8.8 eV.
- A semiconductor, if the conduction band is empty at temperatures close to 0 K, but E_G is small enough to allow thermal excitation. This is the case of silicon, which features a band gap energy of $E_G \approx 1.12$ eV at 300 K.[1]

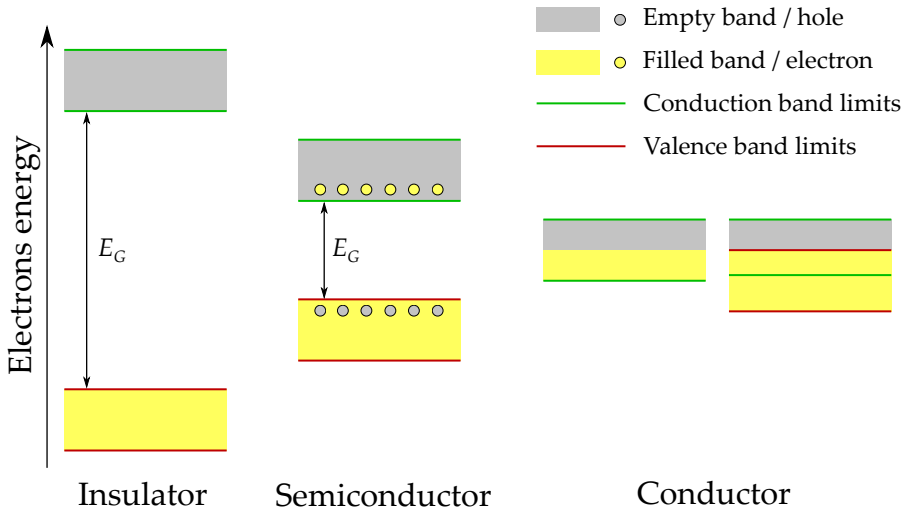

Figure 2.3: In an insulator the conduction and valence bands are separated by a large band gap ($\gtrsim$ 5 eV), while in a semiconductor it is smaller ($\lesssim$ 5 eV), allowing electrons to be thermally excited from the valence to the conduction band. In a conductor either the conduction band is partially filled or conduction and valence bands overlap.

At a very low temperature (close to 0 K) the valence band of a semiconductor is completely filled and the conduction band is completely

1 The band gap energy is temperature dependent, starting at 1.17 eV at 0 K and then decreasing. For the purpose of this work, it can be considered constant.

empty: since all the electrons are part of the covalent bonds, none is available for conduction.

At higher temperatures some electrons can be lifted to the conduction band creating a hole in the valence band, which represents the lack of an electron, but it can be described as a positively charge particle. Both holes and electrons can be described as free particles in the lattice, with effective masses $m_n = 1.18\, m_e$ for electrons and $m_p = 0.81\, m_e$ for holes, where $m_e = 511\,\text{keV}$ is the free electron mass.

It is worthwhile mentioning that silicon is an indirect semiconductor, *i.e.* a transition between the two bands requires a momentum transfer to the crystal lattice, so the energy required has to be greater than E_G.

2.1.2 *Carrier concentration*

Pure silicon is an intrinsic semiconductor, *i.e.* the number of impurities is negligible compared to the number of thermally generated carriers. It is possible to estimate the density of free charge carriers in equilibrium at a given temperature, starting from the Fermi-Dirac function, which gives the occupation probability of an electronic state of energy E at a temperature T:

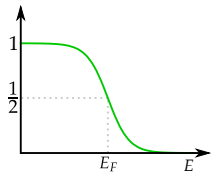

Fermi-Dirac function.

$$F(E) = \frac{1}{1 + e^{(E-E_F)/k_B T}} \tag{2.1}$$

where k_B is the Boltzmann constant and E_F the Fermi energy, defined as the energy of a state that has an occupation probability equal to $1/2$.

Since E_F is close to the middle of the band gap and $|E - E_F| \gg k_B T$ for allowed energy levels, the expression of $F(E)$ can be approximated, for electron and holes respectively, with:

$$F_n(E) \approx e^{-\frac{E-E_F}{k_B T}} \tag{2.2}$$

$$F_p(E) \approx e^{\frac{E-E_F}{k_B T}} \tag{2.3}$$

This approximation is valid for the so-called non-degenerate semiconductors. To obtain the density of charge carriers, it is necessary to combine the above expressions with the density of states, given by:

$$N(E_k) = 4\pi \sqrt{\left(\frac{2m}{h}\right)^3 E_k} \tag{2.4}$$

where m is either m_n or m_p, depending if electrons or holes are considered, h is the Planck constant, and E_k is the kinetic energy measured from the limit of the band gap.

By integrating the product of Equation 2.4 with Equation 2.2 and 2.3 over the conduction and valence bands respectively, the density of electrons n and holes p is obtained:

$$n = N_C e^{-\frac{E_C - E_F}{k_B T}} \tag{2.5}$$

$$p = N_V e^{\frac{E_V - E_F}{k_B T}} \tag{2.6}$$

where N_C and N_V are the density of states of conduction and valence bands, given by:

$$N_{C(V)} = 2\sqrt{\left(\frac{2\pi m_{n(p)} k_B T}{h^2}\right)^3} \tag{2.7}$$

and E_C and E_V are the energies of the limits of the band gap, so that $E_C - E_V = E_G$.

In an intrinsic semiconductor the density of holes is equal to the density of electrons $n = p = n_i$, so:

$$n_i = \sqrt{p \cdot n} = \sqrt{N_C N_V} e^{-\frac{E_G}{2k_B T}} \tag{2.8}$$

known as the mass-action law. Equating it to either Equation 2.5 or 2.6, the Fermi level for intrinsic semiconductors E_i can be obtained:

$$E_i = \frac{E_C + E_V}{2} + \frac{3k_B T}{4} \ln\left(\frac{m_p}{m_n}\right) \tag{2.9}$$

It is possible to notice that the energy of the Fermi level depends on temperature and deviates from the middle of the band gap due to a different effective mass of electrons and holes.

2.1.3 *Doped semiconductors*

Silicon is normally not used in its pure form: it is usually doped, *i.e.* small fractions of impurities (dopants) are added in a controlled manner, substituting silicon atoms in the lattice, to modify its properties.

Silicon has four valence electrons, so its covalent bonds in the lattice are complete: if an impurity has five valence electrons (like phosphorus or arsenic), four will be used to complete the covalent bonds and one will be free for conduction. Conversely, if a dopant has three valence electrons (like boron), the covalent bonds will not be complete, featuring a hole available for conduction. These two situations are sketched in Figure 2.4.

The impurities that add conduction electrons, *i.e.* that *donate* an electron to the conduction band, are called donors and silicon doped with these impurities is called *n*-type silicon. The impurities that add a hole, *i.e.* that can *accept* an electron to complete the covalent bond are called acceptors and silicon doped with them is called *p*-type silicon.

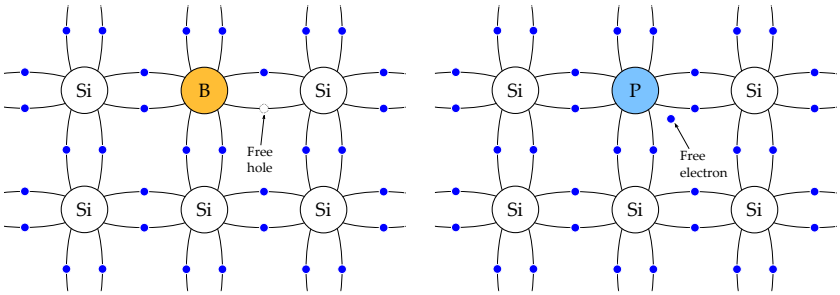

Figure 2.4: Schematic representation of the insertion of a trivalent (boron, on the left) and pentavalent (phosphorus, on the right) impurity in the silicon lattice. The boron creates a free hole, which can accept an electron, phosphorus donates a free electron.

Replacing silicon atoms in the lattice with different atoms has an influence on the energy bands structure as well: localized energy levels of donor or acceptor type, with energies E_D and E_A respectively, are created in the band gap (see Figure 2.5). A donor type level is defined as being neutral if filled by an electron and positive if empty. An acceptor level is negative if filled with an electron and neutral if empty.

These levels, for common dopants such as phosphorus, arsenic and boron, are close to the edges of the band gap ($E_C - E_D$ and $E_A - E_V$ are a few tenths of meV) and are referred to as shallow levels. At room temperature the donor levels will be almost fully ionized, promoting the electrons to the conduction band and the acceptor ones will be completely filled, with holes created in the valence band.

Given the densities of acceptors and donors, and assuming that they are fully ionized, the charge neutrality condition[2] becomes:

$$n + N_A = p + N_D \tag{2.10}$$

where N_A and N_D are the densities of acceptor and donor atoms respectively. By combining it with equation 2.8, the density of electrons and holes can be obtained. For n-type semiconductors, where $N_D \gg N_A$:

$$n = \frac{1}{2}\left[(N_D - N_A) + \sqrt{(N_D - N_A)^2 + 4n_i^2}\right] \approx N_D \tag{2.11}$$

$$p = \frac{n_i^2}{n} \approx \frac{n_i^2}{N_D} \tag{2.12}$$

For p-type semiconductors, where $N_A \gg N_D$:

$$p = \frac{1}{2}\left[(N_A - N_D) + \sqrt{(N_A - N_D)^2 + 4n_i^2}\right] \approx N_A \tag{2.13}$$

$$n = \frac{n_i^2}{p} \approx \frac{n_i^2}{N_A} \tag{2.14}$$

2 Despite the addition of impurities, the doped silicon remains always neutral.

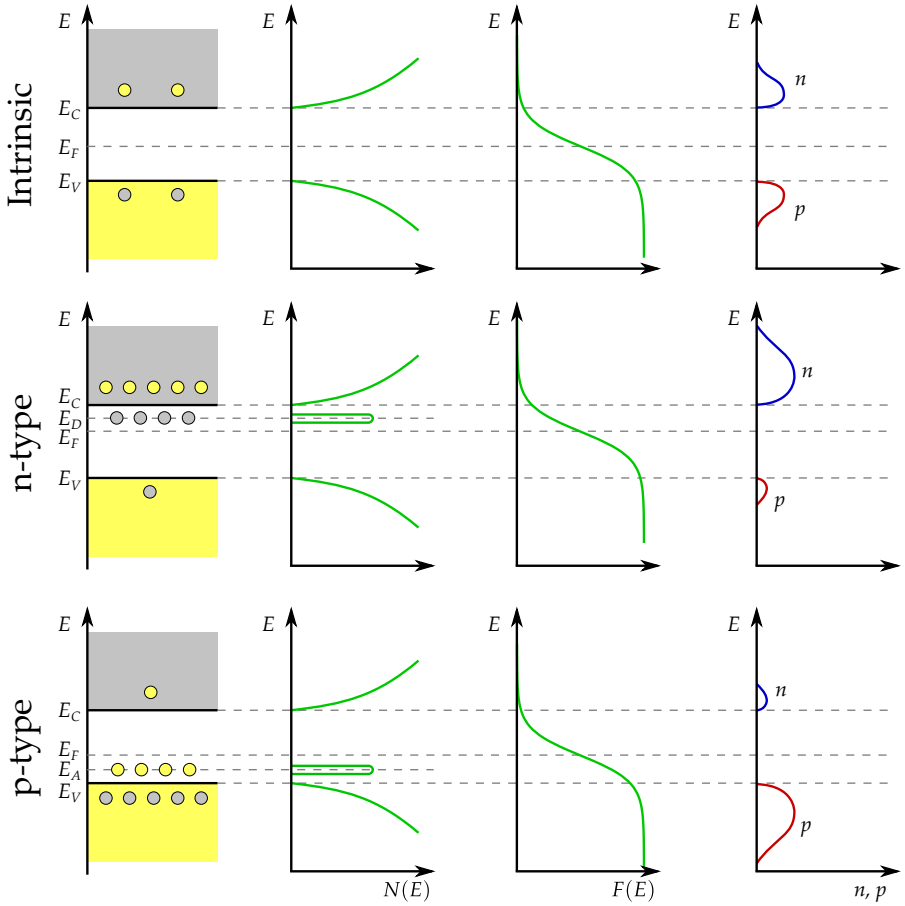

Figure 2.5: Schematic representation of band filling, density of states $N(E)$, Fermi-Dirac function $F(E)$ and carrier concentration for intrinsic, n- and p-type silicon at room temperature [61].

The approximations in Equations 2.11, 2.12, 2.13 and 2.14 are valid when $|N_A - N_D| \gg n_i$. In this case, it is also true that $p \gg n$ in p-type semiconductors and $n \gg p$ in n-type ones: the carriers with higher density are referred to as *majority carriers*, while the others as *minority carriers*.

The presence of ionized dopant levels also implies that the Fermi level will move towards the conduction or valence band, depending on the type of impurities. It can be calculated combining Equations 2.5, 2.6 and 2.8, obtaining:

$$E_F - E_i = k_B T \ln\left(\frac{n}{n_i}\right) \qquad \text{for n-type materials} \qquad (2.15)$$

$$E_F - E_i = -k_B T \ln\left(\frac{p}{n_i}\right) \qquad \text{for p-type materials} \qquad (2.16)$$

The Fermi level moves towards the conduction band in n-type semiconductors and towards the valence band in p-type ones.

2.1.4 *Carrier transport*

In this section the carrier transport phenomena of interest for this work, drift and diffusion, will be introduced. In equilibrium conditions, with no charge gradients and with no electric fields present, charge carriers in a crystal can be described as free particles, with a mean kinetic energy of $\frac{3}{2}k_BT$. Their mean speed at room temperature is of the order of 10^7 cm/s and their mean free path λ_m is around 100 nm.

2.1.4.1 *Drift*

If an electric field is present the carriers will be accelerated in its direction between two subsequent collisions, resulting in a non zero average velocity, the drift velocity, which causes an electric current. The drift velocity v_d depends linearly on the electric field E:

$$\vec{v}_d = \mu\vec{E} \tag{2.17}$$

where μ is the mobility of the charge carriers. This relation holds as long as the variation in velocity due to the electric field is small compared to the thermal velocity. If the field is high enough, the dependence is no longer linear and the velocity tends to saturate (see Figure 2.6).

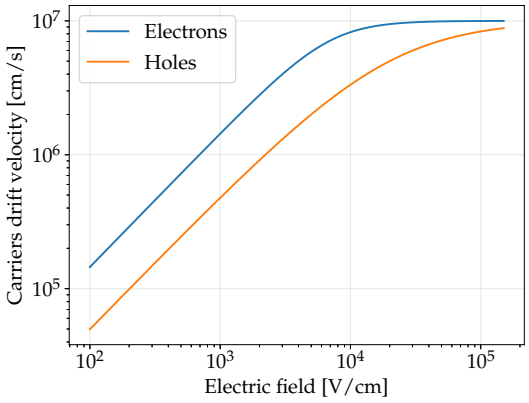

Figure 2.6: Drift velocity of electrons and holes as a function of the electric field. The dependence is linear for low field values and then it tends to saturate to 10^7 cm/s [61].

Using the drift velocity expression, it is possible to calculate the current density:

$$\vec{J}_n = -q\mu_n n\vec{E} \qquad \text{for electrons} \tag{2.18}$$

$$\vec{J}_p = q\mu_p p\vec{E} \qquad \text{for holes} \tag{2.19}$$

where q is the electron charge and holes and electrons mobility is indicated as μ_p and μ_n. The mobility depends on the mean free path through the relation:

$$\mu = \frac{q\lambda_m}{\sqrt{3k_BTm}} \tag{2.20}$$

where m is the effective mass of the carrier (hole or electron). This relation implies that the mobility for electrons and holes is different, in particular in silicon they are $1450\,\mathrm{cm}^2/\mathrm{Vs}$ and $500\,\mathrm{cm}^2/\mathrm{Vs}$ respectively.

Mobility is also directly related to the resistivity ρ, which is given by:

$$\rho_n = \frac{1}{q\mu_n n} \qquad \text{for n-type silicon} \tag{2.21}$$

$$\rho_p = \frac{1}{q\mu_p p} \qquad \text{for p-type silicon} \tag{2.22}$$

2.1.4.2 *Diffusion*

Diffusion of charge carriers occurs when charge is not distributed uniformly in the crystal. Whenever a gradient of charge density exists, carriers will migrate from the region with the higher concentration to a region with a lower concentration, generating a current with density:

$$\vec{J}_n = qD_n\vec{\nabla}n \qquad \text{for electrons} \tag{2.23}$$

$$\vec{J}_p = -qD_p\vec{\nabla}p \qquad \text{for holes} \tag{2.24}$$

where D_n and D_p are the diffusion coefficients for electrons and holes, related to the mobility by the Einstein equation:

$$D = \frac{k_BT}{q}\mu \tag{2.25}$$

2.1.5 *Carriers generation and recombination*

In the previous sections it has been mentioned that, in semiconductors, electrons can be promoted to the conduction band by thermal excitation, creating a hole in the valence band. Other mechanisms to accomplish this are optical excitation or ionization by charge particles, and, in presence of a strong electric field, charge multiplication can occur. These effects, along with the mechanisms to restore the equilibrium, will be briefly described in the following paragraphs.

2.1.5.1 *Thermal generation and recombination*

Thermal carriers generation consists in the excitation of electrons from the valence to the conduction band by thermal energy. In silicon at

room temperature the probability of a direct transition is extremely low, due to the high width of the band gap compared to thermal energy and the requirement to transfer momentum to the crystal, since silicon is an indirect semiconductor. Here excitations usually occur in more than one step, through intermediate energy levels within the band gap, also called trapping centres, created by crystal imperfections and impurities.

Thermal generation can be described by a characteristic time τ_g, which depends on the trapping centres density, their energy and the capture cross sections and thermal velocities for electrons and holes [62]. It describes the time constant required to pass from a non-equilibrium state, with defect of charge carriers, to the thermal equilibrium state.

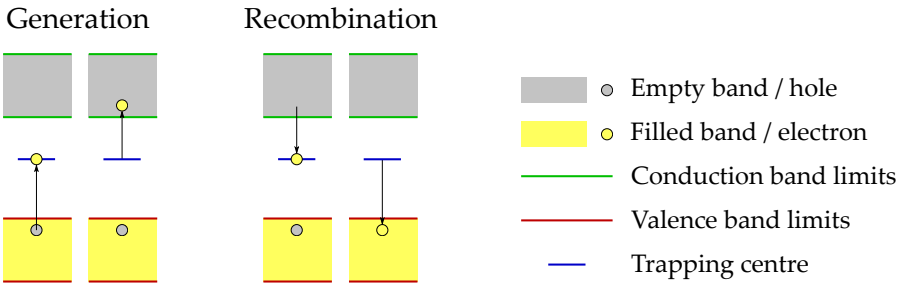

Figure 2.7: Thermal generation and recombination of carriers in silicon requires two steps, involving a trapping centre in the band gap.

If an excess of charge carriers is present, instead, the system will transition back to equilibrium, again exploiting the trapping centres, since a direct transition is suppressed. Recombination is described by its characteristic time τ_r, which is different between p- and n-type silicon and depends on the same parameters of τ_g, with the addition of the majority carrier concentration [62].

2.1.5.2 *Generation by charged particles*

A charged particle that travels through a material loses part of its energy colliding elastically with the electrons of the atoms forming the material, ionizing them and thus creating electron-hole pairs in a semiconductor. The energy loss per unit length is given, for medium-energy particles, by the Bethe-Bloch formula (plotted in Figure 2.8) [62]:

$$\frac{dE}{dx} = 2\pi N_0 r_e^2 m_e c^2 \varrho \frac{Z}{A}\frac{z^2}{\beta^2}\left[\ln\left(\frac{2m_e\gamma^2 v^2 W_{\max}}{I^2}\right) - 2\beta^2 - \delta - 2\frac{C}{Z}\right] \tag{2.26}$$

where:

- N_0 is Avogadro's number,
- r_e is the classical electron radius,

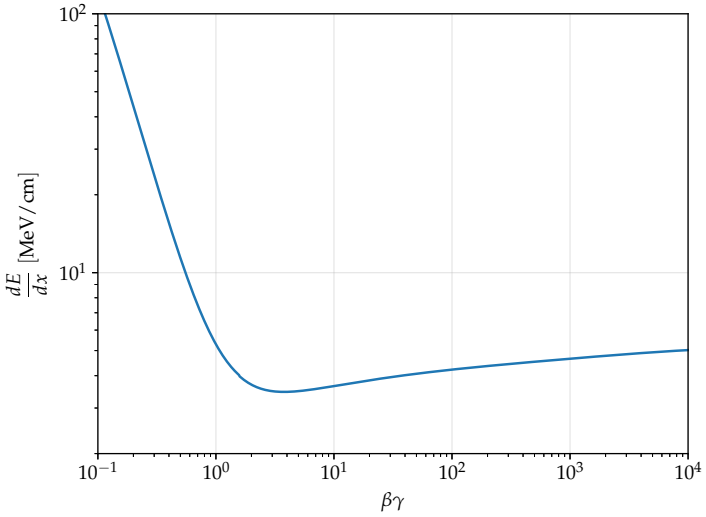

Figure 2.8: Plot of the Bethe-Bloch formula for silicon as a function of the $\beta\gamma$ of the crossing particle.

- m_e is the electron mass,
- c is the speed of light,
- ϱ is the density of the material,
- Z and A are the atomic number and weight of the material,
- z is the charge of the particle,
- $\beta = v/c$, where v is the velocity of the particle,
- $\gamma = \frac{1}{\sqrt{1-\beta^2}}$,
- W_{max} is the maximum energy transfer in a single collision,
- I is the effective ionization potential averaged on all the electrons,
- δ is a density correction and
- C is a shell correction.

Particles with $\beta\gamma \approx 3 - 4$ fall in the minimum of this function and are referred to as minimum ionizing particles (MIPs): they release around 3 MeV/cm when crossing silicon.

The average energy loss in a material can be calculated by integrating the Bethe-Bloch formula over the distance traveled by the particle. However, statistical fluctuations are present and they are described by the Landau distribution: the energy loss distribution is asymmetrical, with a greater tail at higher energies, so the average energy loss becomes different from the most probable value. Example of Landau distributions are shown in Figure 2.9.

Not all the energy lost in silicon is used to create electron-hole pairs, part of it is transferred to the crystal lattice: the average energy required to create them is 3.6 eV per pair, *i.e.* a MIP will generate around 80 electron-hole pairs per micron.

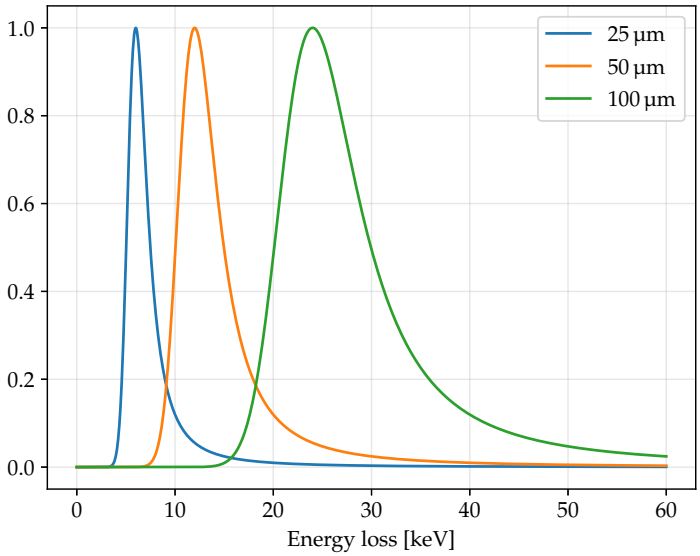

Figure 2.9: Energy loss distributions for particles crossing silicon of different thicknesses.

2.1.5.3 *Charge multiplication*

Charge multiplication happens when a carrier, between two collisions with the lattice atoms, is accelerated enough by an electric field to create an electron-hole pair, which, in turn, can accelerate and create more carriers, causing an avalanche effect. This effect can either be a problem, when it leads to a breakdown (see Section 2.1.6.2), or it can be exploited in a controlled way, to amplify the signal generated in a detector.

The probability of creating a secondary electron-hole pair is different depending on the type of charge carrier: in silicon it is higher for electrons, so they require a lower electric field to initiate charge multiplication.

2.1.6 *The pn junction*

The pn junction is a structure obtained by joining extrinsic semiconductors of opposite doping, forming a diode, *i.e.* a component that conducts current mainly in one direction. Electrons from the n-type material will diffuse into the p-type one and vice-versa, leaving a region around the junction depleted of free charge carriers, the so called *space-charge region* or *depleted region*.

Here a charge density (positive in the n-region and negative in the p-region) is present, due to the unbalanced nuclear charge from the doping atoms, and it is equal to:

$$\rho_p = -qN_A \qquad \text{in the p-region} \tag{2.27}$$

$$\rho_n = qN_D \qquad \text{in the n-region} \tag{2.28}$$

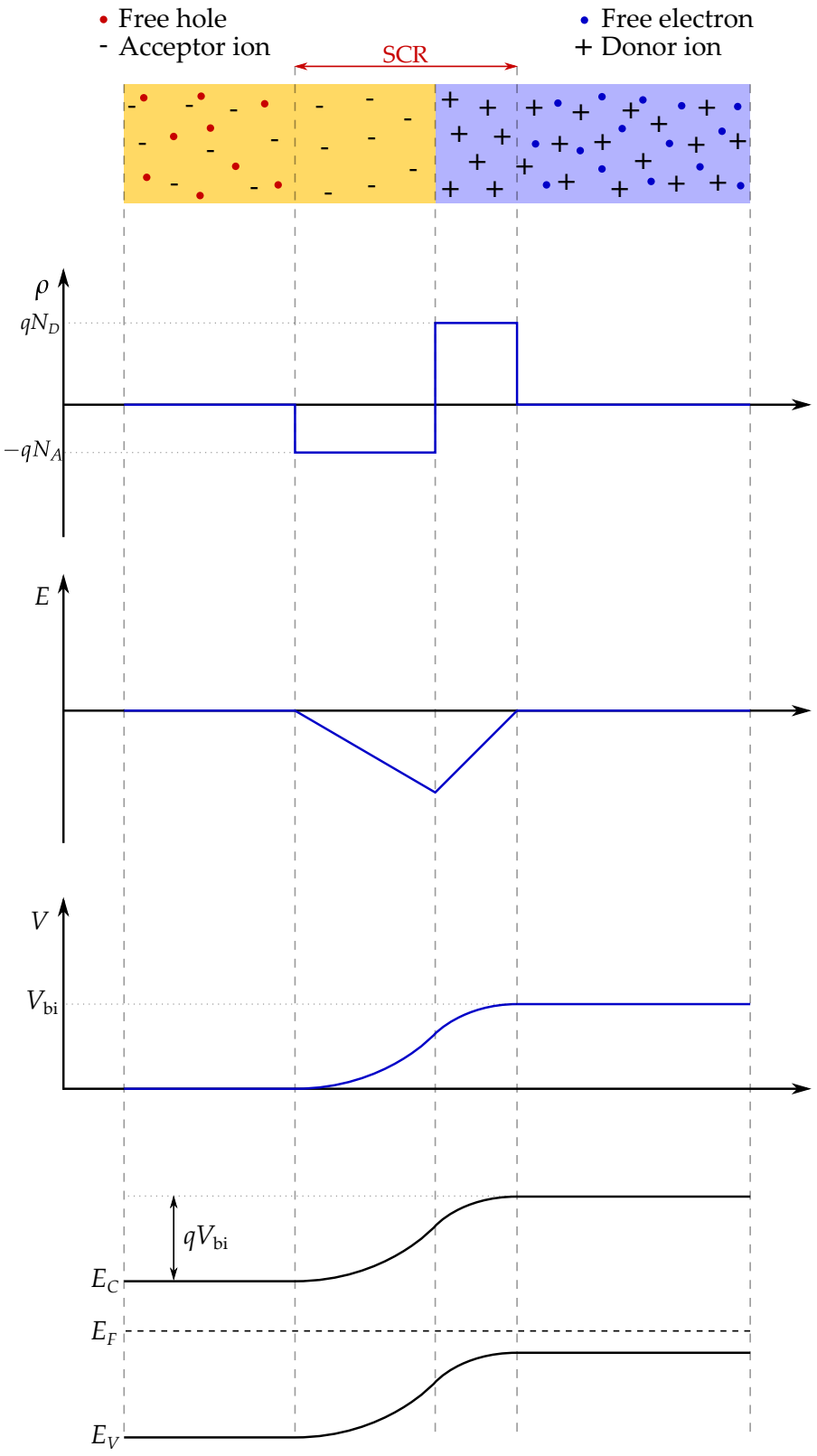

Figure 2.10: A sketch of a pn junction with the plots of the charge density ρ, the electric field E, the potential V and the bands structure as a function of the position. SCR denotes the space-charge region.

where q is the electron charge. These equations assume that the change in charge density between the neutral and the depleted region is a step function, which is a good approximation since the transition region is very thin compared to the width of the space-charge region.

An intrinsic electric field is therefore created in the space-charge region, preventing further diffusion to occur, leading to an equilibrium state and creating a voltage difference V_{bi}, called *built-in voltage*, between the two neutral regions. All these quantities are depicted in Figure 2.10 as a function of the position along the pn junction.

This situation can also be represented with the band model: at thermal equilibrium, Fermi levels must line up, moving the band limits of one region with respect to the other by qV_{bi}. This situation is also sketched in Figure 2.10.

2.1.6.1 *Depletion-region depth*

If a forward bias voltage (positive in the p-region) is applied to the pn junction, it opposes the built-in voltage and the space-charge region shrinks, until the diode starts to conduct current, which increases exponentially with the voltage. In case of a reverse bias voltage instead, the space-charge region grows until breakdown (see Section 2.1.6.2) is reached. The current-voltage characteristics are shown in Figure 2.11.

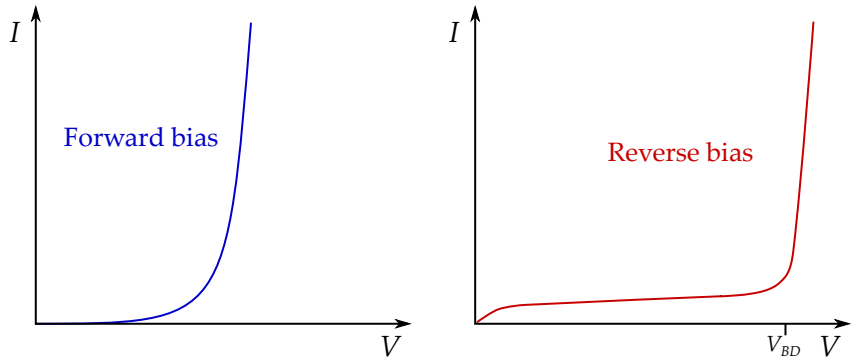

Figure 2.11: The current-voltage characteristics of a pn junction in (a) forward bias and (b) reverse bias configurations. V_{BD} is the breakdown voltage. Note that the scales of the two plots are different: in forward bias the pn junction starts conducting at around 1 V, while V_{BD} can vary from a few tenths to thousands of volts.

The depletion-region depth can be calculated by requiring that the electric field at the boundaries is zero and the voltage difference is the sum of the built-in voltage and the reverse bias voltage. It is thus given by:

$$d = \sqrt{\frac{2\varepsilon(N_A + N_D)}{qN_AN_D}(V_{\text{bi}} + V)} \tag{2.29}$$

where ε is the permittivity of silicon and V is the value of the reverse bias voltage (considered to be positive). Since in silicon detectors one of the two regions has a much higher doping concentration (*e.g.* $N_D \gg N_A$), the expression can be simplified as:

$$d = \sqrt{\frac{2\varepsilon}{qN_A}(V_{\text{bi}} + V)} \tag{2.30}$$

2.1.6.2 *Leakage current and breakdown*

A pn junction in reverse bias condition features a leakage current determined mostly by carriers generation in the space-charge region: here the thermal generation of carriers is dominant, compared to recombination because of the lack of free electrons and holes. This causes a reverse current, whose density is given by:

$$J_R \approx \frac{qn_i d}{\tau_g} \propto \sqrt{V_{\text{bi}} + V} \tag{2.31}$$

which shows a temperature dependence trough τ_g (the leakage current is higher at higher temperatures).

This equation holds until a breakdown condition is reached, that consists in a sudden increase of the reverse current. The main phenomenon that causes breakdown is charge multiplication due to the high field present in the depletion region. The value of the breakdown voltage V_{BD} depends on the dopants concentration, but also on the details of the production process and on the shape of the structures on the chip, due to edge effects.

2.1.6.3 *Junction capacitance*

A pn junction in reverse bias (or unbiased) can be viewed as a capacitor: the space-charge region is not conductive and it is located between two conductive regions. In first approximation this structure can be treated as a planar capacitor, where the capacitance depends on the area A of the electrodes and their distance (which corresponds to the depletion depth d):

$$C = \frac{\varepsilon A}{d}. \tag{2.32}$$

Combining it with Equation 2.30, it can be shown that the junction capacitance is inversely proportional to the squared root of the reverse bias voltage:

$$C \propto \frac{1}{\sqrt{V_{\text{bi}} + V}}. \tag{2.33}$$

2.1.6.4 *The pn junction as a particle detector*

A pn junction can be used as a particle detector. Charge carriers generated by the traversing particle in the space-charge region drift due to the electric field, generating a measurable current, as sketched in Figure 2.12.

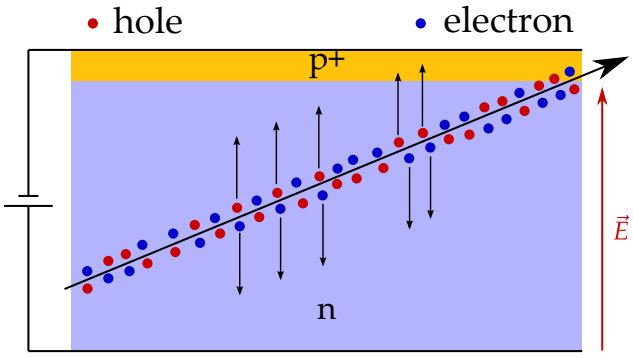

Figure 2.12: Sketch of the electron-hole pairs generated by a ionizing particle in a silicon detector. Once generated, they start drifting due to the electric field, thus generating a current.

For this reason a silicon particle detector is normally operated in reverse bias, to enlarge the depletion region and thus increase its sensitive volume, along with the generated current. Furthermore, charge generated outside the space-charge region can still contribute to the signal by diffusion, but the signal is normally much smaller and slower than if it were generated by drift.

The pn junctions in a silicon detector, and the electrodes connected to it, can be segmented in one or two directions, obtaining strips and pixel respectively. They are then connected to a readout electronic chain, to amplify, shape and digitize the current signal, which can be either on the same chip or on a separate one, as it will be discussed in the following sections.

2.2 SILICON DETECTORS

Silicon detectors normally exploit a reverse biased pn junction to detect ionizing particles. Their characteristics make them appealing to be used as position detectors, where high precision and low material budget is required: the average ionization energy is small compared, *e.g.* to gaseous detectors (3.6 eV against $\sim$ 30 eV), so the generated signal for the same energy loss is one order of magnitude larger. This feature, combined with their high rigidity, enables the production of very thin detectors, of the order of a few hundred microns, which still produce a measurable signal.

In the following section the signal formation and readout electronics will be briefly discussed and a particular type of silicon detectors,

hybrid pixel detectors, the technology currently used for the ATLAS ID (see Section 1.3.1), will be described.

2.2.1 *Signal formation*

A charged particle that crosses the detector generates electron-hole pairs, as described in Section 2.1.5.2. If these carriers start moving, either by drift or diffusion, they induce a current on the electrodes, which can be calculated with the Shockley-Ramo theorem. It states that the instantaneous current i induced on an electrode by a single charge carrier is given by:

$$i = q\vec{E}_w \cdot \vec{v} \tag{2.34}$$

where $\vec{v}$ is the velocity of the carrier and $\vec{E}_w$ is the so called weighting field, obtained setting the potential of the electrode of interest to 1 V and all the others to 0 V and assuming that no charges are present.

The current is generated from the instant when the carriers start moving, until they are all collected at the electrodes or trapped in the lattice. The exact shape of the current pulse depends on the geometry and on the presence of an electric field, but for a depleted sensor it is typically of the order of 1 ns.

2.2.2 *Readout electronics*

After being generated, the current pulse needs to be processed, to be digitized and read out. The electronic chain details depend on the specific application, and here the typical chain for silicon detectors considered in this work will be described (a simplified schematics is shown in Figure 2.13).

The first element is a charge sensitive preamplifier: it integrates the incoming signal pulse, generating a voltage signal proportional to the collected charge, with a long decay time, compared with the timescales of interest for the detector. The signal is then shaped, using a series of differentiators (high pass filters) and integrators (low pass filters), in order to enhance the signal to noise ratio, by limiting the frequency band to the signal frequencies.

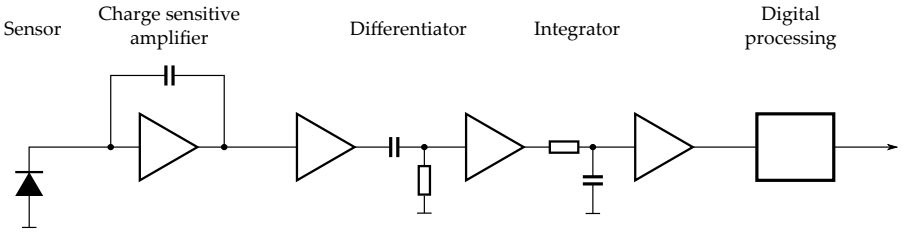

Figure 2.13: A typical readout chain for a silicon detector.

After the shaping stage, the resulting signal can be digitized in several manners. One of the simplest way to digitize it while maintaining the information on the collected charge (and so on the deposited energy) is the so-called Time-over-Threshold (ToT): the signal from the shaper is fed to a discriminator and the duration of the resulting pulse is measured.

Since the relation between ToT and deposited energy can be non-linear, a calibration is often performed using radioactive sources. The ToT is used to measure the collected charge, for example, in the FE-I4 chip (described later), but also in the HV-CMOS prototypes described in the next chapter.

2.2.3 *Pixel detectors*

Silicon detectors can be finely segmented to precisely measure the crossing points of charged particles. In this section, pixel detectors, *i.e.* detectors segmented in two dimensions will be described. The two types of pixel detectors of interest for this work are planar and 3D.

The planar pixel detectors (Figure 2.14) are built on special high resistivity, lightly doped, silicon substrates, on top of which finely segmented pn junctions are created (*e.g.* if the substrate is of type n, the implantations will be of type p), indicated as the collection electrodes. The implantations normally have a higher doping concentration than the substrate (p+ in this example), so the depletion depth in the bulk will be wider, and are connected to a pad each, in order for the sensor to be connected to the read-out electronics. The backside of the sensor is doped to make it of type n+ and metallized, to create a high conductivity part where the bias voltage can be applied.

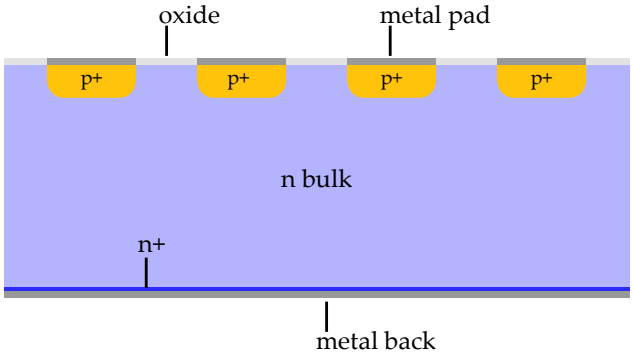

Figure 2.14: Simplified cross section of a planar pixel detector. The space-charge region grows from the top when the reverse bias voltage increases.

An alternative way of building them is to use a n+ implant for the pixels and a p+ implant for the backside, as sketched in Figure 2.15. The planar sensors of the ATLAS Inner Detector [64], described in Section 1.3.1, are built in this way. They have the disadvantage of

needing to be operated in full depletion, in order to keep the pixel isolated from each other, since the space-charge region expands from the back.

However, as it will be discussed in Section 2.4.1.4, the effective doping concentration of the bulk decreases with irradiation, until it reaches type inversion , *i.e.* it changes from n to p, and starts to increase again. After type inversion, the space-charge region begins to expand from the top, and the pixels can be operated even if the bulk is not fully depleted.

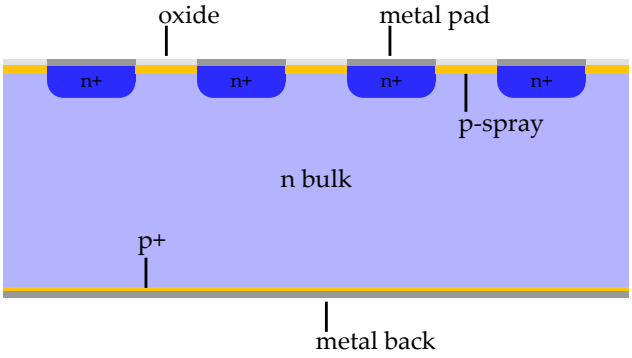

Figure 2.15: Simplified cross section of a planar pixel sensor used in the ATLAS Inner Detector. The depletion depth grows from the back until, due to irradiation, the bulk type inverts. A p-type implant (p-spray) is present between the pixels to isolate them from one another.

A different approach to the sensor geometry are 3D sensors [65]: here the collection electrodes are not implanted on the surface of the sensor, but in columns perpendicular to it, that extend inside the bulk as shown in Figure 2.16. They have the advantages of featuring shorter charge collection distances, and thus higher radiation hardness (due to less charge trapping) and lower voltage to achieve full depletion, but they are more complex to fabricate, have a higher detector capacitance, which causes a higher noise and power consumption, and are inefficient in the regions corresponding to the collection electrodes.

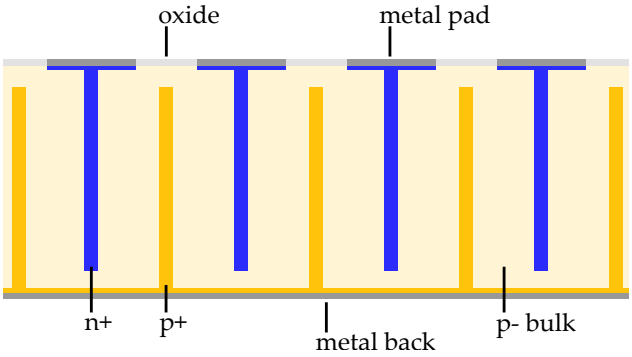

Figure 2.16: Simplified cross section of a 3D pixel sensor, based on the type used in the IBL (see Section 1.3.1).

2.2.4 *Hybrid modules*

The detectors described in the previous section require a dedicated front-end ASIC (Application Specific Integrated Circuit) to amplify, shape and digitize the charge signal generated by ionizing particles. These ASICs usually contain additional logic as well, to determine the time over threshold of each hit, store the recorded hits waiting for a trigger, perform self calibration, etc.

They are connected to the sensor die with bump bonds, forming the hybrid modules. Bump bonding is a process that consists in the deposition of conductive solder bumps on the pads of one chip (*e.g.* the sensor chip), then a second chip (in this case the front-end) is aligned to it, they are put into contact and the bumps are reflowed. Several materials and alloys can be used for the bumps, *e.g.* indium, tin-lead, tin-silver, etc.

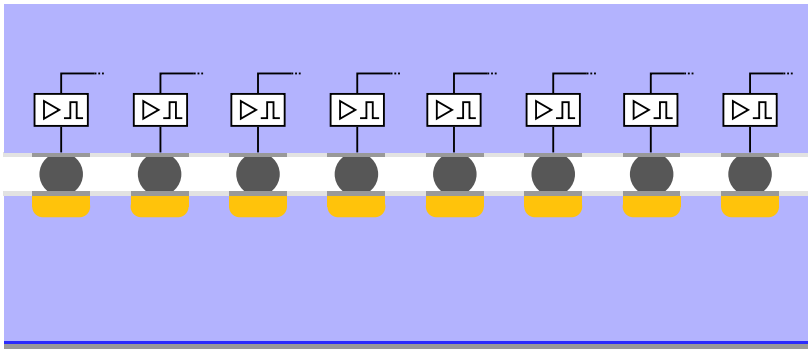

Figure 2.17: Simplified cross section of an hybrid module. The sensor (on the bottom) is connected to the read-out ASIC via metallic bumps.

As an example of a front-end chip, the FE-I4 (Figure 2.18), will be described briefly, since it is used in the current ATLAS pixel detector, but also in the beam telescope modules described in Section 5.3.1. It contains 26 880 pixels, arranged in 80 columns, with a 250 µm pitch, and 336 rows, with 50 µm pitch. Each pixel contains an amplification stage with adjustable shaping and a discriminator with adjustable threshold. It can save the time-of-arrival of a hit and its time-over-threshold with a 4 bit resolution, in counts of the external clock (nominally 40 MHz, equal to the LHC collision rate).

The pixels of the FE-I4 are arranged in column pairs, each divided in regions of 2×2 pixels, which store the hit data locally, until a trigger signal selects the hits to be read out based on their time-of-arrival.

2.3 CMOS PARTICLE DETECTORS

The hybrid detectors introduced earlier are composed of two parts: a silicon sensor, which can withstand high voltages (up to thousands of

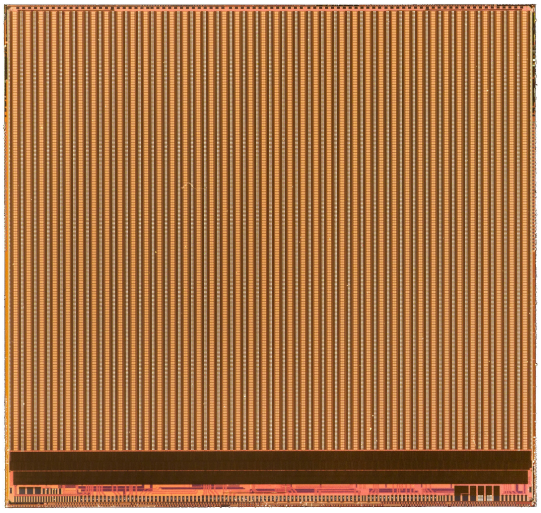

Figure 2.18: The FE-I4 ASIC. It is possible to observe the double-column arrangement and the end-of-column electronics at the bottom, where also the pads are located [66].

volts) and a read-out chip, which works at low voltages. These two devices are DC coupled with a bump bonding process.

A different approach exists, however: the readout electronics (or at least part of it) can be implemented on the same die as the sensor. It can then work stand-alone or, if only a part of the readout chain has been integrated on the sensor, it can be capacitively coupled to a readout ASIC.

In this section the CMOS technology, used to build this kind of sensors, will be briefly introduced and its use for particle detectors will be presented.

2.3.1 *CMOS technology and devices*

CMOS (Complementary Metal-Oxide-Semiconductor) is a type of fabrication process of MOSFETs (Metal-Oxide-Semiconductor Field-Effect Transistors) that uses complementary pairs of p-type and n-type MOSFETs for logic functions. CMOS technology is widely used for constructing digital and analogue integrated circuits. A typical CMOS device is built on a silicon substrate, where different components are implanted and connected by several metal layers placed on top of the silicon and insulated with oxide layers, as shown in Figure 2.19. It is important to note that numerous CMOS technologies exists, characterized by the smallest feature size they can achieve, the possibility to use high voltages, etc.

The basic building blocks of a CMOS technology is the MOSFET, a field effect transistor with an insulated gate. It consists of a stack of metal or polysilicon (the gate), oxide and semiconductor: the gate voltage determines the electrical conductivity of the device, allowing

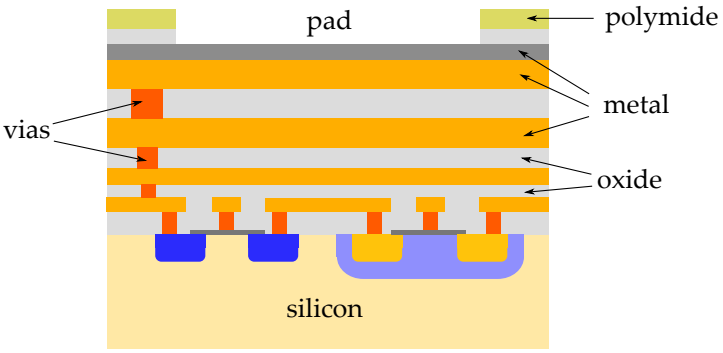

Figure 2.19: A simplified cross section of a CMOS device.

it to be used as an amplifier or a switch. Two complementary types of MOSFETs exists, p-type and n-type, depending on the sign of the charge carriers that are involved in current conduction. A simplified cross section of these two types of transistor is shown in Figure 2.20.

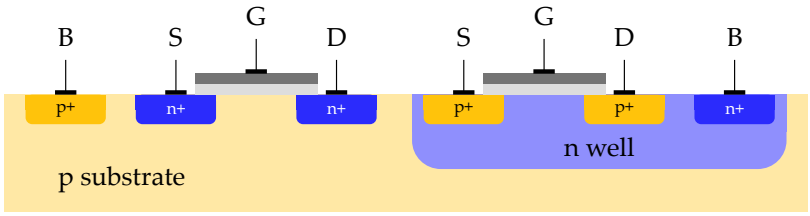

Figure 2.20: A n-type (left) and a p-type (right) MOSFET on the same substrate. The letters indicate the Body, Drain, Gate and Source terminals. The dark grey part is the gate metal (or polysilicon) and the light grey is the gate oxide.

They can vary the current flowing between the source and drain terminals by modulating the voltage difference between the gate and the body. For example, in a nMOS transistor, if the gate voltage is increased, the conduction band and the intrinsic level in the p-type substrate close to the oxide are pushed closer to the Fermi level. If E_i crosses E_F a type inversion occurs and a layer of free electrons is created at the Si-SiO_2 interface, allowing conduction between the source and drain wells. A pMOS transistor work in a similar way, with the signs exchanged: the gate voltage must be more negative and a channel of free holes is created at the interface.

Conventionally, the gate voltage at which the density of electrons at the interface is equal to the hole density in the body is called the threshold voltage V_{th}. It correspond to the situation where $E_i = E_F$ at the interface. Conduction starts when the gate voltage is higher than V_{th} (for nMOS transistors).

Other components, such as resistors and capacitors, are also available in CMOS technologies. They can be implemented in different ways: a common method to build a resistor is by using polycrystalline silicon, while capacitors are usually constituted of two metal surfaces

separated by silicon oxide, in the topmost layers of the chip. Inductors can be implemented as well, by means of a metal spiral, but they are less commonly used and occupy a significant surface area.

2.3.2 *High-Voltage CMOS detectors*

It is possible to build particle detectors using commercially available CMOS technologies: this allows the use of the same die as a sensor and as a read-out ASIC. Here the focus will be on High-Voltage CMOS (HV-CMOS) technologies, which are employed in this work.

The read-out electronics is normally partially placed within each pixel (usually the amplifier, the discriminator and part of the digital processing) and partially at the chip periphery (*e.g.* global processing, data and commands IO, etc.). This scheme is quite flexible and the complexity of the pixels and periphery can be chosen based on the specific application. If the sensor can be used stand-alone, without the need for a read-out ASIC, it is known as a monolithic active pixel sensor.

HV-CMOS detectors are usually built on a p-type substrate with n-type implants to form the pixels. These implants can be almost as big as the pixel, containing the read-out electronics on top, or much smaller, with the readout electronics separated from it: these two approaches are called large fill-factor and small fill-factor respectively. A sketch comparing them is shown in Figure 2.21.

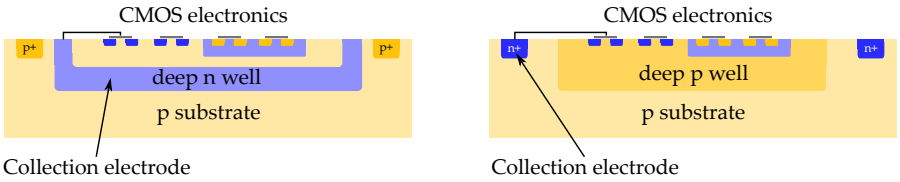

Figure 2.21: Comparison of large (left) and small (right) fill-factor sensors.

If the collection electrode is almost as big as the pixel pitch in both directions (large fill-factor), it makes the drift path short, thus enhancing the radiation hardness of the sensor to bulk damage. However it has the disadvantage of featuring a larger sensor capacitance, which can increase the noise and power consumption. Conversely, small fill-factor sensors have a much lower power consumption and noise, thanks to the much smaller pixel capacitance. The longer path of the charge carriers in the bulk, however, implies a higher probability of trapping, which can significantly reduce the detector efficiency after irradiation.

HV-CMOS detectors have several advantages compared to the hybrid pixel detectors described in the previous section: they can exploit the worldwide development of CMOS technologies, leading to lower production costs and giving the possibility to choose from a wide range of technologies. Furthermore, assembly is simplified, since they

can be made fully monolithic (*i.e.* not requiring and external read-out ASIC) or, if only part of the readout chain is implemented on the sensors, they can be capacitively coupled to a read-out chip, removing the need for bump bonding.

Another advantage is the possibility to make very thin detectors, around 50 µm thick, when it is necessary to have as little material as possible and to apply a high voltage to the substrate to deplete it. The main disadvantages of HV-CMOS sensors are their limited depletion-region depth, compared to hybrid detectors (it usually does not exceed 100–200 µm because the comparatively low bias voltage that can be applied at their substrate) and their lower radiation hardness.

In the next chapter the research and development work to develop HV-CMOS sensors to be used in the ATLAS Inner Tracker will be discussed, with a focus on the prototypes characterized in this work.

2.4 RADIATION DAMAGE

The silicon detectors of interest for this work are used to measure the position of ionizing particles in an extremely harsh radiation environment: the absorbed radiation can have detrimental effects on the performance of the detector in several ways, permanently damaging the bulk of the sensor, the electronics or causing transient effects in the read-out circuitry. Furthermore, the damage can evolve with time, even in absence of further irradiation, due to annealing processes.

2.4.1 *Bulk damage*

The incoming radiation can interact with the lattice nuclei, displacing them from their original lattice position, as shown in Figure 2.22, creating a vacancy and an interstitial, also referred to as a point defect. A silicon atom can be displaced if the recoil energy is high enough: at 25 eV the displacement probability is around 50%. By kinematic considerations, it can be shown that the minimum kinetic energy to create point defects is 190 eV for protons and neutrons and 260 keV for electrons. If the energy is much higher than these values, the recoiling nucleus can create additional point defects, or also a cluster of defects, usually of 5 nm diameter, containing around 100 displacements.

Interstitials and vacancies are mobile at room temperature, so an interstitial atom can migrate in the crystal and if it finds a vacancy, it can fill it, restoring the lattice structure. However there is also the possibility to form stable defects, like a combination of a vacancy with an oxygen atom (known as A-center), a vacancy with a phosphorus atom (E-center), a divacancy (two vacancies right next to each other), etc. These defects can alter the electrical properties of the crystal, by creating additional levels in the band gap that can act as generation-

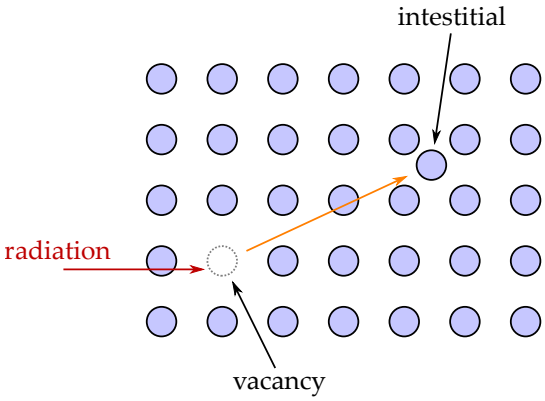

Figure 2.22: An incoming particle can displace a lattice atom creating a vacancy and an interstitial.

recombinations centres, trapping centres, or they can change the charge density in the space-charge region.

These modifications have an impact on macroscopic properties of the silicon detector: the leakage current increases, the collected charge decreases and the depletion depth, at a given bias voltage value, changes.

2.4.1.1 *The NIEL-scaling hypothesis*

The effects described above depend on the Non-Ionizing Energy Loss (NIEL) of the radiation of interest in the material, which can vary with its energy and particle type. The proportionality between the NIEL value and the resulting damage effects is referred to as the *NIEL-scaling hypothesis*: the radiation fluence Φ, *i.e.* the number of particles crossing the material per unit surface, is normalized to the damage caused by 1 MeV neutrons and it is expressed in terms of 1 MeV n_{eq}/cm^2. The relation used for this conversion is the following:

$$\Phi_{eq} = \frac{D(E)}{D_n(1\,\text{MeV})}\Phi = k(E)\Phi \tag{2.35}$$

where Φ is the radiation fluence, Φ_{eq} is the fluence expressed in 1 MeV n_{eq}/cm^2, and D is the displacement damage cross section, which depends on the energy and particle type (D_n is the one for neutrons). The ratio $k(E) = D(E)/D_n(1\,\text{MeV})$ is called *hardness factor* and its value for several particles is shown in Figure 2.23.

This hypothesis, however, is not universally valid and some deviation from it has been observed: protons cause less damage than neutrons on oxygenated substrates [71], but also on standard substrates at a low kinetic energy (7–10 MeV) [72]. A deviation has been observed in this work as well, as discussed in Section 4.8.1.2 on page 108.

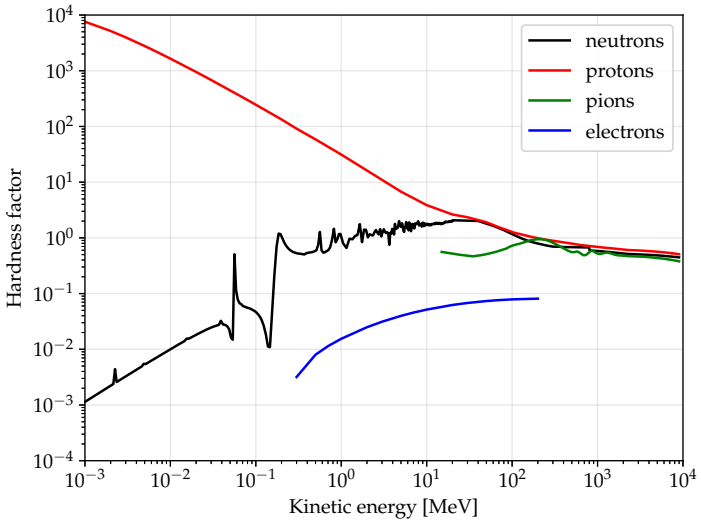

Figure 2.23: Energy dependence of the hardness factor for different types of radiation. Data from [67–70].

2.4.1.2 *Leakage current*

As explained in Sections 2.1.5.1 and 2.1.6.2, the leakage current is inversely proportional to the characteristic generation time τ_g, which, in turn, decreases with an increasing density of trapping centres. This implies an increase of the leakage current, due to carriers generated in the volume of the bulk, that can be parametrized with:

$$\frac{\Delta I_{\text{vol}}}{V} = \alpha \Phi \tag{2.36}$$

where $\Delta I_{\text{vol}}/V$ is the variation in leakage current per unit volume and α is a constant, which depends on the temperature and annealing time, while it appears to be independent of the specific properties of the bulk. It can assume values in the range 10^{-17} to 10^{-16} A/cm [73].

2.4.1.3 *Collected charge*

The additional levels formed in the band gap due to irradiation can act as trapping centres, capturing the mobile carriers that generate the current signal, reducing its intensity. These trapping centres are able to capture charge carriers if they are not already occupied, which is a good assumption in the space-charge region, if the leakage current is low: in this case most traps are empty and have higher probability of capturing signal charge.

It is possible to define the characteristic capture time τ_t (which will be different for electron and holes):

$$\tau_t = \frac{1}{\sigma v_{\text{th}} N_t} \tag{2.37}$$

where σ is the capture cross section, v_{th} is the carriers thermal velocity and N_t is the traps concentration.

Since τ_t is inversely proportional to N_t, which increases linearly with fluence, the dependence of the trapping time constant with Φ is given by:

$$\frac{1}{\tau_t(\Phi)} = \frac{1}{\tau_t(\Phi = 0)} + \gamma\Phi. \tag{2.38}$$

The time τ_t can be used to determine the evolution of the signal charge with time:

$$Q(t) = Q_0 e^{-\frac{t}{\tau_t}} \tag{2.39}$$

where $Q(t)$ is the signal charge at the instant t and $Q_0 = Q(0)$. It is clear that if the collection time is small compared to τ_t, almost all the charge will be used to generate the current signal, while if they are comparable or τ_t becomes smaller than the collection time, the signal will be degraded.

2.4.1.4 *Depletion depth*

Several radiation damage mechanisms can lead to a variation of the space charge, causing a different depletion depth at a given bias voltage or equivalently, a different full depletion voltage. This variation can be described as a change in the effective doping concentration, defined as $N_{\text{eff}} = N_D - N_A$ (negative for p-type semiconductors), due to different effects, that can be summarized in four categories:

- donors removal, due to the inactivation of donor atoms by the formation of a complex with a neutral charge state in the space-charge region (*e.g.* vacancy-phosphorus complex);
- acceptor removal, similar to donor removal, where an acceptor atom is inactivated (*e.g.* vacancy-boron complex);
- donor introduction, due to the formation of complexes with positive charge state in the space-charge region;
- acceptor introduction, due to the formation of complexes with negative charge state in the space-charge region.

These effects can be parametrized with the following equation:

$$N_{\text{eff}}(\Phi) = N_{D0} e^{-c_D\Phi} - N_{A0} e^{-c_A\Phi} + b_D\Phi - b_A\Phi \tag{2.40}$$

where N_{D0} and N_{A0} are the donor and acceptor concentration before irradiation, c_D and c_A are the donor and acceptor removal constants, b_D and b_A are the introduction constants.

The variation of N_{eff} can also lead to type inversion, observed in n-type semiconductors: after an irradiation up to a fluence of $\Phi_{\text{eq}} = 2 \cdot 10^{12}$ 1 MeV $n_{\text{eq}}/\text{cm}^2$ the effective doping concentration would change sign, becoming negative and meaning that the n-type bulk has effectively become of type p [73].

2.4.1.5 *Annealing*

When a defect is formed, there is the possibility that it is mobile and can interact with other defects, modifying their electrical properties, or restoring the original lattice structure. The rate at which the annealing happens is exponentially dependent on the temperature.

The details of the evolution of the defects at microscopic level are complicated and not fully understood, but their effects on macroscopic observables can still be described. A decrease in the leakage current has been observed due to annealing, which is beneficial for detector operation, while the evolution of the effective doping concentration is not monotonic, but consists of an initial beneficial annealing, a constant term and a reverse annealing part. Its behaviour is usually expressed in terms of ΔN_{eff}, the difference in the effective doping concentration after and before irradiation:

$$\Delta N_{\text{eff}}\left(\Phi, t(T_a)\right) = N_A\left(\Phi, t(T_a)\right) + N_C\left(\Phi\right) + N_Y\left(\Phi, t(T_a)\right) \quad (2.41)$$

where N_A, N_C and N_Y are the beneficial, stable and reverse components respectively, dependent on the fluence Φ and on the annealing time t, which is itself dependent on the annealing temperature T_a.

The three components of the annealing can be parametrized in terms of fluence, time and temperature:

$$N_A = g_A \Phi e^{-\frac{t}{\tau_A}} \quad (2.42)$$

$$N_C = N_{C0}\left(1 - e^{-C\Phi}\right) + g_C \Phi \quad (2.43)$$

$$N_Y = N_{Y\infty}\left(1 - \frac{1}{1 + t/\tau_Y}\right) \quad (2.44)$$

where the g parameters represent the rate of defects introduction, C describes the acceptor removal and the τ parameters contain the temperature dependence of the annealing time through the relation:

$$\frac{1}{\tau_X} \propto e^{-\frac{E_X}{k_B T_a}} \quad (2.45)$$

where E_X is the activation energy and k_B the Boltzmann constant [73].

2.4.2 *Surface damage*

The surface of a silicon chip, at the interface between the silicon and the dielectric (silicon oxide), is sensitive to ionizing radiation. As the

crystal structure of silicon oxide is highly irregular, displacements of single atoms due to irradiation do not lead to macroscopic variations. Ionization in the oxide, however, is not fully reversible and may cause steady changes of the interface properties.

After the creation of electron-hole pairs in the oxide layer, caused by ionizing radiation, most of them recombine immediately, but since electrons have high mobility in the oxide ($\mu_{n,SiO_2} \approx 20\,cm^2/Vs$) they can be collected by any positively biased electrode close by. This is the case, for example, when the device is powered on and operated. The holes instead, have a very low mobility in the oxide ($\mu_{p,SiO_2} \approx 2 \cdot 10^{-5}\,cm^2/Vs$) because of a large number of shallow hole traps and they slowly move in the direction of the electric field in the oxide, hopping from one shallow trap into the next.

If the holes arrive in the transition region between silicon and oxide, where many deep hole traps exist, they may be kept there permanently. These charges, which are now fixed, will change the total oxide charge density N_{ox}. The positive oxide charge has an influence on the electric field in the silicon bulk close to the surface and induces a compensating electron accumulation layer in n-type silicon and a depletion layer in p-type material. It leads, for example, to a variation in the threshold voltage of MOSFETs. Since the number of traps is finite, the oxide charge density does not grow indefinitely with irradiation but saturates at values of the order of $10^{12}\,cm^{-2}$.

3

CMOS SENSORS FOR THE ITK UPGRADE

Monolithic CMOS sensors have been considered as a possible technology for the outermost layer of the pixel detector of the future ATLAS Inner Tracker. Important factors that have made them a feasible option for this experiment are the availability of high voltage CMOS technologies and the possibility to build them on non-standard high-resistivity substrates (standard CMOS processes normally use substrates with a resistivity of $\sim 10\,\Omega \cdot \mathrm{cm}$, but substrates of resistivity of $\sim 1000\,\Omega \cdot \mathrm{cm}$ can be used). They both have an impact on the possibility to deplete the sensors, collecting most of the charge by drift and on its radiation hardness, which can be greatly improved compared to a non-depleted monolithic sensor.

They also have several advantages over the hybrid detectors used until now, and that are the baseline technology for the ITk upgrade: the CMOS foundries have an average processing time of three months, allowing for a quick supply of sensors with a fast reaction time in case of problems. Furthermore, CMOS pixel sensors do not need hybridization, removing the time, cost and possible yield loss of this process, but also reducing the production load on the bump-bonding service companies. Finally, CMOS sensors can be made very thin (50–100 µm) compared to hybrid modules (300 µm for sensor and read-out chip), reducing the material budget and the cluster size, which results in a decrease of the necessary data bandwidth [43].

In this chapter an overview of the different developments towards a CMOS sensor module for ITk will be given, a summary of test results of earlier prototypes will be presented and the prototypes characterized in this work, the H35DEMO and the ATLASPIX1, will be described in more details. Finally, two newer prototypes, the ATLASPIX2 and ATLASPIX3, will be briefly described.

3.1 THE EXPLORED TECHNOLOGIES AND DESIGNS

Depleted CMOS pixel sensors for the ITk upgrade have been investigated for several years. Initially a series of demonstrator detectors have been used to characterize CMOS technologies from different foundries (ams, IBM, LFoundry, STMicroelectronics, Toshiba, TowerJazz...) and to compare different sensors and front-ends, evaluating the charge collection, radiation tolerance and rate capabilities. After a first selection, three vendors were found to be the most suitable for this project: ams [74], LFoundry [75] and TowerJazz [76].

The development continued following two main lines: large fill-factor (ams and LFoundry) and small fill-factor designs (Towerjazz). As explained in Section 2.3.2, the difference between these two approaches is that in the former the electronics is contained into the collection well, which is of size comparable with the pixel pitch, while the latter exploits a small collection electrode, with the in-pixel read-out electronics next to it. The main differences in performance are the higher radiation hardness of the large fill-factor designs, but the lower detector capacitance of the small fill-factor, which results in a lower noise and power consumption.

Early prototypes of both lines where not fully monolithic, but had to be coupled to a FE-I4 chip to be read out and were used to validate the design of the analogue part of the front-end. These have been followed by some iterations of fully monolithic prototypes, from smaller chips at the beginning to full size ASICs, with an area of the order of a few cm^2 and several thousands of pixels.

3.1.1 *Large fill-factor designs*

Large fill-factor pixels sensors have been implemented in high-voltage and high-resitivity CMOS technologies. They use a deep n-well, implanted on a p-type substrate, as a collection diode in which further wells are embedded. The extra wells are used to shield pMOS and nMOS transistors from the collection diode and the depleted bulk. High resistivity wafers have been used in the processing line and a high bias voltage (typically around 100 V) can be applied to the substrate through top or back biasing, to generate a substantial depletion volume in the whole area covered by the pixel.

Different digital read-out architectures are being investigated using large fill-factor designs: a column-drain architecture, similar to the current ATLAS FE-I3 front-end chip [14], and a parallel pixel-to-buffer (PPtB) architecture. They have been implemented in LFoundry 150 nm, ams aH18 (180 nm) and aH35 (350 nm) technologies in order to evaluate their performance.

As mentioned earlier, during the prototyping phase pixel sizes compatible with the $50 \times 250\,\mu m^2$ pixel pitch of the FE-I4 have been used, so this ASIC could be used as auxiliary read-out, while fully monolithic designs implemented smaller pixels (*e.g.* the ATLASPix1 prototype, described in details in Section 3.4, features $40 \times 130\,\mu m^2$ and $50 \times 60\,\mu m^2$ pixels).

In Section 3.2 the earlier pixels sensor prototypes by ams will be described and the testing results summarized, while in Sections 3.3 and 3.4 the sensors characterized in this work will be described in details. More details about the LFoundry prototypes can be found in [77].

3.1.2 *Small fill-factor designs*

Small fill-factor designs offer important advantages in terms of a smaller input capacitance, leading to lower power consumption and noise, but also limiting the coupling of the digital part of the read-out chain to the sensor. The main issue of this design is the limited radiation hardness, due to the longer travel path of the charge carriers compared to large fill-factor designs, which increases the trapping probability, and the slow collection time due to the undepleted regions in the bulk, which limit the rate capabilities.

The development for ITk was based on the sensors utilized in the ALICE Inner Tracking System (ITS) [78]: they used the TowerJazz 180 nm technology featuring a 25 µm thick epitaxial layer, as shown in Figure 3.1a. This design limits the lateral depletion to the region around the collection node, leaving a sizeable part of the sensor undepleted.

This issue has been addressed with a process modification [79] consisting in the insertion of a lightly doped n layer over the p epitaxial layer which extends the depleted region to the whole sensor, as shown in Figure 3.1b. This modification does not require layout changes with respect to the standard process, but it has a significant influence on the charge collection.

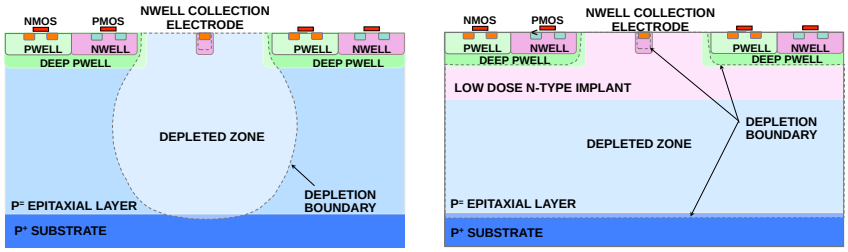

(a) (b)

Figure 3.1: (a) A cross section of a standard small fill-factor sensor. The depleted zone is limited to the region around the collection node. (b) A cross section of a small fill-factor sensor implementing the process modification described in the text. The depleted zone now extends to the whole sensor [43].

Two read-out architectures have been investigated: an asynchronous read-out scheme, in the MALTA (Monolithic ALice to ATLAS) chip and a synchronous one in the TJ-Monopix chip. These two ASICs share the same analogue front-end, which includes a charge sensitive amplifier followed by a discriminator and hit buffer.

The asynchronous read-out in MALTA removes the clock activity in the matrix, limiting the transient couplings in the sensor. In addition its power consumption is low compared to clocked read-out. Address, time stamp and charge information of every hit is encoded in the asynchronous signals propagated through a column bus to the

periphery where decoding is performed, the data is buffered and then transmitted off the matrix. The synchronous design in TJ-MonoPix, instead, is based on the column drain architecture similar to the ATLAS FE-I3 chip [14].

3.2 RESULTS FROM EARLIER AMS PROTOTYPES

Several small-scale prototypes has been produced using a high-voltage CMOS ams technology, in the framework of the development of depleted monolithic sensors for the ATLAS ITk upgrade. They features active pixels with one or more amplification stages and a simple digital part, which requires them to be coupled to a readout ASIC. The characterization of these prototypes has been fundamental to understand the capabilities of the sensor and analogue readout parts, using a well-known read-out ASIC to study them.

3.2.1 *HV2FEI4*

The HV2FEI4 prototype, shown in Figure 3.2a, has been developed in the ams AG aH18 180 nm technology on a $20\,\Omega \cdot$ cm p-type substrate. It features a 60 columns by 24 rows pixels matrix, with $33 \times 125\,\mu m^2$ pixels. In order to be coupled to the FE-I4 ASIC the pixels are arranged in 3×2 groups: three pixels in each group are connected to the same read-out cell and, to distinguish them, each one features a fixed-amplitude output (see Figure 3.2b), so the position of a hit can be reconstructed combining the position of the FE-I4 readout cell and the amplitude value. While this system allows exploiting the FE-I4 to readout smaller pixels, any information about the charge deposited in the sensor is lost [80].

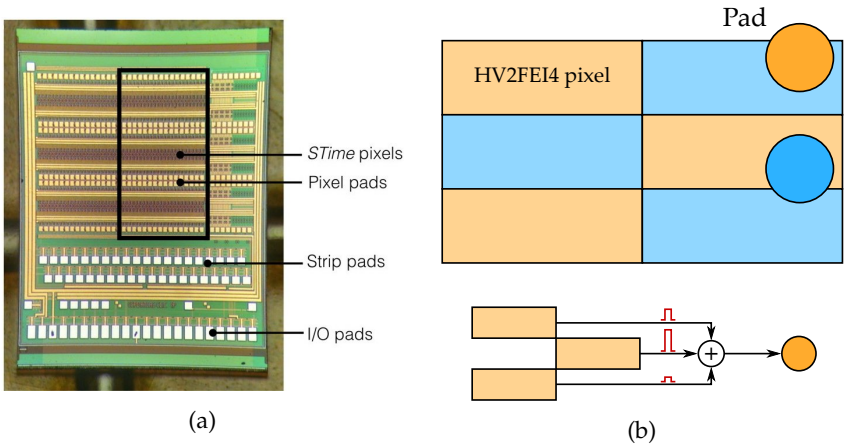

Figure 3.2: (a) The HV2FEI4 chip [81]. (b) Schematic of the pixel encoding: three pixels in each group of six are connected to the same pad and they can be distinguished because each one has a different pulse amplitude.

Each pixel contains a charge sensitive amplifier, a shaping stage and a comparator with tunable threshold. There are three different flavours of pixels, with differences in the complexity of the electronics [82]. The measurements focused on the so-called "standard pixels", that compose the biggest part of the pixel matrix and are designed to achieve a low noise and a reasonably high radiation tolerance.

This prototype has been characterized in laboratory and at testbeams before and after irradiation with x-rays, protons and neutrons. The position-amplitude encoding has been validated using a radioactive source on non-irradiated samples, as shown in Figure 3.3a, while the output of the amplifier has been tested using current injection after several steps of proton irradiation (Figure 3.3b). It shows no significant degradation in performance below 50 Mrad, with a decrease of the response of the preamplifier after 100 Mrad, which is completely restored after four days, due to annealing [83].

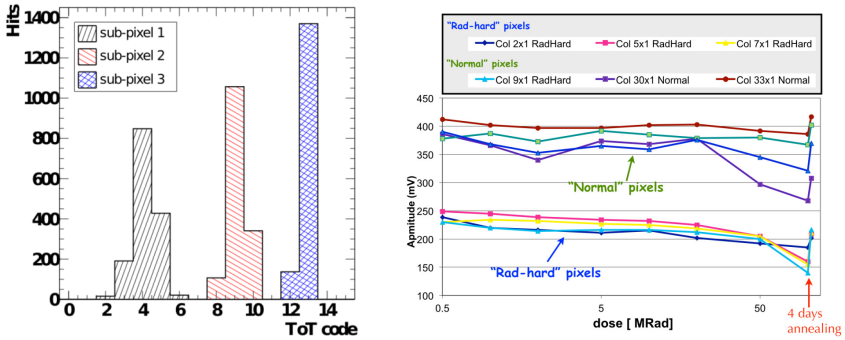

(a) (b)

Figure 3.3: (a) Time-over-threshold distribution for a single pixel, showing the position-amplitude encoding. (b) The pulse amplitude of the amplifier after several steps of x-ray irradiation [83].

Testbeam studies have been performed at the CERN PS, SPS and at DESY using the EUDET JRA1 [84] and the new FE-I4 telescope [85]. Sensors before and after neutron irradiation, up to a fluence of 10^{15} 1 MeV n_{eq}/cm^2 have been studied to determine their efficiency and timing performance. The details of how these measurements are performed is explained in Section 5.6 and here the most important results are summarized. Since the sub-pixel encoding was not implemented in the reconstruction software, the results are presented for $100 \times 250\,\mu m^2$ *macro-pixels* [86].

The HV2FEI4 shows a homogeneous detection efficiency (defined as the ratio between the number of detected tracks and the total number of tracks) of 97% before and after irradiation, as shown in Figure 3.4a and 3.4b (the low efficiency pixels at the bottom are of another pixel type, not considered for this study). The timing distribution (*i.e.* the timestamp difference of the recorded hit with respect to the trigger in units of LHC bunch crossings) of this prototype is insufficient for the requirements of ITk: as shown in Figure 3.4c and 3.4d, the

timing distribution is spread over several 25 ns bins, while a typical distribution for a planar sensor would have entries in two bins at most. Part of this is caused by the presence of a slow diffusion component in the charge collection, which is eliminated after irradiation, leading to an improvement in timing performance. However, part of this issue is also due to the electronics, which has seen important enhancements in subsequent prototypes [86].

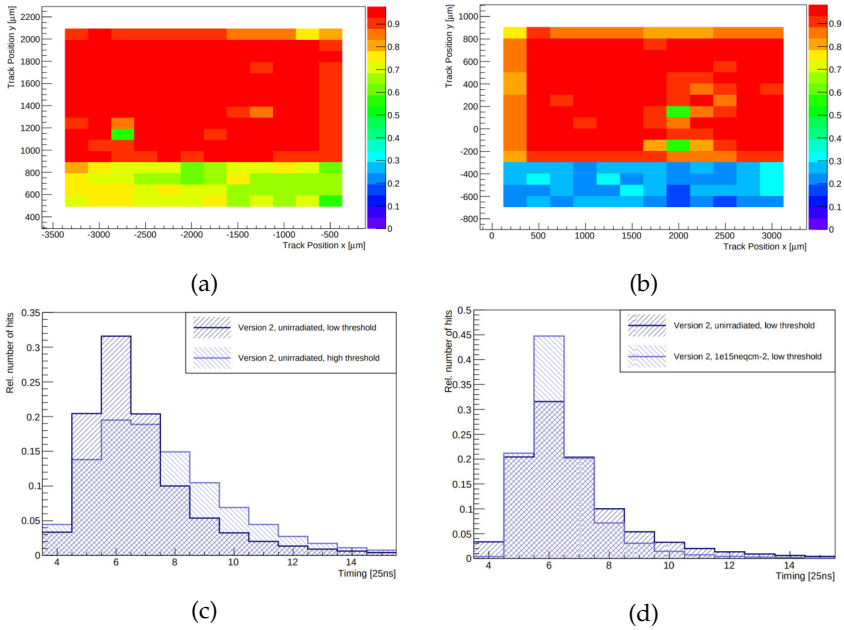

Figure 3.4: Results from the testbeam of the HV2FEI4. HV2FEI4 tracking efficiency (a) before and (b) after irradiation. (c) Timing distributions before irradiation at two different threshold settings and (d) comparison of hit timing before and after irradiation [86].

3.2.2 *CCPDv4*

The CCPDv4 prototype, shown in Figure 3.5a has been developed in the ams AG aH18 180 nm technology on a $20\,\Omega \cdot \text{cm}$ p substrate. It has a total area of $2.4 \times 2.9\,\text{mm}^2$ and contains a pixel matrix with four different flavours of pixels. The pixels are $33 \times 125\,\mu\text{m}^2$ wide and they are grouped in 3×2 cells, in order to be read out by the $50 \times 250\,\mu\text{m}^2$ cells of the FE-I4 ASIC, as shown in Figure 3.5b. The three pixels connected to the same FE-I4 cell were read-out as a single $100 \times 125\,\mu\text{m}^2$ *macro-pixel*.

The characterization of this prototype focused on one pixel flavour, called *STime*: each pixel implements a two-stage amplifier followed by a comparator with tunable output amplitude. The comparator threshold is set globally, but can be tuned on each pixel using a 4-bit DAC to correct for threshold dispersion.

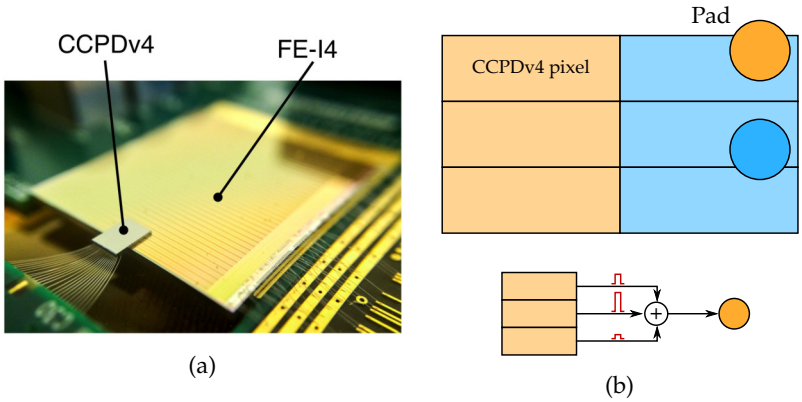

Figure 3.5: (a) The CCPDv4 chip coupled to a FE-I4 ASIC and mounted on a PCB [81]. (b) Schematic of the pixel encoding: three pixels in each group of six are connected to the same pad and they can be distinguished because each one has a different pulse amplitude.

This prototype has been characterized extensively with testbeams at the CERN SPS, using the FE-I4 telescope [85], to estimate its efficiency and timing performance before and after irradiation. Before irradiation, the CCPDv4 shows an excellent detection efficiency above 99%, for a wide range of discriminator threshold and reverse bias voltages. An efficiency map is shown in Figure 3.6a, while the efficiency evolution as a function of reverse bias voltage and threshold are reported in Figures 3.6c and 3.6e respectively [87].

The timing distribution for the non-irradiated CCPDv4 is shown in Figure 3.6b. It is possible to notice an initial peak, followed by a long tail, which is mainly due to a timewalk effect in this HV-CMOS sensor design, so that low amplitude signals, such as the ones resulting from diffusion, have a larger timing because of the slower discriminator rise time. This effect is highlighted in Figures 3.6d and 3.6f, where the timing distributions for events with cluster size one and two are reported: the timing distribution of clusters of size one is very similar to that of the fastest hit of the two-pixel clusters [87].

The CCPDv4 has been characterized after protons and neutrons irradiation as well, performed at the Inselspital cyclotron in Bern (described in Section 4.6.1) and at the TRIGA reactor at the JSI in Ljubljana (described in Section 4.6.3) respectively. The hit detection efficiency as a function of the reverse bias voltage and discriminator threshold is reported in Figure 3.7. It is possible to notice that efficiency close to 100% is reached at a relatively low bias voltage for the intermediate irradiation steps, where the depletion depth is increased due to acceptor removal effects in the substrate.

The lower efficiency at low fluence can be explained with the delayed appearance of acceptor removal effects in low resistivity substrates (see Section 4.7), so there is no increase in depletion depth to compensate for the charge loss by trapping. At very high fluence the depletion

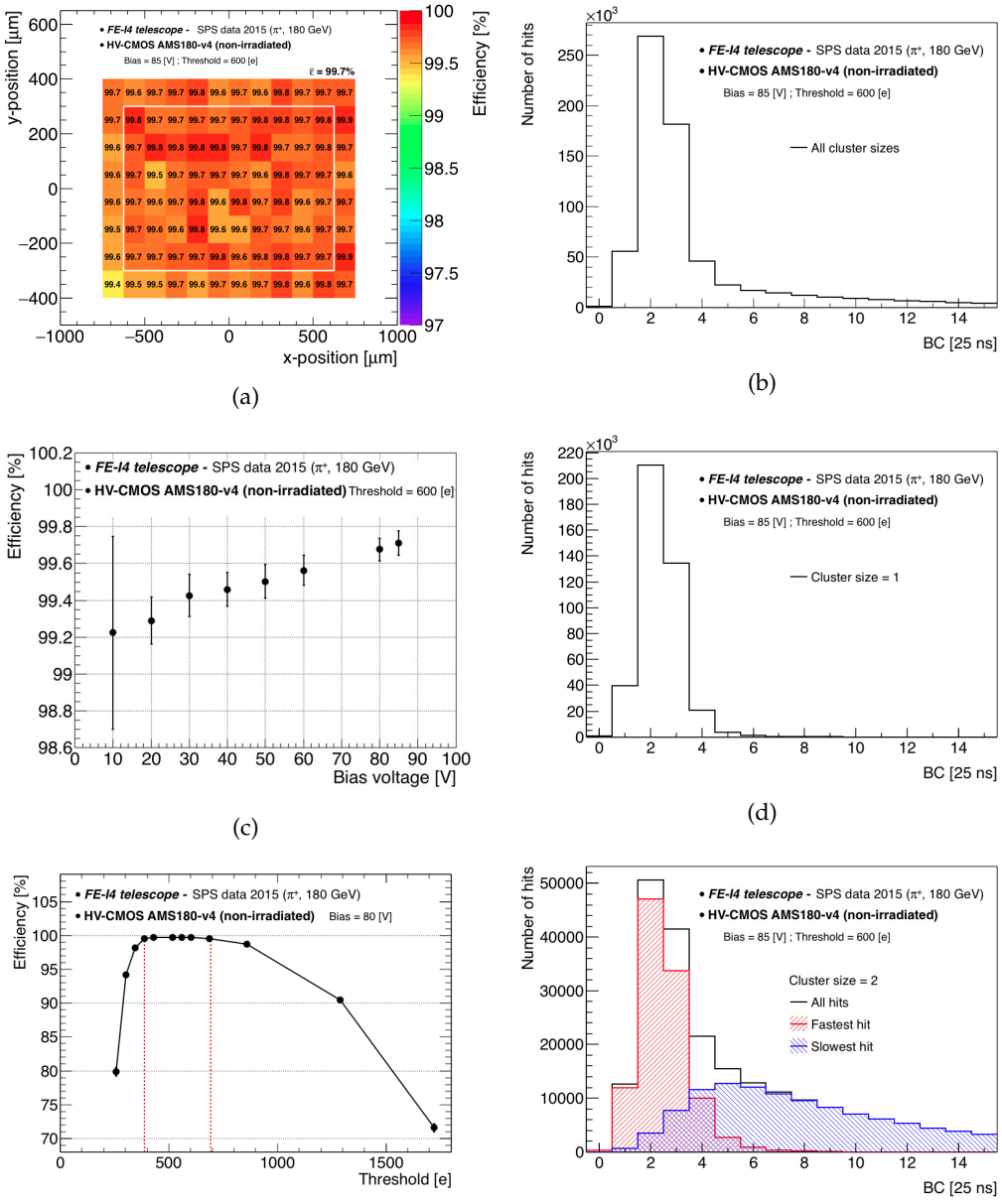

Figure 3.6: Main results from the characterization of CCPDv4. (a) Efficiency map (the average is calculated considering the pixels inside the white rectangle to remove edge effects). (c) Efficiency as a function of the bias voltage. (e) Efficiency as a function of threshold. The two vertical dashed-lines indicate the operating region where the efficiency is larger than 99.5% [87]. (b) Timing distribution for all cluster sizes, (d) cluster size one and (f) cluster size two, with the distribution of the measured time of each of the two pixels in the cluster [87].

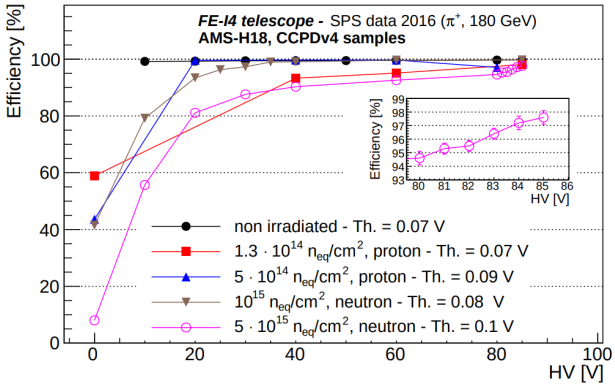

Figure 3.7: Average hit efficiency as a function of applied bias voltage. The inset shows the sudden increase in efficiency between 80 and 85 V, which could be attributed to charge multiplication [88].

depth decreases, while the trapping continues to increase, reducing the efficiency, as expected. It is possible to notice that the efficiency at the highest irradiation fluence features a sudden rise at bias voltages higher that 80 V. This can be explained by the appearance of charge multiplication effects due to the high electric field [88].

The irradiation has also a noticeable effect on the timing, removing the tail in the distribution of Figure 3.6b, since trapping eliminates the possibility to collect charge by diffusion. As a consequence of the absence of diffusion, the cluster size distribution changes as well: while before irradiation almost 22% of the clusters were of size two or more, this number is reduced to 2–4% after irradiation [88].

Despite the excellent efficiency, the timing performance of this prototype is not sufficient to be operated in a HL-LHC experiment as an efficiency higher than 90% is measured within a three 25 ns bunch crossing window, but this characteristic is improved in more recent prototypes, as will be shown in Sections 5.7 and 5.8.

3.3 THE H35DEMO PROTOTYPE

The H35DEMO prototype [89, 90], shown in Figure 3.8, has been developed with the 350 nm HV-CMOS process from ams AG on substrates of different resistivities: 20, 80, 200 and 1000 $\Omega \cdot$ cm. It has a total area of $18.5 \times 24.4\,\mathrm{mm}^2$, containing four pixel matrices, two analogue ones (Analogue 1 and Analogue 2), which need an external ASIC to be read out, and two stand-alone digital ones (Stand-alone nMOS and Stand-alone CMOS), which implement the full readout chain. The four matrices contain a total of 78 columns by 300 rows of pixels. Several test structures are present in the periphery. All the pixels have an area of $50 \times 250\,\mu\mathrm{m}^2$ and have been designed to allow the H35DEMO to be coupled to a FE-I4 in a one-to-one connection.

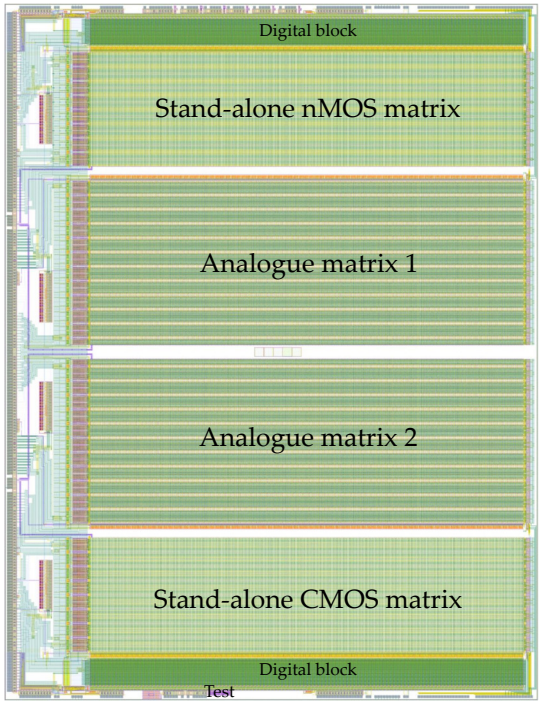

Figure 3.8: The H35DEMO prototype [90].

Each pixel consists of a sensor diode and a readout circuit. A simplified cross-section of a pixel used in the analogue matrix 2 is shown in Figure 3.9. The sensor is implemented by means of a deep n-tub[1]/p-substrate junction, on top of which sits the readout circuit. The deep n-tub (dntub) is biased at the power supply voltage (3.3 V) through a bias circuit that works as a high ohmic resistor, while the substrate is biased at a high negative voltage (up to −165 V) to create a large depleted area.

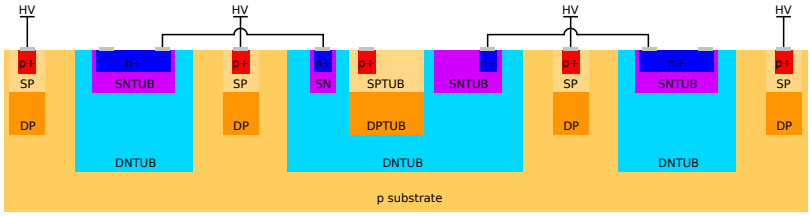

Figure 3.9: Cross section of a H35DEMO pixel. The electronics is contained in the central deep n-tub [90].

In the analogue and stand-alone CMOS pixels, the deep n-tub is split into three different areas to limit the parasitic capacitance of the sensor and the readout circuit is placed in the central one only. In contrast, in the stand-alone nMOS pixels, one large deep n-tub, that occupies the entire available area in the pixel, is used to contain the larger number of transistors due to the more complex electronics.

1 Tub is another term to designate the wells.

The readout circuit includes a bias block, a charge sensitive amplifier (CSA), which is capacitively coupled to the deep n-tub, and a passive RC-CR filter. All the pixels also include a small injection circuit for testing purposes. In all the matrices, each pixel has one output that is attached to a pad for connection to the FE-I4.

3.3.1 *Stand-alone nMOS matrix*

The stand-alone nMOS matrix comprises 16 columns by 300 rows of pixels, along with a digital block, a bias block and digital configuration register. The readout circuit includes, in addition to the CSA and shaper, an in-pixel comparator that uses nMOS transistors only. This choice has been made because in this technology it is not possible to isolate pMOS transistors from the deep n-tub, which is the collecting electrode and at the same time the bulk of pMOS transistors. Since comparators are extremely sensitive circuits, the very small voltage drop that occurs in the deep n-tub upon particle hit might lead to fake comparator outputs.

Two different comparator flavours are included in this matrix. The first 150 rows contain a simple nMOS comparator based on two fully differential amplifiers and an output stage, while the second 150 rows use a more complex comparator that also includes a compensating system to minimize the time-walk.

Each pixel has two outputs: one of them is attached to a pad for connection to the FE-I4, while the other one is connected to its corresponding digital cell placed in the periphery of the matrix. The digital block presents the same functionality as the FE-I3 ASIC [91]: the first stage of each digital cell is a CMOS comparator that converts the low-voltage digital signal generated by the nMOS comparator to a CMOS digital signal. The digital cell also contains electronics to generate and store the pixel address and time-stamp until they are read out.

3.3.2 *Analogue matrix 1*

The first analogue matrix consists of 23 columns by 300 rows of pixels, a bias block and an analogue configuration register. Unlike in the other matrices, the CSA of this matrix uses a folded-cascode with an nMOS transistor as input device. The advantages of using this CSA architecture are lower noise and better radiation tolerance, but at the expenses of a higher power consumption.

Three different pixel flavours are included in this matrix, summarized in Table 3.1. The first 100 rows contain an additional deep p-tub (DPTUB) between the deep n-tubs of each pixel to bias the substrate, whereas in the remaining columns the bias of the sensor is applied from the edges of each pixel only. The first 200 rows use enclosed

layout transistors (ELTs) in the feedback block, like in all the other matrices, while the last 100 use linear transistors. Each pixel has only one output, which is attached to a pad for connection to the FE-I4.

3.3.3 *Analogue matrix 2*

The second analogue matrix is very similar to the first one, with the same layout, bias block and configuration registers. However, the CSA included in all the read-out circuits uses a regulated folded-cascode with a pMOS transistor as input device.

Three different pixel flavours are included in this matrix, summarized in Table 3.1. The first 100 rows contain an additional deep p-tub similarly to the first analogue matrix 1. The last 100 rows of the matrix include an extra capacitor connected between the output of the CR filter and the deep n-tub to achieve higher speed, but at the expenses of lower gain.

The performance of these two analogue matrices, capacitively coupled to the FE-I4 ASIC, have been studied with testbeams and the results will be reported in Section 5.7 on page 137.

Table 3.1: Summary of characteristics of the H35DEMO analogue sub-matrices.

	Rows	Analogue 1	Analogue 2
Sub-matrix 1	0–99	Extra DPTUB ELTs	Extra DPTUB High gain
Sub-matrix 2	100–199	No DPTUB ELTs	No DPTUB High Gain
Sub-matrix 3	200–299	No DPTUB Linear transistors	No DPTUB Low gain

3.3.4 *Stand-alone CMOS matrix*

The stand-alone CMOS matrix comprises 16 columns by 300 rows of pixels, a digital block, a bias block and a digital configuration register. In the stand-alone CMOS matrix, all the power and bias lines are in the highest metal of the technology, so that a lower level can be exclusively used to achieve an excellent shielding.

Here, there is no in-pixel comparator, but the output from the shaper is connected both to a pad (for connection to the FE-I4) and to the corresponding digital cell in the periphery. The digital block and the testing features are the same ones as in the stand-alone nMOS matrix, with the only exception that half of the digital block uses as an

input stage a CMOS comparator that can have two threshold voltages, allowing the measurement of the amplitude of the signal on the chip.

3.3.5 *Test structures*

The H35DEMO features several test structures close to the edges. The one of interest for this work, shown in Figure 3.10, consist of a 3×3 pixel matrix with the well structure shown in Figure 3.9, but with no electronics on it.

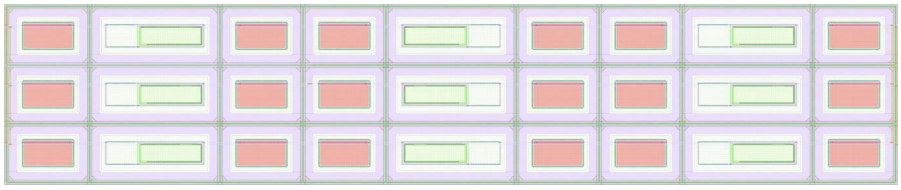

Figure 3.10: The H35DEMO test structures. They consists of 3×3 pixels, with openings in the metal layer (drawn in purple) and no electronics in the central well of each pixel. The red parts are polysilicon, while the green are exposed silicon.

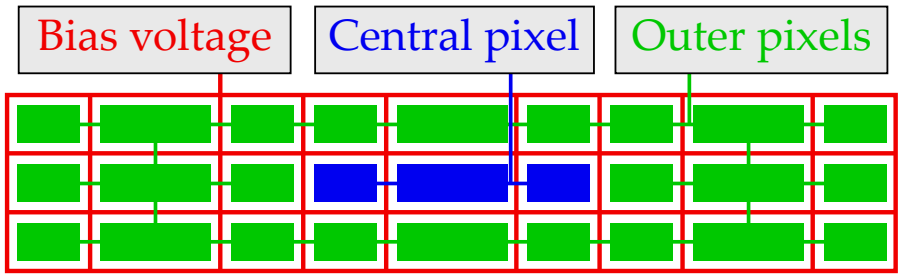

Figure 3.11: Simplified schematic of the connections of the test structures to the pads.

The deep n-tubs of the pixels are not connected to a bias block but to a pad, to be able to read out the current signal generated by the sensor. Two channels are available: the central pixel is read out individually while the eight outer pixels are connected, in parallel, to the same pad, as shown in Figure 3.11.

A p-well is present on the central deep n-tub of each pixel (light-green in Figure 3.10), and they are all connected together to a single pad. Furthermore, the top of these structures is not metallized (with the exception of the lines necessary to connect the various structures).

This structure has been used to perform Transient Current Technique measurements, as explained in Chapter 4.

3.4 THE ATLASPIX1 PROTOTYPE

The ATLASPIX1 prototype [92, 93], shown in Figure 3.12, has been developed with the 180 nm aH18 HV-CMOS process from ams AG

on substrates of different resistivities: 20, 80, 200 and 1000 $\Omega \cdot$ cm. It has a total area of $10 \times 25\,\text{mm}^2$, containing three pixel matrices: one (ATLASPIX_M2), with $50 \times 60\,\mu\text{m}^2$ pixels and a parallel pixel to buffer read-out and two (ATLASPIX_Simple and ATLASPIX_IsoSimple), with $40 \times 130\,\mu\text{m}^2$ pixels and a column-drain readout. It is a fully monolithic chip, so it does not require an external read-out ASIC.

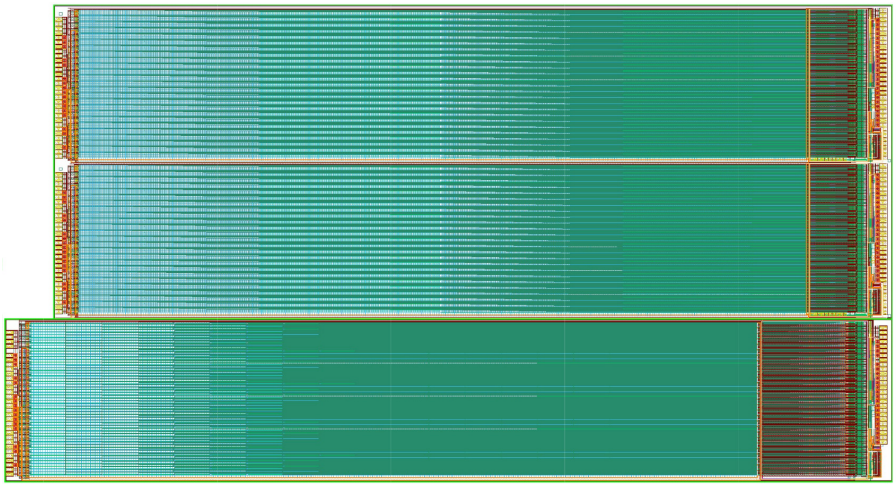

Figure 3.12: The three ATLASPIX1 matrices (from the top: IsoSimple, Simple and M2) [93].

As in the H35DEMO, each sensor is implemented as a deep n-well/p substrate junction, with the read-out electronics contained in the n-well and insulated from the substrate. Each pixel of the three matrices contain a charge sensitive amplifier connected to a comparator with a tunable threshold (the schematic is shown in Figure 3.13). The comparator threshold is set globally and can be tuned with a 4-bit tune DAC (TDAC). Its value is set from the column configuration part and is written with the row configuration.

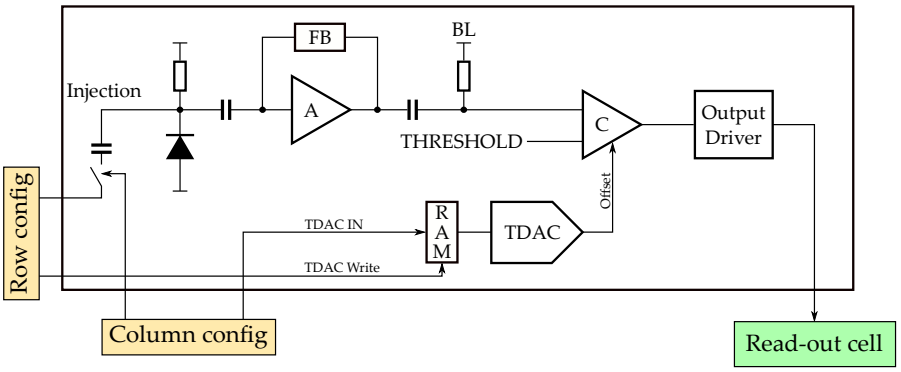

Figure 3.13: The schematic of the in-pixel circuitry. Each pixel contain a CSA (A) with a feedback circuitry (FB) connected to a comparator (C) with a tunable threshold and baseline (BL). Each pixel also contains an injection circuit.

Each pixel features a charge injection circuit as well: it is enabled on a column basis and the charge is injected on a row basis. Furthermore, each pixel can be individually masked.

3.4.1 *The Simple and IsoSimple matrices*

The Simple and IsoSimple matrices consist of 400 rows by 25 columns of pixels, containing the charge sensitive amplifier and comparator, and the read-out logic. The only difference between the two matrices is the in-pixel comparator: the simple matrix features a nMOS comparator, while the IsoSimple a CMOS one, similarly to the two stand-alone matrices of the H35DEMO. The reason for this difference is that a deep p-well is added in the IsoSimple matrix to insulate the pMOS transistors from the deep n-well (Figure 3.14), limiting the possibilities that transients in the collection electrode lead to fake comparator outputs. The Simple matrix does not contain a deep p-well, so the nMOS transistors are the only one that can be insulated.

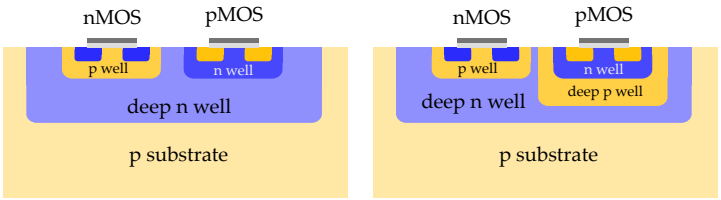

Figure 3.14: Non insulated (left) and insulated (right) pMOS transistor.

The structure of these matrices is reported in Figure 3.15. The read-out is performed on a column basis: each pixel (p0 to p399 in the figure) is connected to a read-out cell (ROCell) that, when a hit arrives, generates the timestamp, address and time-over-threshold. This data is then read by the end-of-column (EoC) circuitry, each connected to 200 ROCells. Two EoCs are used to read out a column of pixels. The data in the EoC, in turn, is read-out by the Digital Part (DP), that serializes and transmits it off chip. The clock is provided externally and it is multiplied by a selectable factor by the phase-locked loop (PLL).

The configuration part allows setting global parameters, as the timestamp clock, the DAC values for the amplifiers and comparators, etc. and the per-pixel settings like masking, comparator threshold tuning, etc. The simple matrix has been extensively characterized using testbeams, as explained in Section 5.5.

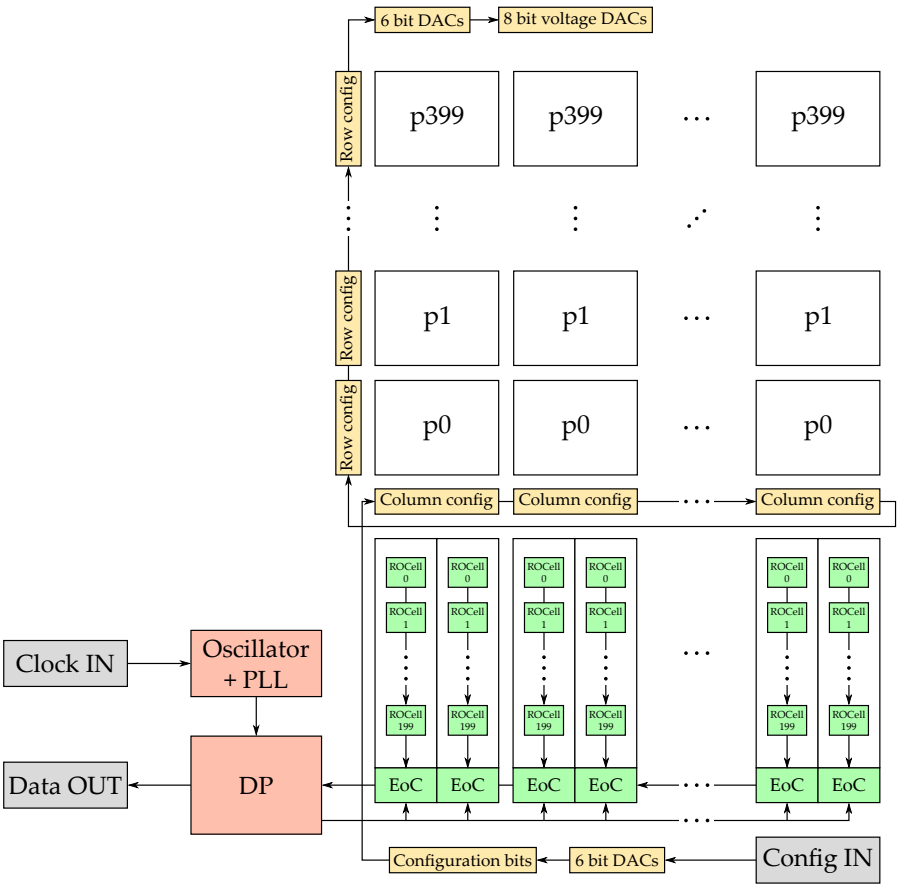

Figure 3.15: The read-out scheme of the Simple and IsoSimple matrices, based on [93].

3.4.2 *The M2 matrix*

The M2 matrix consists of 320 rows by 56 columns of pixels, organized in 28 double-columns containing 40 pixel blocks (composed of 16 pixels each) for a total of 17 920 pixels. Each pixel, as the Simple matrix, contains a charge sensitive amplifier and a nMOS comparator and is connected to the digital read-out circuitry in the periphery.

The structure of the matrix is reported in Figure 3.16. Each pixel block (p0 to p39 in the figure) is connected to a buffer block in the periphery: when a hit is recorded, the buffer block generates the addresses, time stamps and time-over-threshold of the fired pixels and holds them in memory. If a trigger signal arrives after a programmable delay, the hits with the right timestamp are marked as triggered and sent to the end-of-column, where they are transferred to the digital part, which serializes the data and transmits it out of the chip.

The oscillator, PLL and the digital part are identical to the ones used in the Simple matrix. The configuration part is similar to the Simple matrix, but in addition it allows setting the trigger delay.

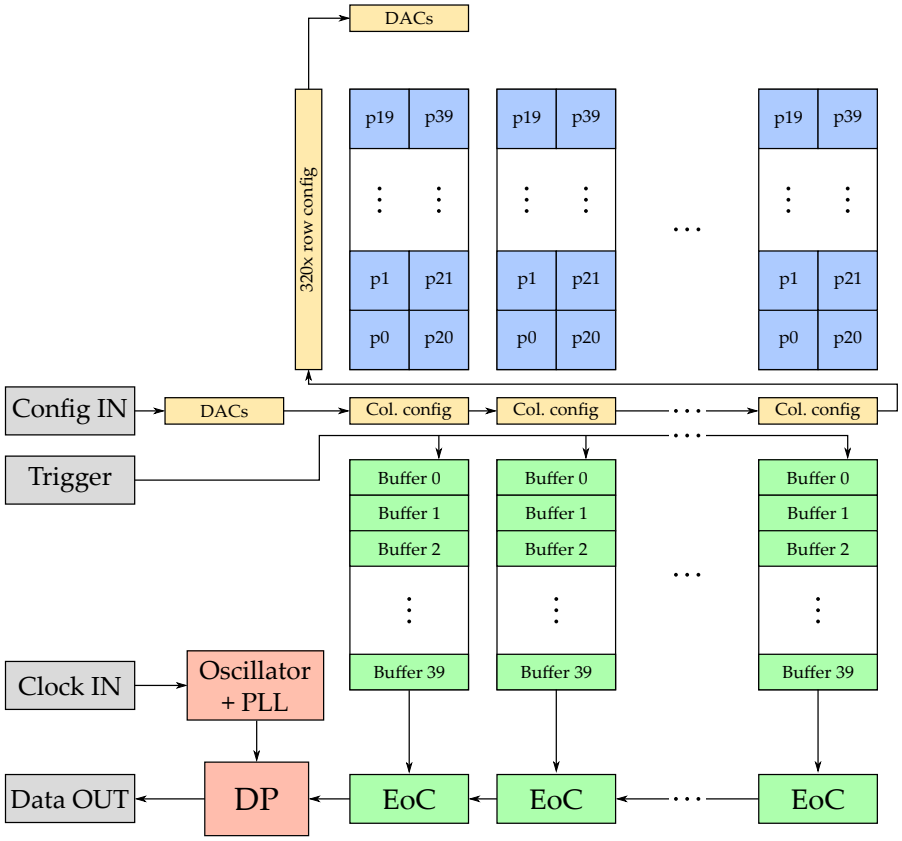

Figure 3.16: The read-out scheme of the M2 matrix, based on [93].

3.5 ATLASPIX2 AND ATLASPIX3

Following ATLASPIX1, two more prototypes, ATLASPIX2 and ATLASPIX3, have been developed. ATLASPIX2 (Figure 3.17a) is a small scale prototype, containing a 24×36 pixel matrix, produced by ams AG and TSI Semiconductors and aimed to qualify various circuit blocks in the periphery. It also contains a memory array, with similar cells to the one implemented in the pixels, designed for Single Events Effects (SEE) tests [94].

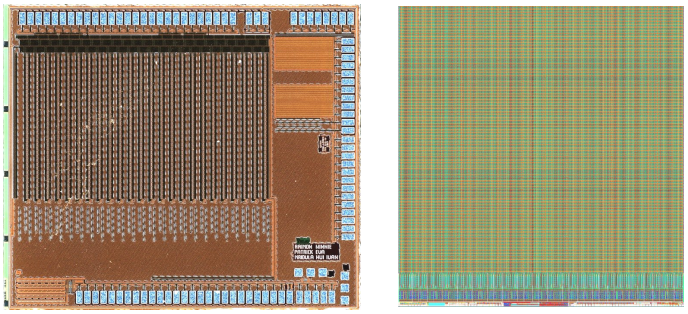

(a) (b)

Figure 3.17: The (a) ATLASPIX2 [94] and (b) ATLASPIX3 prototypes (not to scale) [95].

A detailed electrical characterization has been performed on ATLASPIX2, to determine the differences between the two foundries. The samples produced by TSI feature a higher breakdown voltage ($\sim$100 V) and a lower leakage current than the ams ones ($\sim$50 V). The IV plots at different temperatures can be seen in Figure 3.18. After neutron irradiation, to a fluence between $1 \cdot 10^{15}$ and $2 \cdot 10^{15}$ 1 MeV n_{eq}/cm^2, the leakage current increases, as expected, and there is a variation in the breakdown voltage: it increases slightly for the ams samples and it decreases for the TSI ones, reaching 60 V and 90 V respectively. Studies after several annealing steps have been performed as well, showing an increase of the breakdown voltage and a decrease of the leakage current, as shown in Figure 3.19 [96].

The ATLASPIX3, shown in Figure 3.17b, is a full scale prototype, developed with the 180 nm HV-CMOS process from TSI Semiconductors and designed to be fully compatible with the RD53 read-out interface [95]. It has been produced on $200\,\Omega \cdot cm$ substrates. It has a total area of $20.2 \times 21\,mm^2$ and contains a single matrix, with 132 columns and 372 rows of $50 \times 150\,\mu m^2$ pixels, featuring a triggered column-drain read-out (which can be run triggerless as well). At the time of writing the characterization of this ASIC is at its initial stages and no results are available yet.

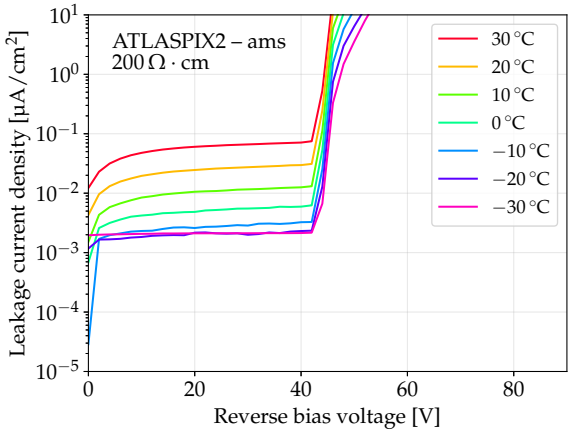

(a)

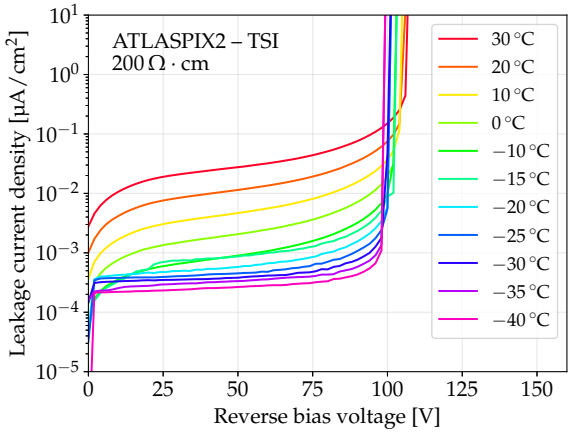

(b)

Figure 3.18: The IV plots for ATLASPIX2 by (a) ams and (b) TSI before irradiation [96].

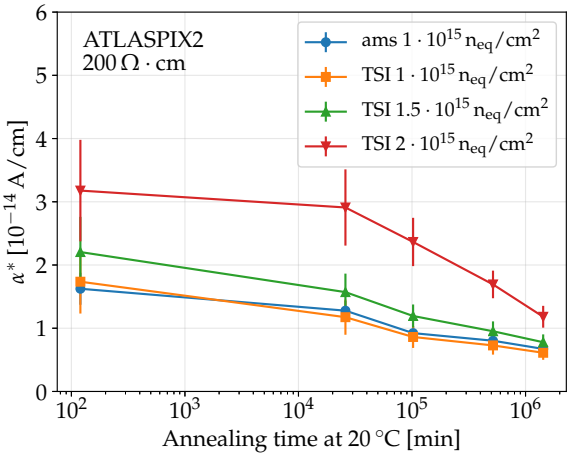

Figure 3.19: The evolution of the damage constant α^* with time. Lower values of α^* indicate a lower leakage current [96].

4

TRANSIENT CURRENT TECHNIQUE

The Transient Current Technique has been developed during the 1990s as an alternative to CV (capacitance-voltage) measurements to estimate the depletion-region depth, and thus the effective doping concentration, of silicon detectors. This technique is particularly useful to characterize heavily irradiated sensors, where the increased leakage current limits the applicability of CV measurements [97]. In addition, it allows studying the charge collection as a function of the position inside the detector bulk and characterizing the shape of the current pulse generated by the free charge carriers.

In this chapter the Transient Current Technique is introduced. The measurements performed on the H35DEMO prototype will be described, starting from the motivation in the framework of the development of HV-CMOS pixels detectors for the ATLAS ITk upgrade. The setup used, its commissioning, the measurement campaigns, the data analysis techniques are described in details and finally the results are discussed.

4.1 INTRODUCTION

The Transient Current Technique (TCT) is based on the analysis of the current pulse caused by the movement of the free charge carriers in the sensor under study. These carriers are usually generated with a laser pulse, focused in the position of interest inside the detector.

An important parameter in the choice of the laser wavelength λ is its penetration depth $\delta_p(\lambda)$, defined by the Beer-Lambert law:

$$I(z) = I_0 e^{-z/\delta_p} \tag{4.1}$$

where I is the light intensity at a given position z and I_0 is the light intensity at $z = 0$, so δ_p is the distance after which the initial intensity is reduced by a factor $1/e$. Figure 4.1 shows a plot of the penetration depth as a function of the wavelength in silicon: it spans 14 orders of magnitude with λ is in the range 250–1450 nm (so from the middle ultraviolet to the middle infrared) [98].

Depending on the results that need to be achieved, different laser wavelengths can be used, based on the desired penetration depth, and the beam can be shone into the detector from various locations (top, edge and backside). Edge-TCT can be used to measure the depletion-region depth or charge collection time as a function of the position. In this case an infrared laser is normally used, since the sensitive region is usually at least a few tenths of µm away from the edge of the sensor.

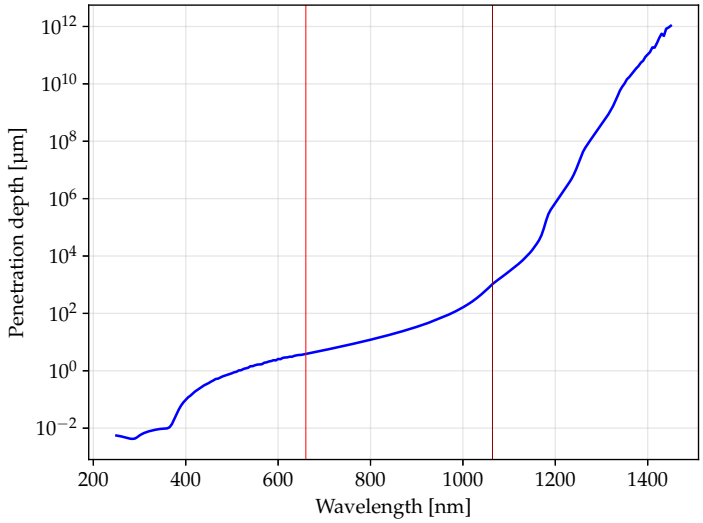

Figure 4.1: Penetration depth in silicon as a function of the light wavelength. The two vertical lines highlight two typical laser wavelengths used for TCT (660 and 1064 nm) [98].

Top and back TCT can be used to study the signal shape (for example to estimate trapping time) and both red and infrared lasers can be useful in this case. To simulate the charge released by a particle crossing the detector, an infrared laser should be used (a 1064 nm laser features a penetration depth of ~ 1 mm, so it can easily pass through the whole thickness of the sensor). A red laser can be used to generate charge close to the surface only (the penetration length of a 660 nm laser is just a few microns), allowing the study of the contribution to the signal of electrons and holes separately, in a fully depleted sensor [97].

4.2 GOALS AND MOTIVATION

TCT measurements have been carried out on the test structures of H35DEMO samples (see Section 3.3.5) of the four available resistivities (20, 80, 200 and 1000 $\Omega \cdot$ cm) to measure the evolution of the depletion depth after irradiation with protons of different energies and reactor neutrons. From these, it is possible to extract the value of the effective acceptor density N_{eff} and evaluate its evolution as a function of the received fluence. Furthermore, the timing characteristics of the current pulses, the rise time and pulse duration, have been investigated.

These studies are fundamental to predict the evolution of the depletion-region depth and charge collection performance of the HV-CMOS pixels sensors in a harsh radiation environment as the HL-LHC. Moreover, they allow decoupling the contribution of the charge collection from the contribution of the electronics to the global performance of the detector (the test structures used for TCT measurements do not

contain in-pixel electronics, the n-well is directly connected to a pad). The TCT measurements have been performed on samples irradiated with three different sources, reactor neutrons, high energy protons (24 GeV) and low energy protons (16.7 MeV), to have a more complete understanding of the effects of different particles.

4.3 DESCRIPTION OF THE SETUP

The setup used for TCT measurements, shown in Figure 4.2 and located in the clean room of the DPNC[1] at the University of Geneva, is produced by Particulars [99]. It consists of three moving stages: two are used to position the Device Under Test (DUT) and move along x and y (the reference system is shown in Figure 4.2) the third one moves the laser focusing optics in parallel with the laser beam along z. The device can be cooled with a Peltier cell and an external chiller.

The DUT can be biased with up to two independent Source Meter Units (SMU) and the current signals are amplified with two broadband amplifiers and digitized with an oscilloscope: this allows reading out two signal channels at the same time. The whole system (with the exception of the chiller) can be controlled by a PC. More details about the different components of the setup are given in the following paragraphs.

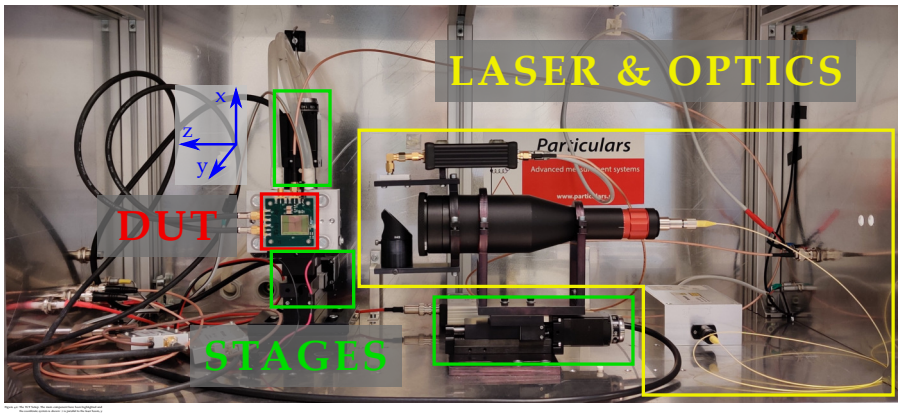

4.3.1 *The laser and the optics*

Two lasers are available in this TCT setup: an infrared one (wavelength of 1064 nm, 50 mW power, model LA-01 IR FC) and a red one (wavelength of 660 nm, 10 mW power, model LA-01 R FC), both produced by Particulars [100]. They are based on a laser diode coupled to an optical fibre and are controlled by a dedicated software: it allows modifying the repetition rate from a few Hz to hundreds of kHz and the pulse duration from 350 to 4000 ps, which, in turn, also affects the pulse energy (shorter pulses carry less energy, but an absolute calibration is not available).

The optical fibre is connected to the optics, which consists of lenses and an iris after them: the lenses focus the laser beam, while the iris allows having a smaller beam width at the focus (FWHM of 15 µm). The complete laser setup is shown in Figure 4.3.

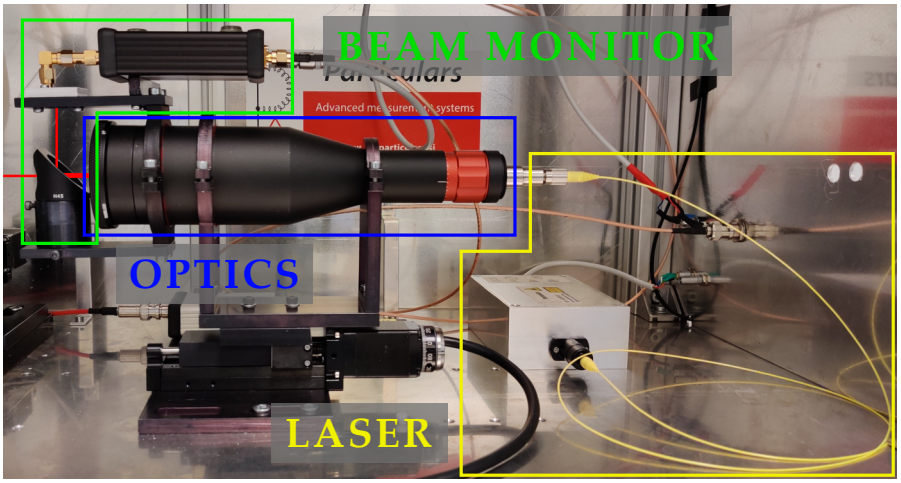

Figure 4.3: The components of the laser system. The laser is fed into the optics with the optical fibre. After the optics the beam is split by a semitransparent mirror: part of it is reflected into the beam monitor, the other part illuminates the DUT.

The laser intensity is not stable in time (see Section 4.5.2), so it is monitored with a beam monitor [101]: a semi-transparent mirror reflects part of the laser onto a light sensor and the value measured by it is saved alongside the current waveforms from the DUT, allowing a correction after the measurement. The estimation of the laser beam width and stability are explained in details in Section 4.5.1 and 4.5.2.

4.3.2 *The moving stages*

The moving stages are three 8MT30-50 produced by Standa [102]. Two of them, placed in a perpendicular arrangement hold the DUT, allowing it to move along the x and y axis. The third one supports the laser optics and moves parallelly to the beam, allowing the adjustment

of the focus position. They are controlled by two USB controllers, models 8SMC4-USB-B8-1 and 8SMC4-USB-B9-2, and can move with a precision of 1 µm.

4.3.3 *The high voltage power supply*

For the measurements of the H35DEMO, a single bias voltage source is necessary and it is provided by a Keithley 2410 Source Meter Unit. It is controlled by the PSTCT software (Section 4.3.7), which allows setting the current compliance and bias voltage and measuring the leakage current while the measurement is running.

If the DUT has to be biased from the same pin connected to the amplifier (not the case for the H35DEMO), a bias-T [103] is available to decouple the high voltage from the signal sent to the amplifier.

4.3.4 *The cooling system*

The cooling system consists of two stages: a Huber *Minichiller-H1 plus* water chiller and a Peltier cell, with its control circuit. The chiller circulates water at a temperature of 2 °C in a water block coupled to the hot side of the Peltier cell.

The Peltier cell can absorb up to 90 W of power (6 A at 15 V): its cold side is placed in contact with the aluminium PCB support and allows cooling the sensor down to −27 °C. It is controlled by a TC-XX-PR-59 controller by Laird Technologies.

To prevent the formation of dew or frost on the DUT, the relative humidity must be kept below 2% at 20 °C, so dry air is constantly supplied to the setup when the cooling system is running. The ambient relative humidity and temperature are constantly monitored by a sensor inside the setup chassis.

4.3.5 *The amplifiers*

The signals generated by the sensor are amplified by two AM-01 A broadband amplifiers by Particulars [104]. Their bandwidth extends from 10 kHz to 2 GHz and their nominal gain is 53 dB. Both input and output feature an impedance of 50 Ω. The gain can be varied by modifying the power supply voltage, however for this work it has been kept at its maximum value. The output of the amplifiers can vary between −1800 mV and 900 mV.

4.3.6 *The oscilloscope*

After being amplified, the signals are digitized by an oscilloscope. For most of the measurements, a DRS4 evaluation board oscilloscope, with

a bandwidth of 700 MHz and a sampling rate[3] of 5 GSa/s has been used [105]. It features four 50 Ω terminated inputs, two of which are used for the signals from the amplifiers, one for the trigger from the laser and one for the beam monitor signal. It is connected via USB 2.0 to the PC and it is completely managed by the PSTCT software (see Section 4.3.7).

For the measurement of the timing characteristics of the current signals (Section 4.7.2) a Lecroy WaveMaster 820Zi-A has been used. It features a bandwidth of 20 GHz, limited internally to 4 GHz for these measurements, and a sampling rate of 40 GSa/s.

4.3.7 *The software*

The TCT setup is managed almost completely by the PSTCT software, by Particulars [106]. It allows controlling the stages, setting the bias voltage, to setup the oscilloscope and performing automated scans in the three dimensions x, y and z for different bias voltage points: at each position a complete current waveform is saved. The waveforms, along with the scan information and the beam monitor data are stored in a binary file, which is then read and converted by the `vtct` software (see Section 4.4).

The laser is controlled by a separate software by Particulars [107], that turns on and off the diode, sets the pulse repetition rate and intensity. A third software, LT_Interface, manages the Peltier cell controller, allowing the setup and monitoring of the temperature on the DUT.

4.4 THE `vtct` SOFTWARE

To simplify and speed up the TCT data processing and analysis, a dedicate Python package called `vtct` has been developed [108]. It features modules to be imported in other Python scripts and stand-alone command line tools. The following tools are available:

`vtct-convert` is used to convert the raw data file generated by PSTCT into a HDF5 file, containing arrays the waveforms, beam monitor information and metadata.

`vtct-merge` allows merging different HDF5 files into one, after checking that the metadata is consistent.

`vtct-charge` is used to calculate the charge and save it into a separate HDF5 file.

3 The sampling rate, *i.e.* the number of voltage samples acquired by an oscilloscope in one second, is normally quoted in samples per second, written as S/s or Sa/s.

`quick-charge` is used to display a two dimensional charge collection map, just as a preliminary check that the collected data do not present any issue.

`quick-focus` is used to estimate the focus position of the laser.

In the following sections the HDF5 file format, used to store the data after conversion, is introduced and the `vtct` tools and modules are described in more details. The data conversion and analysis steps are shown in Figure 4.4.

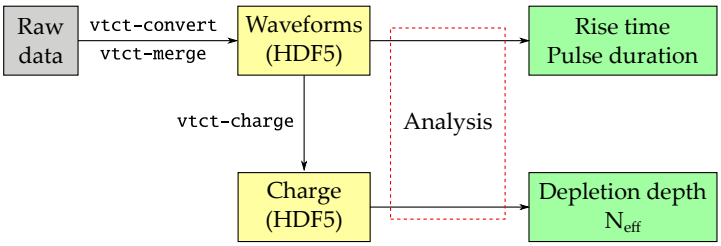

Figure 4.4: The data conversion and analysis steps.

4.4.1 *The HDF5 file format*

The Hierarchical Data Format 5 (HDF5) [109] is a file format designed to store large amounts of data organized in arrays. This file format defines two types of objects:

DATASET a multidimensional array of data of the same type. It supports compression.

GROUP a structure that can contain datasets or other groups. A group can be considered as a directory in a file system.

Each of these objects can store its own metadata, in the form of named attributes.

This file format has been chosen because it fits the data format of the TCT measurements: as mentioned in Section 4.3, the data consists of a 7-dimensional array of waveforms, a 6-dimensional one with the beam monitor information and the metadata that provide the details about the scan, like sample name, movement parameters, bias voltages, etc.

Furthermore, libraries to manipulate HDF5 files are available for most major programming languages. In Python this functionality is provided by the `h5py` package.

4.4.2 *The `pstct_parser` module*

The `pstct_parser` module provides the `parse_data` function that reads a PSTCT raw file and converts it to `numpy` arrays, while saving the metadata (as sample name, scan parameters, etc.) into a

Python dictionary. Furthermore, it allows performing some initial processing, namely:

- Baseline correction: the first portion of each waveform, before the pulse, is averaged to calculate the baseline of the signal and it is subtracted from the waveform.
- Beam monitor data smoothing: as mentioned in Section 4.5.2, the beam monitor data is noisy, and since the effects it corrects for happen on the scale of minutes or hours, it can be smoothed with a moving average, with a selectable number of samples.
- Beam monitor correction: each waveform can be divided by the corresponding beam monitor value, to compensate for laser intensity variation.
- Preliminary processing, as selection of a region of interest, exclusion of voltage points, etc.

The raw file generated by PSTCT is read and the data is processed with dedicated `numpy` functionalities, allowing high performance and fast execution time, compared to the ROOT-based TCTAnalyse library provided by Particulars [110]. The gain in processing time achieved with these Python tools is of the order of 5–7, if compared with the provided analysis library.

4.4.3 *The `vtct-convert` tool*

The `vtct-convert` tool exploits the `parse_data` function described in the previous paragraph and saves the data in a HDF5 file. The waveform and beam monitor data are saved as multidimensional datasets, while the metadata are saved as attributes of the file.

4.4.4 *The `vtct-merge` tool*

The `vtct-merge` tool can be used to combine two separate HDF5 data files with the same x, y and z structure, but with different voltage steps. It will first check if the metadata is consistent (the sample name, the spatial scan parameters, the waveform characteristics and the used channels must be the same) and then it will combine the desired files into a single one, updating the metadata accordingly.

4.4.5 *The `vtct-charge` tool*

The `vtct-charge` tool is needed to calculate the charge for each scan point starting from the HDF5 file containing the waveform data. This calculation is performed by integrating each waveform in the interval specified from the command line and saves the results in a

6-dimensional array in a HDF5 file, along with the metadata from the input file.

4.4.6 *The `quick-charge` tool*

The `quick-charge` tool can be used to quickly display the 2D charge collection map without the need to convert the raw data file into a HDF5 file with `vtct-convert` and to calculate the charge with `vtct-charge`. This functionality is useful to check the preliminary scan used to locate the test structures of a sample or while focusing the laser beam.

4.4.7 *The `quick-focus` tool*

The `quick-focus` tool can aid with the focusing procedure by automating the steps described in Section 4.5.1: it must be provided with data of a scan where the laser moves from a region where it is not allowed to enter the sensitive part of the detector (*e.g.* a region covered in metal, which does not transmit any light) to a region where it is fully contained in it (procedure similar to the one showed in Figure 4.5). The script automatically estimates the FWHM of the laser beam and finds the z position that minimizes it.

4.5 COMMISSIONING OF THE TCT SETUP

Before starting the measurement campaigns, a careful evaluation of the performance of different components of the setup has been carried out. In particular the laser beam profile, its intensity stability and the amplifier performance have been evaluated.

4.5.1 *Estimation of the laser beam profile*

The laser beam profile in the focus region is an important characteristics for a TCT setup because it determines the spatial resolution that can be achieved. For this reason the FWHM of the laser beam has been measured as a function of z (the direction parallel to the laser beam) with the technique described below.

The laser beam intensity profile $I(x, y)$ can be approximated with a gaussian function:

$$I(x, y) = I_0 e^{-\frac{x^2}{2\sigma_x^2} - \frac{y^2}{2\sigma_y^2}} \tag{4.2}$$

where x and y are the coordinates in the plane perpendicular to the laser.

It is useful to define the projection on I_x and I_y on the x and y axes respectively as:

$$I_x(x) = \int_{-\infty}^{+\infty} I(x,y)dy = I_{x_0} e^{-\frac{x^2}{2\sigma_x^2}} \tag{4.3}$$

$$I_y(y) = \int_{-\infty}^{+\infty} I(x,y)dx = I_{y_0} e^{-\frac{y^2}{2\sigma_y^2}} \tag{4.4}$$

which are gaussian as well. The laser has a circular shape, for this reason it's possible to consider $\sigma_x = \sigma_y = \sigma$.

A top TCT scan of a strip sensor has been performed. It has been selected to have alternated metallized and non-metallized lines, much wider that the laser beam width. The selected strip sensor features metal lines 500 µm wide and exposed 50 µm silicon lines.

The FWHM of the laser can thus be determined by moving it from the metallized to the non-metallized part of the sensor surface, perpendicularly to the edge of the metal, with 1 µm steps and by recording a current waveform at each step. Each current waveform is then integrated to obtain the collected charge for each laser position, which is directly proportional to the fraction of the laser spot illuminating the non-metallized part of the sensor (see Figure 4.5).

By plotting the collected charge as a function of the position (*e.g.* x), the function $\int I_x(x)dx$ is reconstructed. It can thus be fitted with:

$$\int I_x(x)dx = A\left[\text{erf}\left(\frac{(x-\mu)}{\sqrt{2}\,\sigma}\right) + 1\right] \tag{4.5}$$

to obtain σ, from which the FWHM is calculated as:

$$\text{FWHM} = \sqrt{8\ln 2}\,\sigma \tag{4.6}$$

An example of a charge profile and fitted function are reported in Figure 4.6a. Equation 4.5 fits the measured charge, but there is slight a deviation that can be explained with the laser profile not being perfectly gaussian.

The procedure reported above is repeated for different values of z, in steps of 5 µm each, in order to extract the laser beam profile around the focus, reported in Figure 4.6b. The laser FWHM remains smaller than 14 µm and varies less than 1.5 µm in the range $z \in [-150\,\mu\text{m}, 150\,\mu\text{m}]$ which determines a uniform charge generation in a 300 µm portion around the focus.

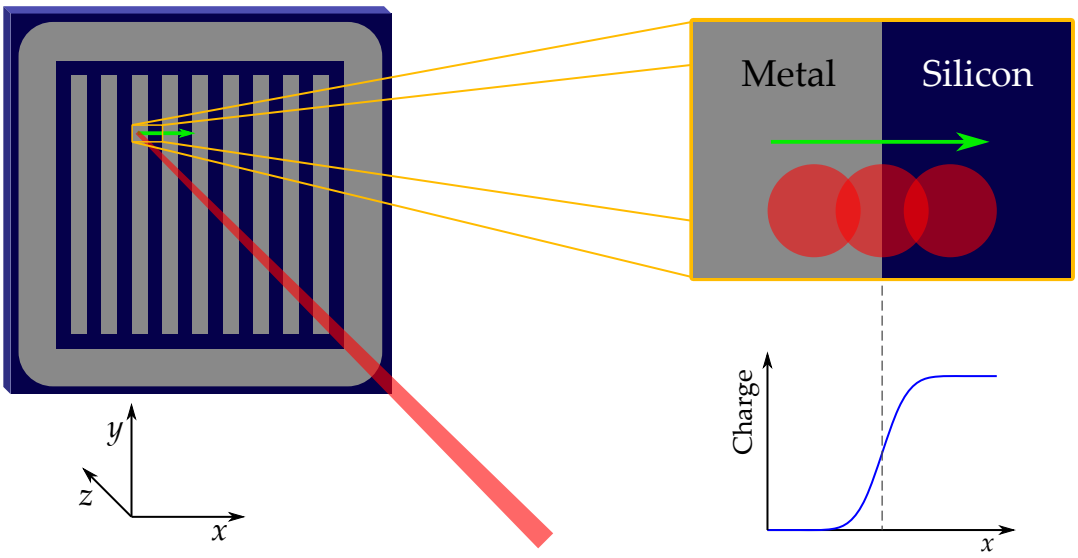

Figure 4.5: Determination of the laser FWHM: the laser beam (in red) illuminates the top of a strip sensor and is moved from a metallized part to a non-metallized one (along the green arrow). The collected charge is proportional to the fraction of the laser beam illuminating the silicon.

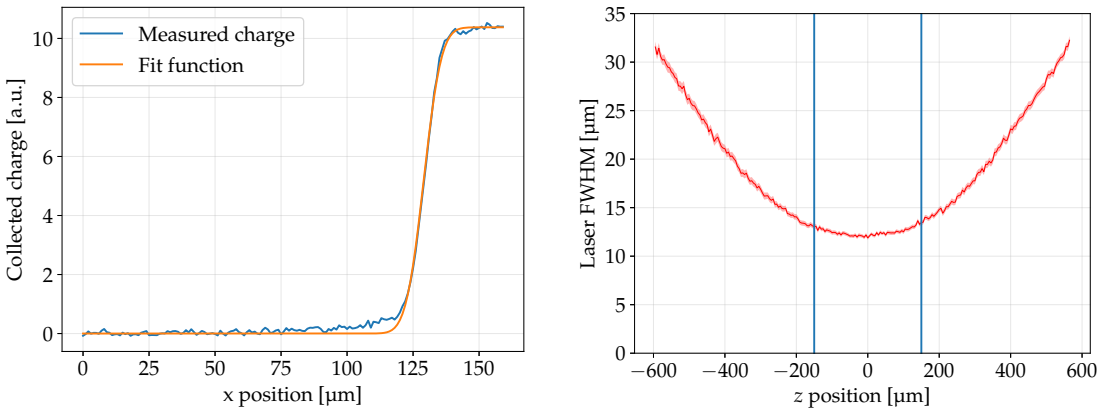

(a) (b)

Figure 4.6: (a) Profile of the collected charge along x and its fit using Equation 4.5. (b) FWHM of the laser as a function of the position along z (the direction parallel to the beam). The focus, *i.e.* the minimum of the curve, is placed in $z = 0$. The blue lines mark the positions $z = \pm 150\,\mu\text{m}$.

4.5.2 *Evaluation of the laser stability*

Another important laser characteristic is its intensity stability over periods of time of 1–2 days. Variations in the intensity can occur due to changes in temperature of the laser diode, influenced by the ambient temperature. Furthermore, an important variation of intensity is present when the laser is turned on and it starts heating.

These variations have been estimated by illuminating the strip sensor mentioned in the previous section without moving the stages and recording one current waveform per second, along with beam monitor data, for 2 days. The sensor has been kept at a constant temperature of 20 °C while recording the data. Each waveform has been integrated to obtain the collected charge as a function of time and the results (intensity before and after beam monitor correction and beam monitor data after noise reduction) are shown in Figure 4.7. A large reduction in intensity can be observed after around 25 hours: this effect does not have a clear explanation and has never been observed during a measurement (the TCT scans described in this work were usually no more than 12–14 hours long).

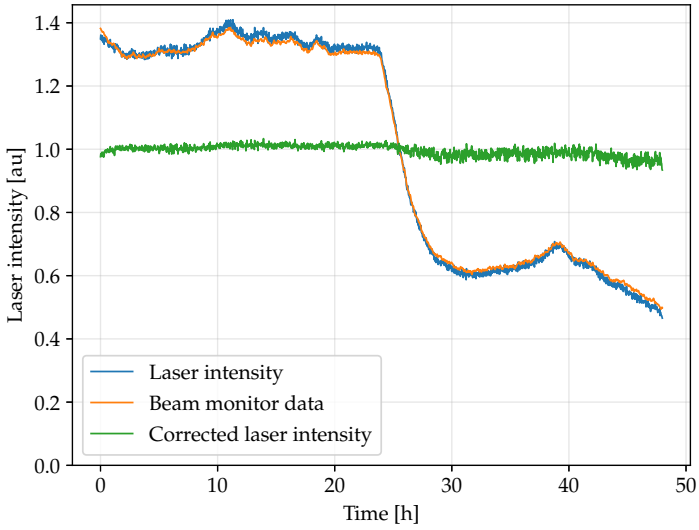

Figure 4.7: Plot of the laser intensity before and after correction, and of the beam monitor data.

Noise has been reduced from beam monitor data by performing a moving average using 500 samples, since the variations on the laser intensity happen on time scales of 10 minutes or more.

The plot shows that the variations in the laser intensity can exceed 80% of the initial intensity, but the beam monitor correction allows limiting the standard deviation of the fluctuations to less than 1% over 12 hours and less then 2% over 48. The fluctuations in laser intensity after correction have a negligible impact on the estimation of the depletion-region depth.

4.5.3 *Evaluation of the amplifiers performance*

The gain of the two amplifiers has been measured with a Rohde & Schwarz ZVL Network Analyzer and the results are shown in Figure 4.8.

The gain of both amplifiers is very similar and features a good uniformity in the band of interest (above 5 MHz). It is consistently lower than the nominal value of 53 dB, however this does not affect the measurements.

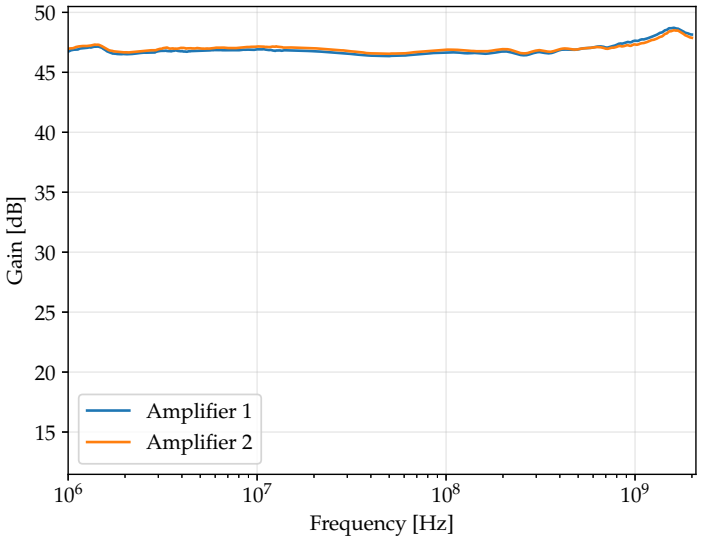

Figure 4.8: Gain of the two amplifiers. Amplifier 1 is connected to the central pixel of the test structures.

4.6 IRRADIATION CAMPAIGN

H35DEMO samples have been irradiated in three different facilities to compare the effects on the charge collection of the damage caused by different particles (protons and neutrons) at different energies. In this section, a brief description of the irradiation facilities techniques will be given. The facilities described here have been used to irradiate the samples for the testbeams as well (Chapter 5).

4.6.1 *Cyclotron at Bern Inselspital*

The Bern University Hospital houses an IBA18/18 medical cyclotron located in an underground bunker (the cyclotron bunker) and delivering the beam to an adjacent bunker (the irradiation bunker) via a beam transfer line (Figure 4.9). This allows conducting research activities during the day and radio-isotope production for medical purposes during the night [111].

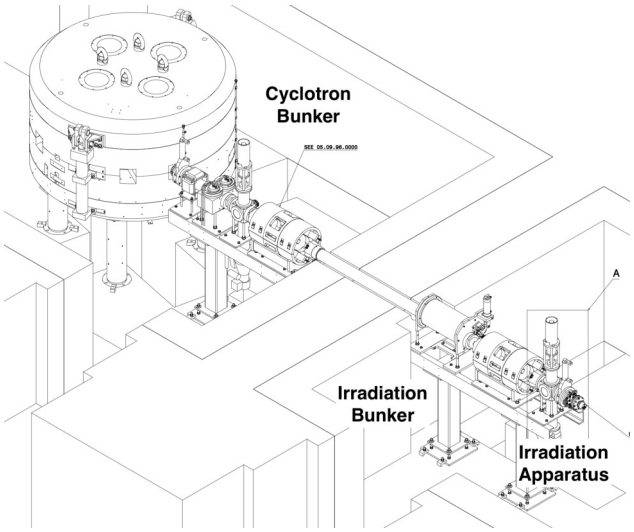

Figure 4.9: The cyclotron facility: the cyclotron bunker is separated from the irradiation bunker. This facilitates the access to the device under irradiation due to the low level of activity in the irradiation bunker [111].

The cyclotron accelerates H^- ions to 18 MeV, then protons are extracted by stripping the electrons from the negative hydrogen ions with 5 µm thick pyrolytic carbon foils. The cyclotron can deliver beam currents from a few pA up to 150 µA: in a typical irradiation, however, the current usually does not exceed a few hundredths of nA.

The protons are focused with two quadrupole doublets and steered with a xy magnet system, before they reach the beam monitoring system (which allows verifying its uniformity), the collimator (which also acts as a Faraday cup, measuring the beam current) and finally are extracted through a 300 µm thick aluminium window, that determines the decrease of their average energy to 16.7 MeV.

The collimator, shown in Figure 4.10, consists of three aluminium rings: a shaping ring with an inner diameter of 35 mm, a high voltage ring, with a diameter of 37.5 mm and the dump ring, available in different sizes, that determines the final shape of the beam. The last ring is connected to a precision ammeter to measure the beam current, from which the current density is obtained, knowing the surface area of the beam determined by the shaping ring. The high voltage ring, biased at -100 V, is needed to prevent the escape of the secondary electrons emitted from the beam dump, which would cause up to a 20% overestimation of the beam current. Given the current density it is possible to extract the proton flux exiting the collimator and, from this, the equivalent fluence in 1 MeV n_{eq}/cm^2, using Equation 2.35, with the hardness factor $k = 3.6$.

The devices to be irradiated can be mounted on a xy stage system, enabling the irradiation of multiple devices (or large area devices) without the need to access the bunker. Furthermore, due to the

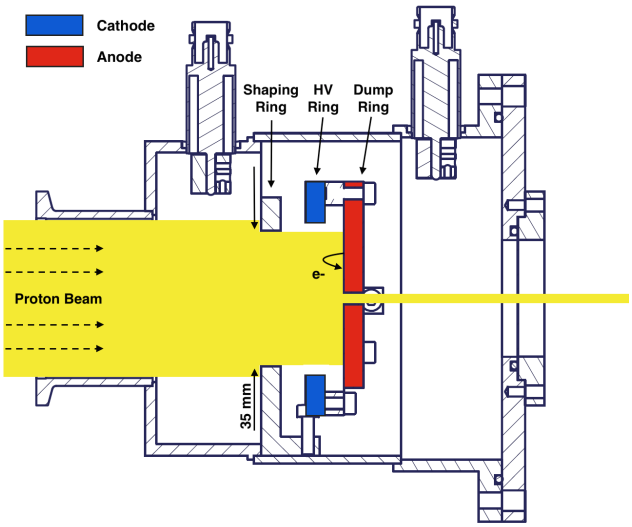

Figure 4.10: Cross section of the collimator [111].

availability of a large space around the stage system to place control and data acquisition equipment, and the possibility to have electrical and data connections between the irradiation bunker and the control room, it has been possible to irradiate devices while powered and running (for example an ATLAPIX1 sample used for testbeams, see Chapter 5 on page 117). During the first irradiations, one of the drawbacks of this facility has been the absence of a freezer to keep the samples cooled while their activation was too high to be taken out. This implies that the annealing study could not be performed on the samples irradiated here.

4.6.2 *PS IRRAD facility at CERN*

The proton irradiation facility (IRRAD), shown in Figure 4.11, is located at CERN in the Proton Synchrotron (PS) East Hall, where a primary proton beam is extracted from the accelerator ring. It is devoted to the study of radiation hardness of particle detectors, electronic components, etc. for the experimental community. The energy of the extracted protons is 24 GeV and the maximum particle rate is $6.7 \cdot 10^{10}\,\mathrm{s}^{-1}$. The beam size can be tuned between 5 and 15 mm RMS. At its maximum capacity PS IRRAD can reach fluences of $1 \cdot 10^{16}\,\mathrm{p/cm}^2$ in about 14 days [112].

The beam profile is monitored by dedicated custom made sensors, shown in Figure 4.12: they consist of 39 separate copper pads, arranged in a circular shape, which generate an electrical signal by secondary electron emission and are individually read out. The current generated in these sensors is proportional to the intensity of the beam and it is amplified and read out with a custom data acquisition system [113].

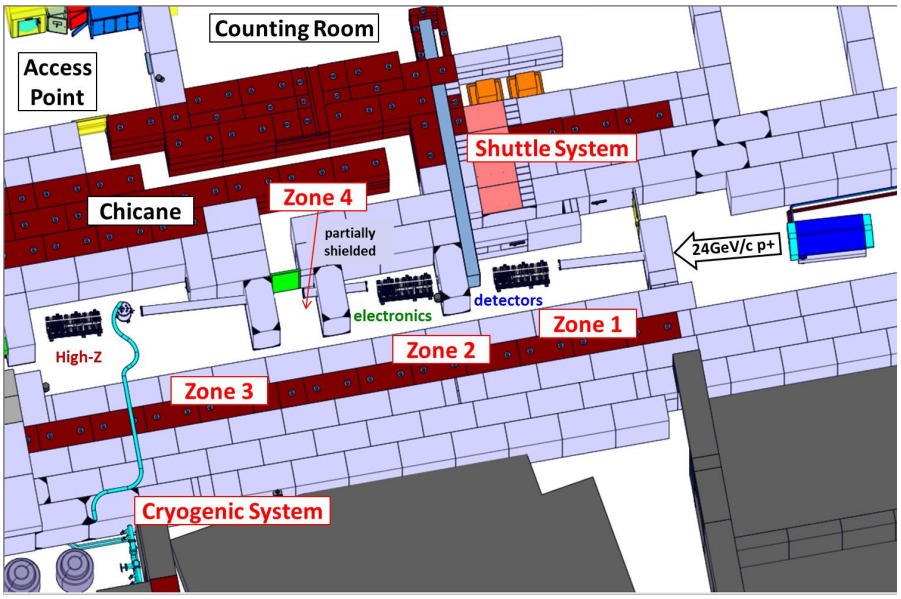

Figure 4.11: Layout of the irradiation area at PS IRRAD [112].

Figure 4.12: The PS IRRAD Beam Profile Monitor (BPM) [113].

The IRRAD facility features a secondary electron emission chamber (SEC) to measure the beam intensity. Since the beam profile is not homogeneous, the SEC cannot be used to reliably measure the intensity to which samples smaller that the transverse beam area are exposed. For this reason the total number of protons hitting a sample is determined with a thin aluminium foil, measuring its activation with gamma spectroscopy.

Two different reactions, $^{27}\mathrm{Al}(\mathrm{p},3\mathrm{pn})^{24}\mathrm{Na}$ and $^{27}\mathrm{Al}(\mathrm{p},3\mathrm{p3n})^{22}\mathrm{Na}$, are exploited by this technique, depending on the duration of the irradiation. If the irradiation lasts less than 12 h, the first one is used (the half-life of ^{24}Na is $\sim$ 15 h), while for longer irradiations, lasting weeks or months, the second one is preferred (the half-life of ^{22}Na is $\sim$ 2.6 years).

Knowing the activity A of the desired isotope t_{wait} seconds after an irradiation lasting t_{irr} allows calculating the beam intensity I in protons per second as:

$$I = \frac{A}{N_A/M \cdot \rho\sigma x(1 - e^{-\lambda t_{\text{irr}}})e^{-\lambda t_{\text{wait}}}} \tag{4.7}$$

where N_A is Avogadro's number, M is the molar mass of aluminium, ρ is its density, x is the foil thickness, σ is the production cross section of the desired isotope and λ its decay constant. The total number of protons can be calculated as $I \cdot t_{\text{irr}}$ [114] and the equivalent fluence in 1 MeV n_{eq}/cm^2 is obtained exploiting Equation 2.35, with the hardness factor $k = 0.6$ [115].

In this facility the annealing could not be controlled: the irradiation was performed at room temperature and it could take several weeks to be completed.

4.6.3 *TRIGA Reactor at the Jožef Stefan Institute*

The Jožef Stefan Institute (Ljubljana) houses a 250 kW TRIGA Mark II nuclear reactor built in 1966 and used for research purposes. Its main applications are neutron activation analysis, neutron radiography, irradiation of samples for radiation hardness studies and activation of materials. In addition, the reactor is used for staff training and education of university students and future reactor operators [116].

The reactor facility, shown in Figure 4.13, include multiple irradiation positions, both inside and outside the reactor core.

The reactor core has an annular configuration with a diameter of 44.2 cm, with 91 in-core positions for fuel elements, 4 control rods, and numerous irradiation positions, as shown in Figure 4.13a. Nuclear fuel is a homogeneous mixture of fuel and moderator in form of uranium-zirconium hydride.

The reactor is also equipped with numerous ex-core irradiation positions. The first set of them is located in a carousel, a rotary device inside the graphite reflector, holding 40 cylindrical positions (ICx) with radii 1.5 cm and lengths of 22.45 cm (Figure 4.13a).

There are also several larger horizontal irradiation positions, shown in Figure 4.13b: two cylindrical tubes of diameter 15.5 cm, the Radial Piercing Port and the Radial Beam Port, extend radially outwards from the core. Additionally, two more tubes of the same diameter, the Tangential Irradiation Port and the Thermal Irradiation port, are present. They are shifted horizontally and vertically compared to the radial ones.

Finally, the two largest irradiation positions extend outside of the reactor tank: the Thermalizing column is a small room, shielded with heavy concrete doors to which neutrons are guided through a graphite stack and lead shielding. The Thermal column is similar, although

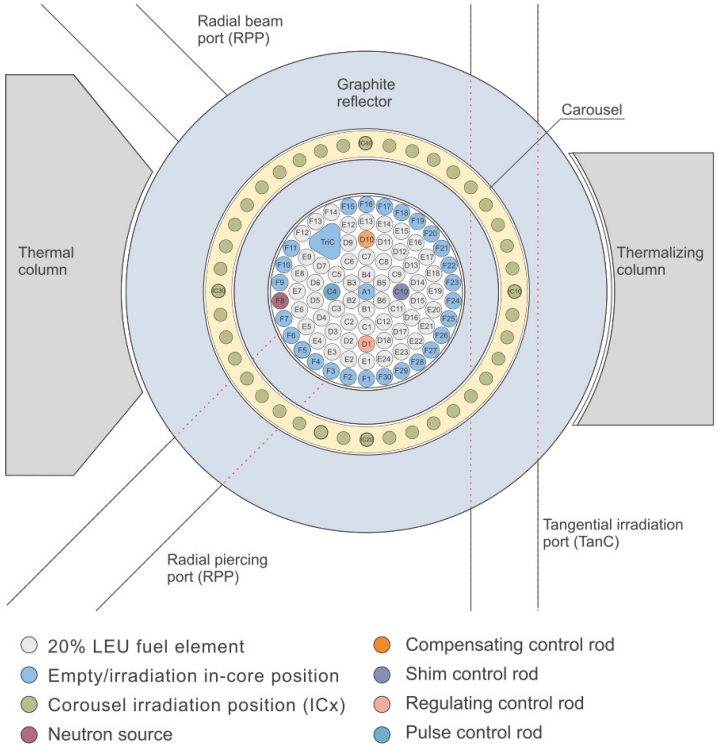

(a)

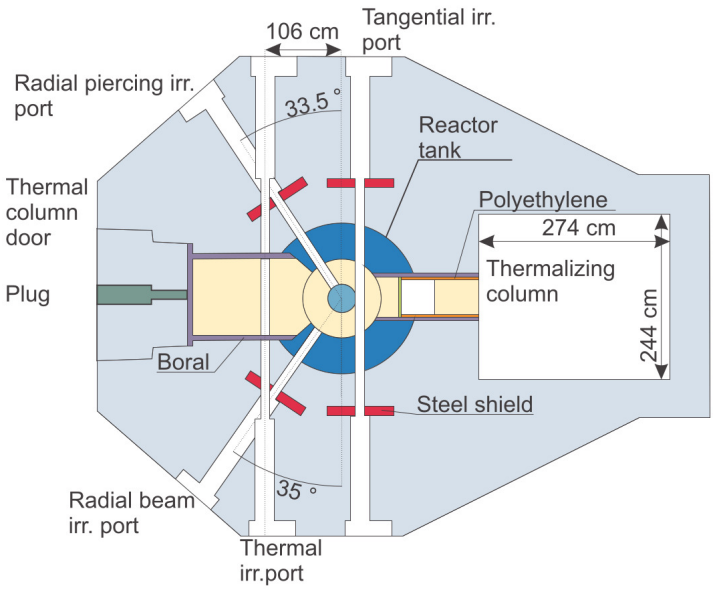

(b)

Figure 4.13: (a) JSI TRIGA Mark II reactor core with typical fuel element configuration and irradiation positions. (b) Top view of the reactor, with the Thermalizing and Thermal columns and the horizontal irradiation channels [117].

the graphite stack is larger, without any lead, and extends further outwards [117].

The neutron irradiated samples characterized in this work exploited the in-core irradiation positions. Since the diameter of the inner irradiation tubes is small, around 3 cm in diameter, the samples could not be placed on a PCB before irradiation, requiring the utilization of one sample for each irradiation step.

4.6.4 *Samples irradiation and annealing*

Several H35DEMO samples have been irradiated in the three facilities described above, with some differences in the procedure depending on the characteristics of the facility.

At the cyclotron in Bern it is possible to irradiate samples mounted on a PCB, the irradiation could be organized in less than a week and it would last less than two hours: this allowed performing multiple irradiation steps on the same sample, which resulted in the need for fewer chips and the possibility to perform up to 12 irradiation steps per resistivity.

In the other two facilities it was not possible to irradiate the sensors mounted on the PCB and the organization and irradiation time was much longer (more than one month in total). For this reason samples were irradiated in batches (different samples for different irradiation levels) and a TCT scan could not be performed before irradiation.

Table 4.1: Annealing steps.

Step	Conditions	Cumulative time @ 20 °C
0	–	∼0 days
1	80 mins @ 60 °C	∼20 days
2	30 mins @ 80 °C	∼70 days
3	120 mins @ 80 °C	∼360 days
4	300 mins @ 80 °C	∼990 days

The H35DEMO samples characterized with the TCT have been irradiated up to a fluence of $2 \cdot 10^{15}$ 1 MeV n_{eq}/cm^2, twice the expected end-of-life fluence of the ITk (see Section 1.5.1). A summary of the irradiated samples, along with the irradiation steps performed in each facility is reported in Tables A.1, A.2 and A.3 in Appendix A. In addition to the ones listed in the tables, four more non-irradiated samples have been used, labelled H35-XX-1 (XX is the resistivity of each sample).

An annealing study has been performed on some of the neutron irradiated samples: a TCT scan has been performed right after irradiation, followed by four accelerated annealing steps, with another TCT scan after each one. The conditions of the annealing steps, along with the equivalent cumulative time at room temperature, are summarized in Table 4.1.

4.7 MEASUREMENT CAMPAIGN AND DATA ANALYSIS

In order to study the evolution of the depletion-region depth, of the effective doping concentration and of the current signal shape caused by irradiation, edge-TCT measurements have been performed on the central pixel of the test structures of H35DEMO samples. They have been carried out at the University of Geneva and at the University of Bern.

To perform them a custom PCB has been developed: it features two controlled-impedance lines for the signals from the central and outer pixels of the H35DEMO test structures, a filtered bias voltage line and a Pt-100 temperature sensor placed as close as possible to the chip, to keep the temperature of the DUT monitored throughout the scan.

The coordinate system used for this measurement campaign is shown in Figure 4.14: the laser is parallel to the z axis, the sensor surface lies in the xz plane, with the top of the sensor is located at positive y.

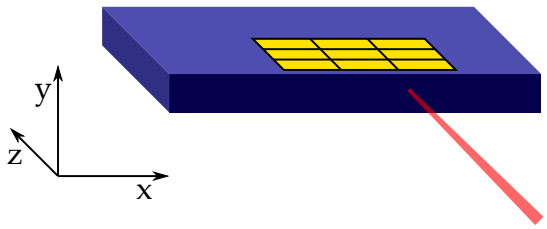

Figure 4.14: Coordinate system used for the TCT measurement campaign. The sketch shown the laser entering from the edge of the H35DEMO, perpendicularly to the long edge of the test structures (in yellow).

The edge-TCT measurements performed on the H35DEMO consist of three parts: after having let the dry air remove the humidity from the TCT enclosure and having brought the temperature of the DUT to $-27\,°C$, a coarse xy scan at the highest bias voltage, with steps of around 10–50 µm, is performed to locate the test structures and define the region where the finer scan will be performed. It is followed by a yz focusing scan, similar to the one described is Section 4.5.1, to correctly position the laser focus below the test structures and finally a fine xy scan, with steps of 1 µm along y and 5 µm along x is launched. The choice of step size is aimed at having the best possible resolution in the depth direction (y) and enough resolution

in x to be able to spot inhomogeneities in the charge collection, while keeping the time required for a full scan at around one day. Each scan consists of several bias voltage steps (from 0 V to −100 V for the proton irradiated samples and to −165 V for the non irradiated and the neutron irradiated ones). The oscilloscope is set to record the average of 40 signals to reduce the noise.

In order to perform the data analysis, a preliminary data processing is necessary. First of all, the raw data produced by the PSTCT software is converted into the HDF5 format using the `vtct-convert` tool and, if necessary, multiple files the constitute the same measurement are merged with the `vtct-merge` tool. The data analysis is then performed on the output files obtained in these steps. The details of each analysis are outlined in the following paragraphs.

4.7.1 *Depletion depth and effective doping concentration*

To obtain the depletion depth of a sensor it is necessary to calculate the collected charge at each position of the scan by integrating the current waveforms over a defined time interval (Figure 4.15). This interval has been chosen to be 8 ns in order to study the drift component of the charge collection,[4] with a minimal influence from the diffusion, and to enhance the signal-to-noise ratio.

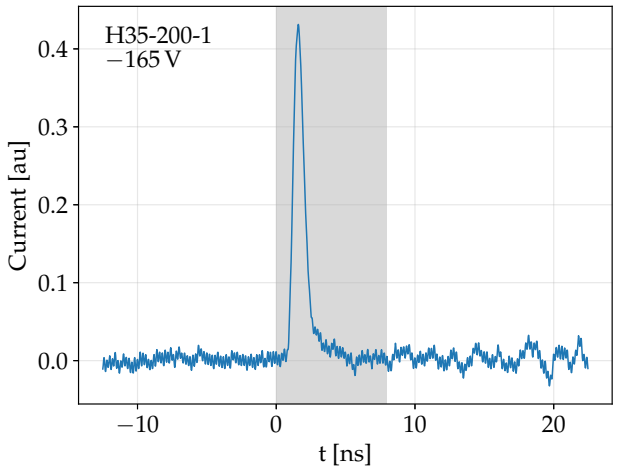

Figure 4.15: Sample of a current waveform with the integration interval is highlighted in grey.

This first integration step is performed using the `vtct-charge` tool and examples of charge collection maps are visible in Figure 4.16 for a 200 Ω · cm and a 1000 Ω · cm samples. In the case of the latter sample, the charge collection is not homogeneous but presents a peak deeper inside the bulk. This effect can be understood by comparing the charge collection map of the central pixel with the one of the outer pixels: the

4 Given the geometry of the sensor and the applied bias voltages, charge carriers are expected to be completely collected by drift within 6 ns. A safety margin of 2 ns has been added to the integration interval.

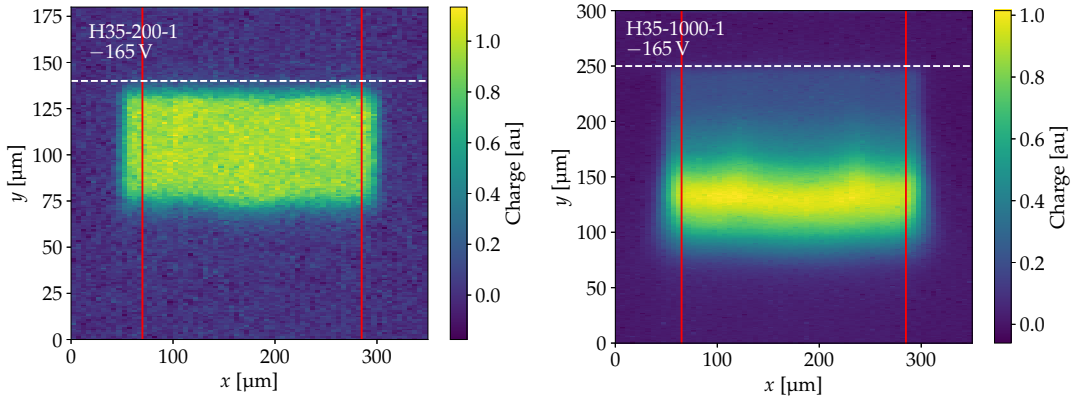

(a) (b)

Figure 4.16: Collected charge as a function of the position of the laser for a (a) 200 Ω · cm and a (b) 1000 Ω · cm samples at a bias voltage of −165 V. The vertical lines represent the range used to estimate the depletion depth (see text for more details). The dashed white lines indicate the approximate position of the sensor surface.

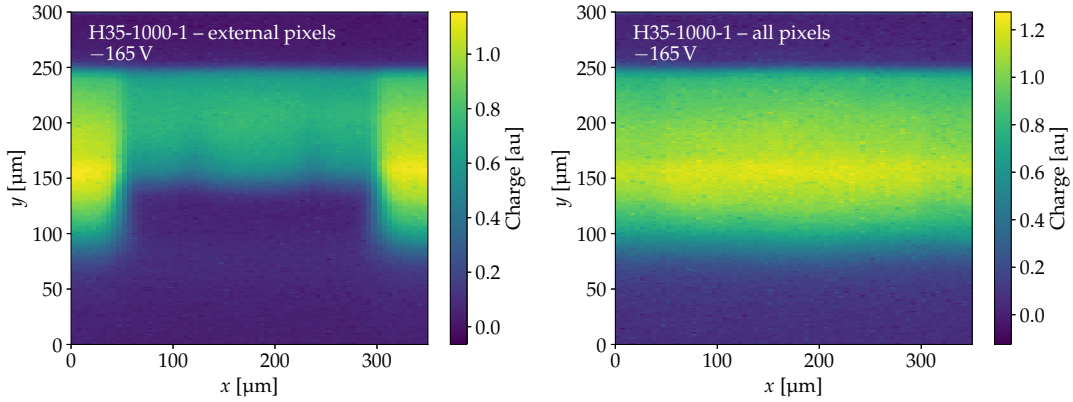

(a) (b)

Figure 4.17: Collected charge (a) in the outer pixels and (b) in all the pixels as a function of the position of the laser for a 1000 Ω · cm sample.

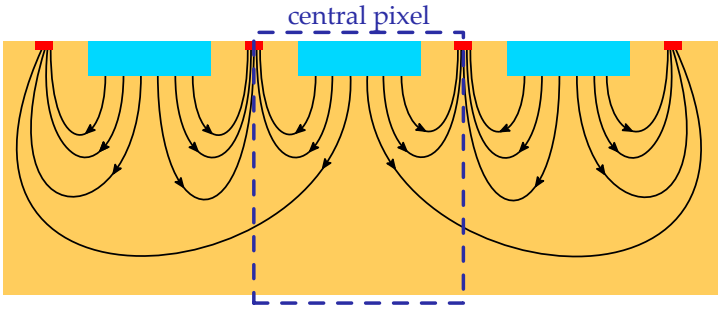

Figure 4.18: Sketch of the electric field in the depletion region. The lines give a qualitative trend of the electric field [118].

two charge maps are complementary and, if they are summed, the resulting charge collection map is homogeneous (see Figure 4.17).

This effect is due to the shape of the electric field lines inside the sensor bulk (Figure 4.18): when electron-hole pairs are generated deeper inside the substrate, part of the charge created below the outermost pixels of the test structure is collected by the central pixel, producing the peak in the charge collection profile [118]. This charge sharing effect appears when the depletion depth exceeds 80–100 µm, as is visible in Figure 4.19, and is taken into account when estimating the depletion depth.

From the charge collection map, the depletion depth is estimated by calculating the Full Width at Half Maximum (FWHM) of the vertical charge profiles (shown in Figure 4.19). To have a good estimation, it is necessary to remove the profiles which are too close to the lateral edge of the pixel, where the laser beam is not fully contained. For this reason, the average charge of each vertical profile is calculated and only the x interval where this value is larger than 0.85 times the maximum average charge is considered [118]. This selection is highlighted by the red vertical lines in Figure 4.16 and designates the Region of Interest (RoI).

The peak produced by the charge sharing mentioned above can cause a bias in the evaluation of the FWHM. Therefore, to separate the different contributions, each charge profile is fitted with the following function:

$$f(y) = \frac{A}{4}\left[\operatorname{erf}\left(\frac{y-y_1}{\sigma_1}\right)+1\right]\cdot \operatorname{erfc}\left(\frac{y-y_2}{\sigma_2}\right) + B\cdot e^{\frac{(y-\mu)^2}{\sigma^2}} + C \quad (4.8)$$

The box function given by the combination of the error functions represents the profile of the charge collected in the depletion region: y_1 and y_2 are the beginning and the end of the region, while σ_1 and σ_2 describe the smearing of the charge profile due to the size of the beam spot, and, in the case of σ_1 , the effect of the decreasing electric field inside the bulk. The Gaussian and its normalisation B represent the position, the width and the amplitude of the peak due to charge sharing and C a possible offset of the baseline. The parameter A, which normalises the error functions and represents the charge collection maximum in absence of charge sharing, is used as the maximum for the FWHM estimation. Conversely, when the depletion depth is comparable with the laser beam diameter, the charge collection profile has a gaussian shape (*e.g.* for the 0 V profile of Figure 4.19a) and in this case the maximum is obtained from the global fitted function. An example of the fit behaviour on two the different kind of profiles is presented in Figure 4.19.

The FWHM of each charge profile in the RoI is calculated with this procedure and the final depletion depth value is obtained by averaging all the FWHMs. The uncertainty on this value is obtained by combining the standard error of the average of the FWHMs with a contribution given by the presence of charge sharing.

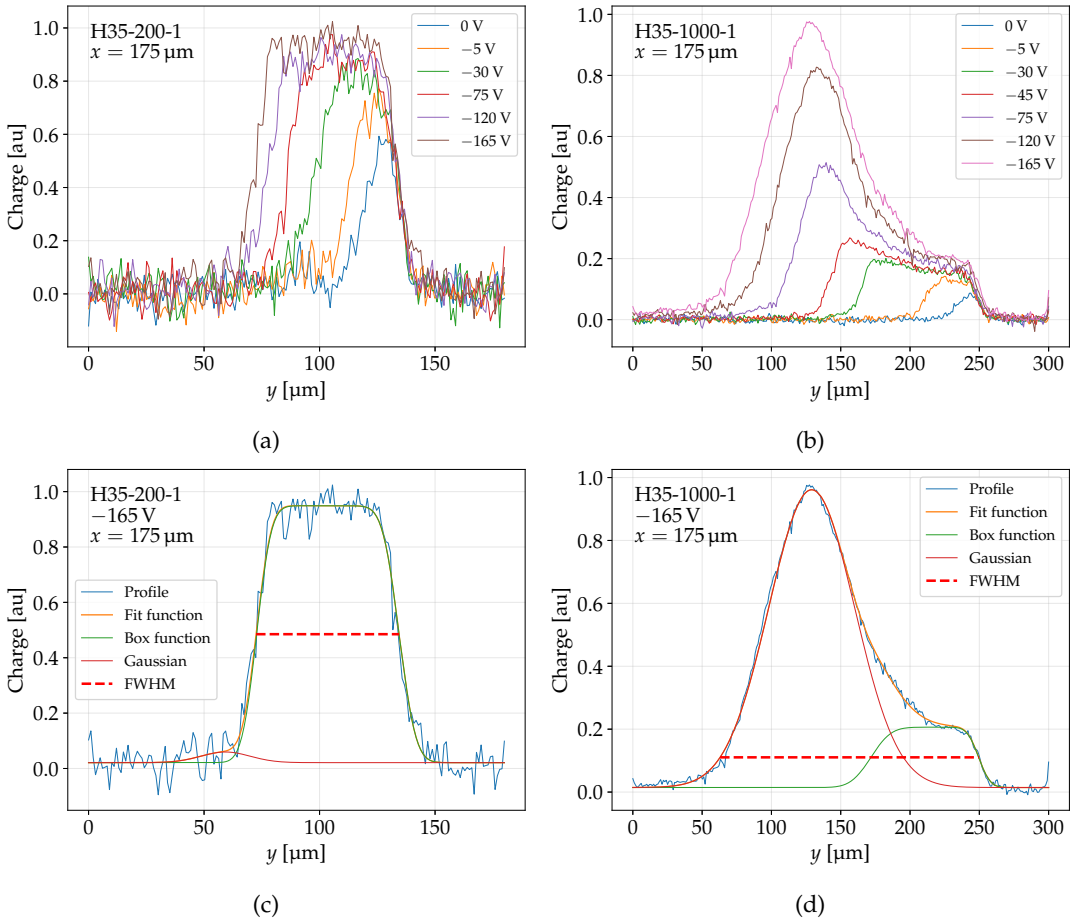

Figure 4.19: Charge profiles of scans (a) without and (b) with charge sharing at different bias voltages. (c, d) An example of fit in these two conditions.

The depletion depth d of each sample is then fitted with the following function to obtain the effective doping concentration N_{eff} (based on Equation 2.30):

$$d(V) = d_0 + \sqrt{\frac{2\varepsilon}{qN_{\text{eff}}}V} \tag{4.9}$$

where ε is the silicon permittivity, q is the electron charge, V is the reverse bias voltage and d_0 is a constant that accounts for the thickness of the n-well and for the built-in voltage of the pn junction.

All the results for the different samples, before and after irradiation, before and after annealing are discussed in Section 4.8.1.

4.7.2 *Pulse shape analysis*

The shape of the current pulses as a function of the position has been studied as well, to evaluate possible effects on the rate of charge collection dependent on the position inside the bulk. The rise time t_{rise} and duration of the pulses t_{pulse} have been measured: the rise time is defined as the time taken for the current pulse to pass from 10% to 90% of its maximum, while the duration as the time required to cross the 10% mark twice (see Figure 4.20).

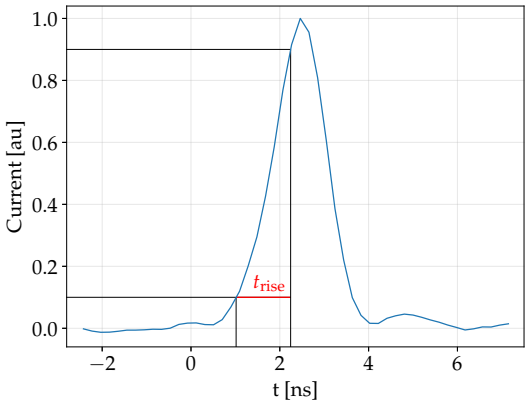

(a)

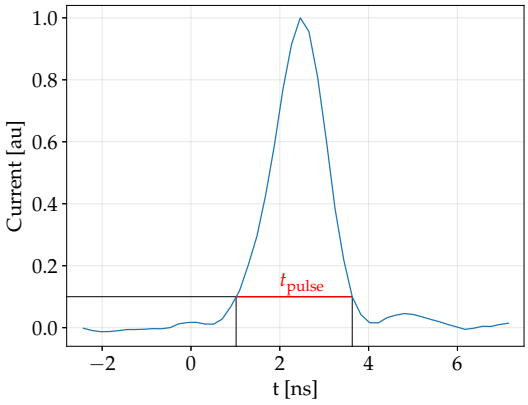

(b)

Figure 4.20: The definition of the (a) rise time t_{rise} and (b) pulse duration t_{pulse}.

This measurement has been performed on a limited set of samples using a fast oscilloscope: the DRS4, used for most of the measurements, has a 700 MHz bandwidth, making it the bottleneck in the read-out electronic chain (the amplifiers have a bandwidth of 2 GHz). For this reason a Lecroy WaveMaster 820Zi-A has been used: it features a 20 GHz bandwidth, which has been limited to 4 GHz to reduce the noise. The results of these measurements are discussed in Section 4.8.2.

4.8 RESULTS

4.8.1 *Charge collection and effective doping concentration*

4.8.1.1 *Before irradiation*

The depletion depth as a function of the bias voltage for samples of the four different resistivities before irradiation is shown in Figure 4.21, along with the fitted curves from Equation 4.9, showing a reasonable good description of the data.

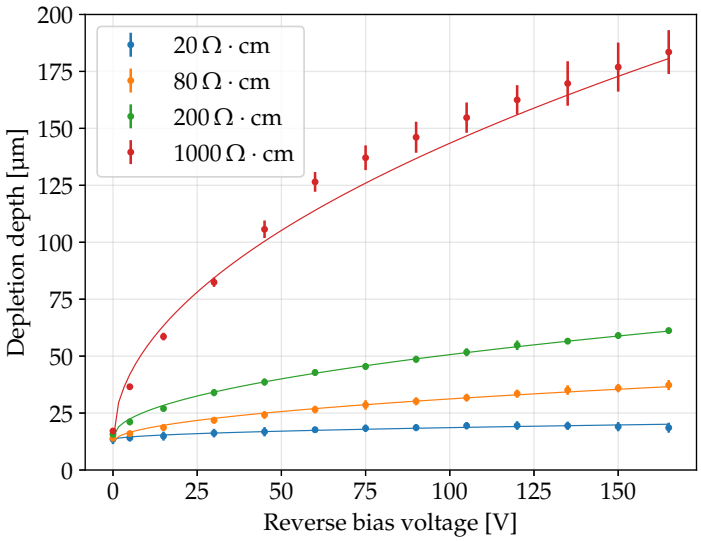

Figure 4.21: Evolution of the depletion depth as a function of the bias voltage. The dots represent the measured points, while the lines are the fitted curves according to Equation 4.9.

In Figure 4.22 the charge collection of the 20 Ω · cm sample at two different bias voltages is shown: while at the lower voltage the charge is collected uniformly in the depleted region, at the higher voltage up to ∼4 times more charge is collected in four spots, which coincide with the p+ implantations used to bias the substrate (see Figure 3.9).

In Figure 4.23 the maximum charge collected by the unirradiated samples of resistivities 20, 80 and 200 Ω · cm is shown (the 1000 Ω · cm has been excluded because the maximum collected charge is influenced by charge sharing, as explained in Section 4.7.1). The 20 Ω · cm sample shows a dramatic increase of the collected charge starting at around 120 V, while the remaining two samples do not exhibit the same behaviour. This observation is compatible with the presence of charge multiplication in the region close to the electrodes, since the electric field reaches its highest value there. This effect has not been observed in samples of higher resistivities because the electric field at a given bias voltage is less intense.

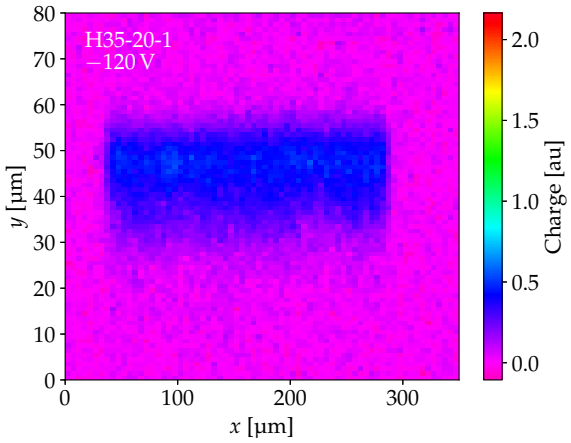

(a)

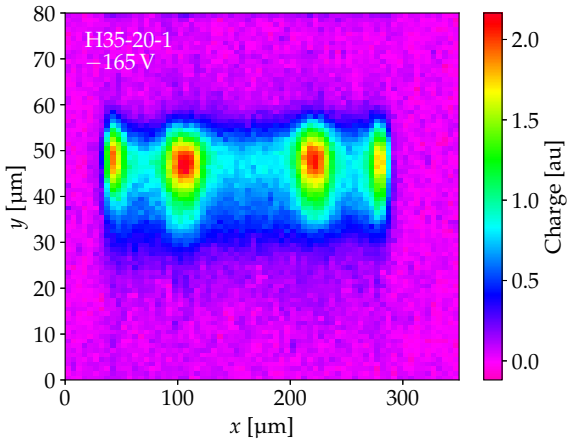

(b)

Figure 4.22: Collected charge as a function of the position for a $20\,\Omega \cdot \mathrm{cm}$ sample at a bias voltage of (a) $-120\,\mathrm{V}$ and (b) $-165\,\mathrm{V}$. In the right plot the charge collection is not uniform, with "hot spots" corresponding to the substrate biasing electrodes.

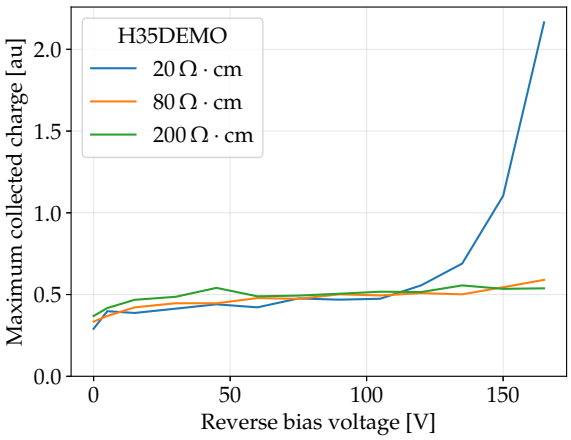

Figure 4.23: Evolution of the maximum collected charge as a function of the reverse bias voltage. The $20\,\Omega \cdot \mathrm{cm}$ sample shows a significant increase after 120 V.

4.8.1.2 *Irradiation effects*

The evolution of N_{eff} as a function of fluence of protons and neutrons is shown in Figure 4.24 and a general trend is visible: the effective doping concentration initially decreases, reaching a minimum at a fluence that is higher for lower resistivities (*e.g.* it is around $5 \cdot 10^{14}$ 1 MeV n_{eq}/cm^2 for the protons-irradiated $80\,\Omega \cdot cm$ sample and around $2 \cdot 10^{14}$ 1 MeV n_{eq}/cm^2 for the $1000\,\Omega \cdot cm$ one), and then it increases at higher fluences.

The total variation in N_{eff} is much more pronounced for the low resistivity samples: the $20\,\Omega \cdot cm$ ones span almost three orders of magnitude, while the $1000\,\Omega \cdot cm$ ones about one. Furthermore, there is a very clear difference in the effect of protons and neutrons on these substrates: after irradiation with protons the effective doping concentration decreases significantly, more than with neutrons, and remains lower when it starts to increase again.

This behaviour is compatible with an initial removal of shallow acceptors in competition with a constant introduction of deep acceptors: at the beginning of irradiation the former is more pronounced, but decreases exponentially with fluence, while the latter dominates at higher fluence, since it increases linearly with it. Similar behaviours have been observed on other sensors built onto p-doped substrates as well [119–121].

However, this combination of effects does not fully explain the observed evolution of N_{eff}: in the $200\,\Omega \cdot cm$ sample an initial increase of the effective doping concentration is present at around $1 \cdot 10^{13}$ 1 MeV n_{eq}/cm^2, after irradiation with low energy protons, and in the $20\,\Omega \cdot cm$ sample N_{eff} has the same values before irradiation and after a fluence of $1 \cdot 10^{14}$ 1 MeV n_{eq}/cm^2: this may hide an increase in that interval, which has been observed on other sensors [122]. Interestingly, this effect is not visible with the high energy protons and with the neutrons.

In Figure 4.25 the same data of Figure 4.24 is arranged based on the radiation type. Here it is visible how the effective doping concentration of samples of different resistivities tends to converge to a value which depends on the radiation type. If the shallow acceptors are completely removed, the effective doping concentration becomes only dependent on the deep acceptors introduced by irradiation, with an introduction rate that depends on the radiation type.

These measurements also show that the NIEL scaling hypothesis (see Section 2.4.1.1 on page 55) is not valid for the substrates studied in this work: the initial acceptor removal is faster when irradiating with protons, while the acceptor introduction is more important in the neutron irradiation.

The charge multiplication observed in the non irradiated $20\,\Omega \cdot cm$ sample is still present after the first three steps on neutron irradiation and from $5 \cdot 10^{14}$ 1 MeV n_{eq}/cm^2 it is no longer visible. A faint charge

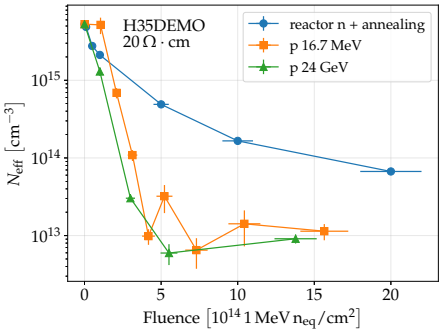

(a) 20 Ω · cm

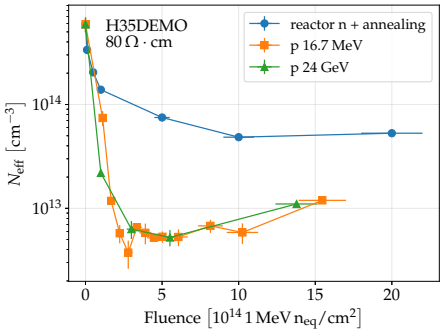

(b) 80 Ω · cm

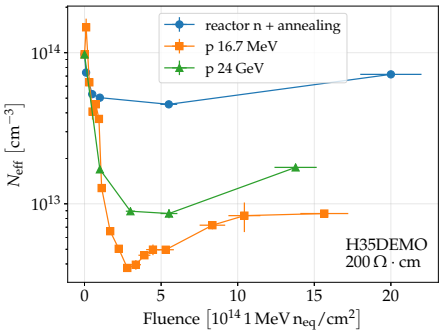

(c) 200 Ω · cm

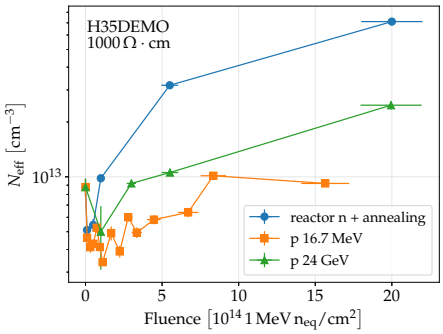

(d) 1000 Ω · cm

Figure 4.24: Evolution of the effective doping concentration for samples of the four resistivities after irradiation with different sources.

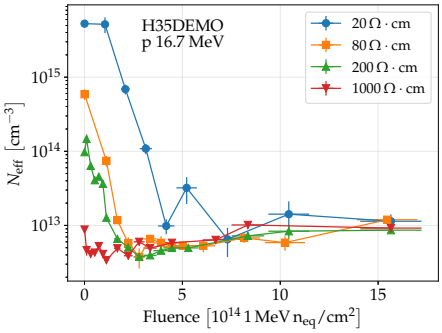

(a) 16.7 MeV protons

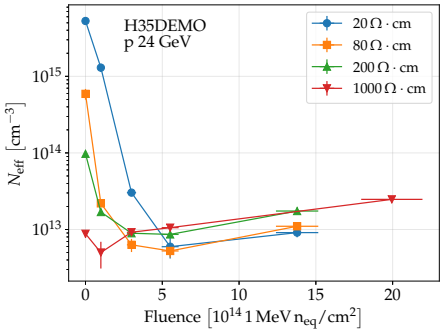

(b) 24 GeV protons

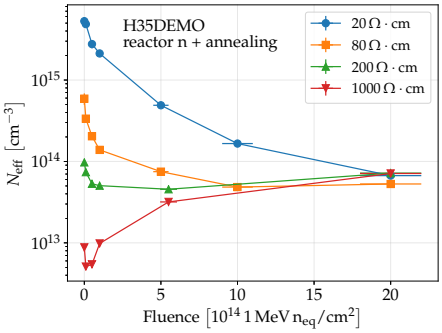

(c) Reactor neutrons

Figure 4.25: Evolution of the effective doping concentration for samples of the four resistivities after irradiation.

multiplication can be observed in the $80\,\Omega\cdot\text{cm}$ one after a neutron fluence of $1\cdot10^{13}$ 1 MeV n_{eq}/cm^2, while in the other samples it is not visible. It is not possible to evaluate its evolution in the proton irradiated samples because they have been measured up to a bias voltage of $-100\,V$.

4.8.1.3 *Annealing effects*

The annealing effects on the effective doping concentration have been studied on neutron-irradiated samples by performing several annealing steps, as listed in Table 4.1.

The first annealing step has been performed on 20 and $80\,\Omega\cdot\text{cm}$ samples (Figure 4.26a) for all the available fluences. Four annealing steps have been performed on the samples of the four resistivities irradiated to the highest fluence (Figure 4.26b). The measurement before annealing is not available for the $200\,\Omega\cdot\text{cm}$ and $1000\,\Omega\cdot\text{cm}$ samples.

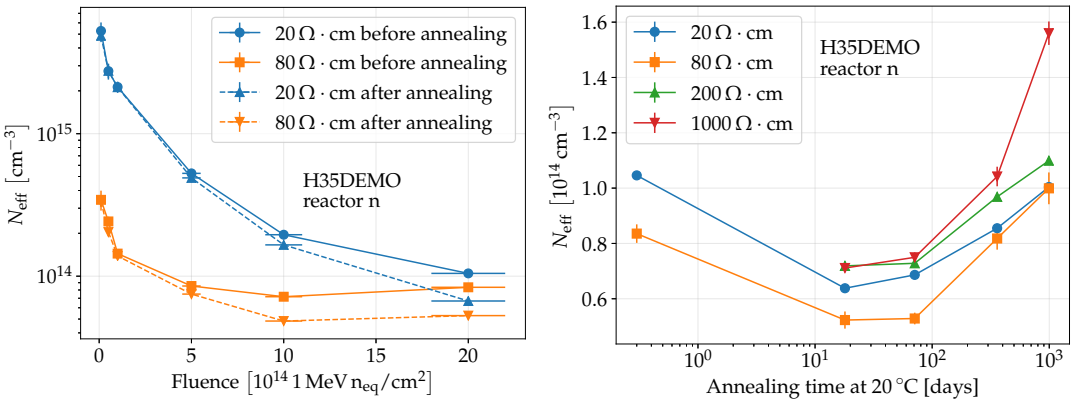

(a) (b)

Figure 4.26: (a) Evolution of the effective doping concentration as a function of the fluence for the lower resistivity samples before and after annealing. (b) The evolution of the effective doping concentration for the samples irradiated at a fluence of $2\cdot10^{15}$ 1 MeV n_{eq}/cm^2.

The effects of annealing after neutron irradiation depend on the received fluence, as shown in Figure 4.26a: at lower fluences almost no effect is visible, while a decrease of N_{eff} is present at fluences higher than $5\cdot10^{14}$ 1 MeV n_{eq}/cm^2, compatible with beneficial annealing (see Section 2.4.1.5). This variation is more pronounced at higher fluences and for this reason the remaining three annealing steps have been performed on the samples irradiated to $2\cdot10^{15}$ 1 MeV n_{eq}/cm^2.

The results of the four annealing steps are shown in Figure 4.26b and are compatible with three annealing components: the initial beneficial annealing, the reverse annealing and the stable damage part, as discussed in Section 2.4.1.5. While the data qualitatively follows Equation 2.41, it is not possible to perform a fit, since the number of data points is too limited compared to the number of free parameters.

4.8.2 *Pulse shape*

The pulse duration and rise time of the current signals measured on non-irradiated H35DEMO samples are shown, as a function of the position, in Figures 4.28 and 4.29 respectively.

The pulse duration is longer for higher resistivity substrates because the electric field is smaller and the travel distance longer. Furthermore, the current signals are longer at the bottom of the depletion region, where a more important part of the charge is collected by diffusion. This is particularly visible between the n-wells of the $20\,\Omega \cdot \mathrm{cm}$ sample and extremely pronounced in the $1000\,\Omega \cdot \mathrm{cm}$ sample, where it reaches values of 35–40 ns at the very bottom of the depletion region.

The rise time of these samples follows a trend similar to the pulse duration, with the exception of a band within the depleted region where it becomes particularly high: this "slow band" corresponds to a region below a p-well implanted into the deep n-well (see Figure 4.27), connected to ground and effectively forming a diode in the off state. This may add parasitic capacitance in the region covered by the p-well, slowing down the current signal. Finally, it's possible to observe that no effect in the signal timing due to the charge multiplication is visible in Figures 4.29a and 4.28a.

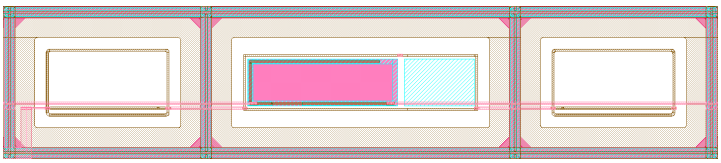

Figure 4.27: Image obtained from the H35DEMO layout showing the central pixel of the test structures: in the central n-well a p-well is present (the pink rectangle). This corresponds to the "slow band" visible in the timing plots.

The shape of the current pulses has been evaluated after neutron irradiation as well: data for the 20 and $80\,\Omega \cdot \mathrm{cm}$ samples are available for the four higher neutron fluences after the first annealing step. The results for the $20\,\Omega \cdot \mathrm{cm}$ samples are shown in Figures 4.31 and 4.30 (The results for the $80\,\Omega \cdot \mathrm{cm}$ sample are very similar and not shown here). After the first irradiation step the long pulses present at the bottom of the depleted region before irradiation, and caused by a contribution from a diffusion component to the charge collection, disappear due to the reduced trapping time caused by radiation damage. At higher fluences, however, this effect appears again, but in this case it can be attributed to the reduced effective doping concentration that increases the depleted region and reduces the electric field.

To summarize, the evolution of the timing characteristics can be considered a result of two competing effect: a lower electric field caused by the lower N_{eff}, which tends to increase the rise time and

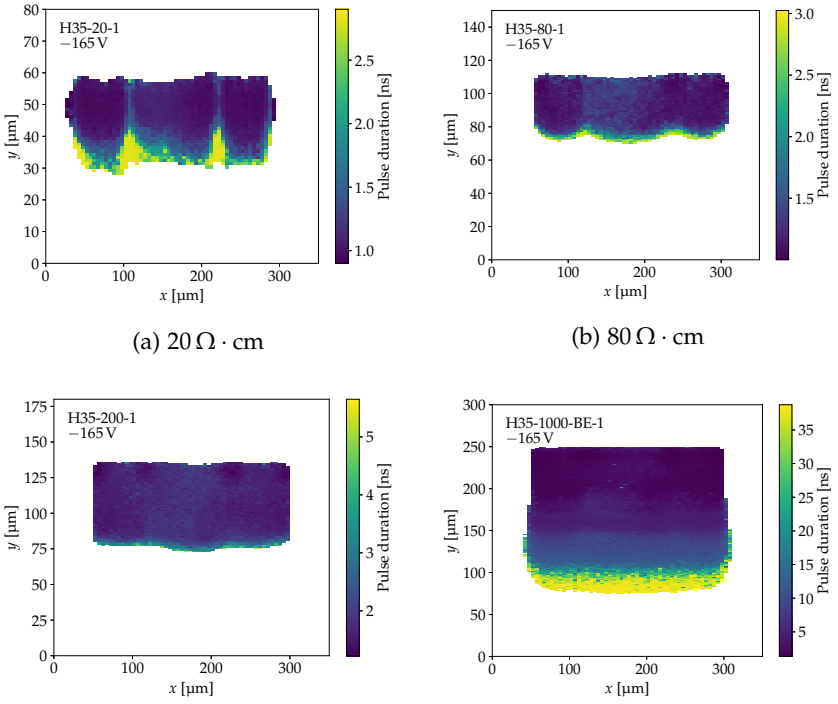

(a) 20 Ω · cm (b) 80 Ω · cm

(c) 200 Ω · cm (d) 1000 Ω · cm

Figure 4.28: The current pulse duration as a function of the position for the non irradiated H35DEMO samples.

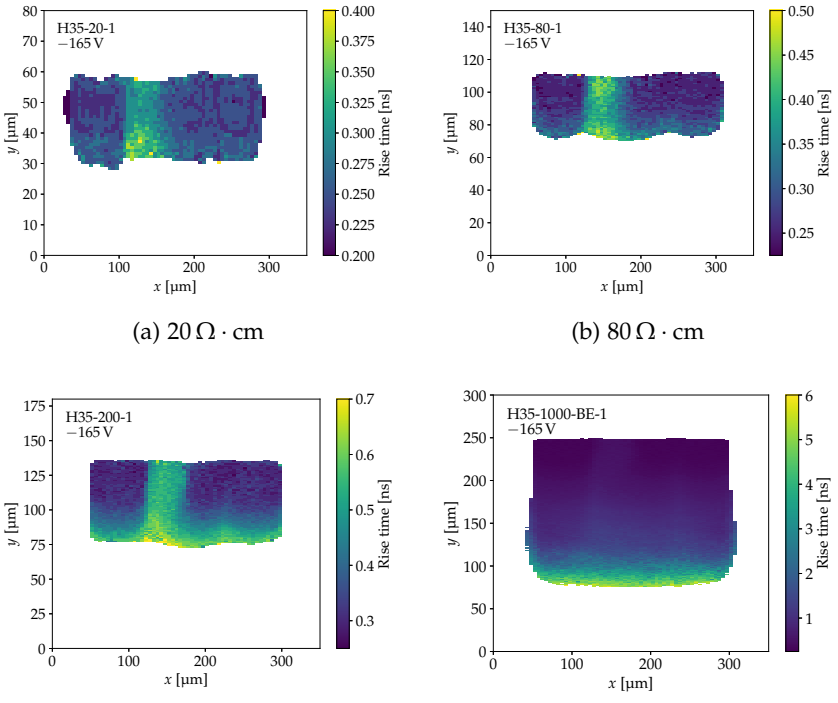

(a) 20 Ω · cm (b) 80 Ω · cm

(c) 200 Ω · cm (d) 1000 Ω · cm

Figure 4.29: The rise time of the current pulses as a function of the position for the non irradiated H35DEMO samples.

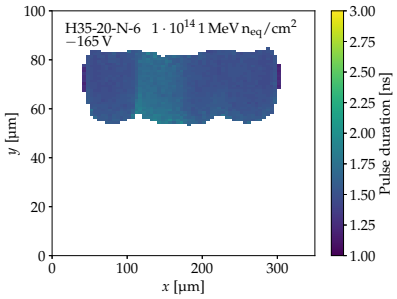

(a) $1 \cdot 10^{14}$ 1 MeV n_{eq}/cm^2

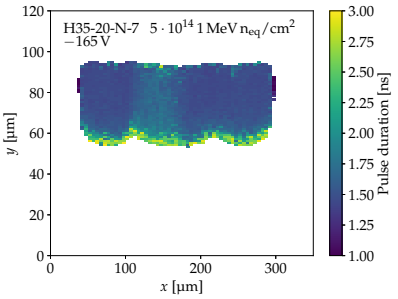

(b) $5 \cdot 10^{14}$ 1 MeV n_{eq}/cm^2

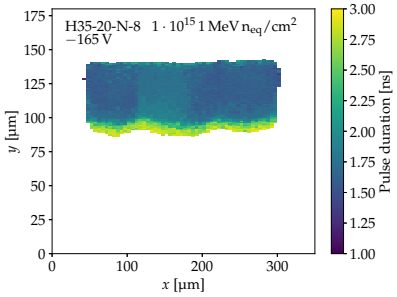

(c) $1 \cdot 10^{15}$ 1 MeV n_{eq}/cm^2

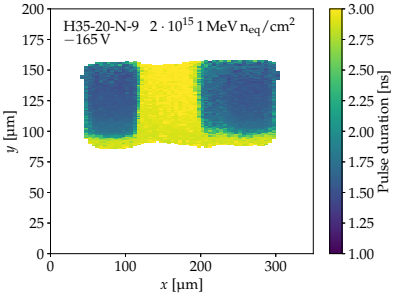

(d) $2 \cdot 10^{15}$ 1 MeV n_{eq}/cm^2

Figure 4.30: The duration of the current pulses as a function of the position for the neutron irradiated $20\,\Omega \cdot cm$ H35DEMO samples after the first annealing step.

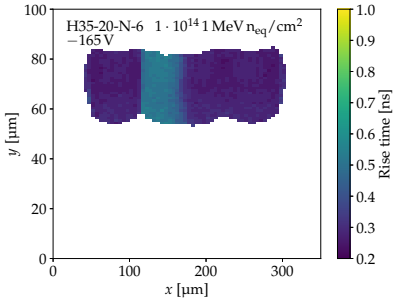

(a) $1 \cdot 10^{14}$ 1 MeV n_{eq}/cm^2

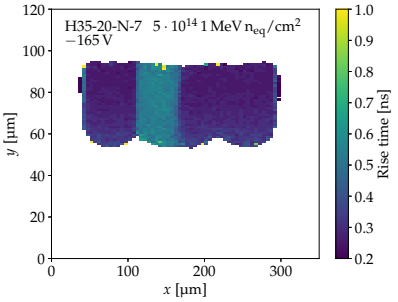

(b) $5 \cdot 10^{14}$ 1 MeV n_{eq}/cm^2

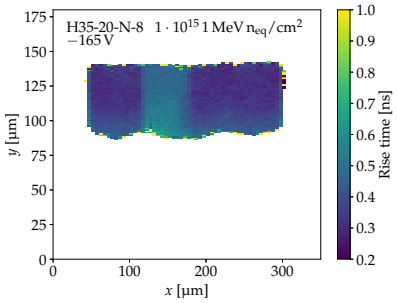

(c) $1 \cdot 10^{15}$ 1 MeV n_{eq}/cm^2

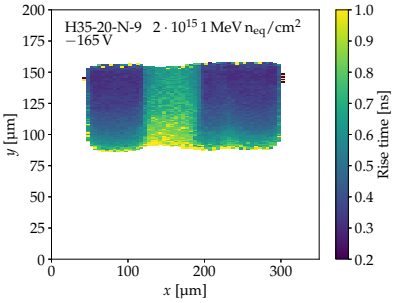

(d) $2 \cdot 10^{15}$ 1 MeV n_{eq}/cm^2

Figure 4.31: The rise time of the current pulses as a function of the position for the neutron irradiated $20\,\Omega \cdot cm$ H35DEMO samples after the first annealing step.

pulse duration of the signals, and a decrease in the trapping time, which has an opposite effect.

It can also be observed that irradiation enhances the effect of the "slow band" visible in the rise time plots before irradiation. This band is now visible in the pulse duration ones as well and has the most visible effect at the highest fluence. The reason of such an enhancement of this effect is not clear. Furthermore, this effects is reduced again after the following annealing steps, as shown in Figure 4.32.

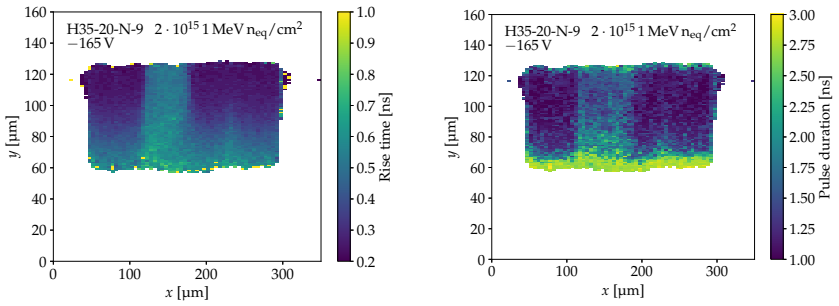

(a) (b)

Figure 4.32: The duration of the current pulses as a function of the position for the neutron irradiated $20\,\Omega \cdot$ cm H35DEMO samples after the second annealing step.

4.9 CONCLUSIONS

Transient Current Technique measurements have been carried out on the test structures of the H35DEMO prototypes. The study focused on the evaluation of the charge collection and of the evolution of the effective doping concentration after irradiation with three different sources (reactor neutrons, low energy protons and high energy protons). These studies have shown that the effective doping concentration decreases significantly after irradiation, reaching a minimum before increasing again. In most cases its value would remain lower to the one before irradiation up to the highest measured fluence of $2 \cdot 10^{15}$ 1 MeV n_{eq}/cm^2.

A decrease in the effective doping concentration translates in an increased depth of the depleted region of the detector, which can compensate the loss of collected charge due to the increased trapping. In the framework of the use of HV-CMOS sensors in ITk, these results are very promising, especially for the intermediate resistivities of 80 and $200\,\Omega \cdot$ cm: before irradiation they feature a good depletion depth, which increases after irradiation up to the end-of-life fluences of ITk ($\sim 1 \cdot 10^{15}$ 1 MeV n_{eq}/cm^2 for the outermost pixel layer). This is true for the $20\,\Omega \cdot$ cm samples as well, but before irradiation they feature a very small depleted region, which may worsen at fluences below $1 \cdot 10^{14}$ 1 MeV n_{eq}/cm^2. The effects of annealing have been studied on

neutron irradiated samples: it begins to become significant only after $5 \cdot 10^{14}$ 1 MeV n_{eq}/cm^2 and its behaviour follows the expected trend. A study on proton irradiated samples can be very useful to completely assess this phenomenon.

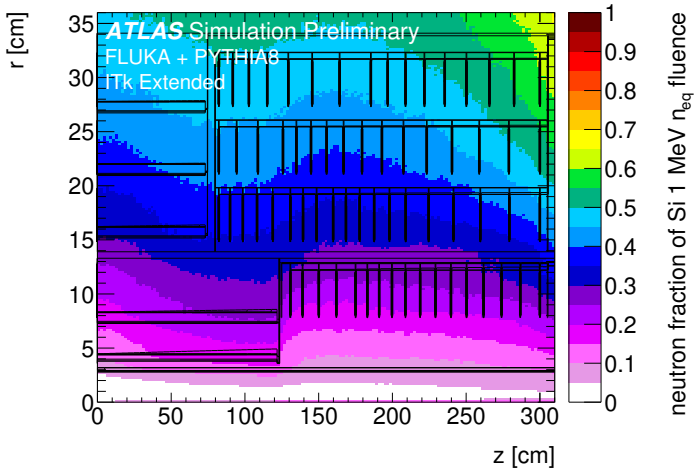

Figure 4.33: Neutron fraction in the particle fluence in the Phase II Pixel detector [123]. The neutron fraction is higher in the outermost layers because of the neutron albedo from the calorimeter.

Even if the general evolution of N_{eff} after irradiation with different particles is similar (decrease and then increase at high fluence), a significant difference in the effect of protons and neutrons is present. Acceptor removal appears to be slower when irradiating with neutrons, while the later acceptor introduction is more important, leading to an effective doping concentration several times larger than the one after proton irradiation. It is important to study both particles, since the expected damage in ITk will have contributions from both, as shown in Figure 4.33.

Great care must be taken, however, in extrapolating the effects of mixed irradiation from the effects of a single particle type: recent studies have shown that there are significant differences in the performance of a silicon detector after mixed irradiation (*i.e.* with protons followed by neutrons or vice-versa), with different annealing behaviour, depending on the irradiation sequence [124]. In the light of this, a better approach to study the expected detectors performance in the HL-LHC radiation environment would be to perform a simultaneous irradiation with protons and neutrons, but none of the facilities utilised for this work is able to perform it.

The characterization of the pulse shape has highlighted a possible influence from the implantation in the deep n-well of an HV-CMOS sensors, showing that they can increase the rise time and the duration of the current pulses. This influence varies with irradiation and with annealing and is not completely understood. This effect should not present an issue for an application of HV-CMOS detectors in the ITk

because the time scale of the current pulses is small compared to the timing requirements. It may become a concern, however, if fast HV-CMOS sensors, with time resolutions of the order of the nanosecond, will be developed in the future.

5 TESTBEAMS

Testbeams are a fundamental part of the characterization of a pixel detector: they are performed by placing the Device Under Test (DUT) in a particle beam, to reproduce the conditions that it would face in a real experiment, and by characterizing its performance with the aid of a beam telescope.

A beam telescope consists of several planes of position-sensitive detectors used to reconstruct the tracks of the particles crossing them: these tracks can then be extrapolated on the DUT plane and used to measure important parameters as the particle detection efficiency or the time and spatial resolution.

In this chapter the measurements performed on the analogue matrices of the H35DEMO and on the Simple matrix of ATLASPIX1 will be discussed, starting from the motivation, describing the experimental setup in details, along with the reconstruction software and the data analysis and finally presenting the results.

5.1 GOALS AND MOTIVATION

Pixel sensors designed for the ATLAS ITk must respect strict performance levels: the particle detection efficiency is required to be superior to 99% and can decrease to 97 % after the sensor has received a fluence close to the one expected at the end-of-life of the detector ($1 \cdot 10^{15}$ 1 MeV n_{eq}/cm^2 in the case of the outermost pixel layer) [43].

To asses the performance of HV-CMOS pixel sensors produced by ams AG, testbeam measurements have been carried out on H35DEMO and ATLASPIX1 prototypes in several campaigns. These studies have been fundamental to estimate their efficiency and timing performance and to identify flaws in the circuitry, addressed in subsequent designs.

The characterization of the H35DEMO analogue matrices, which contain six different pixel flavours, has allowed the determination of the best design approach for the analogue part of the pixels (charge sensitive amplifier and shaper), while the tests on the ATLASPIX1 have been fundamental to determine the performance of the full read-out circuitry.

Testbeam measurements have been performed on non-irradiated H35DEMO samples and on ATLAPIX1 samples before and after irradiation with protons and neutrons.

5.2 THE TESTBEAM FACILITIES

Testbeam campaigns have been carried out in two facilities: at the CERN Experimental Hall North 1 (EHN1), beam line H8, and at the Femilab Test Beam Facility (FTBF). They both feature high momentum hadron beams. In the following paragraphs these two facilities are described in more details.

5.2.1 *CERN EHN1*

The CERN EHN1 is part of the SPS North Area, which is one of the Secondary Beam Areas of the SPS accelerator. The different beam lines available in the North Area are produced by colliding the 450 GeV proton beam of the SPS onto three fixed targets (T2, T4 and T6), as schematically shown in Figure 5.1. Four beams (H2, H4, H6 and H8) are then delivered to the EHN1, while the remaining ones are used for experiments as COMPASS [125] and NA62 [126].

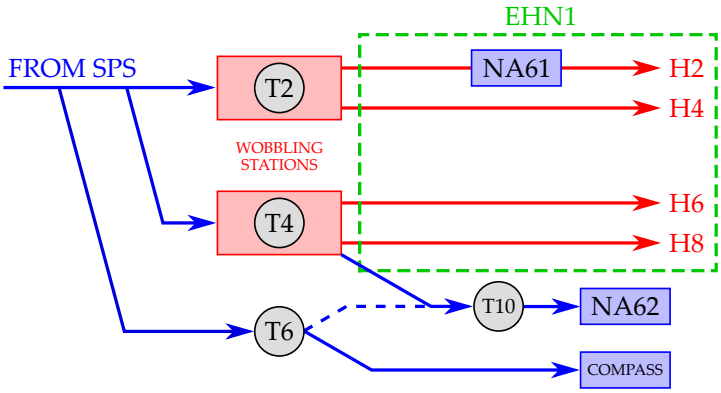

Figure 5.1: Sketch of the North Area beam lines. Adapted from [127].

Upon interaction with the targets, the protons produce a shower of particles, which are filtered and steered into the different beam lines. Electrons or hadrons (pions, kaons and protons) can be selected and their momentum can be tuned with a 2% accuracy. For the work described in this thesis, 180 GeV pions have been used.

The selection of beam momentum, charge and intensity is performed by the *wobbling stations*, which consist of several sets of dipoles, located before and after the target, in combination with a special thick collimator. The dipoles allow hitting the target at a specific angle and perform a selection of the particles emerging from it.

After this selection, the beams are delivered to the experimental areas, shown in Figure 5.2, by long and complex beam lines composed of several parts: dipole magnets are used to guide the particles through the tunnels towards the experimental areas, trims are small dipoles that allow the correction of the beam steering, quadrupoles help to control the beam size and dispersion and, together with adjustable

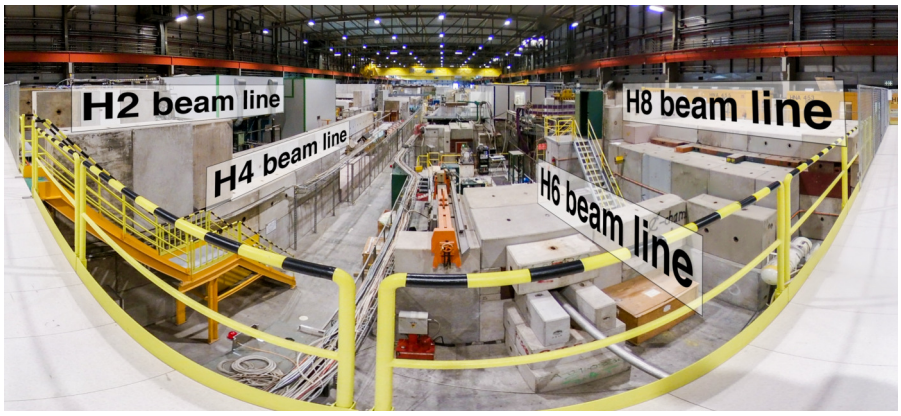

Figure 5.2: A picture of the four beam lines in EHN1. The measurements described in this work have been carried out in H8 [128].

collimators, they define the acceptance of the beam line in momentum and angle.

Several types of detectors allow checking the beam intensity and shape along the line. These detectors comprise scintillators, various types of wire chambers and filament scanners [129].

The beam is delivered to H8 in *super-cycles*, which depend on the requests from the users of the other beam lines, and usually last between 30 s and 60 s. Each super-cycle contains one or more spills, usually 4.8 s long.

5.2.2 *The Femilab Test Beam Facility*

During the winter shutdown periods of the CERN accelerator complex in 2017 and 2018, testbeam measurements have been performed at the Fermilab Test Beam Facility (FTBF) [130].

The Fermilab accelerator complex, shown in Figure 5.3, consists of several stages of increasingly higher energy. The acceleration chain begins with an ion source that feeds H^- ions to a 150 m linear accelerator (the Linac) that brings the protons to an energy of 400 MeV.

This is followed by the Booster, where the electrons are stripped and the energy is risen up to 8 GeV. This beam is either used for low-energy neutrino experiments or sent to the Main Injector, which accelerates the protons up to 120 GeV. From here, they can be delivered to high-energy neutrino experiments, muons experiments or to the FTBF.

In the FTBF there is the possibility to use the primary 120 GeV protons or to insert a target into the beam line to obtain a lower energy particles. For the measurement described in this work, the primary proton beam has been used.

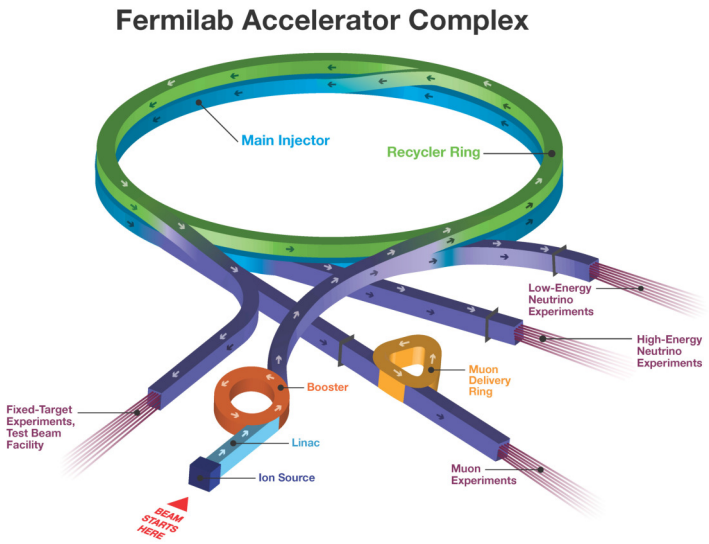

Figure 5.3: The Fermilab accelerators complex [131].

5.3 THE UNIGE FE-I4 TELESCOPE

The telescope used for the characterization of the H35DEMO and ATLASPIX1, the UniGe FE-I4 telescope [85], has been developed at the University of Geneva and it is based on six planar pixel modules, the same used in the ATLAS IBL (see Section 1.3.1).

It consists of several components necessary to position, power and monitor the telescope modules and the DUT, described in details in the following sections.

5.3.1 *The telescope modules*

The telescope modules are built around the planar pixel detectors modules used for the IBL upgrade in 2014. Each one of these consists of a 200 µm thick planar silicon sensor coupled, with bump bonds, to two FE-I4B ASICs. These modules feature a total of 160×336 pixels (each FE-I4B contains 80×336 of them) with pitch $50 \times 250\,\mu m^2$.

For the testbeams, only one of the two read-out ASICs was used, limiting the number of pixels on a plane to 80×336. This configuration was chosen because, since two of the telescope modules are rotated 90° as explained in the next section, using both ASICs would not increase the acceptance significantly (the FE-I4 is almost squared). Furthermore, the unused chip is kept as a backup in case of a failure of the first one.

The sensor assembly is mounted on a flexible PCB (the module flex) which contains the wire bonds, some passive components and a connector for power and data. This is then connected to an adapter PCB, to interface the power, control and data lines of the detector to the telescope data acquisition system. In particular, it features two

RJ-45 connectors for communication, a Molex connector for the low voltage power, a coaxial connector for the bias voltage and one for the hit-bus, a logical OR of all (or a subset of) the pixels discriminator output. The hit-bus signals of two the telescope modules are used in coincidence to generate the trigger, as explained in Section 5.3.5.

Each pixel can be individually connected to the hit-bus, allowing the creation of arbitrary complex Regions-of-Interest for the trigger. This is particularly useful when the DUT is small compared to the telescope sensors, for example in the case of the HV2FEI4 and CCPDv4 prototypes (see 3.2 on page 64), allowing the number of tracks crossing the DUT to be maximized.

The module flex and adapter PCB assembly are mounted on an aluminium support, to provide mechanical rigidity and to allow its installation on the support rail of the telescope. This aluminium support is opened in the detector region to reduce multiple scattering as much as possible. A plastic cover is used to protect the sensor assembly. The 3D rendering of a complete telescope plane is visible in Figure 5.4.

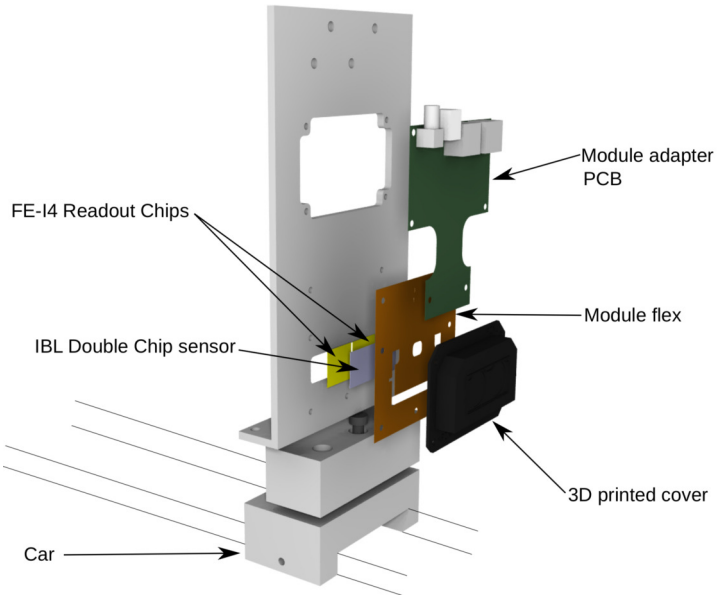

Figure 5.4: 3D render of a telescope plane [128].

5.3.2 *The telescope assembly*

The UniGE FE-I4 telescope features 6 modules arranged in two arms of three modules each: one placed upstream and one downstream with respect to the DUT (Figure 5.5). Since the pixels have a rectangular shape, the middle plane in each arm is rotated by 90° to have a comparable spatial resolution in the vertical and horizontal direction. The telescope planes are mounted on two 40 cm long and 35 cm tall

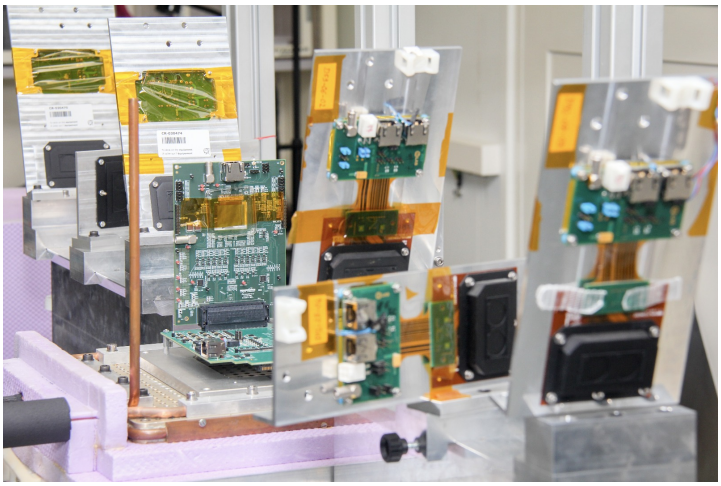

Figure 5.5: The six telescope planes with the DUT board placed between them [132]. A first version of the DUT box (open in this picture) is visible: the new version has a round shape to allow seamless rotations.

rails, with a moving stage system in the middle which allows a fine position and rotation adjustment of the DUT.

The DUT is placed in a dedicated insulated enclosure (the DUT box), mounted on the moving stages. It is designed to allow cooling the detector to below 0 °C, while keeping the humidity controlled to prevent frost and allow its operation. This enclosure is constituted of a metal base cooled by a pipe where cold silicone oil is circulated by a chiller. This base supports the DUT PCB and features an embedded gas inlet, which allows introducing and cool dry air or nitrogen. This system enables obtaining an air temperature of around −25 °C in the DUT box.

The rails and the stages are mounted on a 8″ optical breadboard, supported by four pressurized dampers, to isolate the telescope assembly from possible vibrations in the experimental area. In addition, an aluminium frame is present around the setup to facilitate the cables routing and a patch-panel is used to interface the telescope to the rest of the system, greatly simplifying the connection of the numerous cables required for the power, bias voltage, data, etc. The complete setup is visible in Figure 5.6.

The hardware needed to control, power and monitor the telescope and to communicate with the data acquisition PC, described in the following sections, is housed in a movable rack and connected to the telescope through the patch panel. A local telescope network is available for the communication between the DAQ PC and the rest of the system.

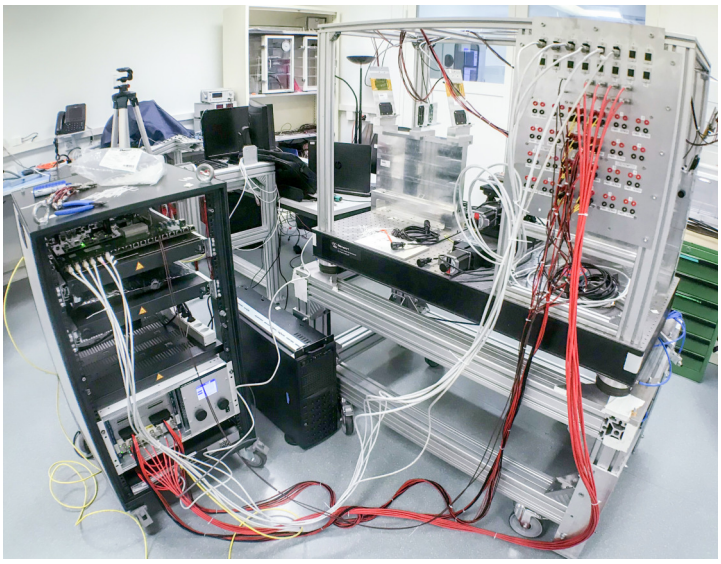

Figure 5.6: The telescope system assembled in the clean room at the DPNC for testing purposes [128].

5.3.3 *The power supplies*

The power supply system is needed to provide low-voltage (LV) power and the high voltages (HV) to to the telescope planes and the DUT. This functionality is provided by a MPOD mini-crate by Wiener: it consists of a 19″ rack-mountable chassis equipped with four power supply cards:

- one 8-channels ISEG EHS-8210n-F HV module is used for the sensor bias voltages. It can provide an output voltage of 1000 V, with a maximum current of 8 mA through SHV connectors.
- Two 8-channels WIENER MPV 8008D LV modules are used to provide the low-voltage power to the sensors. They can provide up to 8 V and 10 A per channel through two 37-pins sub-D connectors with 4 channels each (each channel features two power and two sense lines).
- One additional WIENER MPV 8210D LV module that can provide up to 120 V and 100 mA per channel, if a higher voltage is required.

The voltages and current limits can be set on a per-channel basis in all the four modules. The MPOD can be controlled locally, but it is normally controlled remotely by the DCS (Detector Control System) PC via Ethernet.

5.3.4 *The cooling system*

The DUT box is cooled by a Unistat 705 chiller by Huber. It is capable of circulating silicone oil in the cooling loop at a minimum temperature of $-75\,^{\circ}\mathrm{C}$ and is controlled by a RS-232 serial interface by the DCS PC. It allows reaching a temperature of $-25\,^{\circ}\mathrm{C}$ in the air inside the DUT box and of $-15\,^{\circ}\mathrm{C}$ on the DUT board.

The temperature and humidity in the enclosure and the temperature of the DUT board are continuously monitored with a Yocto-Meteo-V2 by Yoctopuce and with a PT-104 by Pico Technology to ensure that no dew or frost can form on the boards and that the measurement is running in known and controlled conditions.

5.3.5 *The data acquisition system*

The Data Acquisition (DAQ) is based on the HSIO-II [133] and on the CaRIBOu [134] systems. The former is used for the read-out of the FE-I4 based sensors (the telescope planes and the H35DEMO), while the latter is used for the ATLAPIX1 (and to power and configure the H35DEMO).

HSIO-II

The HSIO-II system, visible in Figure 5.7, has been developed at SLAC to operate FE-I4 based detectors [133]. It is located in the rack close to the telescope assembly and is connected to the DAQ PC with a standard Ethernet interface. It is used to read-out the telescope planes and the FE-I4 capacitively coupled to the H35DEMO chip. The HSIO-II is based on a Xilinx Artix 200 FPGA, which implements the low-level command and data protocols to communicate with the FE-I4 ASICs, sending the commands and buffering the data received from them. Furthermore, it generates the clock and trigger signals sent to the detectors front-ends.

The HSIO-II board contains several coaxial connectors that are used for triggering purposes. Two of them receive the hit-bus signal from the first and last telescope planes to generate the trigger, which can be relayed to the DUT with a third connector. A fourth one can be configured as a *busy* input which prevents the HSIO-II from generating further triggers (it is useful, for example, when the DUT is processing the data and cannot accept a trigger). The board is connected to the detectors trough the *CosmicBoard* adapter, which interfaces to the FE-I4 ASICs trough RJ-45 connectors.

The HSIO-II FPGA is interfaced to the Data Transport Module (DTM) trough high-speed GTP interfaces. This module, based on a Xilinx Zynq XC7Z030 System-on-Chip (SoC) and running a Linux-based real-time operating system, performs a higher-level processing

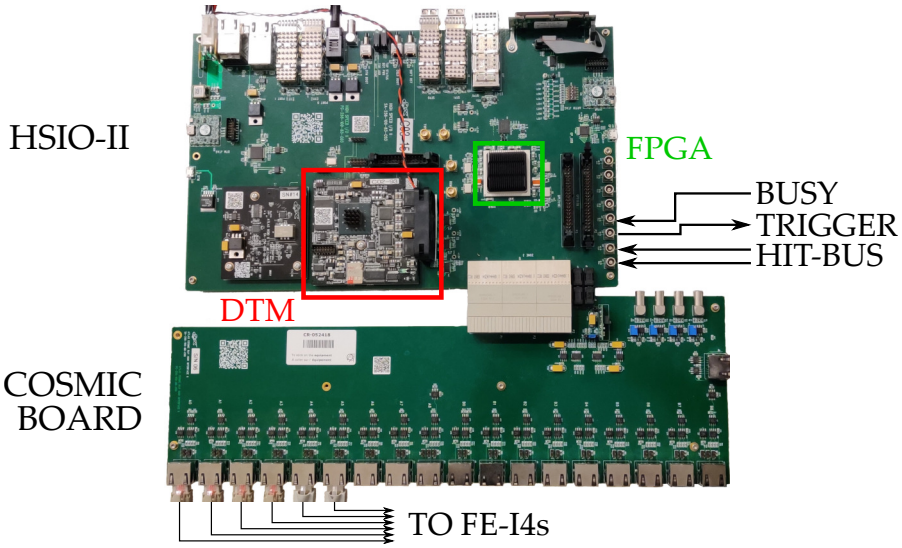

Figure 5.7: The HSIO-II board connected to the "CosmicBoard".

of the data received from the front-ends and allows the communication between the DAQ PC and the Artix 200 FPGA.

The HSIO-II is controlled by the DAQ PC, which is a standard computer running a Linux-based OS, trough two tools: `calibGui` and `cosmicGui`. `calibGui` is used to perform the calibration and tuning of the FE-I4 modules: it allows testing the functionality of the analogue and digital parts of the ASICs and performing scans to calibrate the discriminator thresholds and ToT response of each chip. This calibration is performed prior to data taking, to ensure that all the front-ends have a uniform response and are working in optimal conditions. The front-ends configuration determined by `calibGui` is saved on disk and retrieved by `cosmicGui` for data taking.

The `cosmicGui` tool is used to configure the trigger and to acquire data. It allows setting up the desired trigger scheme, the configuration of parameters as the front-end latency, the trigger delay and the read-out window duration and starting and stopping the data acquisition. The data, along with the current telescope configuration is saved on a per-run basis.

CaRIBOu

Several HV-CMOS prototypes, with different requirements in terms of resources needed for their operation and read-out, have been characterized. To simplify these studies, CaRIBOu (Control and Read-out for ITk Board), an open-source modular system to provide the resources needed by these prototypes, has been developed in a collaboration between the Brookhaven National Laboratories, the University of Geneva and CERN [134].

It consists of both hardware and software parts. The hardware configuration used in this work is composed by a Xilinx SoC ZC706

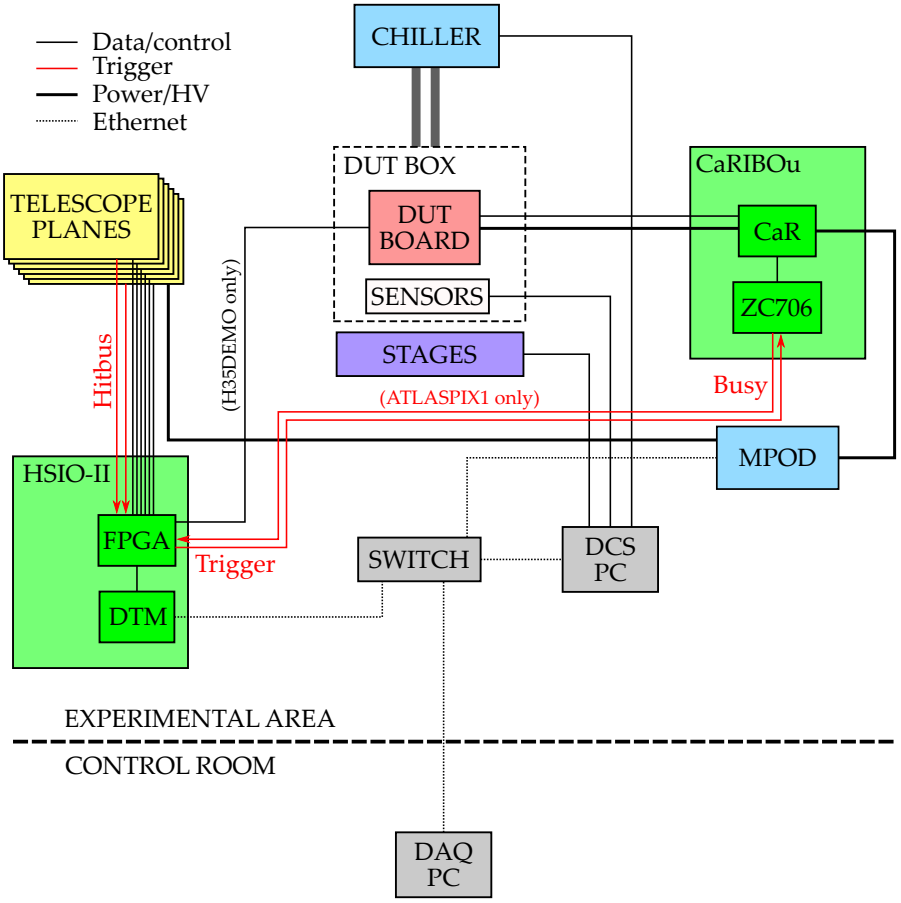

Figure 5.8: Schematic of the telescope assembly.

Evaluation Kit, featuring the Zynq-7000 FPGA and a dual core ARM Cortex-A9 processor, by the Control and Read-out (CaR) board and a custom DUT board, to host the device under test.

The Zynq-7000 SoC runs a customized Linux distribution [135] on the processor and a custom firmware on the FPGA. A dedicated software called Peary [136] provides hardware abstraction to control the CaR board components, to configure the DUT and to run the data acquisition. The ZC706 can be connected to the CaR board through a FMC connector and to the local network of the telescope, for communication with the DAQ PC.

The CaR board (Figure 5.9) is a custom PCB designed to provide several power rails and data lines to the DUT boards. It features 8 general purpose power supplies (0.8–3.6 V, 3 A) with voltage/current monitoring, 8 SERDES (serializer-deserializer) links, 16 14-bit ADC channels, 4 charge injection channels, a clock generator and several CMOS data lines and LVDS pairs. It is designed to be connected to the FMC connector of the ZC706 and is interfaced to the custom DUT board through a Samtec SEAF 320-pins connector.

The custom DUT boards are designed to allow a specific ASIC to be connected to the CaR board and to communicate with the DAQ

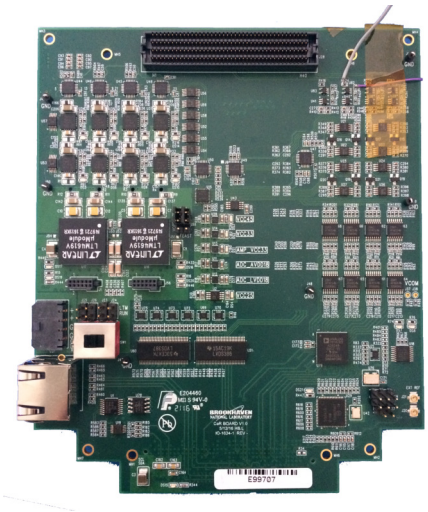

Figure 5.9: The CaR board [128].

system. Two boards have been developed, one for the H35DEMO and one for the ATLASPIX1. Since the H35DEMO is coupled to a FE-I4 chip to be read out, the data taking is managed by the telescope DAQ system, while the CaRIBOu system takes care of the configuration and power of the H35DEMO. In the case of ATLASPIX1 the CaRIBOu system is used to power, configure and read out the DUT.

5.3.5.1 *The trigger systems*

The trigger scheme used during data taking depends on the DUT. The trigger signal is normally generated by the coincidence of the two hit-bus lines from the first and last telescope planes.

When a trigger is generated, the HSIO-II reads out the hits recorded by the telescope planes in a time interval dependent on the front-end latency, the trigger delay and the read-out window set using the `calibGui` tool.

For the measurements of the H35DEMO, being coupled to a FE-I4 chip, it is read out together with the telescope planes, allowing for a seamless integration in the setup.

The ATLASPIX1, instead, being read out by the CaRIBOu system, implements the so-called trigger/busy scheme: the trigger signal is generated by the HSIO-II, as described above, and it is sent to the CaRIBOu system. This raises the busy flag, which prevents the telescope from acquiring more triggers until it has completed the read-out of the data.

5.3.6 *The Detector Control System software*

The Detector Control System (DCS) includes the the moving stages, the MPOD mini-crate and the cooling. The DCS is managed by a dedicated PC using a custom interface, developed using LabVIEW.

This software runs on the DCS PC hosted in the telescope rack and can be controlled remotely by the DAQ PC, allowing the user to position the stages, to set the voltages and current limits of the power supplies, to setup and operate the chiller and to monitor the temperatures and humidity inside the DUT box.

In the last testbeam campaign part of the DCS software has been re-implemented using Python, to enable easier maintenance and extension, but also to limit the dependence on proprietary software. At the time of writing, this software, called `minidcs` [137], can control the chiller, monitor the ambient conditions and log them, along with the beam information in EHN1.

5.3.7 *Performance of the UniGE FE-I4 telescope*

The UniGE FE-I4 telescope has been characterised at the CERN EHN1 H8 beamline in 2014 and 2015, where it has been used to test small-area and full-size FE-I4 sensors. In particular, the trigger rate and spatial resolution have been assessed.

The trigger rate has been measured to be 18.3 kHz in absence of a DUT and 5.7–6.3 kHz depending on the DUT readout window, the DUT size and the use of a trigger RoI in the telescope planes.

The spatial resolution has been estimated to be 11.7 µm in the x direction and 8.3 µm in y at the DUT position (between the two arms). The difference in the two directions is caused by having two planes rotated 90°. The main contributions to the spatial resolution comes from the telescope geometry (the relative position and rotation of the planes), the pixels size and the contribution of multiple scattering (which is negligible for the beams used for this work) [85].

5.4 THE RECONSTRUCTION SOFTWARE

Before performing the data analysis, the beam particle tracks must be reconstructed. Starting from the hits recorded by the telescope, an algorithm identifies in each plane the hits belonging to a track and a fit is performed to obtain the track parameters. Each track is then extrapolated on the DUT plane and an association with the hits recorded by the DUT is attempted.

This process requires an initial preprocessing to remove noisy pixels and to calculate the exact geometry of the setup, *i.e.* the position and rotation of each module. The full reconstruction chain is schematically shown in Figure 5.10. These steps are handled by the Proteus soft-

ware [138], an open-source framework written in C++ and composed of tools that handle the different reconstruction steps. These tools are described below, along with the necessary configuration files.

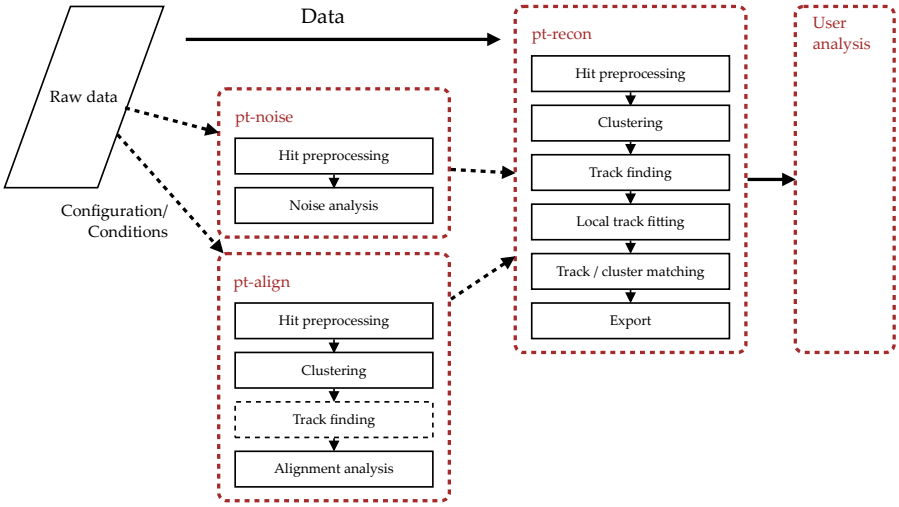

Figure 5.10: The Proteus reconstruction flow [139].

Before proceeding, it is useful to define the coordinate systems and the data structure used within Proteus. The global coordinate system xyz is defined with the z axis along the beam direction, the y axis pointing upwards and the x axis pointing horizontally in the direction that forms a right-handed coordinates system.

Local coordinates systems uvw are defined for each sensor, with u and v being along the columns and rows of pixels respectively and w being perpendicular to the surface, forming again a right-handed coordinates system. Rotations are defined in the local coordinates: α, β and γ are the rotations angles around u, v and w respectively and, given the three angles, they are performed in the $\gamma \rightarrow \beta \rightarrow \alpha$ order.

The data processed by Proteus is structured in events: one event corresponds to a trigger and contains the hits recorded by each sensor. Events are identified by an ID and a timestamp. Each hit is described by its position (column and row), Time-of-Arrival (ToA, defined relative to the event timestamp) and Time-over-Threshold (ToT).

Proteus groups the hits generated by the same particle in clusters: a cluster is identified by its position, ToA and ToT and retains the information of the hits that compose it. Tracks are identified by the parameters to describe their trajectory (*e.g.* position and slope, in the case of straight lines) and the reduced χ^2 obtained by the fit. They can have an associated cluster.

5.4.1 *The configuration files*

The reconstruction is set-up using three main TOML [140] configuration files: device, analysis and geometry. The device configuration file defines the types of sensor used in the setup, in terms of their number of columns and rows, pixel pitch, etc. and lists the sensors used in the setup. The geometry one specifies the position and rotation of each sensor listed in the device file. The analysis file specifies the configuration of each step of the reconstruction chain, as mentioned in the following paragraphs.

In addition mask files can be used: they list the pixels that have to be ignored by the reconstruction chain. They are produced during the noise-scan, but can be generated manually as well.

5.4.2 *Noise-scan*

The `pt-noise` tool performs a noise-scan on the telescope planes and DUT: this is aimed to identify noisy pixels and mask them in the subsequent analysis steps. This identification is based on the occupancy of each pixel, defined as the average number of hits per event.

The noise-scan consists of two steps. First of all, the software looks for pixels with an occupancy greater than a threshold defined in the analysis configuration file. This is needed to mask pixels with a very high occupancy, compared to the remaining ones, that could affect the results of the second step.

The second step is based on the calculation of the expected occupancy of each pixel, based on the neighbouring ones, using a kernel density estimator to cope with non-uniform beam profiles. The local significance, calculated as $\frac{O_{\text{obs}}-O_{\text{exp}}}{\sqrt{O_{\text{exp}}}}$ (O_{obs} and O_{exp} are the observed and expected occupancies respectively), is used as discriminating variable to determine the noisy pixels (the cut is defined in the analysis configuration file). The masks produced by the noise-scan are then used in the following steps of the reconstruction.

5.4.3 *Clustering*

Clusters are identified by Proteus with a process that starts with a seed hit and iteratively groups all the connected ones. When no more connected hits are found, it continues with a new seed hit, grouping the remaining ones, until all of them are assigned to a cluster.

The position of the clusters can be calculated in different ways. The most basic method (binary clustering) consists in calculating the barycentre of the hits as shown in Figure 5.11a (this method was used for the CCPDv4 and HV2FEI4). If the hits contain charge information,

like the ToT, the determination of the position of the cluster can be improved by weighing each hit position with the collected charge (centre-of-gravity clustering, see Figure 5.11b). This method is used for the telescope planes and the DUTs discussed in this work.

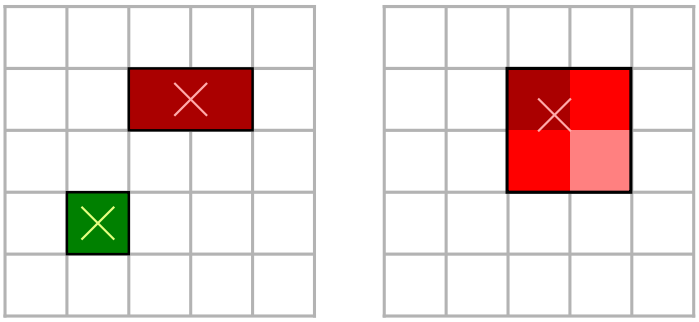

(a) (b)

Figure 5.11: Schematic representation of (a) binary clustering and (b) centre-of-gravity clustering. In the former the cluster position (indicated with $\times$) is calculated as the barycentre of the hits, while in the latter, it is weighed with the collected charge [139].

Each cluster is assigned a ToA and ToT as well: in this work, the ToT is defined as the sum of the time-over-threshold of each hit, while the ToA is the minimum time-of-arrival of the hits that compose the cluster.

5.4.4 *Alignment*

The alignment step, performed by the `pt-align` tool, is necessary to calculate the position and rotation of the telescope planes and of the DUT as precisely as possible, along with the beam parameters (slope and divergence). This tool must be provided with an initial geometry configuration file, with an estimation of the position and rotation of each plane.

The alignment is normally articulated in two steps, performed separately for the telescope planes and the DUT. The first step is a coarse alignment, but is very robust, while the second is finer, but requires a better initial geometry. In the first step, the residuals between clusters of subsequent planes are calculated in the x and y directions and used to correct the position of each plane with respect to the previous one (the first plane is normally kept as a fixed reference). This procedure can correct for misalignment in x and y.

The second step is more complex and is based on a preliminary reconstruction of tracks using a limited number of events. The correction are calculated by minimizing the tracks χ^2 as a function of the geometry parameters, to converge to the final position estimation. This procedure can in principle calculate corrections in the six degrees

of freedom and automatically determines whether any of them is not reliable.

In the analysis performed for this work, the first and last planes are kept fixed to limit the weak modes, *i.e.* variations of a coordinate that does not result in a significant variation of the χ^2. Since the trajectories of the beam particles are almost parallel, if the algorithm tries to perform corrections along z, it can result in an unstable behaviour. For this reason, corrections along z are automatically ignored by Proteus.

The alignment procedure produces an updated geometry file to be used in the following reconstruction step.

5.4.5 *Track reconstruction*

After having masked the noisy pixels and aligned the sensors, the track reconstruction is performed by the `pt-recon` tool. This tool works on the clusters by identifying the ones belonging to the same track with a combinatorial Kalman filter and performing a fit to obtain the track parameters, such as its position and slope.

In this work tracks are fitted with straight lines since the energy of the beams is high enough to make multiple scattering on the various planes negligible. However, if multiple scattering is not negligible, it is possible to use the GBL (General Broken Lines) fitter, which accounts for this effect [141].

After having calculated the tracks, Proteus tries to associate them to the corresponding clusters in the DUT by determining all the possible combinations of tracks and clusters in each event and selecting the best ones among them, based on the distance. The results are saved in a ROOT file containing the clusters with the matched track, if available, and the tracks that have not been matched to any cluster. This file is then used for the data analysis, as explained in the Section 5.6.

5.5 MEASUREMENT CAMPAIGNS

Several testbeam campaigns have been carried out to characterize the H35DEMO and ATLAPIX1 prototypes, both at the CERN EHN1 and at the FTBF. Each sample has been tested in multiple configurations, with different bias voltages and discriminator thresholds to determine the optimal working point.

5.5.1 *H35DEMO*

The two analogue matrices of the H35DEMO, described in Section 3.3 on page 69, have been characterized: their pixels contain a preamplifier and a shaper, connected to a pad.

The H35DEMO samples have been capacitively coupled to FE-I4 ASICs with a thin layer of epoxy (Araldite 2011), using an Accµra 100

flip-chip bonder. The glue is automatically dispensed on the pad columns of the H35DEMO (Figure 5.12a) and then the two chips are aligned and coupled. The H35DEMO/FE-I4 assembly is then glued and wire bonded to the dedicated DUT board (Figure 5.12b).

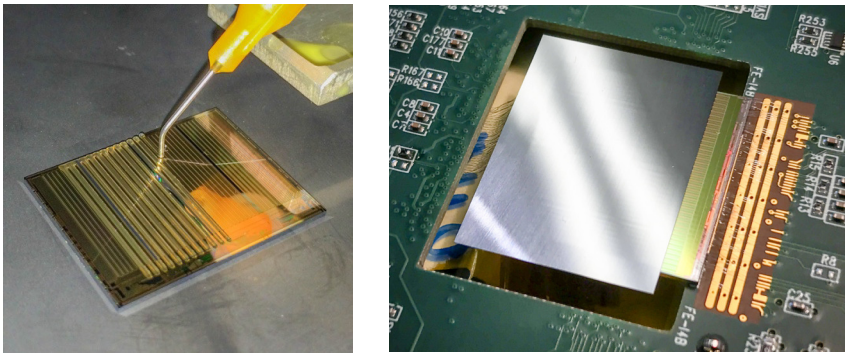

(a) (b)

Figure 5.12: (a) Deposition of epoxy on the H35DEMO matrix by the automatic glue dispenser of the Accµra 100. (b) The H35DEMO/FE-I4 assembly glued and wire-bonded to the DUT board [142].

Four samples, of resistivity 80, 200 and 1000 $\Omega \cdot$ cm have been tested at different working points, summarized in Table 5.1.

Table 5.1: Summary of the testbeam measurements performed on the H35DEMO prototypes.

Resistivity [$\Omega \cdot$ cm]	Matrix	Bias voltage [V]	FE-I4 threshold [e]
80	Analogue 2	0–160	1500, 2000
200	Analogue 1	0–160	2500, 3000, 4000
200	Analogue 2	0–140	2000, 2500, 3000, 4000
1000	Analogue 1	0–160	1500, 2000, 2500, 3000

The read-out is performed by the HSIO-II board. The CaRIBOu system is used to power the H35DEMO/FE-I4 assembly and to configure the H35DEMO.

The read-out chain is shown in Figure 5.13: each H35DEMO pixel contains a charge sensitive amplifier, a shaper and is capacitively coupled to a FE-I4 cell, containing an amplifier, the discriminator and the rest of the digital read-out circuitry.

The value of the coupling capacitance has been simulated and it resulted 3.5 fF per pad. From the simulation of the signal in the H35DEMO [89], it is possible to find a relation between the charge collected by the sensor and the corresponding threshold value on the FE-I4: a threshold of 2000 e on the FE-I4 corresponds to a 1500 e signal

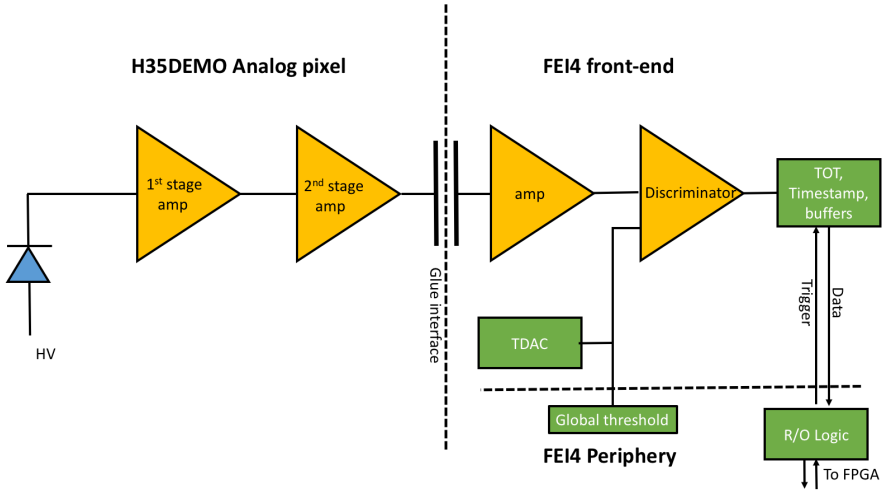

Figure 5.13: Readout chain of the H35DEMO prototype capacitively coupled to the FE-I4 ASIC [142].

on the H35DEMO. In the results, shown later in Section 5.7, the FE-I4 threshold is quoted.

5.5.2 *ATLASPIX1*

The Simple matrix of the ATLASPIX1, described in Section 3.4.1 on page 75, has been characterized. It is read out in a trigger-less fashion, *i.e.* all hits are transmitted to and buffered on the ZC706 board of the CaRIBOu system, used for configuration and read-out.

A trigger/busy scheme is implemented: when a trigger from the telescope arrives, the CaRIBOu system raises the busy flag and saves the hits recorded in a defined time interval to permanent storage. After this operation is complete, the busy flag is released and new triggers can be accepted.

Four different samples of resistivity $200\,\Omega \cdot \mathrm{cm}$, from two different production batches, have been characterized. Samples from Batch 1 had a production problem with one of the metal layers and, despite being functional, they were not guaranteed by the foundry to work as expected. This issue has been corrected in Batch 2.

Two of the samples have been tested after irradiation with neutrons at JSI up to a fluence of $1 \cdot 10^{15}$ 1 MeV $\mathrm{n_{eq}/cm^2}$, two of them before and after irradiation with protons at the Bern Cyclotron. The latter have been irradiated while operating them, to reproduce the radiation damage to electronics expected in an experiment as closely as possible (this damage is more important if an electric field is present in the oxide, as explained in Section 2.4.2 on page 58).

These samples have been characterized at different working points, summarized in Table 5.2.

Table 5.2: Summary of the testbeam measurements performed on the ATLASPIX1 prototypes.

Sample	Batch	Bias Voltage [V]	Threshold [e]	Fluence [1 MeV n_{eq}/cm^2]
A09	1	25–60	543–1482	0
		10–58	741–1482	$1 \cdot 10^{14}$ (p 16.7 MeV)
		75–90	741–1729	$1 \cdot 10^{15}$ (p 16.7 MeV)
JN03	1	35–90	741–1729	$1 \cdot 10^{15}$ (reactor n)
JN04	1	35–90	741–1729	$1 \cdot 10^{15}$ (reactor n)
W23-S10	2	25–75	790–1482	0
		40–90	642–1729	$5 \cdot 10^{14}$ (p 16.7 MeV)

5.6 DATA ANALYSIS

5.6.1 *Preliminary characterization*

Before bringing the sensors to a testbeam, a preliminary characterization is performed: the IV (current-voltage) characteristics of the sensors is measured in a probe station. Later, the sensor is mounted on the PCB and its functionality is validated in more details, verifying that it is possible to configure the detector and read it out.

In the case of ATLASPIX1, a threshold calibration is performed with a X-ray radioactive source: the hit rate at different discriminator thresholds is measured and, knowing the energy of the photons, it is possible to associate a threshold in mV to the photons energy deposition, measured in electrons. In addition, the threshold dispersion is estimated by using the charge injection on one pixel at a time and performing a threshold scan.

5.6.2 *Event selection*

The testbeam data analysis has been performed using the data files generated by Proteus, containing the reconstructed tracks and the corresponding matched clusters on the DUT.

As a first step, an event selection based on tracks is performed: each event is required to contain exactly 1 track, passing through the DUT, composed of a cluster on each of the six telescope planes and with a reduced χ^2 smaller than 5. This cut has an efficiency of $\sim$96% on average, meaning that $\sim$4% of the recorded events are discarded.[1]

1 This efficiency has been calculated after selecting the tracks passing through the DUT.

Furthermore, a cut is applied on the cluster-track distance: 250 µm in both directions for the H35DEMO, 260 µm in u and 200 µm in v for the ATLASPIX1. The events that do not pass this cut are not discarded, but contribute to the calculated efficiency.

The analyses described in the following sections utilize the data filtered with this selection.

5.6.3 *Cluster size and timing*

The distribution of the Time-of-Arrival (ToA) of the clusters in the sensor is an important indication of its time resolution. The ToA is defined as the difference between the timestamp of a cluster on the DUT and the timestamp of the corresponding track. In the case of the FE-I4 telescope used for these studies, the track time resolution is 25 ns.

The cluster size is evaluated as well: defined as the number of hits composing a cluster, it gives information about the charge sharing between pixels and is related to the spatial resolution of the DUT.

5.6.4 *Residuals and spatial resolution*

Residuals Δ_u and Δ_v are defined as the difference between the u and v positions of a track and the corresponding cluster. They are an important control of the quality of the alignment and give an indication of the spatial resolution of the DUT. If the resolution is dominated by the pixel size, like in the case of the H35DEMO and ATLASPIX1 (see Sections 5.7.2 and 5.8.3), this distribution is expected to reproduce the ideal response of a pixel (a box function with a width W equal to the pixel pitch), smeared by the finite reconstruction resolution and possible edge inefficiencies, modelled as a Gaussian with standard deviation σ:

$$f(\Delta_{u/v}) = \frac{A}{4} \operatorname{erfc}\left(-\frac{\Delta_{u/v} - C + 1/2W}{\sqrt{2}\sigma}\right) \operatorname{erfc}\left(\frac{\Delta_{u/v} - C - 1/2W}{\sqrt{2}\sigma}\right) \tag{5.1}$$

where A is the amplitude, C is the centre of the distribution, which is $\sim$0 if the alignment is performed correctly.

If W is compatible with the pixel pitch, σ represent the tracking resolution, otherwise it also contains a contribution from edge effects.

5.6.5 *Efficiency and in-pixel efficiency*

The particle detection efficiency of a pixel detector is defined as the ratio between the number of particles detected and the ones that have crossed it. In this case, the number of crossing particles is given by

the number of reconstructed tracks, so the efficiency is calculated as the ratio between the number of tracks with an associated cluster and the total number of tracks.

The excellent UniGE FE-I4 telescope tracking resolution allows the study of possible inefficiencies determined by the position of the track within each pixel: in this case all the groups of 2×2 pixels of the DUT are combined together and divided in $10 \times 10\,\mu m^2$ bins, in so-called in-pixel efficiency distributions. The efficiency in each bin is then calculated as described above.

5.7 H35DEMO RESULTS

5.7.1 *IV characterization*

The IV curves for sensors of the different resistivities under study are shown in Figure 5.14. The 80 and $200\,\Omega \cdot cm$ samples show a low leakage current, well below $1\,\mu A/cm^2$ at all temperatures, and feature a breakdown voltage of $\sim$180 V.

The $1000\,\Omega \cdot cm$ sample presents an early increase of the leakage current at a bias voltage of 30 V. While this was initially mistaken for an early breakdown, further measurements have shown that a plateau is reached before a second increase in current at 180 V, corresponding to the real breakdown.

This is known as the Rise-And-Flatten (RAF) effect: the additional leakage current is caused by a surface current generated in other unbiased test structures of the H35DEMO, located at the periphery of the chip, when reached by the depletion zone, larger laterally for the higher resistivity substrate [144].

To better understand the RAF effect, an Arrhenius plot, showing the leakage current at a given bias voltage as a function of the inverse of the absolute temperature, was extracted from the data (Figure 5.14d).

The leakage current I generated in the bulk of the sensor follows the Shockley-Read-Hall (SRH) model of generation-recombination of thermal carriers in a silicon bulk [143] and can be parametrized, as a function of the temperature T, as:

$$I(T) \propto T^2 e^{-\frac{E_{\text{eff}}}{2k_B T}}, \tag{5.2}$$

where k_B is the Boltzmann constant and $E_{\text{eff}} = 1.21\,\text{eV}$ is the effective energy for the current generated through a mid-gap level [145]. A deviation from this parametrization implies that part of the leakage current is not generated in the bulk.

Figure 5.14d confirms that the greatest part of the leakage current, at bias voltages where the RAF effect is present, is not generated in the bulk of the sensor, since it deviates from the SRH model.

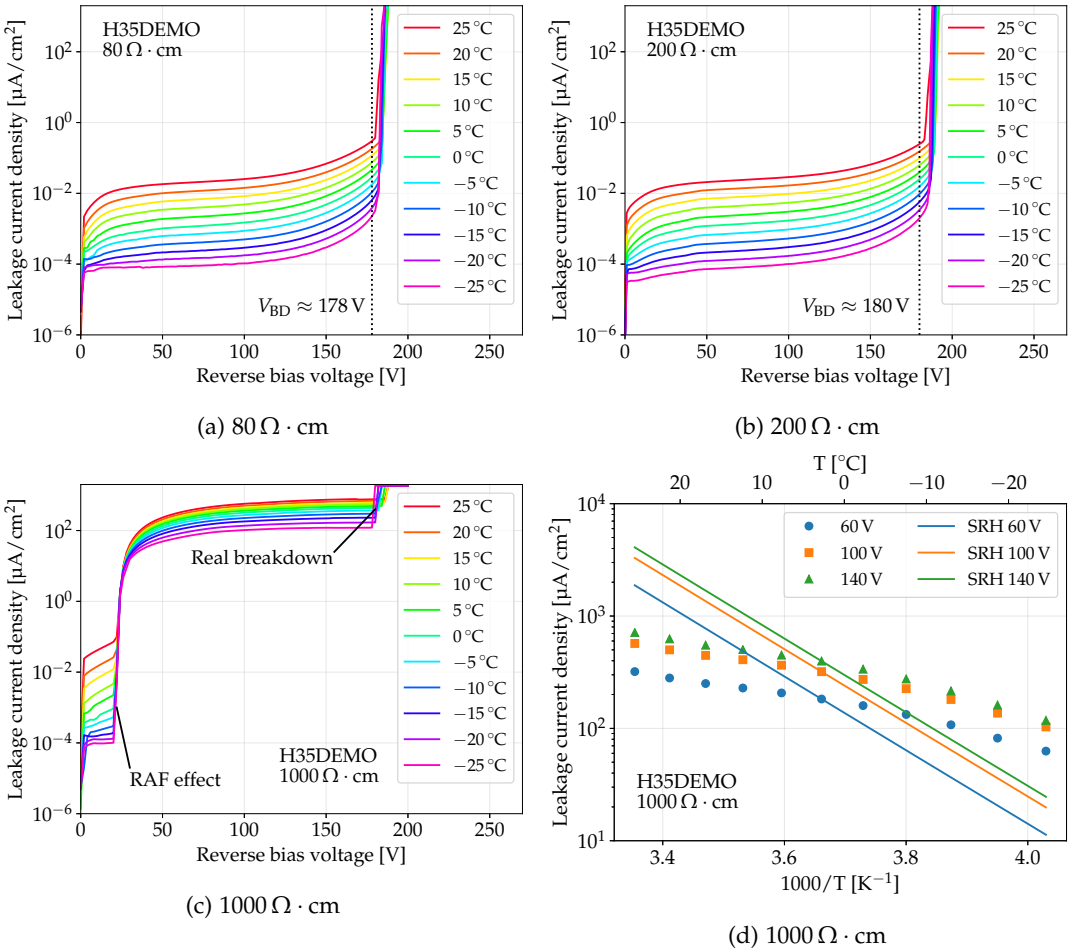

(a) 80 Ω · cm

(b) 200 Ω · cm

(c) 1000 Ω · cm

(d) 1000 Ω · cm

Figure 5.14: IV curves at different temperatures for samples of resistivity (a) 80 Ω · cm, (b) 200 Ω · cm and (c) 1000 Ω · cm. (d) The Arrhenius plot for the 1000 Ω · cm sample is shown as well, along with the Shockley-Read-Hall (SRH) model prediction [142, 143]. The Arrhenius plots for the other samples follow the prediction and are not shown.

5.7.2 *Cluster size and spatial resolution*

In Figure 5.15 the distributions of the cluster size for the high-gain sub-matrix are shown. They are representative of the other sub-matrices as well. Due to the relatively large size of the pixels ($50 \times 250\,\mu m^2$), compared to the depletion depth (25–180 µm, see Figure 4.21 on page 106), the greatest part of the clusters have size 1.

The tail of the distribution of the 1000 Ω · cm sample, which features the widest depletion region, is larger at the intermediate bias voltage of 80 V, compared to 20 V and 160 V (Figure 5.15c). This fact can be explained by the presence of two competing phenomena: with the increase of the bias voltage the depletion-region depth increases, allowing charge to be collected deeper inside the bulk, which takes more time to drift to the collecting electrodes, increasing the probability to diffuse laterally and inducing a signal in the neighbouring pixels. The higher bias voltage, however, also increases the drift speed, reduc-

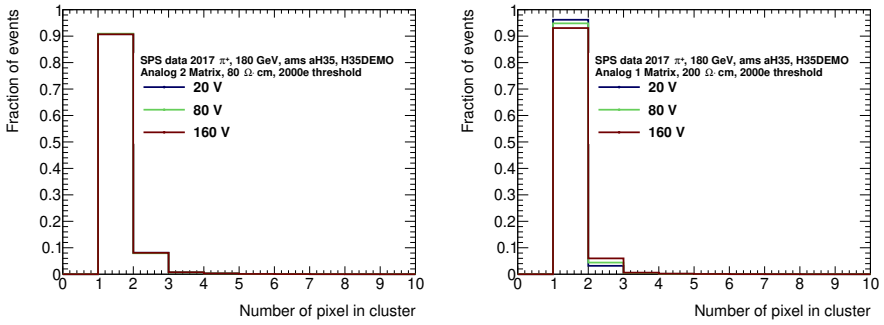

(a) $80\,\Omega \cdot \mathrm{cm}$

(b) $200\,\Omega \cdot \mathrm{cm}$

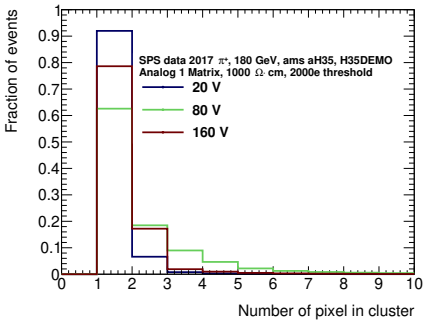

(c) $1000\,\Omega \cdot \mathrm{cm}$

Figure 5.15: Distribution of the cluster size for the three resistivities at different bias voltages [142].

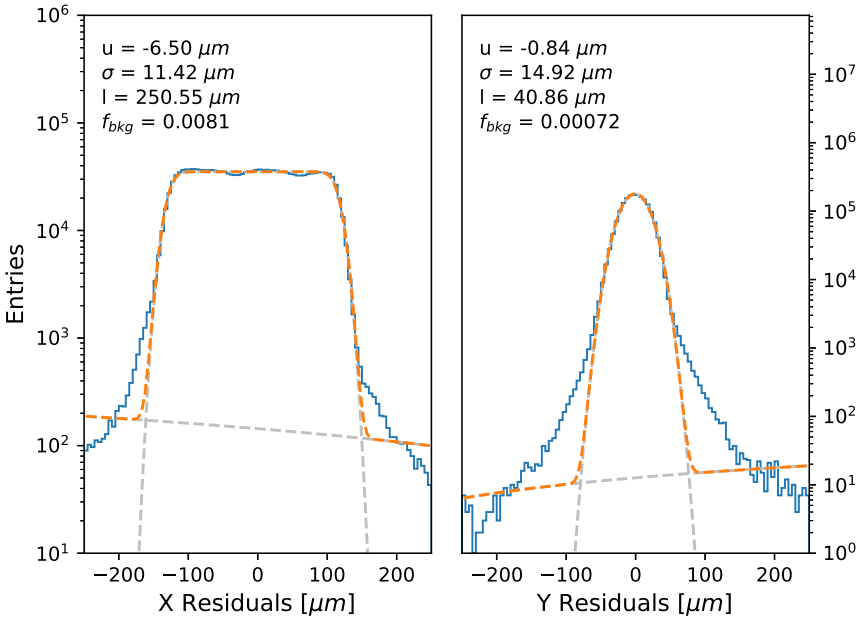

Figure 5.16: The distribution of the residuals for the analogue matrix 1 of the $200\,\Omega \cdot \mathrm{cm}$ sample at 160 V bias voltage and 2000 e FE-I4 threshold is shown in blue. The fit using Equation 5.1, with the addition of a linear background component, is shown in orange. f_{bkg} is the fraction of background events [142].

ing the drift time, and thus the probability of charge sharing. This effect has been observed in other capacitively coupled pixel sensors as well [146].

Figure 5.16 shows a typical residual distribution for a $200\,\Omega \cdot \mathrm{cm}$ sample operated with a bias voltage of 160 V and a FE-I4 threshold of 2000 e. As most clusters are of size one, the spatial resolution of the H35DEMO is determined by the size of the pixels, and the width of the fitted box function is compatible with the pixels size.

Tails in the residual distributions can be observed. They have not been taken into account in the fit because they contain a negligible fraction of events and do not influence significantly the final result.

These tails can be explained with two phenomena. Since the H35DEMO pixels are capacitively coupled to the FE-I4, some cross talk is present between a pad and its neighbours and this can modify the ToT value recorded by the FE-I4, resulting in a modification of the cluster position [142].

Furthermore, a contribution can be attributed to the distribution of the multiple scattering angle: it can be approximated with a Gaussian with large tails due to Rutherford scattering [24].

5.7.3 *Efficiency*

Figure 5.17 shows the efficiency for each pixel of the second high-gain matrix for each of the three resistivities, at 2000 e FE-I4 threshold and 160 V bias voltage. These results show that the detection efficiency is homogeneous over the matrix, resulting from the uniformity of the pixels electrical behaviour within the columns, of the glue interface and of the preamplifier properties.

A few pixels with efficiency lower than 99% are present: the left column of analogue matrix 2 and the right column of analogue matrix 1 show lower efficiency due to the proximity with the pixels of the monolithic nMOS and CMOS matrices, which can compete for the charge signal [142]. In addition, lower efficiency pixels are present within each matrix: most of them, along with the columns mentioned above, have an average efficiency of $\sim$95%, while fewer than 10 of them have an efficiency of $\sim$90% or lower.

From the plots of Figure 5.17 the global efficiency of the matrix can be extracted and the results at different FE-I4 thresholds and substrate bias voltages are presented in Figure 5.18. Lower resistivity samples and higher discriminator threshold require a higher voltage to reach a good detection efficiency, as expected. High gain sub-matrices reach an efficiency closer to 100%, compared to the low-gain one, while the presence of the extra DPTUB appears to be detrimental. The use of high resistivity substrates is beneficial since a lower bias voltage is necessary to obtain a high detection efficiency.

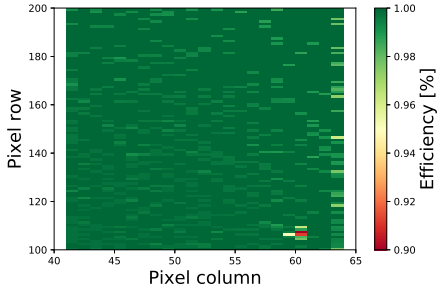

(a) 80 Ω · cm, 160 V, Analogue 2

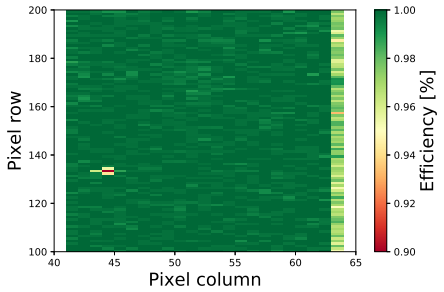

(b) 200 Ω · cm, 160 V, Analogue 2

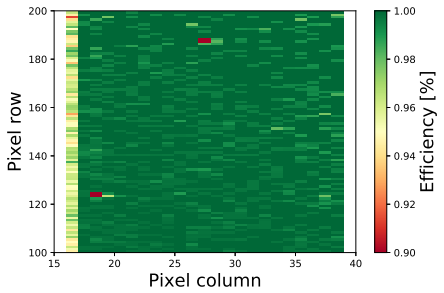

(c) 1000 Ω · cm, 160 V, Analogue 1

Figure 5.17: Efficiency for the analogue high-gain sub-matrices.

A detection efficiency above 99% is obtained with samples of all the characterized resistivities with a FE-I4 threshold of 2000 e, corresponding to a 1500 e signal in the H35DEMO.

Figure 5.19 shows the in-pixel efficiency measured for the high-gain matrices for a low and a high value of the bias voltage. In the plots at a low bias voltage, inter-pixel regions with lower efficiency are visible for the 80 Ω · cm sample.

This phenomenon can be explained with the limited lateral depletion in low-resistivity samples at low bias voltage, in fact it is not visible in higher resistivity samples. Furthermore, it disappears at higher bias voltages, since the lateral depletion increases, bringing the in-pixel particle detection efficiency uniformly above 99%.

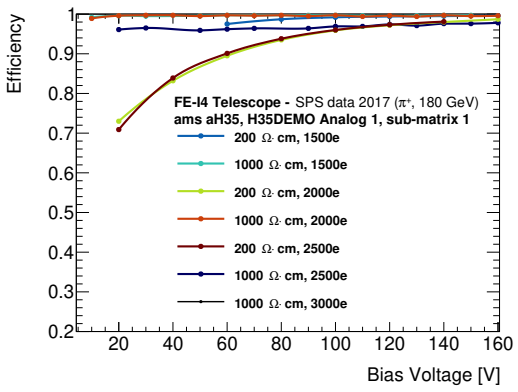

(a) Analogue 1, sub-matrix 1

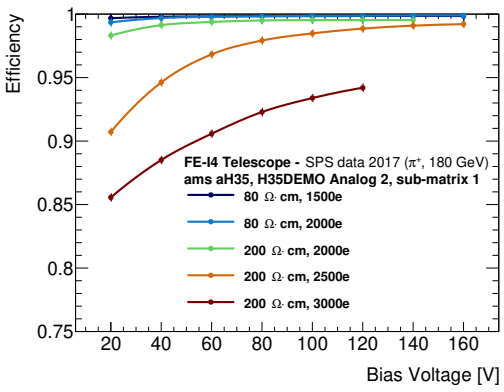

(b) Analogue 2, sub-matrix 1

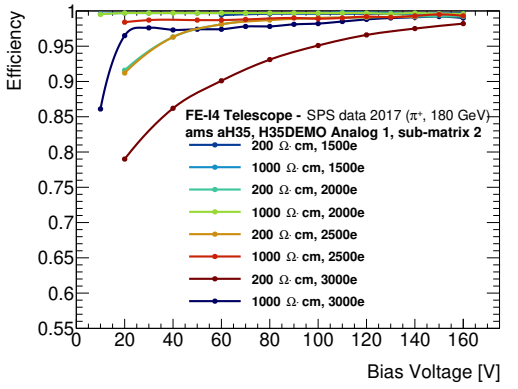

(c) Analogue 1, sub-matrix 2

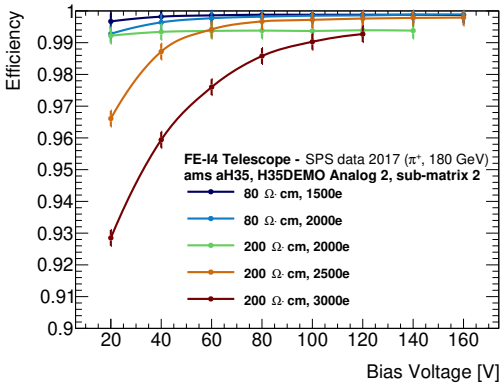

(d) Analogue 2, sub-matrix 2

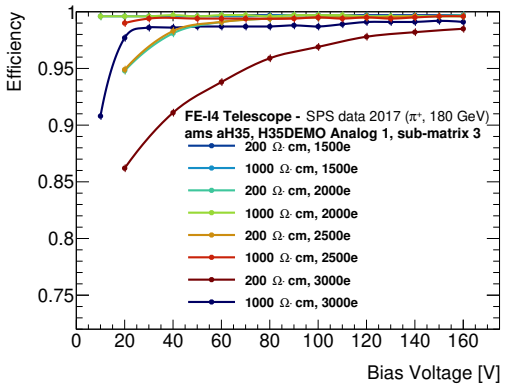

(e) Analogue 1, sub-matrix 3

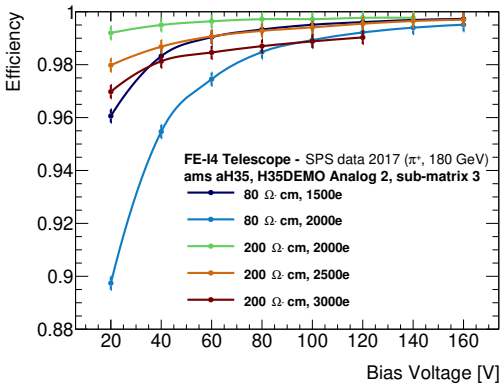

(f) Analogue 2, sub-matrix 3

Figure 5.18: Global efficiency of the six characterized sub-matrices of the H35DEMO for different resistivities and FE-I4 thresholds [142].

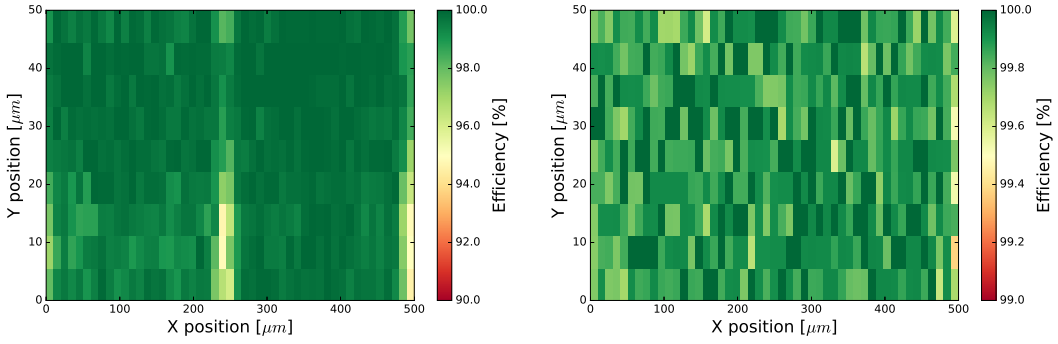

(a) 80 Ω · cm, 20 V

(b) 80 Ω · cm, 160 V

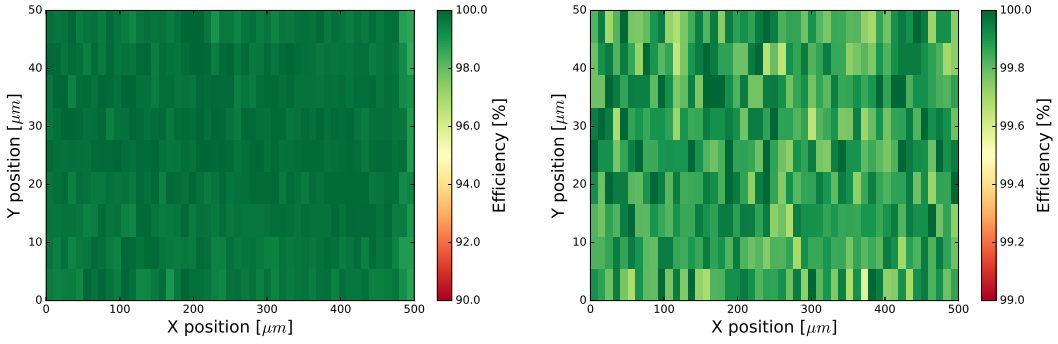

(c) 200 Ω · cm, 20 V

(d) 200 Ω · cm, 160 V

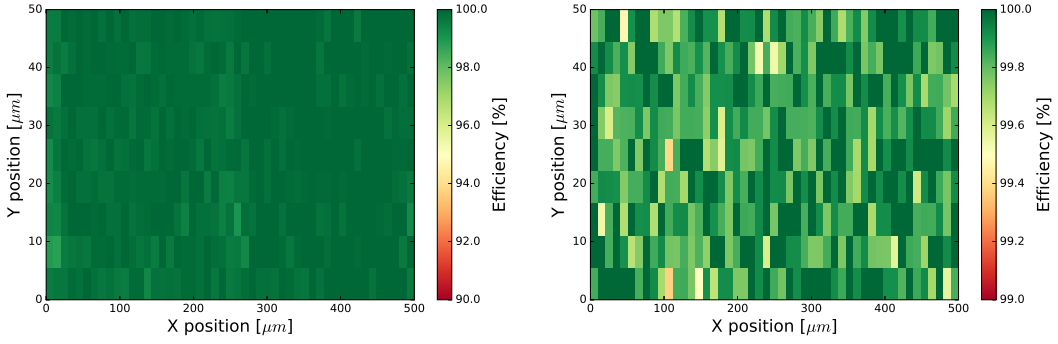

(e) 1000 Ω · cm, 10 V

(f) 1000 Ω · cm, 160 V

Figure 5.19: In-pixel efficiency for the pixels of sub-matrix 2 (Analogue 2 for 80 and 200 Ω · cm, Analogue 1 for 1000 Ω · cm). Note the difference in the colour scale between data at 20 and 160 V [142].

5.7.4 *Timing*

Figure 5.20 shows the time-of-arrival distribution of the clusters recorded by the H35DEMO at different bias voltages. Results for the second high-gain sub-matrix are shown, which are also representative of the other sub-matrices. The timing distribution is constrained in two 25 ns bins for bias voltages over 80 V: part of the reason for the width of the timing distribution is the 25 ns time resolution of the telescope. No clear dependence of the timing resolution on resistivity, gain or presence of the deep p-well is visible. These results show that the timing resolution is dominated by the intrinsic jitter of the preamplifier and not by the sensor signal amplitude or rise time [142]. Furthermore, they are a great improvement compared to the earlier HV2FEI4 and CCPDv4 (see Section 3.2 on page 64), which featured a timing distribution spread over four to nine 25 ns bins.

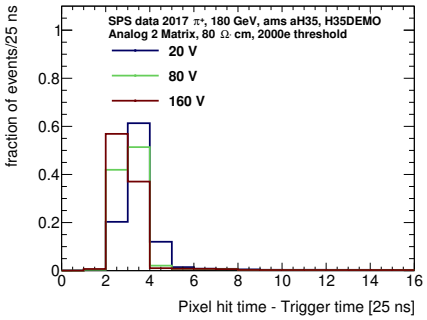

(a) 80 Ω · cm

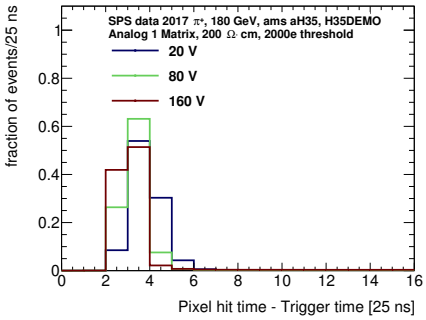

(b) 200 Ω · cm

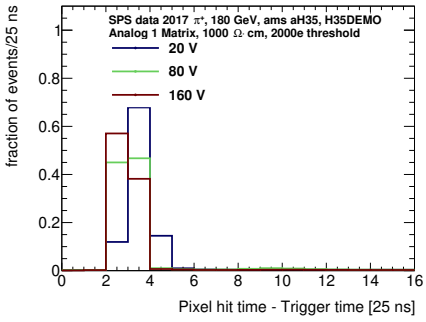

(c) 1000 Ω · cm

Figure 5.20: Distribution of the ToA of the signals for the sub-matrix 2 for samples of the three studied resistivities [142].

5.8 ATLASPIX1 RESULTS

5.8.1 *IV characterization*

The results of the IV measurements for the ATLASPIX1 before irradiation are visible in Figure 5.21a. They show a leakage current

density below 4 µA/cm^2 at all temperatures and feature a breakdown voltage of ∼70 V. The Arrhenius plot of Figure 5.21b shows a clear disagreement of the measured data with the SRH prediction [143], indicating that the leakage current generated in the periphery is much more important than the one generated in the bulk.

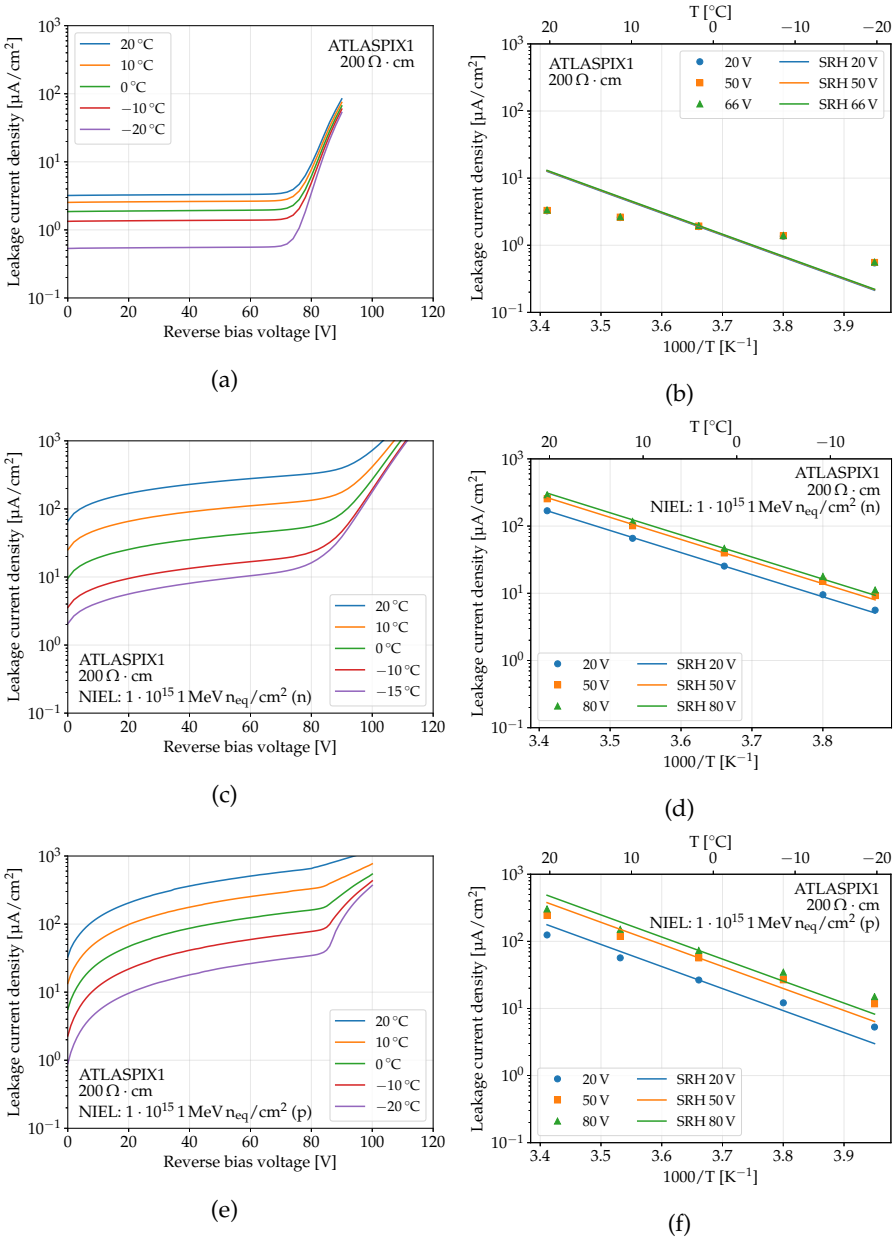

Figure 5.21: IV curve and Arrhenius plot for a ATLASPIX1 prototype (a, b) before irradiation, after (c, d) neutron and (e, f) proton irradiation [94].

In Figures 5.21c, d, e, f are shown the results of the IV characterization after irradiation with neutrons (at JSI in Ljubljana) and with protons (at the Bern cyclotron) at a fluence of $1 \cdot 10^{15}$ 1 MeV n_{eq}/cm^2.

The current is increased by more than one order of magnitude, compared to the measurement before irradiation. The Arrhenius plots show that there is a significant increase in the contribution of bulk-generated currents to the leakage current, due to the damage induced by the radiation [94].

5.8.2 *Threshold calibration and dispersion*

The threshold dispersion has been measured before and after irradiation with neutrons, and the results are reported in Figure 5.22a. The threshold distribution features a standard deviation of ∼200 e before irradiation and ∼190 e after a fluence of $1 \cdot 10^{15}$ 1 MeV n_{eq}/cm^2.

The difference in the mean value of the two distribution is caused by a different preamplifier and shaper configuration, required to operate the sensor after irradiation. Unfortunately, due to an issue in the circuitry controlling each row, it was not possible to perform a threshold tuning [147].

The threshold of the ATLASPIX1 prototype has been calibrated using a ^{55}Fe source, which features an X-ray spectrum with a peak at 5.9 keV. The result is shown in Figure 5.22b: assuming that 3.6 eV are required to generate one electron-hole pair in silicon, the calibration result is 988 e/100 mV.

This result allows the conversion of the discriminator threshold in mV set in the ATLASPIX1 to the equivalent value in electrons, quoted in the results of the following sections.

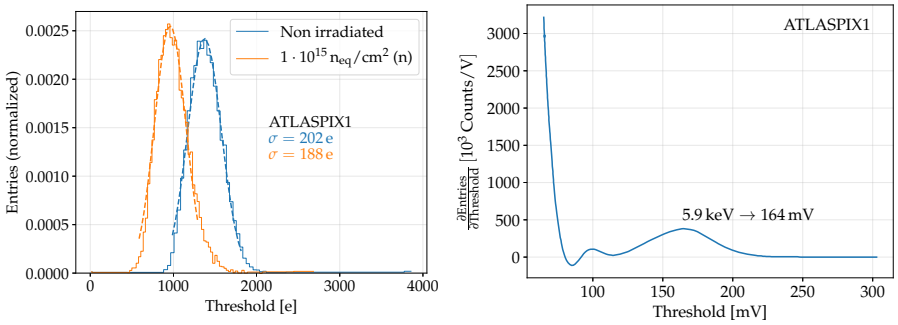

(a) (b)

Figure 5.22: (a) ATLASPIX1 threshold dispersion before and after neutron irradiation. (b) Threshold calibration result using a ^{55}Fe source.

5.8.3 *Spatial resolution and cluster size*

The distribution of the cluster size of the ATLASPIX1 samples at different voltages, thresholds and irradiation steps is shown in Figure 5.23. Before irradiation (Figure 5.23a) the largest part of the clusters has size one, with a higher fraction of clusters of size two, compared

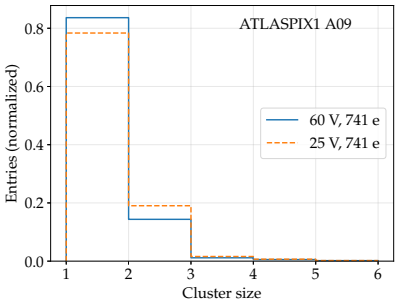

(a) Non irradiated

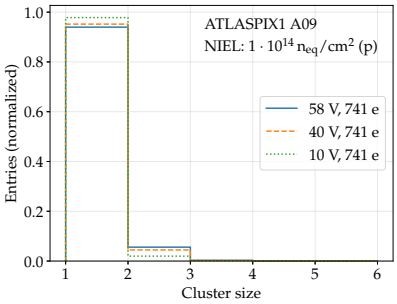

(b) $1 \cdot 10^{14}$ 1 MeV n_{eq}/cm^2 (p)

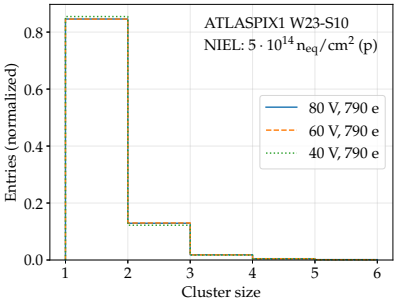

(c) $5 \cdot 10^{14}$ 1 MeV n_{eq}/cm^2 (p)

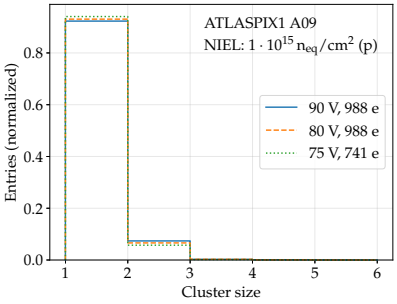

(d) $1 \cdot 10^{15}$ 1 MeV n_{eq}/cm^2 (p)

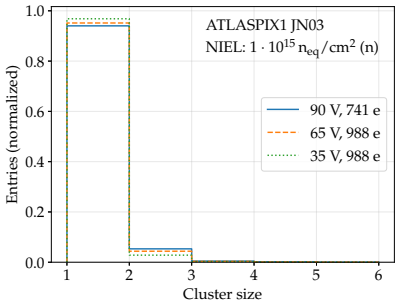

(e) $1 \cdot 10^{15}$ 1 MeV n_{eq}/cm^2 (n)

Figure 5.23: Distribution of the cluster sizes for different irradiation steps.

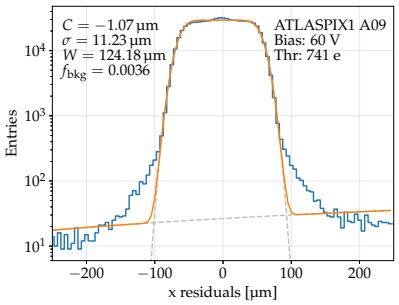

(a)

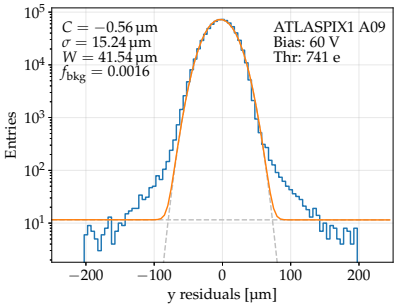

(b)

Figure 5.24: Residual distribution (blue) and fit using Equation 5.1 (orange). f_{bkg} is the fraction of background events.

to the H35DEMO. This can be expected, since the pixel size of the ATLASPIX1 ($40 \times 130\,\mu m^2$) is smaller than the one of the H35DEMO ($50 \times 250\,\mu m^2$).

After irradiation the fraction of clusters of size two and above decreases, since the increased trapping probability limits the diffusion of the charge carriers, and thus the charge sharing. It is interesting to notice that the fraction of size-two clusters is higher for the samples irradiated at $5 \cdot 10^{14}$ 1 MeV n_{eq}/cm^2, compared to the samples irradiated at a higher and lower fluence ($1 \cdot 10^{14}$ and $1 \cdot 10^{15}$ 1 MeV n_{eq}/cm^2 respectively)

This effect can be understood recalling the evolution of the effective doping concentration from Figure 4.24c on page 109. N_{eff}, which is inversely proportional to the squared value of the depletion-region depth, is close to a minimum at $5 \cdot 10^{14}$ 1 MeV n_{eq}/cm^2: this implies that charge carriers generated deeper inside the bulk are collected and they are more likely to diffuse into the neighbouring pixels.

Figure 5.24 shows a typical residual distribution for the ATLASPIX1 prototype (the results after irradiation are very similar and not shown here). Similarly to the H35DEMO, the spatial resolution of ATLASPIX1 is determined by the pixel size, since the great majority of the clusters have size one.

The tails in the distribution are still present, but in this case they are caused by the Rutherford scattering only, since there is no capacitively coupled front-end chip.

5.8.4 *Efficiency*

Figure 5.25 shows the efficiency of each pixel of the Simple matrix of the ATLASPIX1 prototype. Before irradiation (Figure 5.25a) the efficiency is uniform and, on average, above 99%, despite the lower efficiency parts in the first and last pixel columns, which can be affected by the neighbouring matrices.

In Figures 5.25a, c entire rows of pixels are masked before analysis: due to an issue in the row circuitry, if a pixel is masked on the DUT, the whole row would be affected, showing a low efficiency. For this reason, each row containing a masked pixel, has been removed from the analysis. This problem has been mitigated during the testbeam campaign by implementing the masking at the level of the ZC706 board and not on the DUT (this is the case of Figure 5.25b).

A non-uniform low-efficiency region is visible at the top of the matrix in Figures 5.25b, c. It is not likely to be caused by the bulk damage because the profile of the beam used for irradiation was flat and neither from the particle rate at the test beam, which again featured a uniform distribution. A possible explanation could be related to the damage to bias rails: the rows of pixels are powered from the sides, so if a voltage drop is present on the rail, it should

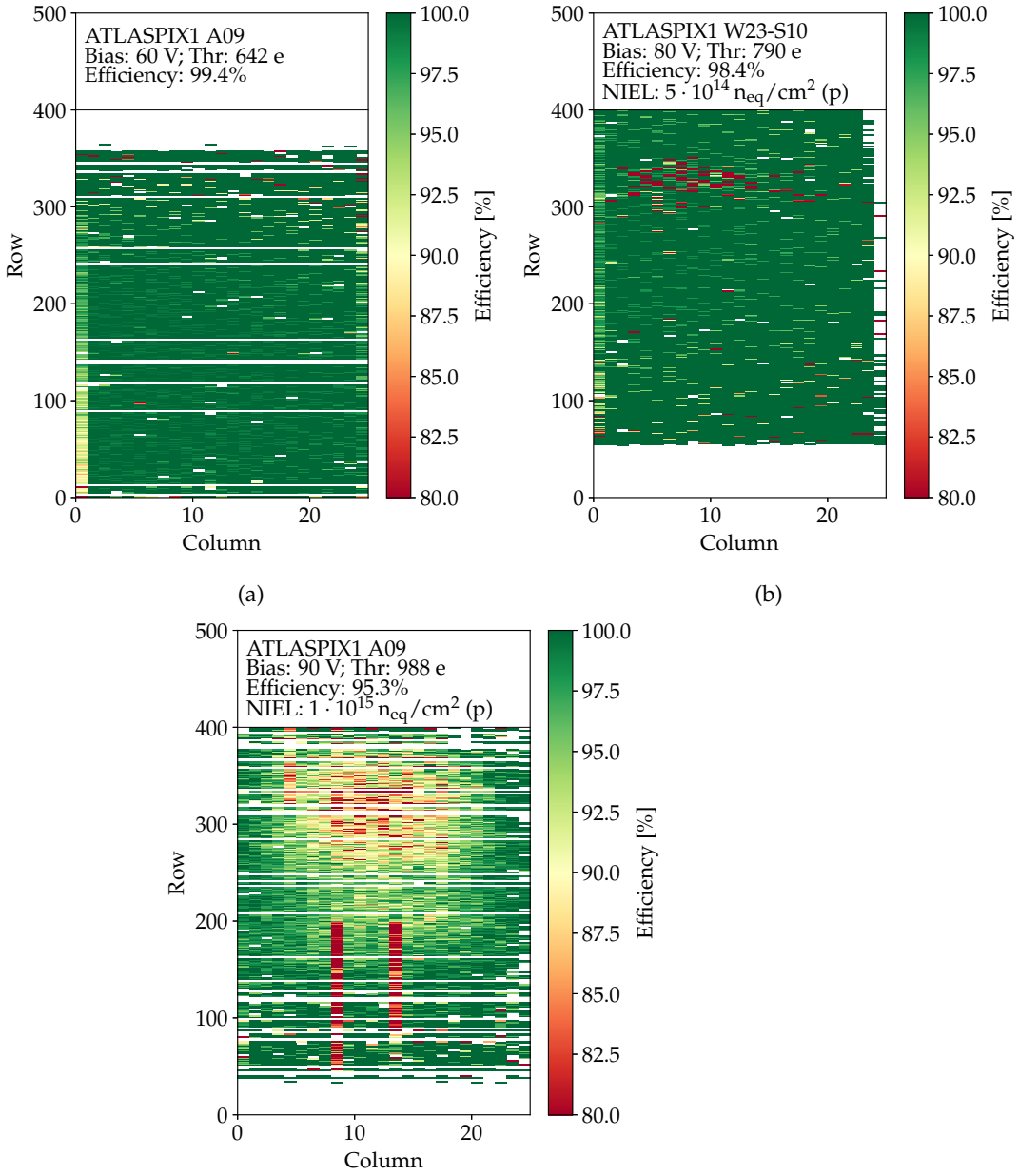

Figure 5.25: Efficiency of the ATLASPIX1 Simple matrix (a) before irradiation and (b, c) after proton irradiation. Results after the first step of proton irradiation and after neutron irradiation are not shown, as they are compatible with the ones before irradiation.

affect more the pixels in the centre of the matrix. This, however, should not be considered a final explanation since no additional tests have been performed to verify it.

Furthermore, two half-columns have an extremely low efficiency, hinting to damage to the end-of-column circuitry (as explained Section 3.4.1 on page 75, one EoC block reads out half column of 200 pixels).

In addition, the ATLASPIX1 sensor is larger that the acceptance of the telescope and for this reason it could not be fully contained and a band of inactive pixels is visible either at the top or at the bottom of the matrix.

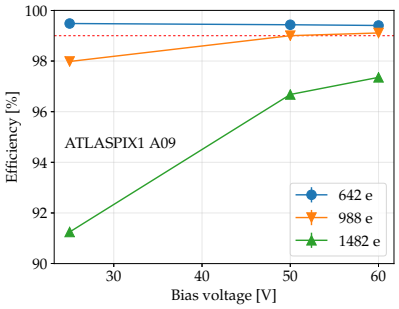

(a) Non irradiated

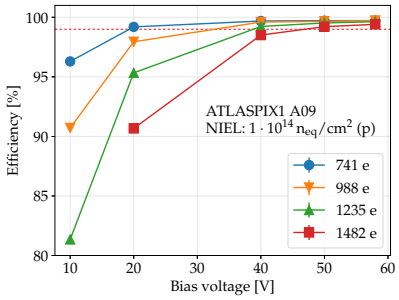

(b) $1 \cdot 10^{14}$ 1 MeV n_{eq}/cm^2 (p)

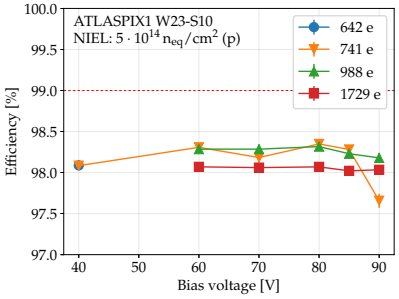

(c) $5 \cdot 10^{14}$ 1 MeV n_{eq}/cm^2 (p)

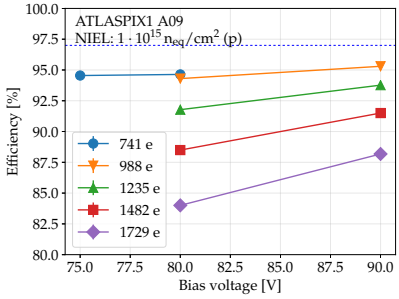

(d) $1 \cdot 10^{15}$ 1 MeV n_{eq}/cm^2 (p)

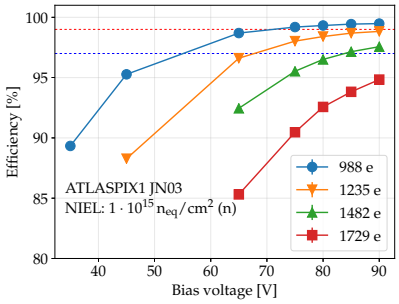

(e) $1 \cdot 10^{15}$ 1 MeV n_{eq}/cm^2 (n)

Figure 5.26: Average efficiency as a function of the bias voltage at different discriminator thresholds. The dashed red and blue lines indicate the 99% and 97% efficiency respectively. The error bars representing the statistical uncertainties, although present, are too small to be visible in the plots.

In Figures 5.26a and 5.27a the average efficiency is shown for different bias voltage and discriminator threshold points: as expected, it increases at higher bias voltages and lower thresholds, while remaining above 99% for a wide range of parameters.

After the first step of proton irradiation ($1 \cdot 10^{14}$ 1 MeV n_{eq}/cm^2) the efficiency remains uniform over the matrix and well above 99%. Figures 5.26b and 5.27b shows that high efficiency is maintained for thresholds over 1400 e, while before irradiation the efficiency would dip below 99% beyond 1000 e. This can be explained with the increase in depletion depth caused by the initial acceptor removal induced by the irradiation.

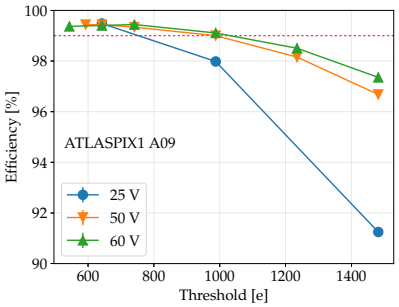

(a) Non irradiated

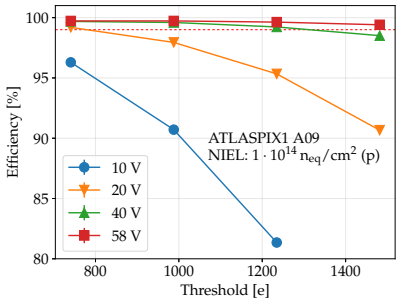

(b) $1 \cdot 10^{14}$ 1 MeV n_{eq}/cm^2 (p)

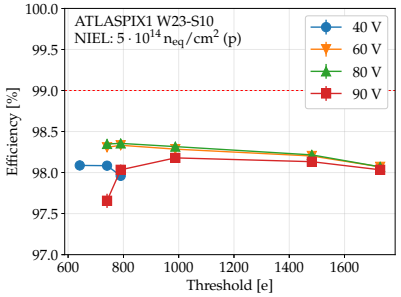

(c) $5 \cdot 10^{14}$ 1 MeV n_{eq}/cm^2 (p)

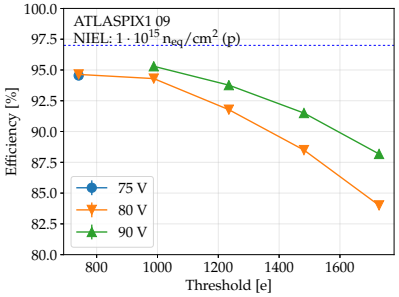

(d) $1 \cdot 10^{15}$ 1 MeV n_{eq}/cm^2 (p)

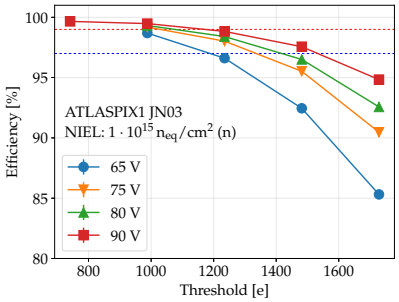

(e) $1 \cdot 10^{15}$ 1 MeV n_{eq}/cm^2 (n)

Figure 5.27: Average efficiency as a function of the discriminator threshold. The dashed red and blue lines indicate the 99% and 97% efficiency respectively. The error bars, although present, are too small to be visible in the plots.

This effect is still visible after $5 \cdot 10^{14}$ 1 MeV n_{eq}/cm^2 (Figures 5.26c and 5.27c), albeit with a lower efficiency: it remains superior to 98% up to thresholds above 1600 e. Figure 5.25b, however, shows that a region with pixels of lower efficiency begins to appear at the top of the matrix, while the remaining part still features a uniform efficiency.

After a proton fluence of $1 \cdot 10^{15}$ 1 MeV n_{eq}/cm^2 the sensor performance are significantly degraded, with the efficiency reaching a maximum above 95% in a limited space of parameters (Figures 5.26d and 5.27d) and showing significant non-uniformities (Figure 5.25c) in the matrix, as discussed before. At this fluence the depletion depth is significantly decreased, compared to the previous fluence step and concurs, with the increased damage to the electronics, to deteriorate the performance of the detector.

This degradation of performance is not present after the same neutron fluence, at which the efficiency is comparable to the non-irradiated samples (Figures 5.26e and 5.27e). This highlights the difference between neutral and charged hadrons: the former are responsible for damage to the bulk, while the latter, being ionizing particles, significantly affect the electronics as well.

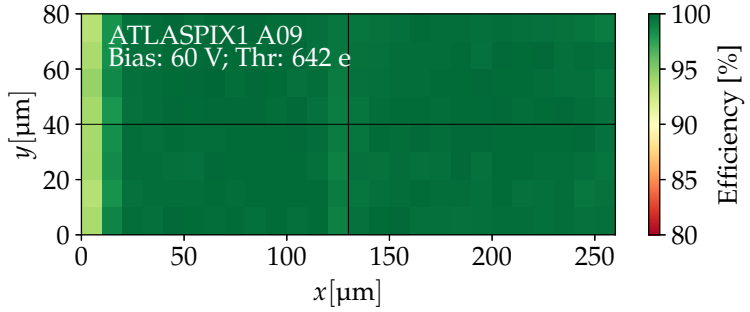

(a)

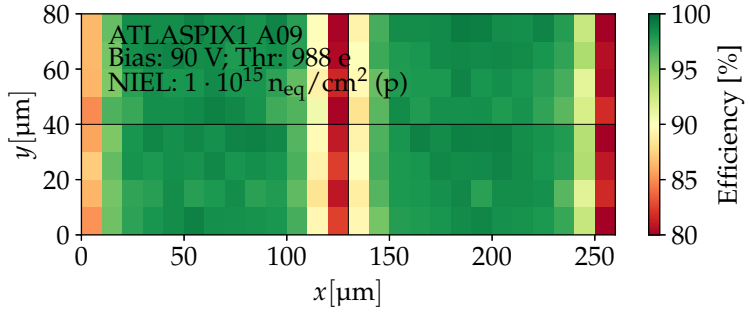

(b)

Figure 5.28: In-pixel efficiency of the ATLASPIX1 Simple matrix (a) before irradiation, and (b) after proton irradiation to a fluence of $1 \cdot 10^{15}$ 1 MeV n_{eq}/cm^2.

In Figure 5.28 the in-pixel efficiency before irradiation and after the last proton irradiation step is shown. Before irradiation the in-pixel efficiency is uniform, with a slight decrease in the left edge, which

could be caused by a small misalignment. A similar behaviour is observed after the various irradiation steps, with the exception of the $1 \cdot 10^{15}$ 1 MeV n_{eq}/cm^2 proton fluence: here the efficiency drops to around 80% in the regions between the short sides of the pixels.

5.8.5 *Timing*

In Figure 5.29a the distribution of the time of arrival of the clusters for the ATLASPIX1 at two different bias voltages is shown. It spans almost 100 ns, corresponding to four 25 ns bins. Several factors contribute to the width of the distribution:

- the time resolution of the telescope of 25 ns;
- the clear dependence of the time-of-arrival on the row of the sensor, with a difference of up to 40 ns, as shown in Figure 5.29b, caused by the different delays in the transmissions lines;
- the absence of time-walk correction in ATLASPIX1.

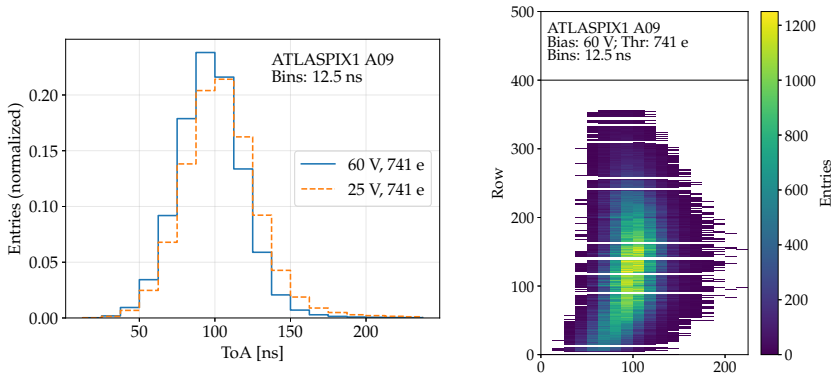

(a) (b)

Figure 5.29: (a) Time-of-Arrival (ToA) distribution for a non-irradiated ATLASPIX1 sample. (b) ToA distribution in each row of the sensor.

A timing measurement has been performed by the CLIC group, using the Timepix3 telescope, with a time resolution of 1 ns and the results are reported in Figure 5.30. Here the row dependence has been corrected, while the time-walk has not. The distribution is fitted with a convolution of a box function and a Gaussian: these results show an excellent time resolution, with $\sigma = 5.2$ ns [148].

After irradiation the timing distribution is tighter, contained in less than three 25 ns bins at a high bias voltage (Figures 5.31a to d). This behaviour can be explained with a reduction in the diffusion component of the current signals, but also with an increase in their amplitude, thanks to the larger depletion depth after irradiation, leading to more consistent timing.

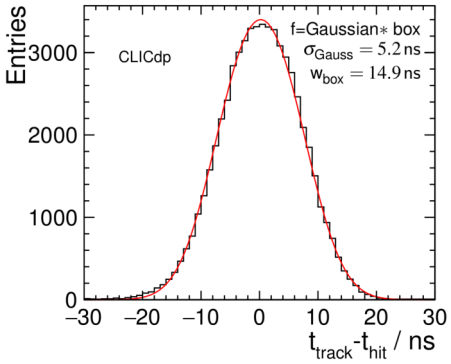

Figure 5.30: Time-of-Arrival distribution for a non-irradiated ATLASPIX1 sample obtained with the Timepix3 telescope [148].

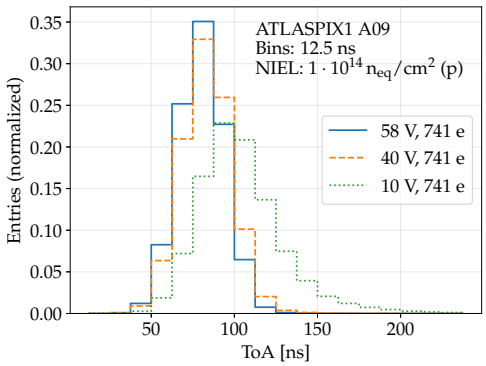

(a) $1 \cdot 10^{14}$ 1 MeV n_{eq}/cm^2 (p)

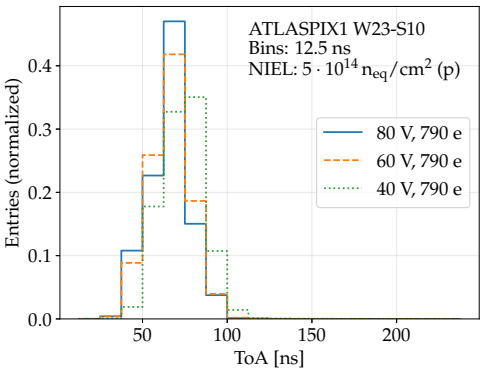

(b) $5 \cdot 10^{14}$ 1 MeV n_{eq}/cm^2 (p)

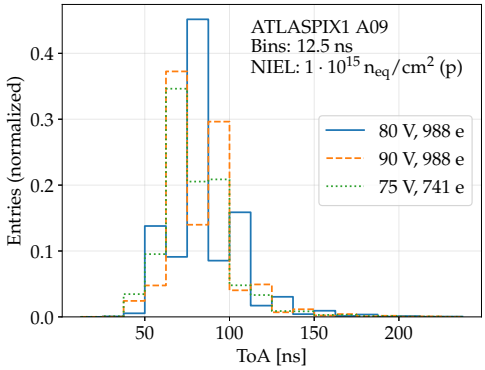

(c) $1 \cdot 10^{15}$ 1 MeV n_{eq}/cm^2 (p)

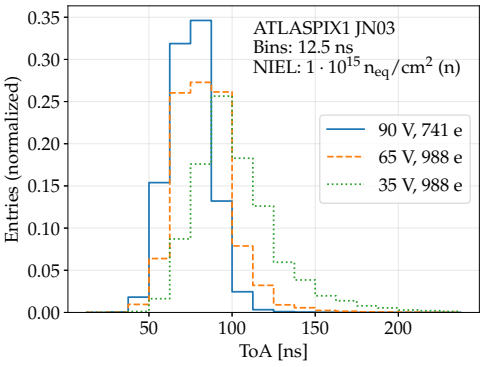

(d) $1 \cdot 10^{15}$ 1 MeV n_{eq}/cm^2 (n)

Figure 5.31: ATLASPIX1 Time-of-Arrival distribution after several irradiation steps.

5.9 CONCLUSIONS

The analogue matrices of the H35DEMO and the Simple matrix of the ATLASPIX1 have been characterized in testbeams. These measurements aimed at determining the performance of these sensors mostly in terms of particle detection efficiency and spatial and time resolution.

The H35DEMO shows an excellent efficiency, above 99% over a wide range of bias voltages. This range appears to be wider for high-resistivity samples, due to the larger depletion depth. The timing of the different prototypes has been studied as well and the results show little dependence on the substrate resistivity. This indicates that the time resolution is determined by the preamplifier itself, with a negligible influence from the signal strength and the varying rise time.

The studies of the H35DEMO have been fundamental to determine the optimal design of the analogue part of the future prototypes. In particular the measurements, summarized in Figure 5.32, show that high gain is required to achieve a good detection efficiency over a large range of bias voltages and thresholds, especially when using low resistivities, and that the extra DPTUB should not be used, in order to reduce the input capacitance of the preamplifier. Furthermore, a threshold of 1500 e or less must be achieved to ensure an efficiency superior to 99% when the discriminator is integrated in the pixel [142].

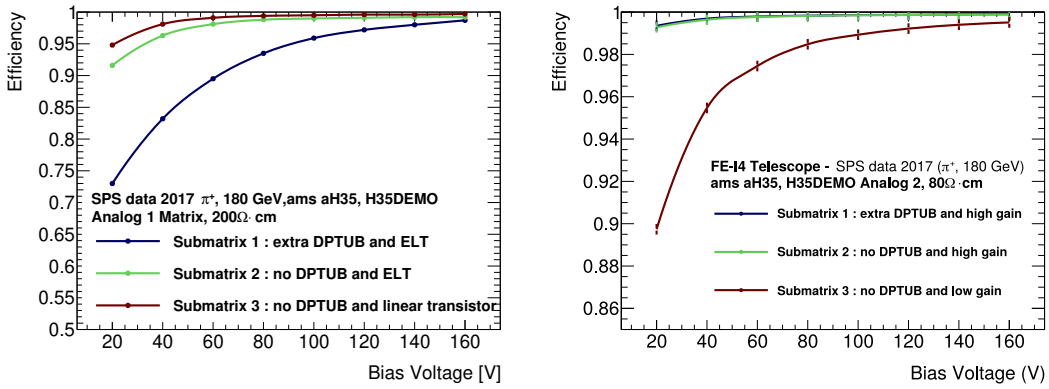

(a) (b)

Figure 5.32: Detection efficiency as a function of bias voltage of (a) the three sub-matrices of the analogue matrix 1 of a 200 Ω · cm sample and (b) the three sub-matrices of the analogue matrix 2 of a 80 Ω · cm sample [142]. DPTUB and ELT refer to the deep p-tub presence and the use of enclosed layout transistors (see Section 3.3 on page 69 for more details)

ATLASPIX1 features a homogeneous detection efficiency before irradiation, in excess of 99% over a wide range of bias voltages and thresholds. Furthermore, after correcting for known row-dependency of the time of arrival, it reaches a time resolution with $\sigma = 5.2\,\text{ns}$.

These studies have been extremely important to identify shortcomings in the design of the read-out: in particular issues in the row circuitry managing the threshold tune and masking have been identified, along with a significant row dependence of the hits time-of-arrival. These issues have been addressed in the ATLASPIX3 prototype design [95].

Measurements after proton irradiation have shown an initial increase in detection efficiency, after a fluence of $1 \cdot 10^{14}$ 1 MeV n_{eq}/cm^2, followed by a degradation at higher fluences, partly due to the damage to the read-out electronics, reaching 95% at $1 \cdot 10^{15}$ 1 MeV n_{eq}/cm^2. This is validated by the presence of inefficient half-columns (that can be linked to the malfunction of an EoC cell), by the TCT measurements, that show an increase in the depletion depth after irradiation and by the results of the neutron-irradiated samples, that show performance similar to non-irradiated samples.

These results show that, in addition to the improvements mentioned above, the read-out electronics should become more radiation-hard in future prototypes.

CONCLUSIONS

Monolithic pixel detectors, built on a high resistivity substrate using a high-voltage CMOS technology, have been considered as a replacement for the outermost pixel layer of the ATLAS Inner Tracker.

They have several advantages compared to the traditional detector modules: CMOS foundries have a faster processing time, allowing for a quick supply and a fast reaction time in case of problems. Monolithic sensors do not need to be bump-bonded to a readout ASIC, removing the time, cost and possible yield loss of this process. Furthermore, HV-CMOS sensors can be a factor of 5 times thinner than hybrid modules, reducing the material budget and the number of pixels activated by a single particle, resulting in a lower data bandwidth.

HV-CMOS pixel detectors prototypes produced by ams AG have been characterized in this work, focusing on the charge collection capabilities, particle detection efficiency and spatial and time resolution.

The evolution with irradiation of the depletion depth, the effective doping concentration and the current pulse shape have been studied using the Transient Current Technique (TCT). Edge TCT measurements have been performed on the test structures of the H35DEMO. They have shown that the effective doping concentration N_{eff} decreases significantly after irradiation, reaching a minimum and then increasing again. A decrease in N_{eff} translates in an larger depletion depth, which can increase the collected charge, compensating a possible carriers loss due to trapping. Furthermore, it has been shown that the annealing is not expected to have a detrimental effect on charge collection. In the framework of ITk, these results are very promising, showing that the charge collection capabilities of HV-CMOS sensors are not expected to degrade due to radiation damage.

A significant difference in the effect of protons and neutrons has been observed: the acceptor removal effect caused by neutron appears to be slower, while the later acceptor introduction is more significant. It is important to study the effect of both charged and neutral hadrons, since the radiation damage in ITk will have contributions from both.

Testbeam measurements have been performed on the analogue matrices of the H35DEMO, coupled to FE-I4 chips and on the Simple matrix of the ATLASPIX1. The characterization of the H35DEMO has allowed the determination of the optimal characteristics of the analogue read-out electronics (requiring high-gain and the absence of the deep p-tub) to obtain a particle detection efficiency superior to 99%, which can be achieved over a wide range of bias voltages. The time resolution has been studied as well, resulting independent from the substrate resistivity and mainly determined by the preamplifier.

The ATLASPIX1 has been characterized before and after irradiation using protons and neutrons. Before irradiation it shows a homogeneous detection efficiency, above 99% over a wide range of bias voltages and thresholds. It also shown a good time resolution, with $\sigma = 5.2\,\text{ns}$, after correcting for the row-dependency of the time of arrival.

Measurements after proton irradiation show an initial improvement of the performance (efficiency and time resolution both), that can be correlated with the increase in depletion depth caused by acceptor removal, followed by a degradation in particle detection efficiency, which reaches 98% after a fluence of $5 \cdot 10^{14}$ 1 MeV n_{eq}/cm^2 and 95% after $1 \cdot 10^{15}$ 1 MeV n_{eq}/cm^2. Part of the reason for this degradation can be attributed at the damage to the read-out electronics. After a neutron fluence of $1 \cdot 10^{15}$ 1 MeV n_{eq}/cm^2, instead, the performance remain comparable to before irradiation.

Results from these sensors show great improvements overs earlier prototypes, like the HV2FEI4 and CCPDv4, and have allowed the identification of shortcomings which have been addressed in the ATLASPIX3 design. They have shown that monolithic HV-CMOS sensors can be considered as a realistic option in a so-demanding environment as the ITk at the HL-LHC.

Despite the good results obtained by the different groups collaborating in the development and testing of this technology, these sensors will not be employed for the outermost layer of the ITk. This decision has been driven by the risks connected to the use of different sensor technologies and to the schedule of the development and testing, considered too impacting on the construction of the Inner Tracker.

The development of HV-CMOS sensors has nonetheless produced extremely important results, improving the state of the art of monolithic pixel detectors, pushing their radiation harness and rate capabilities up to unprecedented levels.

A

TCT H35DEMO SAMPLES

In this appendix, the H35DEMO samples used for transient current technique measurements are listed (see Chapter 4 on page 81).

Table A.1: Samples irradiated at CERN PS.

Sample	Resistivity [$\Omega \cdot$ cm]	Dose [Mrad]	Fluence [1 MeV n_{eq}/cm^2]
H35-20-PS-1	20	4.45	$1 \cdot 10^{14}$
H35-20-PS-2	20	13.33	$3 \cdot 10^{14}$
H35-20-PS-3	20	24.53	$5.5 \cdot 10^{14}$
H35-20-PS-4	20	61.32	$1.4 \cdot 10^{15}$
H35-80-PS-1	80	4.45	$1 \cdot 10^{14}$
H35-80-PS-2	80	13.33	$3 \cdot 10^{14}$
H35-80-PS-3	80	24.53	$5.5 \cdot 10^{14}$
H35-80-PS-4	80	61.32	$1.4 \cdot 10^{15}$
H35-200-PS-1	200	4.45	$1 \cdot 10^{14}$
H35-200-PS-2	200	13.33	$3 \cdot 10^{14}$
H35-200-PS-3	200	24.53	$5.5 \cdot 10^{14}$
H35-200-PS-4	200	61.32	$1.4 \cdot 10^{15}$
H35-1000-PS-1	1000	4.45	$1 \cdot 10^{14}$
H35-1000-PS-2	1000	13.33	$3 \cdot 10^{14}$
H35-1000-PS-3	1000	24.53	$5.5 \cdot 10^{14}$
H35-1000-PS-4	1000	88.77	$2 \cdot 10^{15}$

Table A.2: Samples irradiated at the Bern Inselspital cyclotron.

Sample	Resistivity [$\Omega \cdot$ cm]	Dose [Mrad]	Fluence [1 MeV n_{eq}/cm^2]
H35-20-BE-1	20	0	0
		10	$1 \cdot 10^{14}$
		20	$2.1 \cdot 10^{4}$
		30	$3.1 \cdot 10^{14}$
		40	$4.2 \cdot 10^{14}$
		50	$5.2 \cdot 10^{14}$
		70	$7.3 \cdot 10^{14}$
		100	$1 \cdot 10^{15}$
		150	$1.6 \cdot 10^{15}$
H35-80-BE-1	80	0	0
		10.7	$1.1 \cdot 10^{14}$
		16.05	$1.7 \cdot 10^{14}$
		21.4	$2.2 \cdot 10^{14}$
		26.8	$2.8 \cdot 10^{14}$
		32.1	$3.4 \cdot 10^{14}$
		37.5	$3.9 \cdot 10^{14}$
		42.8	$4.5 \cdot 10^{14}$
		48.2	$5 \cdot 10^{14}$
		58.2	$6.1 \cdot 10^{14}$
		78.2	$8.2 \cdot 10^{14}$
		98.2	$1 \cdot 10^{15}$
		148.2	$1.6 \cdot 10^{15}$

Table A.2: Samples irradiated at the Bern Inselspital cyclotron (continued).

Sample	Resistivity [$\Omega \cdot$ cm]	Dose [Mrad]	Fluence [1 MeV n_{eq}/cm^2]
H35-200-BE-1	200	0	0
		5.35	$5.6 \cdot 10^{13}$
		10.7	$1.1 \cdot 10^{14}$
		16.05	$1.7 \cdot 10^{14}$
		21.4	$2.2 \cdot 10^{14}$
		26.8	$2.8 \cdot 10^{14}$
		32.1	$3.4 \cdot 10^{14}$
		37.5	$3.9 \cdot 10^{14}$
		42.8	$4.5 \cdot 10^{14}$
		50.8	$5.3 \cdot 10^{14}$
		80	$8.4 \cdot 10^{14}$
		100	$1 \cdot 10^{15}$
		150	$1.6 \cdot 10^{15}$
H35-200-BE-2	200	0	0
		1	$1 \cdot 10^{14}$
		3	$1 \cdot 10^{14}$
		5	$3.1 \cdot 10^{14}$
		7	$5.2 \cdot 10^{14}$
		9	$9.4 \cdot 10^{14}$
H35-1000-BE-1	1000	0	0
		5.35	$5.6 \cdot 10^{13}$
		10.7	$1.1 \cdot 10^{14}$
		16.05	$1.7 \cdot 10^{14}$
		21.4	$2.2 \cdot 10^{14}$
		26.8	$2.8 \cdot 10^{14}$
		32.1	$3.4 \cdot 10^{14}$
		42.8	$4.5 \cdot 10^{14}$
		64.2	$6.7 \cdot 10^{14}$
		80	$8.4 \cdot 10^{14}$
		100	$1 \cdot 10^{15}$
		150	$1.6 \cdot 10^{15}$
H35-1000-BE-2	1000	0	0
		1	$1 \cdot 10^{14}$
		3	$1 \cdot 10^{14}$
		5	$3.1 \cdot 10^{14}$
		7	$5.2 \cdot 10^{14}$
		9	$9.4 \cdot 10^{14}$

Table A.3: Samples irradiated at JSI in Ljubljana. The annealing steps refer to Table 4.1.

Sample	Resistivity [$\Omega \cdot$ cm]	Fluence [1 MeV n_{eq}/cm^2]	Annealing steps
H35-20-N-1	20	$1 \cdot 10^{13}$	0, 1
H35-20-N-2	20	$5 \cdot 10^{13}$	0, 1
H35-20-N-3	20	$1 \cdot 10^{14}$	1
H35-20-N-4	20	$5.5 \cdot 10^{14}$	1
H35-20-N-5	20	$2 \cdot 10^{15}$	1, 2, 3, 4
H35-20-N-6	20	$1 \cdot 10^{14}$	0, 1
H35-20-N-7	20	$5 \cdot 10^{14}$	0, 1
H35-20-N-8	20	$1 \cdot 10^{15}$	0, 1
H35-20-N-9	20	$2 \cdot 10^{15}$	0, 1
H35-80-N-1	80	$1 \cdot 10^{13}$	0, 1
H35-80-N-2	80	$5 \cdot 10^{13}$	0, 1
H35-80-N-3	80	$1 \cdot 10^{14}$	1
H35-80-N-5	80	$2 \cdot 10^{15}$	1, 2, 3, 4
H35-80-N-6	80	$1 \cdot 10^{14}$	0, 1
H35-80-N-7	80	$5 \cdot 10^{14}$	0, 1
H35-80-N-8	80	$1 \cdot 10^{15}$	0, 1
H35-80-N-9	80	$2 \cdot 10^{15}$	0, 1
H35-200-N-1	200	$1 \cdot 10^{13}$	0, 1
H35-200-N-2	200	$5 \cdot 10^{13}$	0, 1
H35-200-N-3	200	$1 \cdot 10^{14}$	1
H35-200-N-4	200	$5.5 \cdot 10^{14}$	1
H35-200-N-5	200	$2 \cdot 10^{15}$	1, 2, 3, 4
H35-1000-N-1	1000	$1 \cdot 10^{13}$	0, 1
H35-1000-N-2	1000	$5 \cdot 10^{13}$	0, 1
H35-1000-N-3	1000	$1 \cdot 10^{14}$	1
H35-1000-N-4	1000	$5.5 \cdot 10^{14}$	1
H35-1000-N-5	1000	$2 \cdot 10^{15}$	1, 2, 3, 4

BIBLIOGRAPHY

[1] The ATLAS Collaboration. *ATLAS: a 25-year insider story of the LHC experiment*. Advanced series on directions in high energy physics. Singapore: World Scientific, 2019. DOI: 10.1142/11030.

[2] M. Brice. "Aerial View of the CERN taken in 2008." 2008. URL: http://cds.cern.ch/record/1295244.

[3] The ALICE Collaboration. "The ALICE experiment at the CERN LHC". In: *Journal of Instrumentation* 3.08 (2008), S08002–S08002. DOI: 10.1088/1748-0221/3/08/s08002.

[4] The ATLAS Collaboration. "The ATLAS Experiment at the CERN Large Hadron Collider". In: *Journal of Instrumentation* 3.08 (2008), S08003–S08003. DOI: 10.1088/1748-0221/3/08/s08003.

[5] The CMS Collaboration. "The CMS experiment at the CERN LHC". In: *Journal of Instrumentation* 3.08 (2008), S08004–S08004. DOI: 10.1088/1748-0221/3/08/s08004.

[6] The LHCb Collaboration. "The LHCb Detector at the LHC". In: *Journal of Instrumentation* 3.08 (2008), S08005–S08005. DOI: 10.1088/1748-0221/3/08/s08005.

[7] E. Mobs. "The CERN accelerator complex - August 2018. Complexe des accélérateurs du CERN - Août 2018". General Photo. 2018. URL: https://cds.cern.ch/record/2636343.

[8] L. Evans and P. Bryant. "LHC Machine". In: *Journal of Instrumentation* 3.08 (2008), S08001–S08001. DOI: 10.1088/1748-0221/3/08/s08001.

[9] *ATLAS Experiment – Public Results*. 2018. URL: https://twiki.cern.ch/twiki/bin/view/AtlasPublic/LuminosityPublicResultsRun2#Pileup_Interactions_and_Data_Tak.

[10] *LHC/HL-LHC Plan*. URL: https://project-hl-lhc-industry.web.cern.ch/content/project-schedule.

[11] G. Apollinari et al. "Chapter 1: High Luminosity Large Hadron Collider HL-LHC. High Luminosity Large Hadron Collider HL-LHC". In: *CERN Yellow Report* arXiv:1705.08830. 5 (2017). 21 pages, chapter in High-Luminosity Large Hadron Collider (HL-LHC) : Preliminary Design Report, 1–19. 21 p. DOI: 10.5170/CERN-2015-005.1.

[12] B. Schmidt. "The High-Luminosity upgrade of the LHC: Physics and Technology Challenges for the Accelerator and the Experiments". In: *Journal of Physics: Conference Series* 706 (2016), p. 022002. DOI: 10.1088/1742-6596/706/2/022002.

[13] M Capeans et al. *ATLAS Insertable B-Layer Technical Design Report*. Tech. rep. CERN-LHCC-2010-013. ATLAS-TDR-19. 2010. URL: https://cds.cern.ch/record/1291633.

[14] I. Peric et al. "The FEI3 readout chip for the ATLAS pixel detector". In: *Nucl. Instrum. Meth.* A565 (2006), pp. 178–187. DOI: 10.1016/j.nima.2006.05.032.

[15] A. La Rosa. *ATLAS Pixel Detector: Operational Experience and Run-1 to Run-2 Transition*. Tech. rep. arXiv:1410.6347. ATL-INDET-PROC-2014-007. Comments: presented at VERTEX 2014 - 23rd International Workshop on Vertex Detectors, Doksy, Czech Republic, 15 Sep 2014. PoS(Vertex2014)001. Geneva: CERN, 2014. DOI: 10.22323/1.227.0001.

[16] The FE-I4 Collaboration. *The FE-I4B Integrated Circuit Guide*. Tech. rep. 2014. URL: https://indico.cern.ch/event/261840/contributions/1594374/attachments/462649/641213/FE-I4B_V2.3.pdf.

[17] S. Grinstein. "The ATLAS Forward Proton Detector (AFP)". In: *Nuclear and Particle Physics Proceedings* 273-275 (2016). 37th International Conference on High Energy Physics (ICHEP), pp. 1180 –1184. ISSN: 2405-6014. DOI: 10.1016/j.nuclphysbps.2015.09.185.

[18] A. Ruiz Martínez. "The Run-2 ATLAS Trigger System". In: *Journal of Physics: Conference Series* 762 (2016), p. 012003. DOI: 10.1088/1742-6596/762/1/012003.

[19] M. zur Nedden. "The LHC Run 2 ATLAS trigger system: design, performance and plans". In: *Journal of Instrumentation* 12.03 (2017), pp. C03024–C03024. DOI: 10.1088/1748-0221/12/03/c03024.

[20] The ATLAS Collaboration. "Observation of a new particle in the search for the Standard Model Higgs boson with the ATLAS detector at the LHC". In: *Physics Letters B* 716.1 (2012), pp. 1 –29. ISSN: 0370-2693. DOI: https://doi.org/10.1016/j.physletb.2012.08.020.

[21] The CMS Collaboration. "Observation of a new boson at a mass of 125 GeV with the CMS experiment at the LHC". In: *Physics Letters B* 716.1 (2012), pp. 30 –61. ISSN: 0370-2693. DOI: https://doi.org/10.1016/j.physletb.2012.08.021.

[22] The ALEPH, DELPHI, L3 and OPAL Collaborations. "Search for the Standard Model Higgs boson at LEP". In: *Physics Letters B* 565 (2003), pp. 61 –75. ISSN: 0370-2693. DOI: 10.1016/S0370-2693(03)00614-2.

[23] ALEPH Collaboration, CDF Collaboration, Do Collaboration, DELPHI Collaboration, L3 Collaboration, OPAL Collaboration, SLD Collaboration, LEP Electroweak Working Group, Tevatron Electroweak Working Group, SLD electroweak and heavy flavour groups. *Precision Electroweak Measurements and Constraints on the Standard Model*. Tech. rep. arXiv:1012.2367. 2010. URL: https://cds.cern.ch/record/1313716.

[24] M. Tanabashi et al. "Review of Particle Physics". In: *Phys. Rev. D* 98 (3 2018), p. 030001. DOI: 10.1103/PhysRevD.98.030001.

[25] The ATLAS Collaboration. "Evidence for the spin-0 nature of the Higgs boson using ATLAS data". In: *Physics Letters B* 726.1 (2013), pp. 120 –144. ISSN: 0370-2693. DOI: https://doi.org/10.1016/j.physletb.2013.08.026.

[26] The ATLAS Collaboration. *Combined measurements of Higgs boson production and decay using up to 80 fb^{-1} of proton-proton collision data at $\sqrt{s} = 13$ TeV collected with the ATLAS experiment*. Tech. rep. arXiv:1909.02845. Geneva: CERN, 2019. URL: http://cds.cern.ch/record/2688596.

[27] The ATLAS collaboration. "Evidence for the Higgs-boson Yukawa coupling to tau leptons with the ATLAS detector". In: *Journal of High Energy Physics* 2015.4 (2015), p. 117. ISSN: 1029-8479. DOI: 10.1007/JHEP04(2015)117.

[28] The ATLAS Collaboration. "Observation of $H \to b\bar{b}$ decays and VH production with the ATLAS detector". In: *Physics Letters B* 786 (2018), pp. 59 –86. ISSN: 0370-2693. DOI: https://doi.org/10.1016/j.physletb.2018.09.013.

[29] *Standard Model Summary Plots Summer 2019*. Tech. rep. ATL-PHYS-PUB-2019-024. Geneva: CERN, 2019. URL: http://cds.cern.ch/record/2682186.

[30] The ATLAS Collaboration. "Measurement of the Inelastic Proton-Proton Cross Section at $\sqrt{s} = 13$ TeV with the ATLAS Detector at the LHC". In: *Phys. Rev. Lett.* 117 (18 2016), p. 182002. DOI: 10.1103/PhysRevLett.117.182002.

[31] The ATLAS collaboration. "Measurement of inclusive jet and dijet cross-sections in proton-proton collisions at $\sqrt{s} = 13$ TeV with the ATLAS detector". In: *Journal of High Energy Physics* 2018.5 (2018), p. 195. ISSN: 1029-8479. DOI: 10.1007/JHEP05(2018)195.

[32] ATLAS Collaboration. "Search for new phenomena in dijet events using 37 fb^{-1} of pp collision data collected at $\sqrt{s} = 13$ TeV with the ATLAS detector". In: *Phys. Rev. D* 96 (5 2017), p. 052004. DOI: 10.1103/PhysRevD.96.052004.

[33] The ATLAS collaboration. "Constraints on mediator-based dark matter and scalar dark energy models using $\sqrt{s} = 13$ TeV pp collision data collected by the ATLAS detector". In: *Journal of High Energy Physics* 2019.5 (2019), p. 142. ISSN: 1029-8479. DOI: 10.1007/JHEP05(2019)142.

[34] The ATLAS Collaboration. "Search for long-lived, weakly interacting particles that decay to displaced hadronic jets in proton-proton collisions at $\sqrt{s} = 8$ TeV with the ATLAS detector". In: *Phys. Rev. D* 92 (1 2015), p. 012010. DOI: 10.1103/PhysRevD.92.012010.

[35] The ATLAS Collaboration. "Search for magnetic monopoles and stable high-electric-charge objects in 13 TeV proton-proton collisions with the ATLAS detector". In: (2019). arXiv: 1905.10130 [hep-ex]. URL: https://cds.cern.ch/record/2676159.

[36] S. P. Martin. "A Supersymmetry primer". In: (1997), pp. 1–98. DOI: 10.1142/9789812839657_0001,10.1142/9789814307505_0001. arXiv: hep-ph/9709356 [hep-ph].

[37] The ATLAS Collaboration. *SUSY July 2019 Summary Plot Update*. Tech. rep. ATL-PHYS-PUB-2019-022. Geneva: CERN, 2019. URL: http://cds.cern.ch/record/2682063.

[38] The ATLAS Collaboration. "Evidence for light-by-light scattering in heavy-ion collisions with the ATLAS detector at the LHC". In: *Nature Phys.* 13.9 (2017), pp. 852–858. DOI: 10.1038/nphys4208.

[39] The ATLAS Collaboration. *Observation of light-by-light scattering in ultraperipheral Pb+Pb collisions with the ATLAS detector*. Tech. rep. ATLAS-CONF-2019-002. Geneva: CERN, 2019. URL: http://cds.cern.ch/record/2667214.

[40] "The ATLAS Collaboration". In: *Phys. Rev. Lett.* 105 (25 2010), p. 252303. DOI: 10.1103/PhysRevLett.105.252303.

[41] The ATLAS Collaboration. "Observation of Electroweak Production of a Same-Sign W Boson Pair in Association with Two Jets in pp Collisions at $\sqrt{s} = 13$ TeV with the ATLAS Detector". In: *Phys. Rev. Lett.* 123 (16 2019), p. 161801. DOI: 10.1103/PhysRevLett.123.161801. URL: https://link.aps.org/doi/10.1103/PhysRevLett.123.161801.

[42] A. Dainese et al. *Report on the Physics at the HL-LHC, and Perspectives for the HE-LHC*. Tech. rep. CERN-2019-007. Geneva, Switzerland, 2019. DOI: 10.23731/CYRM-2019-007. URL: https://cds.cern.ch/record/2703572.

[43] The ATLAS Collaboration. *Technical Design Report for the ATLAS Inner Tracker Pixel Detector*. Tech. rep. CERN-LHCC-2017-021. ATLAS-TDR-030. Geneva: CERN, 2017. URL: https://cds.cern.ch/record/2285585.

[44] The ATLAS Collaboration. *Technical Design Report for the ATLAS Inner Tracker Strip Detector*. Tech. rep. CERN-LHCC-2017-005. ATLAS-TDR-025. Geneva: CERN, 2017. URL: https://cds.cern.ch/record/2257755.

[45] C. ATLAS. *Letter of Intent for the Phase-II Upgrade of the ATLAS Experiment*. Tech. rep. CERN-LHCC-2012-022. LHCC-I-023. Draft version for comments. Geneva: CERN, 2012. URL: https://cds.cern.ch/record/1502664.

[46] The ATLAS Collaboration. "Simulated HL-LHC collision event in the ATLAS detector". General Photo. 2019. URL: https://cds.cern.ch/record/2674770.

[47] T. G. McCarthy. "Upgrade of the ATLAS liquid argon calorimeters for the high-luminosity LHC". In: *2016 IEEE Nuclear Science Symposium, Medical Imaging Conference and Room-Temperature Semiconductor Detector Workshop (NSS/MIC/RTSD)*. 2016, pp. 1–7. DOI: 10.1109/NSSMIC.2016.8069859.

[48] K. Hildebrand. "Upgrade of the ATLAS Hadronic Tile Calorimeter for the High Luminosity LHC". In: *Nuovo Cim.* C40.6 (2018), p. 197. DOI: 10.1393/ncc/i2017-17197-y.

[49] C. Amelung. "Upgrade of the ATLAS muon system for the HL-LHC". In: *Nuclear Instruments and Methods in Physics Research Section A: Accelerators, Spectrometers, Detectors and Associated Equipment* 936 (2019). Frontier Detectors for Frontier Physics: 14th Pisa Meeting on Advanced Detectors, pp. 420 –423. ISSN: 0168-9002. DOI: https://doi.org/10.1016/j.nima.2018.09.005.

[50] F. Pastore. "Upgrades of the ATLAS trigger system". In: *PoS* EPS-HEP2017 (2017), p. 510. DOI: 10.22323/1.314.0510.

[51] M. Elsing et al. *Final Report of the second ITk Pixel Layout Task Force*. Tech. rep. ATL-ITK-INT-2019-001. Geneva: CERN, 2019. URL: https://cds.cern.ch/record/2692192.

[52] M. Garcia-Sciveres and F. Loddo. *RD53B Manual*. Tech. rep. CERN-RD53-PUB-19-002. Geneva: CERN, 2019. URL: https://cds.cern.ch/record/2665301.

[53] *RD-53 Collaboration*. URL: https://rd53.web.cern.ch/rd53.

[54] K. G. McKay. "A. Germanium Counter". In: *Phys. Rev.* 76 (10 1949), pp. 1537–1537. DOI: 10.1103/PhysRev.76.1537.

[55] K. G. McKay. "Electron-Hole Production in Germanium by Alpha-Particles". In: *Phys. Rev.* 84 (4 1951), pp. 829–832. DOI: 10.1103/PhysRev.84.829.

[56] "A new apparatus in nuclear physics for the investigation of β- and γ-rays. Part I". In: *Physica* 16.6 (1950), pp. 505 – 516. ISSN: 0031-8914. DOI: https://doi.org/10.1016/0031-8914(50)90007-3.

[57] B. Tore Knudsen. "Presentation of the WA97 experiment at CERN". In: *Czechoslovak Journal of Physics* 47.9 (1997), pp. 925–929. DOI: 10.1023/A:1021200315694.

[58] P. A. Aarnio et al. "The DELPHI detector at LEP". In: *Nucl. Instrum. Meth.* A303 (1991), pp. 233–276. DOI: 10.1016/0168-9002(91)90793-P.

[59] H. Ohnishi et al. "The NA60 experiment at CERN SPS: first results and prospects". In: *Nucl. Phys. A* 364 (2004), pp. 49–52. DOI: 10.1016/j.nuclphysa.2004.01.009.

[60] M. Turala. "Silicon tracking detectors—historical overview". In: *Nuclear Instruments and Methods in Physics Research Section A: Accelerators, Spectrometers, Detectors and Associated Equipment* 541.1 (2005). Development and Application of Semiconductor Tracking Detectors, pp. 1 –14. ISSN: 0168-9002. DOI: 10.1016/j.nima.2005.01.032.

[61] S. Sze and K. N. Kwok. *Physics of Semiconductor Devices; 3rd ed.* Hoboken, NJ: Wiley, 2007. DOI: 10.1002/0470068329.

[62] G. Lutz. *Semiconductor radiation detectors: device physics*. Berlin: Springer, 1999.

[63] Wikipedia contributors. *Orbital hybridisation sp3*. URL: https://en.wikipedia.org/wiki/Orbital_hybridisation#/media/File:AE4h.svg.

[64] G. Aad et al. "ATLAS pixel detector electronics and sensors". In: *Journal of Instrumentation* 3.07 (2008), P07007–P07007. DOI: 10.1088/1748-0221/3/07/p07007.

[65] S. Parker et al. "3D — A proposed new architecture for solid-state radiation detectors". In: *Nuclear Instruments and Methods in Physics Research Section A: Accelerators, Spectrometers, Detectors and Associated Equipment* 395.3 (1997). Proceedings of the Third International Workshop on Semiconductor Pixel Detectors for Particles and X-rays, pp. 328 –343. ISSN: 0168-9002. DOI: https://doi.org/10.1016/S0168-9002(97)00694-3.

[66] M Garcia-Sciveres. *ATLAS Experiment Pixel Detector Upgrades*. Tech. rep. ATL-UPGRADE-PROC-2011-006. ATL-UPGRADE-PROC-2011-006. Geneva: CERN, 2011. URL: http://cds.cern.ch/record/1384138.

[67] G. P. Summers et al. "Damage correlations in semiconductors exposed to gamma, electron and proton radiations". In: *IEEE Transactions on Nuclear Science* 40.6 (1993), pp. 1372–1379. ISSN: 0018-9499. DOI: 10.1109/23.273529.

[68] M. Huhtinen and P. Aarnio. "Pion induced displacement damage in silicon devices". In: *Nuclear Instruments and Methods in Physics Research Section A: Accelerators, Spectrometers, Detectors and Associated Equipment* 335.3 (1993), pp. 580 –582. ISSN: 0168-9002. DOI: https://doi.org/10.1016/0168-9002(93)91246-J.

[69] A. Konobeyev et al. "Neutron displacement cross-sections for structural materials below 800 MeV". In: *Journal of Nuclear Materials* 186.2 (1992), pp. 117 –130. ISSN: 0022-3115. DOI: https://doi.org/10.1016/0022-3115(92)90328-I.

[70] P. Griffin et al. *SNL RML recommended dosimetry cross section compendium*. Tech. rep. SAND-92-0094. Nov. 1993. DOI: 10.2172/10115441.

[71] G. Lindström et al. *3rd RD48 status report: the ROSE collaboration (R&D on silicon for future experiments)*. Tech. rep. CERN-LHCC-2000-009. Geneva: CERN, 1999. URL: http://cds.cern.ch/record/421210.

[72] D. Bechevet et al. "Results of irradiation tests on standard planar silicon detectors with 7–10MeV protons". In: *Nuclear Instruments and Methods in Physics Research Section A: Accelerators, Spectrometers, Detectors and Associated Equipment* 479.2 (2002), pp. 487 –497. ISSN: 0168-9002. DOI: https://doi.org/10.1016/S0168-9002(01)00925-1.

[73] M. Moll. "Radiation damage in silicon particle detectors: Microscopic defects and macroscopic properties". PhD thesis. Hamburg U., 1999. URL: http://www-library.desy.de/cgi-bin/showprep.pl?desy-thesis99-040.

[74] ams AG. URL: http://ams.com.

[75] LFoundry GmbH. URL: http://www.lfoundry.com/.

[76] Tower Semiconductor Ltd. (TowerJazz). URL: https://towerjazz.com/.

[77] T. Wang et al. "Development of a Depleted Monolithic CMOS Sensor in a 150 nm CMOS Technology for the ATLAS Inner Tracker Upgrade". In: *Journal of Instrumentation* 12.01 (2017), pp. C01039–C01039. DOI: 10.1088/1748-0221/12/01/c01039.

[78] P. Riedler. "Upgrade of the ALICE Inner Tracking System". In: *Nuclear Physics A* 956 (2016). The XXV International Conference on Ultrarelativistic Nucleus-Nucleus Collisions: Quark Matter 2015, pp. 866 –869. ISSN: 0375-9474. DOI: https://doi.org/10.1016/j.nuclphysa.2016.02.061.

[79] W. Snoeys et al. "A process modification for CMOS monolithic active pixel sensors for enhanced depletion, timing performance and radiation tolerance". In: *Nuclear Instruments and Methods in Physics Research Section A: Accelerators, Spectrometers, Detectors and Associated Equipment* 871 (2017), pp. 90 –96. ISSN: 0168-9002. DOI: https://doi.org/10.1016/j.nima.2017.07.046.

[80] I Peric. "Active pixel sensors in high-voltage CMOS technologies for ATLAS". In: *Journal of Instrumentation* 7.08 (2012), pp. C08002–C08002. DOI: 10.1088/1748-0221/7/08/c08002.

[81] F. A. Di Bello. "Search for boosted Higgs boson and other resonances decaying into b-quark pairs using the ATLAS detector and studies of CMOS pixel sensors for the HL-LHC". PhD thesis. Université de Genève, 2019. URL: http://dpnc.unige.ch/THESES/THESE_DIBELLO.pdf.

[82] I. Perić. *HVCMOS2FEI4 Detector Description*.

[83] A Miucci et al. "Radiation-hard Active Pixel Sensors for HL-LHC Detector Upgrades based on HV-CMOS Technology". In: *Journal of Instrumentation* 9.05 (2014), pp. C05064–C05064. DOI: 10.1088/1748-0221/9/05/c05064.

[84] T. Haas. "A pixel telescope for detector R&D for an international linear collider". In: *Nuclear Instruments and Methods in Physics Research Section A: Accelerators, Spectrometers, Detectors and Associated Equipment* 569.1 (2006). Proceedings of the 14th International Workshop on Vertex Detectors, pp. 53 –56. ISSN: 0168-9002. DOI: https://doi.org/10.1016/j.nima.2006.09.011.

[85] M. Benoit et al. "The FE-I4 telescope for particle tracking in testbeam experiments". In: *Journal of Instrumentation* 11.07 (2016), P07003–P07003. DOI: 10.1088/1748-0221/11/07/p07003.

[86] B. Ristic. "Measurements on HV-CMOS active sensors after irradiation to HL-LHC fluences". In: *Journal of Instrumentation* 10.04 (2015), pp. C04007–C04007. DOI: 10.1088/1748-0221/10/04/c04007.

[87] M. Benoit et al. "Results of the 2015 testbeam of a 180 nm AMS High-Voltage CMOS sensor prototype". In: *Journal of Instrumentation* 11.07 (2016), P07019–P07019. DOI: 10.1088/1748-0221/11/07/p07019.

[88] M. Benoit et al. "Testbeam results of irradiated ams H18 HV-CMOS pixel sensor prototypes". In: *Journal of Instrumentation* 13.02 (2018), P02011–P02011. DOI: 10.1088/1748-0221/13/02/p02011.

[89] E. Vilella et al. "Prototyping of an HV-CMOS demonstrator for the High Luminosity-LHC upgrade". In: *Journal of Instrumentation* 11.01 (2016), pp. C01012–C01012. DOI: 10.1088/1748-0221/11/01/c01012.

[90] E. Vilella et al. *H35DEMO documentation*. URL: https://hep.ph.liv.ac.uk/twiki/pub/CleanroomTestStands/H35DEMO/H35DEMO_documentation_v1.0_20160111.pdf.

[91] I. Perić et al. "The FEI3 readout chip for the ATLAS pixel detector". In: *Nuclear Instruments and Methods in Physics Research Section A: Accelerators, Spectrometers, Detectors and Associated Equipment* 565.1 (2006), pp. 178 –187. ISSN: 0168-9002. DOI: https://doi.org/10.1016/j.nima.2006.05.032.

[92] I. Perić et al. "A high-voltage pixel sensor for the ATLAS upgrade". In: *Nuclear Instruments and Methods in Physics Research Section A: Accelerators, Spectrometers, Detectors and Associated Equipment* 924 (2019). 11th International Hiroshima Symposium on Development and Application of Semiconductor Tracking Detectors, pp. 99 –103. ISSN: 0168-9002. DOI: https://doi.org/10.1016/j.nima.2018.06.060.

[93] I. Perić et al. *Description of the ATLASPIX_Simple and ATLASPIX_M2*.

[94] D. Sultan et al. "Electrical characterization of AMS aH18 HV-CMOS after neutrons and protons irradiation". In: *Journal of Instrumentation* 14.05 (2019), pp. C05003–C05003. DOI: 10.1088/1748-0221/14/05/c05003.

[95] I. Perić et al. *ATLASPIX3 user manual – Version 1*.

[96] D. M. S. Sultan et al. "Electrical Characterization of 180 nm ATLASPix2 HV-CMOS Monolithic Prototypes for the High-Luminosity LHC". In: (2019). arXiv: 1910.11750 [physics.ins-det].

[97] V. Eremin et al. "Development of transient current and charge techniques for the measurement of effective net concentration of ionized charges (N_{eff}) in the space charge region of p-n junction detectors". In: *Nuclear Instruments and Methods in Physics Research Section A: Accelerators, Spectrometers, Detectors and Associated Equipment* 372.3 (1996), pp. 388 –398. ISSN: 0168-9002. DOI: 10.1016/0168-9002(95)01295-8.

[98] C. Schinke et al. "Uncertainty analysis for the coefficient of band-to-band absorption of crystalline silicon". In: *AIP Advances* 5.6 (2015), p. 067168. DOI: 10.1063/1.4923379.

[99] Particulars advanced measurements system. URL: http://particulars.si.

[100] *Particulars Laser – Hardware Manual*. URL: http://www.particulars.si/downloads/ParticularsLaserHardware-UserGuideV2.0.pdf.

[101] *Beam Monitor for Scanning-TCT*. URL: http://www.particulars.si/downloads/ParticularsBias-BeamMonitor-InBeam.pdf.

[102] Standa Ltd. URL: http://www.standa.lt.

[103] *Particulars Bias-T*. URL: http://www.particulars.si/downloads/ParticularsBias-T-Manuals.pdf.

[104] *Particulars Wide Band Current Amplifiers*. URL: http://www.particulars.si/downloads/ParticularsAmps-Manuals.pdf.

[105] S. Ritt. *DRS4 Evaluation Board User's Manual*. URL: https://www.psi.ch/sites/default/files/import/drs/DocumentationEN/manual_rev51.pdf.

[106] *Scanning TCT data acqusition software*. URL: http://www.particulars.si/downloads/ScanTCT_DAQ-V1.81.pdf.

[107] *Particulars Lasers – Software Manual*. URL: http://www.particulars.si/downloads/ParticularsLaserControl-UserGuide.pdf.

[108] E. Zaffaroni. *vtct*. URL: https://gitlab.cern.ch/ezaffaro/vtct.

[109] *The HDF5 library & file format*. URL: https://www.hdfgroup.org/solutions/hdf5/.

[110] *TCTAnalyse library*. URL: http://particulars.si/TCTAnalyse/index.html.

[111] J. Anders et al. *A facility for radiation hardness studies based on the Bern medical cyclotron*. 2018. arXiv: 1803.01939 [physics.ins-det].

[112] F. Ravotti et al. *Upgrade scenarios for irradiation lines:: Upgrade of the Proton Irradiation Facility in the CERN PS EAST AREA*. 2014. URL: https://cds.cern.ch/record/1951308.

[113] B. Gkotse et al. *The Beam Profile Monitoring System for the IRRAD Proton Facility at the CERN PS East Area*. 2015. URL: https://cds.cern.ch/record/2235836.

[114] A. Curioni et al. "Single- and multi-foils ^{27}Al(p, 3pn)^{24}Na activation technique for monitoring the intensity of high-energy beams". In: *Nuclear Instruments and Methods in Physics Research Section A: Accelerators, Spectrometers, Detectors and Associated Equipment* 858 (2017), pp. 101–105. ISSN: 0168-9002. DOI: 10.1016/j.nima.2017.03.058.

[115] I. Mateu et al. *NIEL hardness factor determination for the new proton irradiation facility at CERN*. 2016. URL: https://cds.cern.ch/record/2162852.

[116] A. Kolšek et al. "Using TRIGA Mark II research reactor for irradiation with thermal neutrons". In: *Nuclear Engineering and Design* 283 (2015), pp. 155 –161. ISSN: 0029-5493. DOI: 10.1016/j.nucengdes.2014.03.012.

[117] K. Ambrožič et al. "Computational analysis of the dose rates at JSI TRIGA reactor irradiation facilities". In: *Applied Radiation and Isotopes* 130 (2017), pp. 140 –152. ISSN: 0969-8043. DOI: 10.1016/j.apradiso.2017.09.022.

[118] J. Anders et al. "Charge collection characterisation with the Transient Current Technique of the ams H35DEMO CMOS detector after proton irradiation". In: *Journal of Instrumentation* 13.10 (2018), P10004–P10004. DOI: 10.1088/1748-0221/13/10/p10004.

[119] M. F. García et al. "Radiation hardness studies of neutron irradiated CMOS sensors fabricated in the ams H18 high voltage process". In: *Journal of Instrumentation* 11.02 (2016), P02016–P02016. DOI: 10.1088/1748-0221/11/02/p02016.

[120] I. Mandić et al. "Charge-collection properties of irradiated depleted CMOS pixel test structures". In: *Nuclear Instruments and Methods in Physics Research Section A: Accelerators, Spectrometers, Detectors and Associated Equipment* 903 (2018), pp. 126 –133. ISSN: 0168-9002. DOI: https://doi.org/10.1016/j.nima.2018.06.062.

[121] A. Affolder et al. "Charge collection studies in irradiated HV-CMOS particle detectors". In: *Journal of Instrumentation* 11.04 (2016), P04007–P04007. DOI: 10.1088/1748-0221/11/04/p04007.

[122] D. Muenstermann. "edge-TCT results from AMS H18 HV-CMOS test chips irradiated with 800 MeV protons". In: 13th "Trento" Workshop on Advanced Silicon Radiation Detectors. URL: https://indico.cern.ch/event/666427/contributions/2885111/.

[123] *ATLAS Experiment - Public Results*. 3–2018. URL: https://twiki.cern.ch/twiki/bin/view/AtlasPublic/RadiationSimulationPublicResults#Phase_II_Upgrade_Mar_2018.

[124] J. Gosewisch and A. Dierlamm. "Sequence Dependent Mixed Irradiations". In: 33rd RD50 Workshop. URL: https://indico.cern.ch/event/754063/contributions/3222724/.

[125] P. Abbon et al. "The COMPASS experiment at CERN". In: *Nuclear Instruments and Methods in Physics Research Section A: Accelerators, Spectrometers, Detectors and Associated Equipment* 577.3 (2007), pp. 455 –518. ISSN: 0168-9002. DOI: https://doi.org/10.1016/j.nima.2007.03.026.

[126] G. Ruggiero. "Status of the CERN NA62 Experiment". In: *Journal of Physics: Conference Series* 800 (2017), p. 012023. DOI: 10.1088/1742-6596/800/1/012023.

[127] *North Area*. URL: https://en-ea-le.web.cern.ch/experimental_areas/north-area.

[128] M. Vicente Barreto Pinto. "New pixel-detector technologies for the ATLAS ITk upgrade and the CLIC vertex detector". PhD thesis. Université de Genève, 2019. URL: http://dpnc.unige.ch/THESES/THESE_VICENTE_BARRETO_PINTO.pdf.

[129] *How to control the North Area beam lines*. URL: https://sba.web.cern.ch/sba/Documentations/How2controlNAbeams.htm.

[130] *Fermilab Test Beam Facility*. URL: https://ftbf.fnal.gov/.

[131] *Graphics: Fermilab*. URL: https://vms.fnal.gov/asset/detail?recid=1823624.

[132] M. Vicente Barreto Pinto. *Private communications*.

[133] D. Nelson. *HSIO II Development Platform Users Guide*. URL: https://www.slac.stanford.edu/~djn/Atlas/HSIO_II/HSIO%20II%20Development%20Platform%20Users%20Guide_rev3_c03.pdf.

[134] H. Liu et al. "Development of a modular test system for the silicon sensor R&D of the ATLAS Upgrade". In: *Journal of Instrumentation* 12.01 (2017), P01008–P01008. DOI: 10.1088/1748-0221/12/01/p01008.

[135] *Peary Caribou DAQ Software*. URL: https://peary-caribou.web.cern.ch/peary-caribou/.

[136] *meta-caribou*. URL: https://gitlab.cern.ch/Caribou/meta-caribou.

[137] *minidcs*. URL: https://gitlab.cern.ch/msmk/minidcs.

[138] *Proteus beam telescope reconstruction*. URL: https://doi.org/10.5281/zenodo.2586736.

[139] M. Kiehn. *Private communications*.

[140] *Tom's Obvious, Minimal Language*. URL: https://github.com/toml-lang/toml.

[141] C. Kleinwort. "General broken lines as advanced track fitting method". In: *Nuclear Instruments and Methods in Physics Research Section A: Accelerators, Spectrometers, Detectors and Associated Equipment* 673 (2012), pp. 107 –110. ISSN: 0168-9002. DOI: https://doi.org/10.1016/j.nima.2012.01.024.

[142] M. Benoit et al. "Test beam measurement of ams H35 HV-CMOS capacitively coupled pixel sensor prototypes with high-resistivity substrate". In: *Journal of Instrumentation* 13.12 (2018), P12009–P12009. DOI: 10.1088/1748-0221/13/12/p12009.

[143] W. Shockley and W. T. Read. "Statistics of the Recombinations of Holes and Electrons". In: *Phys. Rev.* 87 (5 1952), pp. 835–842. DOI: 10.1103/PhysRev.87.835.

[144] D. Sultan et al. "Characterization of the first double-sided 3D radiation sensors fabricated at FBK on 6-inch silicon wafers". In: *Journal of Instrumentation* 10.12 (2015), pp. C12009–C12009. DOI: 10.1088/1748-0221/10/12/c12009.

[145] A Chilingarov. "Temperature dependence of the current generated in Si bulk". In: *Journal of Instrumentation* 8.10 (2013), P10003–P10003. DOI: 10.1088/1748-0221/8/10/p10003.

[146] N. A. Tehrani et al. "Capacitively coupled hybrid pixel assemblies for the CLIC vertex detector". In: *Nuclear Instruments and Methods in Physics Research Section A: Accelerators, Spectrometers, Detectors and Associated Equipment* 823 (2016), pp. 1 –8. ISSN: 0168-9002. DOI: https://doi.org/10.1016/j.nima.2016.03.072.

[147] M. Benoit. *Private communications*.

[148] D. Dannheim et al. *Detector technologies for CLIC*. Ed. by D. Dannheim. CERN Yellow Reports: Monographs. 2019. DOI: 10.23731/CYRM-2019-001.